Climate impacts of atmospheric low volatility organic compounds

Kamalika Sengupta

Submitted in accordance with the requirements for the degree of

Doctor of Philosophy

The University of Leeds

School of Earth and Environment

October 2017

Declaration of Authorship

The candidate confirms that the work submitted is her own, except where work which has formed part of jointly-authored publications have been included. The contribution of the candidate and the other authors to this work have been explicitly indicated below. The candidate confirms that appropriate credit has been given within the thesis where reference has been made to the work of others.

The work contained in Chapter 3 forms the basis of a jointly-authored manuscript published in Proceedings of the National Academy of Sciences (details below). All the work presented in Chapter 3 were done prior to the work presented in Gordon et al. (2016). The model set-up and results of Chapter 3 are broadly similar to that used in Gordon et al. (2016) but with some changes. Conclusions reached in Chapter 3 and Gordon et al. (2016) are essentially the same.

The new parameterisation for nucleation implemented in the model was provided by J. Almeida and the CLOUD consortium. Modelling the growth of sub-3 nm particles in GLOMAP-mode was implemented by K. Pringle. All model simulations used in Chapter 3 including the implementation of parameterisation were performed by the candidate. New oxidant fields used in Chapter 3 were provided by N. Richards and implemented in the model by the candidate. New approach to calculate offline cloud droplet number concentrations was implemented in the model by H. Gordon. All tests related to model development presented in this thesis were done by the

candidate. All radiative forcing calculations shown in Chapter 3 were performed by A. Rap. The analysis of results in Chapter 3 was carried out by the candidate with guidance from K. Carslaw, J. Kirkby, H. Gordon and the CLOUD team. Publications associated with Chapter 3 are:

- Kirkby, J., Duplissy, J., Sengupta, K., Frege, C., Gordon, H., Williamson, C., ... & Tröstl, J. (2016). Ion-induced nucleation of pure biogenic particles. Nature, 533(7604), 521-526.

- Gordon, H., Sengupta, K., Rap, A., Duplissy, J., Frege, C., Williamson, C., ... & Tröstl, J. (2016). Reduced anthropogenic aerosol radiative forcing caused by biogenic new particle formation. Proceedings of the National Academy of Sciences, 113(43), 12053-12058.

Other CLOUD publications with minor contribution (such as data collection/comment on manuscripts/model simulations) of the candidate :

- Tröstl, J., Chuang, W. K., Gordon, H., Heinritzi, M., Yan, C., Molteni, U., ... & Simon, M. (2016). The role of low-volatility organic compounds in initial particle growth in the atmosphere. Nature, 533(7604), 527-531.

- Dunne, E. M., Gordon, H., Kürten, A., Almeida, J., Duplissy, J., Williamson, C., ... & Barmet, P. (2016). Global atmospheric particle formation from CERN CLOUD measurements. Science, 354(6316), 1119-1124.

- Nichman, L., Järvinen, E., Dorsey, J., Connolly, P., Duplissy, J., Fuchs, C., ... & Schnaiter, M. (2017). Intercomparison study and optical asphericity measurements of small ice particles in the CERN CLOUD experiment. Atmospheric Measurement Techniques, 10(9), 3231.

- Kim, J., Ahlm, L., Yli-Juuti, T., Lawler, M., Keskinen, H., Tröstl, J., ... & Donahue, N. M. (2016). Hygroscopicity of nanoparticles produced from homogeneous nucleation in the CLOUD experiments. Atmospheric Chemistry and Physics, 16(1), 293-304.

- Järvinen, E., Ignatius, K., Nichman, L., Kristensen, T. B., Fuchs, C., Hoyle, C. R., ... & Ehrhart, S. (2016). Observation of viscosity transition in α-pinene secondary organic aerosol. Atmospheric Chemistry and Physics, 16(7), 4423-4438.

The work contained in Chapter 4 forms the basis of a jointly-authored manuscript in preparation to be submitted to Atmospheric Chemistry and Physics. A. Rap performed the radiative forcing calculation for this chapter. Rest of the work were designed and executed by the candidate with guidance from K. Carslaw and K. Pringle.

K. Sengupta, K. Pringle, A. Rap, C.E. Scott, K. S. Carslaw, (2017). Climatic implication of representing extremely low volatility, low volatility and semi-volatile highly oxygenated molecules in GLOMAP-mode. In preparation.

The work contained in Chapter 5 forms the basis of a jointly-authored manuscript in preparation to be submitted to Atmospheric Chemistry and Physics. Observational data used in the chapter were provided by C.L. Reddington and J. Browse. The work presented in the chapter were designed and executed by the candidate with guidance from K. Carslaw, K. Pringle and J. Johnson.

K. Sengupta, K. Pringle, J. Johnson, C.L. Reddington, J. Browse, K.S. Carslaw, (2017). Perturbed parameter ensemble study on secondary organic aerosol formation. In preparation.

Acknowledgements

I thank my supervisors Ken Carslaw and Kirsty Pringle without either of whose time, guidance and patience writing this thesis would not have been possible. I also thank Anja Schmidt for her support and encouragement.

I thank the entire CLOUD consortium and the CLOUD co-ordinator, Joachim Curtius, for the opportunity CLOUD brings to young scientists. I am grateful for the EU CLOUD-TRAIN Marie Curie Initial Training Network fellowship which made this research possible. Working within a large research team on a high-impact paper proved to be a huge learning experience for which I thank Jasper Kirkby and everyone associated with Kirkby et al. (2016). For making memories worth revisiting, I thank my fellow PhD students in the collaboration especially Anne Bernhammer, Claudia Fuchs, Antonio Dias, Robert Wagner, Leonid Nichman, Chao Yan and the Frankfurt group. I am also very grateful to Jill Craven and Sebastian Ehrhart for their helpful insights.

I have very much appreciated being a part of the Aerosol modelling group at Leeds and thank all the members for their feedback and help over the years. I especially thank Alex Rap for doing all the radiative forcing calculations shown in this thesis, Cat Scott for providing me her version of the model to start from, Nigel Richards for providing the oxidant fields used in this thesis, Carly Reddington and Jo Browse for providing observational data for Chapter 5 and Jill Johnson for her guidance

in Chapter 5. A huge thanks to Richard Rigby and IT for their prompt support whenever needed. In the last four years I have enjoyed being a part of the ICAS community with its many scientific and social events. The Friday Night Drinks (FNDs) and its attendees deserve a special vote of thanks.

For self-delegating themselves with the task of 'educating' me in the 'English' way and creating wonderful memories in the process, I thank Tim Keslake and Stewart Jennings. I thank Arjya Sarkar for his invaluable support across the Atlantic. I am immensely grateful to my parents, Debasish and Tripti, and my sister, Rebeka, for their love, support and sacrifice - which kept me going through the last four years. I thank the Jennings family for their love and Stewart Jennings for feeding me home-cooked Bengali meals the past several months of writing-up. Lastly I thank myself for embarking on and experiencing this roller-coaster ride.

Abstract

There exist huge gaps in the knowledge of how cloud-aerosol interaction affects climate. Consequently global models estimating the radiative forcing by anthropogenic aerosols show considerable discrepancy. Especially challenging to quantify is the role of volatile organic compounds in forming aerosol particles which can act as cloud condensation nuclei.

Volatile organic compounds are emitted into the atmosphere in large quantities by biogenic and anthropogenic sources. In the atmosphere they undergo chemical oxidation reactions and typically produce products that are highly oxygenated and have lower volatility. Volatility of these highly oxygenated molecules span a wide range and determine the ease with which they transfer to the aerosol phase - either via participation in new particle formation or by contributing to the growth of bigger particles. The extent to which the highly oxygenated molecules contribute to new particle formation or their subsequent growth impacts the number concentration of cloud condensation nuclei in the atmosphere. Hence to accurately estimate cloud condensation nuclei, global models need to take into account the role of highly oxygenated molecules of varying volatility in modulating the atmospheric aerosol size distribution.

In this thesis a new nucleation parameterisation based solely on highly oxygenated species of extremely low volatility is added to the model and its impact on the

estimated cloud albedo effect is assessed. The nucleation mechanism is based on the findings of the CLOUD Experiment at CERN. The implementation of this new parameterisation reduces previous model estimates of cloud albedo forcing through its impact on the pre-industrial atmosphere.

The thesis then goes on to introduce a new secondary aerosol formation scheme from highly oxygenated organic molecules based on the understanding of recent scientific advancements and assesses the effect of implementing the scheme on the estimated cloud albedo effect. Results show highly oxygenated molecules of semi-volatile nature play a significant role in determining the number concentration of cloud relevant particles. Although their higher volatility renders them incapable of new particle formation, their atmospheric abundance and contribution to the growth of particles which are relatively larger, provide an efficient pathway for producing cloud condensation nuclei in the atmosphere.

Further, an ensemble of simulations are produced and analysed to explore a 6-D parameter space based on pre-defined uncertainty ranges of these highly oxygenated molecules. The work identifies plausible and implausible regions within the 6-D space, based on model-observation comparison against three model outputs - number concentration of all particles, number concentration of CCN-relevant sized particles and organic aerosol concentration. The work provides a top-down estimate of yields of highly oxygenated molecules (that contribute to SOA formation) based on model skill score against ground-based observations. Such yields are typically based on laboratory experiments and is broadly considered to be an important reason behind the failure of global models to estimate realistic mass of secondary organic aerosols produced in the atmosphere. The work particularly highlights the importance of simulating cluster growth from low-volatility organic compounds to account for atmospheric cloud droplets.

Contents

List of Figures

List of Tables

Abbreviations

AIE	Aerosol Indirect Effect
AIF	Aerosol Indirect Forcing
BC	Black Carbon
BHN	Binary Homogeneous Nucleation
BLN	Boundary Layer Nucleation
BVOC	Biogenic Volatile Organic Compounds
CCN	Cloud Condensation Nuclei
CDNC	Cloud Droplet Number Concentration
CI-APiToF	Chemical Ionization Time-of-Flight Mass Spectrometer
CLOUD	Cosmics Leaving OUtdoor Droplets
CPC	Condensation Particle Counter
EC	Elemental Carbon
ELVOC	Extremely Low Volatility Organic Compounds
GASSP	The Global Aerosol Synthesis and Science Project
GLOMAP	Global Model of Aerosol Processes
HOM	Highly Oxygenated Molecules
IVOC	Intermediate Volatility Organic Compounds

LHS	Latin Hypercube Sampling
LVOC	Low Volatility Organic Compounds
N3	Number concentration of particles with dry diameter > 3 nm
N50	Number concentration of particles with dry diameter > 50 nm
NMBF	Normalised Mean Bias Factor
NMHC	Non-methane Hydrocarbons
PD	Present-day
PI	Pre-industrial
POA	Primary Organic Aerosol
POM	Particulate Organic Matter
PPEM	Perturbed Parameter Ensemble Member
PSM	Particle Size Magnifier
OA	Organic Aerosol
SOA	Secondary Organic Aerosol
SVOC	Semi Volatile Organic Compounds
TSS	Taylor Skill Score
UM	Unified Model
UKCA	United Kingdom Chemistry and Aerosols Model
VBS	Volatility Basis Set
VOC	Volatile Organic Compounds

Chapter 1

Introduction

1.1 Overview

Aerosols are suspended particles in the atmosphere that have been a major area of research in the last few decades because of their huge impact on the hydrological cycle, long-term climate and human health (Ramanathan et al., 2001; Menon et al., 2002). Aerosols directly influence the climate by scattering and absorbing the incoming solar radiation (Kiehl and Briegleb, 1993) but depending on their composition, diameter and the in-cloud super-saturation, aerosols may also affect the climate indirectly through their interaction with clouds. At present global models show a large diversity when quantifying the effect of cloud-aerosol interaction on climate (Forster et al., 2007; Stocker et al., 2013). A key focus of research in the last couple of decades has been to understand the evolution of aerosol particles to size ranges at which they can interact with clouds in the atmosphere.

A large fraction of atmospheric aerosol comprises of secondary organic aerosols (SOA) that are produced when volatile organic compounds (VOCs) released from biogenic or anthropogenic sources are oxidised in the atmosphere (Kanakidou et al., 2005). Currently many global models adopt a simplistic approach to simulate SOA

formation (Tsigaridis et al., 2014) using yields derived from laboratory experiments which lead to an underestimation of SOA production from VOCs (Hallquist et al., 2009; Spracklen et al., 2011b). In recent years several studies have discovered new pathways of SOA production (Riccobono et al., 2014; Kirkby et al., 2016) from previously unidentified organic compounds (Sipilä et al., 2010; Ehn et al., 2014; Tröstl et al., 2016), to date unrepresented in global models. These pathways result in the formation of new particles which subsequently grow contributing to the aerosol mass. Several studies highlight the importance of the approach adopted to model SOA formation in the atmosphere in estimating possible climatic implications (Riipinen et al., 2011; Scott et al., 2015; D'Andrea et al., 2013).

This thesis brings together the understanding of recent advances in atmospheric new particle formation (or nucleation) from the CERN CLOUD experiment (Kirkby et al., 2016) and the understanding of modelling atmospheric SOA formation from VOCs (Spracklen et al., 2011b; Scott et al., 2015) to estimate the potential impact on the first aerosol indirect effect. Further this thesis uses a perturbed parameter ensemble to explore the uncertainty space associated with SOA formation in the model.

The following sections give a brief background of the Earth's radiative balance, atmospheric aerosols and how they affect the radiative balance, what volatile organic compounds are and their role in aerosol production in the atmosphere. At the end of this chapter an outline of the thesis is provided which describes the motivation and aims for each individual chapter that follows.

1.2 The Earth's radiation balance

The Earth receives short-wave radiation emitted by the Sun and itself emits long-wave radiation back into space. When the incoming and outgoing radiation are

exactly balanced the Earth is said to be at radiative equilibrium. The balance between the incoming and outgoing radiation determines the equilibrium temperature of the Earth. Any factor that perturbs the radiative balance of the Earth can force the Earth's temperature to rise or fall and is considered a radiative forcing agent. Such perturbations can be natural, such as volcanic eruptions, or anthropogenic, such as deforestation and increase in concentrations of radiatively active trace gases in the atmosphere.

It is important to estimate the radiative forcing caused by various anthropogenic forcing agents with confidence because radiative forcing is an important component in determining the Earth's equilibrium climate sensitivity (ECS) and therefore in predicting its future climate. ECS is commonly defined in the context of radiative forcing by CO_2, referring to the equilibrium change in global mean near-surface air temperature which would result from a sustained doubling of atmospheric CO_2. The first estimates of ECS were given to be between $1.5-4.5$ °C by Charney et al. (1979). After more than three decades of extensive research, estimate of ECS remains the same (Stocker et al., 2013). The primary reason why scientists have not been able to narrow down the ECS uncertainty range is the uncertainty associated with atmospheric mechanisms that counter the warming caused by CO_2.

A dominant source of uncertainty in predicting climate change is determining the cooling effect exerted by tropospheric aerosols emitted as a result of human activities. Changes in tropospheric aerosol concentrations contribute substantially to the top-of-atmosphere radiative forcing - the magnitude of the contribution being globally comparable to that exerted by changes in greenhouse gases (GHGs) but opposite in sign (Coakley et al., 1992). The positive forcing (resulting in warming of the Earth's surface) exerted by changes in GHGs is well constrained. By contrast the negative forcing caused by changes in anthropogenic aerosols is highly uncertain

(Anderson et al., 2003; Stocker et al., 2013). The climatic impact of the change in anthropogenic aerosols is estimated by quantifying the forcing due to anthropogenic aerosols since pre-industrial times. Figure 1.1 summarises the identified mechanisms by which aerosols may exert a radiative forcing.

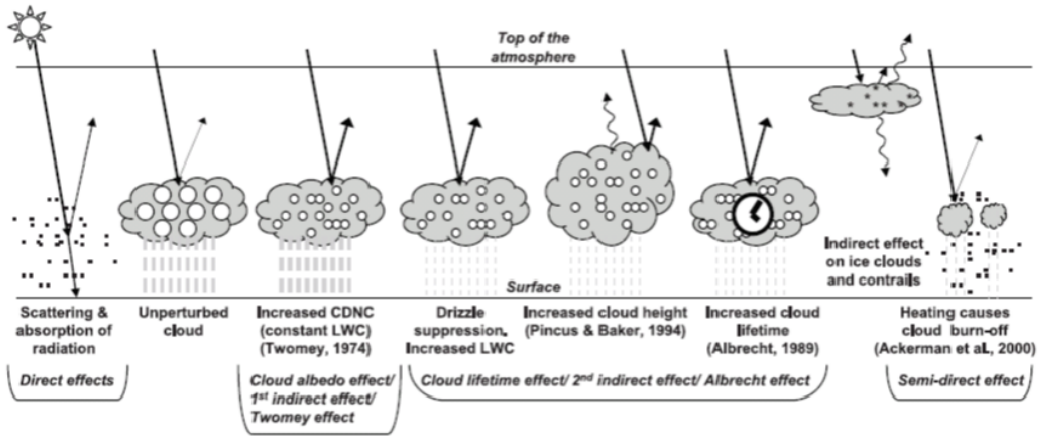

Figure 1.1: Schematic from Forster et al. (2007) showing the various cloud-aerosol interactions that have been identified as significant in modulating radiative effects. The small black dots represent aerosol particles, larger open circles represent cloud droplets, straight lines represent incident shortwave radiation, wavy line represents outgoing longwave radiation. The vertical gray dashes represent rainfall and LWC refers to cloud liquid water content.

Increase in aerosols may cause an increased scattering of incoming shortwave radiation (direct effect), localised heating and shrinking of clouds (semi-direct effect), an increase in the number of cloud droplets leading to increased reflectivity of the cloud (cloud albedo effect or the first aerosol indirect effect) and reduction in cloud droplet size leading to longer cloud lifetime (cloud lifetime effect or second aerosol indirect effect). The direct effect of aerosols is fairly constrained (Forster et al., 2007). The confidence level for estimating forcing associated with aerosol-cloud interaction (first aerosol indirect effect) is low (Stocker et al., 2013) spanning a large range from -0.3 to -1.8 W m^{-2} (Forster et al., 2007; Carslaw et al., 2013). Understanding of the other aerosol effects is poor and uncertainty in their estimates too high (Rotstayn and Liu, 2005; Levy et al., 2013). Throughout this thesis only the first aerosol indirect radiative effect is estimated to assess climatic implications.

1.3 Aerosol particles in the atmosphere

Aerosol particles may be emitted into the atmosphere from natural (such as wind-borne dust, volcanoes, forest fires, sea-spray) and anthropogenic sources (such as combustion of fuel) or produced in-situ from gas-to-particle conversion or nucleation. Directly emitted aerosols constitute primary aerosol while aerosols produced from atmospheric processes constitute secondary aerosol. Once in the atmosphere aerosol particles evolve in size and composition through condensation and evaporation, coagulation with other particles or by activation.

Aerosol particles have diameters ranging from a few nanometers to several hundred micrometers. Different sources produce particles in different size ranges. Mechanisms that remove aerosols from the atmosphere are also highly dependent on the size of the aerosol particles. Because of the dependency of various atmospheric processes on aerosol particle size, aerosol particles are commonly classified in different modes according to their diameters: nucleation mode consisting of particles with diameter below 10 nm, Aitken mode consisting of particles with diameter between $10-100$ nm, accumulation mode consisting of particles with diameter between $100-1000$ nm and coarse mode consisting of particles with diameter above 1000 nm.

Aerosols may be removed from the atmosphere by dry (such as gravitational settling, Brownian diffusion, impaction scavenging) and wet (such as below-cloud scavenging and nucleation scavenging) processes. Larger aerosol particles (with diameter larger than 1 μm) tend to be influenced more by gravity and settle. This form of removal is less efficient for particles of smaller sizes. Smaller particles tend to diffuse more due to collisions with larger particles as a result of Brownian motion. This form of removal is less efficient for particles of larger sizes. Within the size range 0.1 to 1 μm dry deposition is least effective and particles tend to accumulate and grow by

condensation. Depending on the hygroscopic properties of these accumulated particles, they may be activated to form cloud droplets and removed by rain-out (Raes et al., 2000). In the lower troposphere particle lifetime is typically less than a week and in the free-troposphere 3−10 days on average. Particles in the accumulation mode have the longest lifetime (7−10 days) in the atmosphere.

In the atmosphere aerosol particles may undergo various microphysical processes and chemical reactions which can substantially alter their chemical composition. Tropospheric aerosol composition varies widely across the globe comprising mainly of inorganic salts, insoluble mineral dust and carbonaceous material (Jacobson et al., 2000; Forster et al., 2007). Multi-component aerosols may exist as a single particle (internally mixed aerosol) or as a mixture of individual particles (externally mixed aerosol). Typically nucleation and primary emissions give rise to externally mixed particles while all other atmospheric processes give rise to internally mixed aerosol. The degree of internal mixing, i.e. the degree to which composition of each individual particle resembles that of the bulk, is dependent on the residence time of the particle or time available for interaction between the individual components (Raes et al., 2000).

Tropospheric aerosols consist of inorganic salts, mineral dust and carbonaceous aerosols. Carbonaceous aerosol is typically divided into two fractions: elemental carbon (EC) and organic carbon (OC). EC is a chemical term that refers to pure carbon with graphitic structure. However pure carbon or graphite are not commonly observed in the atmosphere. Instead EC is generally coated with organic compounds; i.e. EC is almost always linked with organic aerosol though the latter may exist independent of EC (Jacobson et al., 2000). Black Carbon (BC) is an optical term used to denote highly light absorbing carbon (Lavanchy et al., 1999). BC and EC are often used interchangeably in the literature to denote highly absorbing

aerosol, also called soot. However BC may consist of not only EC but also OC that sufficiently absorbs light (Chow et al., 2009). BC or the highly light-absorbent component of carbonaceous aerosols is usually produced from incomplete combustion of fossil fuel, bio fuel and biomass burning. Due to their strong absorbing properties they are considered to contribute to the aerosol semi-direct effect (aerosol warming leading to localised reduction of cloud cover in atmospheric regions of high BC particles; Hansen et al., 1997; Koch and Del Genio, 2010).

If EC is removed from the total carbonaceous mass, the remainder comprises of organic aerosol containing covalently bound carbon (Pöschl, 2003). The mass of chemically bound carbon is referred to as OC. The sum of the mass of chemically bound carbon and mass of all atoms bound with it (such as hydrogen, oxygen, nitrogen) comprises the total organic aerosol and is referred to as particulate organic matter (POM) or organic aerosol (OA). Throughout this thesis the term OA is used to denote organic aerosol of which the primary fraction is referred to as primary organic aerosol (POA) and secondary fraction is referred to as secondary organic aerosol (SOA). Observations suggest that OA compounds are relatively weakly hygroscopic. However a considerable fraction of OA is considered to be water-soluble to an extent. At low relative humidity more water is often associated with the organic fraction of aerosols than the inorganic (Forster et al., 2007). Their ability to be or become hygroscopic makes estimating atmospheric OA important for aerosol indirect effects. The large number of organic compounds in the atmosphere and their varying physical and chemical properties make quantifying atmospheric OA and their climatic impacts extremely challenging (Shrivastava et al., 2016).

A schematic showing aerosol size distribution and the processes associated with each size range is shown in Figure 1.2 taken from Bakshi et al. (2015). The figure shows the number, surface area and volume distribution of atmospheric aerosols.

Particles in the nucleation mode have high surface-to-volume ratio but have small total surface area and volume compared to those in the other modes. The number concentration of nucleation and Aitken mode particles are largest in the atmosphere followed by those in accumulation and coarse modes. The accumulation mode accounts for a significant fraction of aerosol mass and have the greatest surface area. The atmospheric lifetime of particles in the accumulation mode are longest due to inefficient removal processes at this size range. This makes accumulation mode particles particularly important for gaseous phase deposition and heterogeneous chemistry. Coarse mode particles are low in number (due to highly efficient removal mechanisms at this size range) and with the accumulation mode constitute most of the aerosol mass. The loss processes for each mode are depicted by the yellow arrows in Figure 1.2. The figure shows the evolution of new particles formed in the atmosphere from low-volatility vapours through different size ranges by atmospheric processes such as nucleation, condensation and coagulation.

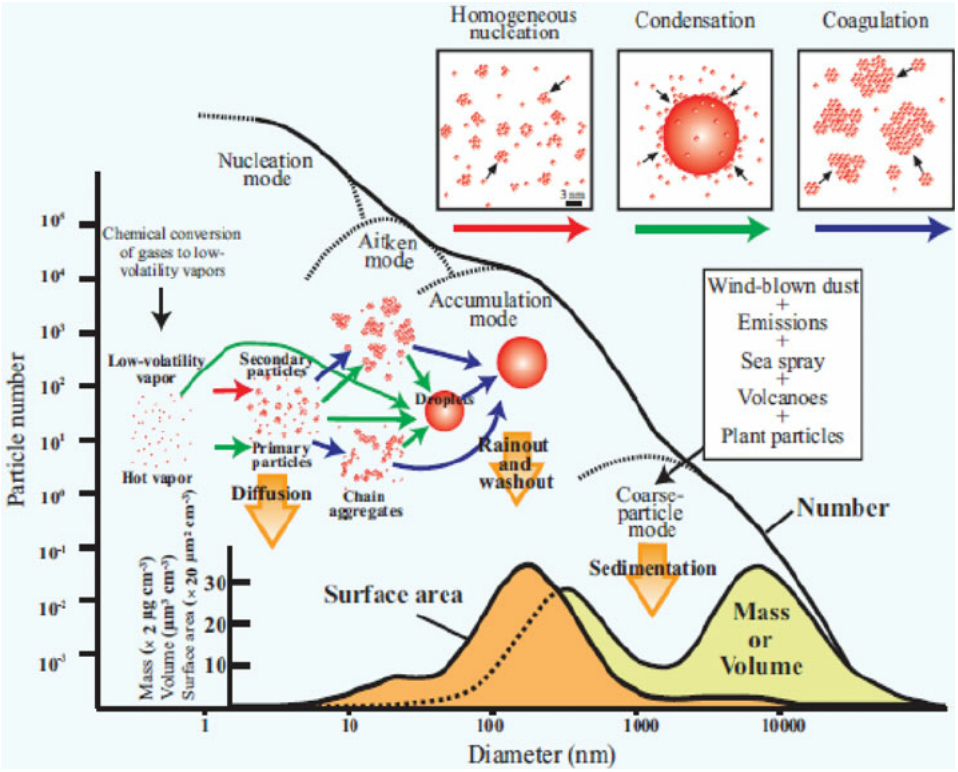

Figure 1.2: Schematic from Bakshi et al. (2015) showing aerosol particle size distribution, source of particles and different processes associated with each size range.

Of the many known and unknown complex processes that govern the life cycle of aerosol particles in the atmosphere this thesis revolves around nucleation of secondary aerosol particles and the subsequent evolution of aerosol particles from a few nm to cloud droplet sizes - with particular focus on the contribution of highly oxygenated organic molecules which constitute atmospheric SOA.

1.3.1 Secondary organic aerosol in the atmosphere

A major component of fine-particle mass throughout the atmosphere is organic in nature (Kanakidou et al., 2005; Zhang et al., 2007) which may either be primary or secondary in origin. The relative contribution of POA and SOA to the overall SOA budget is controversial (Donahue et al., 2009). While several studies estimate POA to dominate the urban OA budget, recent field measurements (De Gouw et al., 2005; Volkamer et al., 2006) indicate a SOA dominance that cannot be explained by the

oxidation of known SOA precursors (Robinson et al., 2007).

SOA is produced as a result of atmospheric oxidation of VOCs that are released by biogenic or anthropogenic sources. In the troposphere VOCs are readily oxidised by atmospheric oxidants such as ozone (O_3), hydroxyl radical ($OH^{\cdot}$) and nitrate radical ($NO_3^{\cdot}$). Tropospheric O_3 is either transported into the troposphere from the stratosphere or produced from reactions between VOCs and NO_x in the presence of sunlight. O_3 is a highly reactive species and unsaturated organic compounds in the atmosphere are particularly susceptible to an attack by O_3 (Jonsson et al., 2006). $OH^{\cdot}$ is produced in large quantities primarily from photolysis of O_3, nitrous acid in the daytime (Kleffmann et al., 2005). At nighttime reactions between O_3 and organic compounds (alkenes) act as a major source of $OH^{\cdot}$ (Paulson and Orlando, 1996). $OH^{\cdot}$ is a key oxidising species that reacts with most of the atmospheric organic compounds (Atkinson, 2000). $NO_3^{\cdot}$ arises from the oxidation of nitrogen dioxide by O_3 and is principally active at night dominating nighttime VOC chemistry due to its rapid photolysis in sunlight (Ng et al., 2017).

Once oxidised by the atmospheric oxidants these VOCs typically produce a range of gaseous phase compounds with varying volatility. Each oxidation product may be oxidised further, giving rise to multiple later generations of highly oxygenated products. Eventually the oxygenated VOCs with sufficiently low volatilities condense on the aerosol particles, increasing the atmospheric SOA burden. Some oxidation products of atmospheric VOCs with sufficiently low volatility may take part in new particle formation in the atmosphere (Metzger et al., 2010; Ehn et al., 2014; Kirkby et al., 2016). VOCs with higher volatility tend to partition between the gaseous and particle phase or remain in the gaseous phase until multiple oxidation reactions render them capable of addition to the particle phase (Pandis et al., 1992; Pankow, 1994) .

1.4 Volatile organic compounds in the atmosphere

VOCs are non-methane hydrocarbons (NMHC) and oxygenated NMHC (such as alcohols, aldehydes and acids). Apart from contributing to the atmospheric SOA burden, VOCs play an important role in atmospheric chemistry by influencing the tropospheric concentrations of O_3, $OH^{\cdot}$ and conversion rates of NO_x. Reaction of VOCs and $OH^{\cdot}$ produces peroxy radical (RO_2) which reacts with atmospheric NO, converting it to NO_2. Photolysis of NO_2 (producing atomic oxygen which reacts with oxygen to produce O_3) is the primary source of tropospheric O_3 (Jacobson et al., 2000). Increased VOC and NO_x concentrations have led to a doubling of lower tropospheric O_3, making O_3 the third most important GHG after CO_2 and CH_4. Increased levels of tropospheric O_3 also has harmful effects on vegetation (Ainsworth et al., 2012) which are an important sink for atmospheric CO_2.

VOCs are emitted into the atmosphere primarily by vegetation. Once emitted their atmospheric lifetime varies widely between a few minutes to years. VOC sources and sinks vary spatially and temporally causing their atmospheric concentrations to fluctuate between ten of parts per billion in the polluted atmosphere to below 1 parts per billion in non-polluted areas.

1.4.1 Biogenic VOC

Global emissions of biogenic VOCs are estimated to be about 1150 TgC yr^{-1}, exceeding anthropogenic VOC emissions by about a factor of 10 worldwide (Atkinson and Arey, 2003). Apart from having a large emission source, many BVOCs show a higher reactivity towards atmospheric oxidants (compared to anthropogenic VOCs) which adds further to their significance (Kanakidou et al., 2005). BVOCs are commonly classified into four categories: isoprene, monoterpenes, other reactive VOC and other VOC (Guenther et al., 1995). BVOCs are highly reactive and once air-

borne, get quickly oxidised by atmospheric oxidants typically leading to less volatile products. The highest concentrations of ambient BVOCs occur near forested regions reflecting both their source and high reactivity (Graedel, 1979).

The dominant emitted BVOC is isoprene (C_5H_8) with emissions of approximately 600 Tg yr^{-1} (Carlton et al., 2009). Although the two double bonds in isoprene make it highly reactive, early laboratory studies (Pandis et al., 1991) found products of isoprene oxidation to be volatile and inferred SOA formation from isoprene would require isoprene concentrations higher than those found in the atmosphere. Consequently SOA formation from isoprene is traditionally considered insignificant. Recent re-examinations have found that subsequent oxidation of isoprene oxidation products in the atmosphere leads to less-volatile end products which may potentially form SOA (Carlton et al., 2009). Given the overall global source strength of isoprene it is thought that even a small contribution to SOA from multi-stage oxidation products of isoprene, would result in substantial atmospheric SOA (Carlton et al., 2009).

Derived from isoprene (also called a hemiterpene) are terpenes such as monoterpenes (consisting 2 isoprene units with molecular formula $C_{10}H_{16}$), sesquiterpenes (consisting of 3 isoprene units with molecular formula $C_{15}H_{24}$). Examples of monoterpenes include α-pinene, β-pinene, Limonene, Myrcene, 2-Carene, 3-Carene - of which the most important and extensively studied compound for atmospheric SOA formation is α-pinene. Of particular importance is the high reactivity of terpenes towards O_3, unlike isoprene. Such ozonolysis of terpenes generate a local, non-photolytic source of $OH^{\cdot}$, which can further enhance the oxidation (Donahue et al., 2005). For example the lifetimes (time taken by a BVOC to reduce to 1/e of its initial concentration) of a monoterpene, α-pinene (4.6 h), a sesquiterpene, β-Caryophyllene (2 min) with isoprene (1.3 day) in presence of ozone clearly indicates the atmospheric reactivity

of terpenes (Atkinson and Arey, 2003).

In general there are two reaction mechanisms by which BVOCs get oxidised - addition to C=C and H-atom abstraction (Ehn et al., 2014; Ng et al., 2017). Unsaturated BVOCs such as isoprene, monoterpenes and sesquiterpenes are particularly susceptible to oxidation by attack at the C=C.

1.4.2 Anthropogenic VOC

Although biogenic VOCs are known to contribute the majority of global SOA, recent studies have highlighted the importance of anthropogenic sources of SOA. Weber et al. (2007) found SOA formation from biogenic VOCs is strongly linked with anthropogenic VOCs. Ding et al. (2012) showed anthropogenic VOCs to be the dominant SOA precursor in highly industrialised regions. Volkamer et al. (2006) estimated the global anthropogenic SOA to contribute one-third of the global SOA. In a modelling study including biogenic and anthropogenic VOCs, Tsigaridis and Kanakidou (2003) estimated annual production of anthropogenic SOA to vary between 0.05 to 2.62 Tg yr^{-1}. Spracklen et al. (2011b) found the best model-observation agreement between modelled and observed organic aerosol with a model simulation producing 140 Tg yr^{-1} of SOA of which 100 Tg yr^{-1} is anthropogenic. Volkamer et al. (2006) estimated anthropogenic VOCs to contribute between $3-25$ Tg yr^{-1} of SOA causing upto -0.1 W m^{-2} additional radiative cooling.

Of the anthropogenic VOCs aromatic compounds from vehicle emissions produce the majority of atmospheric SOA (Odum et al., 1997). Aromatic VOCs may be emitted from fuel combustion (gasoline, diesel engines) and evaporative emissions (from solvent usage in printing, painting etc., gasoline spillage, evaporation during vehicle refuelling). In a measurement study based in Seoul, Na et al. (2005) found

aromatic VOC concentrations are higher in the winter with 58 % of the total aromatic VOC concentrations coming from vehicle exhaust. Adhesives and tobacco smoke have been found to be major sources of indoor VOC emissions (Sack et al., 1992; Baek and Jenkins, 2004). Gentner et al. (2012) quantified the SOA-production potential of VOCs emitted from gasoline and diesel vehicles and found diesel can be responsible for up to 90 % of vehicular-derived SOA (depending on regional fuel use), with substantial contributions from aromatic and aliphatic hydrocarbons. In a study investigating air samples from one urban, one suburban and two rural sites in the Pearl River Delta region in China, Zhang et al. (2013) found solvent usage, vehicle exhaust and biomass burning can account for about 89−94 % of observed aromatic hydrocarbons and that biomass burning acts as an important source of benzene particularly in rural areas. Hoyle et al. (2011) found anthropogenic VOCs enhance SOA formation from naturally emitted VOCs.

A significant sink of atmospheric VOCs is oxidative processes that subsequently lead to SOA production, as mentioned in Section 1.3.1. Thus quantifying VOC emissions and understanding their oxidative pathways in the troposphere is important to better constrain the budget of atmospheric SOA. Figure 1.3 taken from Shrivastava et al. (2016) highlights the most important aspects of atmospheric SOA that have been known to affect the Earth's long-term climate through their effects on cloud-aerosol interactions.

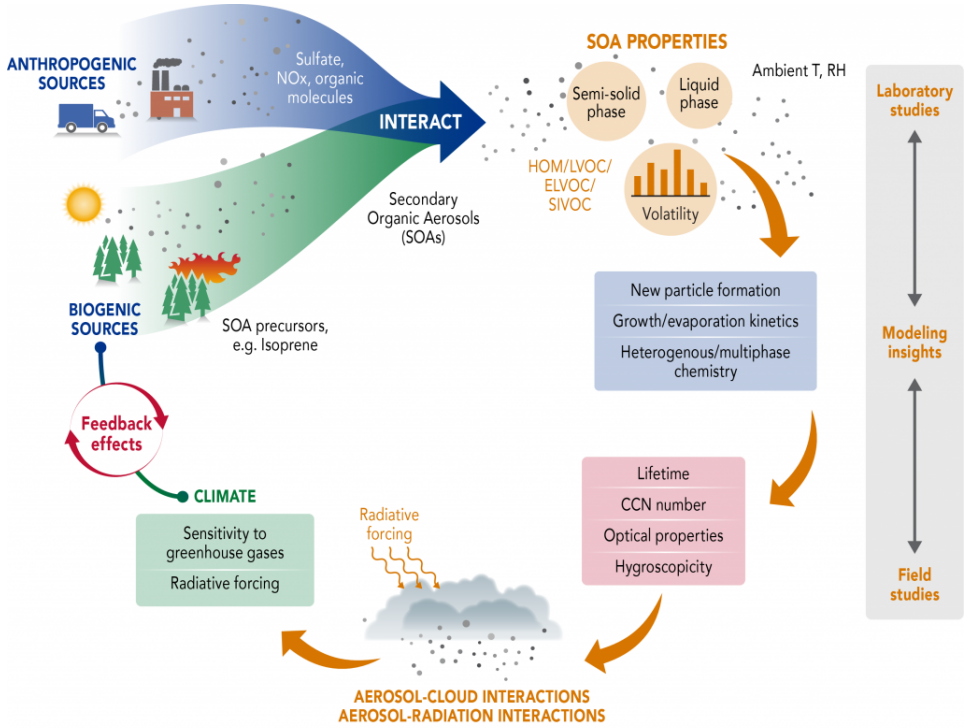

Figure 1.3: Schematic from Shrivastava et al. (2016) showing processes that govern the climatic impact of atmospheric secondary organic aerosol (SOA).

1.5 Challenges in modelling aerosol formation from volatile organic compounds in the atmosphere

A comprehensive characterisation of atmospheric VOCs and hence their reaction pathways and products has not been possible due to tens of thousands of VOCs that have been measured and more that are yet to be detected (Goldstein and Galbally, 2007). For those precursor gases that have been identified questions remain as to the extent of their conversion to SOA, accurate characterisation of their emission sources, their global distribution and the critical concentrations at which SOA formation takes place. The picture is further complicated by the interaction between precursor gases, chemistry with other gases, availability of oxidants, transport from surrounding regions, topography and meteorological conditions all of which may impact formation processes of SOA. Thus from a global modelling point of view, it is

extremely challenging to simulate SOA formation from VOCs in different regions of the globe and the atmosphere. There can be various sources of uncertainty in the estimation of atmospheric SOA particles that may act as cloud droplets associated with various intermediate processes (Figure 1.3). This thesis concerns two aspects of simulating global SOA: (1) the total estimate of SOA produced from oxidation products of VOCs in the atmosphere (2) the approach adopted to model the transfer of gaseous phase molecules to the condensed phase (to produce new or grow existing particles).

The uncertainty in model estimates of total global SOA production is substantial: 12−1820 Tg yr^{-1} (Kanakidou et al., 2005; Hallquist et al., 2009; Spracklen et al., 2011b). Studies like Heald et al. (2005); Johnson et al. (2006) and Spracklen et al. (2011b) show models significantly underestimate SOA production in different parts of the atmosphere and different regions of the globe compared to measurements. Bottom-up estimates (based on laboratory derived yields of SOA from VOCs) by models result in up to 70 Tg yr^{-1} (Kanakidou et al., 2005). This underestimation of modelled SOA (compared to the estimates from top-down approaches based on estimating the eventual fate of all VOCs in the atmopshere) is thought to arise because large-scale global models typically use yields derived from chamber experiments (for example, 10 % in (Riipinen et al., 2011) and 13 % in (Mann et al., 2010) for biogenic terpenes) to produce oxidised organic molecules in the gaseous phase which transfer to the aerosol phase to produce particles (nucleation) or grow particles. These yields are an underestimation of atmospheric yields as chamber experiments last for shorter duration than that required for all oxidation products to reach their final (less volatile) state and contribute to SOA (Goldstein and Galbally, 2007). Further Zhang et al. (2014); La et al. (2016) estimate the chamber yields to be affected by as much as a factor of 4 (Zhang et al., 2014) by the loss of organic vapours to the chamber walls, imposing additional limitation to bottom-up SOA estimates.

The second aspect of modelling SOA formation that this thesis concerns with is the impact of the approach adopted to simulate the transfer of gaseous phase molecules to the aerosol phase, contributing to the growth of aerosol particles and nucleation of secondary aerosol particles. Typically models simulate SOA formation either by assuming instant thermodynamic equilibrium between gaseous phase oxidised VOCs and aerosol particles (Pankow, 1994) or by assuming kinetic condensation (Mann et al., 2010). Adopting only the thermodynamic approach ignores the size-dependency of kinetic condensation and favours the growth of large particles over small ones. Adopting only the kinetic approach on the other hand neglects the evaporation of molecules from the aerosol phase back to the gaseous phase (Riipinen et al., 2011). Scott et al. (2015) explored the effect of using the two different gas-to-particle transfer approaches and estimated a 24 % reduction (-0.66 to -0.5 W m^{-2}) of global mean aerosol indirect effect when the thermodynamic approach is adopted, arising from a suppressed growth of small particles in the model.

Nucleation rates in large scale global models traditionally depend on sulphuric acid only (Riipinen et al., 2011). In recent times several studies have brought forward the importance of other molecules such as ammonia (Ball et al., 1999; Coffman et al., 1995; Kirkby et al., 2011), amines (Murphy et al., 2007; Kurtén et al., 2008; Berndt et al., 2010; Almeida et al., 2013) and ions (Raes et al., 1986; Lovejoy et al., 2004; Sorokin and Arnold, 2007; Kirkby et al., 2016) in new particle formation. This has motivated modelling studies to include nucleation mechanisms involving ammonia (Dunne et al., 2016), or sulphuric acid and organic compounds (Scott et al., 2015; Riccobono et al., 2014; Gordon et al., 2016). Riccobono et al. (2014) estimated a 10 % difference (-1.04 and -1.15 W m^{-2}) between the first aerosol indirect forcing estimated using two nucleation mechanisms both driven by sulphuric acid and biogenic organic compounds. Riccobono et al. (2014) concluded considerable uncer-

tainty in RF may be associated with the varying dependencies of different nucleation schemes on the same participating vapours. Scott et al. (2015) showed the impact of kinetic or mass-based approach on present-day cloud droplet number concentration (which directly modulates the first aerosol indirect forcing) is much greater (21 % for kinetic and 16.8 % for mass-based approach) when organic compounds participate in nucleation compared to when they do not (3.4 % for kinetic and 1.4 % for mass-based approach).

Questions concerning atmospheric SOA raised in Kanakidou et al. (2005) persist after a decade of extensive aerosol research, huge advances in instrumentation, methodology and new discoveries. To reiterate some of them - "How important is organic nucleation on a global scale? What are the mechanisms of SOA formation? And how much SOA is formed in the atmosphere?" While new research continues to be planned to understand the nuances of atmospheric chemistry, this thesis takes a top down approach to constrain the modelled particle number concentration and evaluate the climatic impact of atmospheric SOA-producing VOCs.

1.6 Thesis aims

This thesis has been funded by the Marie Curie Initial Training Network Fellowship (CLOUD-TRAIN Grant no: 31662) of the European Commission's Seventh Framework Programme. The CLOUD consortium consists of a global network of scientists from 17 institutes in 9 countries who work together to provide an advanced level infra-structure, scientific equipments and expertise to perform systematic experiments - with the aim to better understand atmospheric aerosols. The CLOUD experiments are carried out in an unique chamber at CERN which is able to simulate and measure atmospheric particle formation and subsequent growth under extremely controlled laboratory conditions (Kirkby et al., 2011). This PhD, based

at the University of Leeds, aims to assess the atmospheric implications of the CERN results on a global scale using a complex aerosol microphysics model developed at Leeds (Mann et al., 2010).

As a CLOUD-TRAIN Early Stage Researcher, the candidate participated in 3 CLOUD campaigns at CERN (CLOUD 8 in October 2013, CLOUD 9 in 2014 and CLOUD 10 in 2015) usually for 10−15 days. The CLOUD experiments are run 24 hours a day in three shifts. Before each campaign experiments are designed with inputs from the entire consortium. During the campaign day-to-day experimental plans are constantly revised based on results analysed on the day, technical failures/errors and other practicalities. During the candidate's stay at CERN, the candidate along with one other scientist, was in charge of running the experiments in the CLOUD chamber for about 8−12 shifts every campaign. The candidate took part in daily scientific meetings held to analyse the previous 24-hours result, discuss their implications and draw up the next run-plan for the next 24 hours. The candidate also took part in several post-campaign meetings and workshops with the international collaborators such as the modelling meeting in Leeds (February 2014), data-analysis meetings in Manchester, UK (March 2014) and Paul Scherrer Institute, Switzerland (February 2015), summer schools held by the CLOUD-TRAIN network at Hyytiala (August 2014) and at Portugal (June 2015) and the CLOUD-TRAIN Final Conference in Konigsteiin Germany (June 2016).

The motivation for this thesis was the experimental results of the 8^{th} CLOUD campaign (2013) wherein it was discovered that biogenic vapours in the atmosphere can nucleate (termed pure biogenic nucleation) and produce new aerosol particles without contribution from any other vapour (Kirkby et al., 2016). This thesis starts with implementation of pure biogenic nucleation (parameterisation based on CERN CLOUD results) in GLOMAP-mode and goes on to improve the representation of

SOA production from oxidised VOCs based on recent advances in the understanding of atmospheric SOA-production processes.

In Chapter 2, the aerosol microphysics model (GLOMAP-mode) as used in this thesis is described. Model developments made for each individual chapter are described in the relevant chapter.

In Chapter 3, the atmospheric relevance of a new nucleation parameterisation based on the CERN CLOUD experiment is assessed. The chapter investigates the effects of pure biogenic nucleation on the number concentration of CCN-relevant sized particles in the present-day atmosphere and the pre-industrial atmosphere as well as the indirect radiative effect due to the change in cloud droplet number concentrations. Chapter 3 also gives an account of how much the model's estimate of aerosol indirect effect has changed due to various model developments (related to SOA production) made in the study.

In Chapter 4, the existing SOA-production treatment in GLOMAP-mode is modified to include contributions from three classes of VOC with varying volatility: extremely low volatility ELVOC that nucleates, low-volatility LVOC that grow particles by kinetic condensation and semi-volatile SVOC that grow particles by atmospheric mass-based partitioning. The chapter investigates the effects of the modified SOA treatment on the number concentration of all particles in the present-day atmosphere and the pre-industrial atmosphere, the number concentration of CCN-relevant sized particles in the present-day atmosphere and the pre-industrial atmosphere, the aerosol size distribution in the model, the model-observation agreement in total particle number concentrations, the number concentration of cloud droplets in the present-day atmosphere and the pre-industrial atmosphere and the indirect radiative effect due to the change in cloud droplet number concentrations.

In Chapter 5, a pre-defined uncertainty space, related to 6 SOA-producing oxidised VOC parameters, is explored using a perturbed parameter ensemble of 60 model simulations. The aim is to constrain the 6-D parameter space based on model-observation agreement in particle number concentrations (N3, N50) and organic aerosol mass concentrations (OA). The primary questions explored in this chapter are:

- Atmospheric organic molecules from single or multi-stage oxidation reactions of precursor VOCs (ox-VOCs) are known to span a large range of volatility. From a global modelling perspective, which ox-VOC interactions are necessary to simulate a realistic number concentration of particles along with the mass concentration of SOA? Which SOA production pathways (from ox-VOCs) are not crucial to account for?

- How do additional complexities in chemical pathways of particle formation (which aim towards better model-observation agreement of particle number concentration), affect the model estimate of atmospheric SOA mass?

Chapter 2

A brief overview of GLOMAP-mode

This chapter gives a general overview of the global aerosol microphysics model (GLMOAP-mode) used in Chapters 3, 4 and 5. Any model development made as a part of the work for each chapter is described in the corresponding chapter. GLOMAP-mode is described in detail in Mann et al. (2010) and has been used in several studies such as Spracklen et al. (2010, 2011b); Lee et al. (2011, 2012, 2013, 2016); Schmidt et al. (2012); Browse et al. (2013); Carslaw et al. (2013); Scott et al. (2014, 2015); Hamilton et al. (2014); Regayre et al. (2014, 2015); Dunne et al. (2016); Gordon et al. (2016).

The GLObal Model of Aerosol Processes (GLOMAP), is a size-resolving global aerosol microphysics model developed as an extension of the 3-D chemical transport model (CTM) Toulouse Off-line Model of Chemistry And Transport (TOMCAT; Chipperfield, 2006). GLOMAP simulates aerosol microphysical processes viz. emission of primary aerosols, formation of secondary aerosol, growth of aerosol by condensation, coagulation and in-cloud processing and removal of aerosols by dry deposition and wet deposition while TOMCAT calculates chemistry and transport. For this thesis GLOMAP is run at a horizontal resolution of 2.8° (latitude and longitude) with 31 hybrid σ-p levels from surface to 10 hPa. The vertical resolution

varies from 60 m in the boundary layer to 1 km in the higher troposphere.

Large-scale atmospheric transport, precipitation rates and ambient conditions in TOMCAT are forced by meteorological fields from the European Centre of Medium-range Weather Forecasts (ECMWF) analyses which are updated every 6 hours and linearly interpolated to the model time step. TOMCAT advects tracers according to the scheme described in Prather (1986) and calculates sub-grid scale moist convection according to Tiedtke (1989). For in-cloud processing and aqueous phase chemistry, low-cloud fraction in the model is specified from cloud top pressure and cloud fractions derived by the International Satellite Cloud Climatology Project (ISCCP) for the year 2000 (Rossow and Schiffer, 1999).

The shape of the aerosol size distribution in the modal version of the model, GLOMAP-mode, is parameterised as a series of modes that are assumed to be log-normal, each covering defined regions of the particle radius range. The model (Mann et al., 2010) follows the aerosol dynamics framework of M7/HAM scheme (Vignati et al., 2004; Stier et al., 2005; Vignati et al., 2010) while representing aerosol processes according to GLOMAP-bin (Spracklen et al., 2005a). The M7/HAM scheme allows for the representation of aerosol size distribution in 7 modes which are: a hydrophilic nucleation mode (geometric mean diameter of particles in nm, D_g <10), hydrophilic and non-hydrophilic modes for each of Aitken (10<D_g<100 nm), accumulation (100<D_g<1000 nm) and coarse (D_g>1000 nm or 1 μm) size ranges. For work in this thesis all four hydrophilic modes and the non-hydrophilic Aitken mode in GLOMAP-mode are considered. The geometric mean diameter (D_g) for each mode is calculated online while the standard deviation for each mode is fixed and the mode width pre-defined, to prevent indefinite growth of particles due to coagulation or condensation processes. D_g for each mode varies with time as the aerosol size distribution evolves following the micophysical processes in the model. When D_g

exceeds the upper size limit for any mode, particle mass and number get transferred to the next mode, referred to as mode-merging. The two prognostic quantities in the model are the particle number concentration in each mode and the mass of each component in each mode.

Each of the five aerosol modes is considered to be an internal mixture of two or more of the following four components: sulphate (SU), sea salt (SS), elemental carbon (BC) and organic carbon components (OC) i.e, contribution of each of the components in the aerosol particles within each mode cannot be separated out. The source of each aerosol component and the atmospheric processes represented in GLOMAP are detailed in Spracklen et al. (2005a,b); Mann et al. (2010) and are briefly outlined below.

2.1 Gas phase

Gas phase species in GLOMAP includes 8 sulphur species (SO_2, H_2SO_4, H_2S, CS_2, COS, DMSO, DMS, MSA), a terpene tracer (MONOTER) and offline oxidant fields of $OH^{\cdot}$, O_3, $NO_3^{\cdot}$. Monthly monoterpene emissions from the GEIA database (Guenther et al., 1995) fed into MONOTER are used as a proxy for VOCs that are emitted by vegetation and contribute to atmopsheric SOA. Biogenic VOC emissions are updated for simulations used in Chapters 4 and 5, as described therein. The oxidant fields used in this study (Monks et al., 2017; updated from Arnold et al., 2005 in Chapter 3) are 6-hourly monthly mean values calculated offline from a TOMCAT simulation and interpolated to the model chemical time step. Binary reactions between MONOTER and the oxidants produce secondary organic compounds (referred to as SEC_ORG in the model) at a fixed yield of 13 % following Tunved et al. (2006). Chapters 4 and 5 also include an additional source of biogenic VOC from isoprene, fed into tracer ISOPU. Production of secondary organic aerosol from

ISOPU is described in Chapter 4.

Of the 8 sulphur species, monthly phytoplankton emissions of DMS are calculated every 6 h using sea-water DMS concentration fields of Kettle and Andreae (2000), sea-air exchange parameterisation from Nightingale et al. (2000) and ECMWF wind fields. Gas phase SO_2 emissions are included from anthropogenic sources such as industrial, power-plant, domestic, shipping, road-transpor and off-road sources based on Cofala et al. (2005). Natural SO_2 sources include continuously (Andres and Kasgnoc, 1998) and explosively (Halmer et al., 2002) erupting volcanoes. SO_2 from biomass burning is also included based on Van Der Werf et al. (2003) and injected at 6 altitude intervals between 0 to 6 km following Dentener et al. (2006). Anthropogenic carbon disulphide, CS_2 and carbonyl sulphide, COS, are represented by a constant molar emission (0.3 and 0.08 % respectively) in proportion to anthropogenic SO_2 emission levels. Biogenic CS_2 and COS are represented by a constant molar emission at 1 % of the calculated DMS emission.

2.2 Aerosol Phase

2.2.1 Primary aerosol in GLOMAP

Following the AEROCOM recommendation (Dentener et al., 2006), 2.5 % of the SO_2 emission is assumed to be emitted as primary sulphate particles to represent sub-grid scale nucleation of sulphate particles. 50 % of all sub-grid scale sulphate is emitted into the accumulation mode (number mean diameter 150 nm and σ of 1.59). For shipping, power plants and industrial sources of SO_2, the remaining 50 % is emitted into the coarse mode (number mean diameter of 1.5 μm and σ of 2.00). For transport, domestic, wildfire and volcanic sources of SO_2, the remaining 50 % is emitted into the Aitken mode (number mean diameter 60 nm and σ of 1.59).

Annual mean emissions of carbonaceous aerosols (BC and OC) for 2000 are taken from biofuel and fossil fuel sources following Bond et al. (2004). Monthly emissions from biomass burning sources are represented in the model for the year 2000 according to the Global Fire Emissions Database (GFEDv1) inventory (Van Der Werf et al., 2003). For simulations used in Chapters 4 and 5, the anthropogenic emissions of SO_2, BC and OC are specified using the MACCity emissions inventory (Lamarque et al., 2010; Granier et al., 2011) for the year 2008. In Chapters 4 and 5, anthropogenic VOCs for 2008 are represented using spatially correlated CO emissions - also taken from the MACCity inventory.

Primary carbonaceous particles are emitted in the model assuming distribution characteristics described in Stier et al. (2005). Particles from biomass burning and biofuel emissions are emitted, with number median diameter 150 nm and modal width 1.59, into the accumulation mode. Particles from fossil fuel emissions are emitted, with number median diameter 60 nm and modal width 1.59, into the Aitken mode. Fossil fuel and biofuel emissions are injected into grid boxes below 100 m and emissions from biomass burning are injected into grid boxes between the surface and 6 km (depending on the type of vegetation that is burning) following Dentener et al. (2006).

Bin-resolved sea-salt emissions are calculated using a sea-spray source function from Gong (2003) which produces emissions at particle sizes between 0.07 μm to 20 μm. Emitted bins of sea-spray particles are added to the accumulation or coarse mode depending on whether particle dry diameter is less or more than 1 μm.

2.2.2 Secondary aerosol source: nucleation

Gas to particle conversion in the atmosphere produces particles in the atmosphere, also known as nucleation or new particle formation. Nucleation starts with a few molecules colliding and sticking together leading to stable clusters of $1-2$ nm in diameter. Once formed these clusters may grow to CCN relevant sizes. Nucleation is known to occur throughout the atmosphere, although understanding of mechanisms that drive nucleation remain incomplete (Kulmala et al., 2004). Two separate schemes control cluster formation in GLOMAP - one dominating particle production in the boundary layer and the other in the free troposphere.

For the free troposphere, the binary homogeneous nucleation of sulphuric acid is used throughout this thesis (Kulmala et al., 1998). This nucleation mechanism has been established to reproduce observed particle concentration in the upper troposphere in GLOMAP (Spracklen et al., 2005a). The nucleation rate (J_{BHN} in cm^{-3} s^{-1}) is calculated using,

$$J_{BHN} = exp\left\{Alog\left(\frac{[H_2SO_4]}{[H_2SO_4]_{crit}}\right) + B\chi_{al} + C\right\} \tag{2.1}$$

where $[H_2SO_4]_{crit}$ is the gaseous phase concentration of sulphuric acid above which nucleation will occur, χ_{al} is the mole fraction of sulphuric acid in the critical nucleus and A,B,C are temperature dependent coefficients from Kulmala et al. (1998).

Nucleation in the boundary layer has been observed to occur at higher rates than predicted by the BHN mechanism described above (Weber et al., 1996; Clarke et al., 1998; Kulmala et al., 2000) and has been shown to contribute substantially to total particle concentrations (Spracklen et al., 2006; Merikanto et al., 2009; Pierce and Adams, 2009). Consequently several laboratory and experimental studies, including the CERN CLOUD experiment, have sought to identify nucleating molecules in the

atmosphere (Coffman et al., 1995; Almeida et al., 2013; Kirkby et al., 2011, 2016) and parameterise nucleation mechanisms (Napari et al., 2002; Metzger et al., 2010; Riccobono et al., 2014; Dunne et al., 2016; Gordon et al., 2016).

Several nucleation mechanisms involving sulphuric acid, ammonia and organic compounds have been examined in GLOMAP to reproduce observed particle formation rates in the boundary layer (Spracklen et al., 2006, 2008; Laakso et al., 2013; Scott et al., 2014; Riccobono et al., 2014; Dunne et al., 2016; Gordon et al., 2016). Throughout this thesis, boundary layer nucleation is represented by two mechanisms to represent sulphuric acid-dependent and sulphuric acid-independent nucleation of atmospheric organic molecules.

1. Sulphuric acid-dependent mechanism:

   Formation rate (J in cm^{-3} s^{-1}) of 1.7 nm particles from sulphuric acid and BioOxOrg nucleation, where BioOxOrg represents oxidation product of pinandiol (a first generation oxidation product of α-pinene) and $OH^{\cdot}$. BioOxOrg is produced in GLOMAP using the MONOTER tracer and reaction rate constants of α-pinene and $OH^{\cdot}$ (Riccobono et al., 2014).

   $$J = k_m[H_2SO_4]^2[BioOxOrg] \tag{2.2}$$

   where $k_m = 3.27 \times 10^{-21} s^{-1}$

2. Sulphuric acid-independent mechanism:

   The latest nucleation mechanism is based on the experimental findings of the CERN CLOUD experiment (the CLOUD8 campaign in 2013) which show that certain organic compounds in the atmosphere can initiate nucleation in absence of sulphuric acid. This mechanism is implemented in GLOMAP as a part of this thesis and is described in Chapter 3.

A more detailed description of the nucleation mechanism used in this thesis is given in Chapter 3, where the sulphuric acid-independent mechanism is implemented in GLOMAP-mode.

Survival of freshly formed clusters is a critical step in determining the number concentration of CCN-relevant particles. For such small clusters, the Kelvin effect[1] acts as a significant destabilising factor. Additionally small clusters are preferentially scavenged by some aerosol removal mechanisms. Therefore in GLOMAP, the effective rate of nucleation is used to calculate the appearance rate (J_{app} in cm^{-3} s^{-1}) of 3 nm sized particles (which are then added to the nucleation mode) taking into account the loss of some nucleated clusters following Kerminen and Kulmala (2002).

$$J_{app} = J_{crit} exp\left(0.23 \frac{CS'}{GR}\left(\frac{1}{D_{app}} - \frac{1}{D_{crit}}\right)\right) \tag{2.3}$$

where J_{crit} is the cluster formation rate in cm^{-3} s^{-1} and D_{crit} the diameter of the critical cluster which is taken to be 1.7 nm throughout the thesis, D_{app} is the diameter of the measured particle i.e. 3 nm. CS' is the reduced condensation sink in m^{-2} and GR is the constant growth rate of particles from 1.7 to 3 nm in nm hr^{-1}. The reduced condensation sink, CS', is calculated by integrating over all aerosol modes according to Kulmala et al. (2001). In the molecular regime CS' is effectively proportional to the surface area of the particle. GR in GLOMAP traditionally takes into account growth by condensation of sulphuric acid. In this thesis GR is proportional to the gaseous phase concentrations of sulphuric acid as well as organic compounds i.e. organic compounds participate in the growth of sub-3 nm particles.

Throughout this thesis POA from primary emissions and SOA from gaseous phase

[1]Greater the curvature i.e. smaller the size of a droplet, easier for the molecules to escape from the droplet. This is knows as curvature effect or Kelvin effect.

organic compounds are treated together and given identical properties within the 'OC' component in GLOMAP-mode. The OC component is assumed to exist in all particles as POM or OA with a mass of 1.4 × OC (Dentener et al., 2006). The OA/OC mass ratio can range from 1.3 to 2.6 (Philip et al., 2014; Tsigaridis et al., 2014) and is known to vary seasonally and regionally (Simon et al., 2011; Philip et al., 2014). However global models commonly use a global mean value for the OA/OC ratio, traditionally with a value of 1.4 (Grosjean and Friedlander, 1975; White and Roberts, 1977; Aiken et al., 2008; Appel et al., 2008; Pye and Seinfeld, 2010; Reddington et al., 2016). Throughout this thesis the same convention (i.e. a SOA/OC mass ratio of 1.4) is adopted for consistency with immediately preceeding GLOMAP-mode studies on atmospheric nucleation (Riccobono et al., 2014; Scott et al., 2014, 2015).

2.2.3 Condensation

Particle growth by condensation is simulated in GLOMAP-mode by allowing gaseous H_2SO_4 and organic compounds (SEC_ORG) to condense onto existing particles. The condensable gases condense according to existing particle surface area in each mode (Mann et al., 2010). The process of condensation as simulated in GLOMAP-mode is described in detail in Chapter 4 where the gaseous phase condensable organic vapours are classified according to their volatility and an additional approach to add gaseous phase organic compounds to the aerosol phase is explored.

2.2.4 Coagulation

In GLOMAP after every 3 mins freshly formed 3 nm particles are added to the nucleation mode which may then either grow due to condensation as described above or get scavenged by a larger particle via intra or inter-modal coagulation. Due to their higher mobility and higher diffusion coefficients smaller particles have a greater

tendency to coagulate compared to larger particles. Coagulation therefore favours the survival of the larger particles. For every aerosol mode, GLOMAP-mode allows for coagulation between particles within the same mode (intra-modal coagulation) as well as with particles in all the larger modes (inter-modal coagulation).

2.2.5 In-Cloud Processing

In-cloud processing refers to the growth of activated aerosol particles inside non-precipitating clouds by uptake of and reaction with soluble gases. A fixed activation dry radius of 50 nm corresponding to 0.2 % supersaturation is used globally to indicate the smallest size of aerosol that can be activated to cloud droplets. In GLOMAP the fraction of particle mass and the number of particles with radius greater than activation radius in the soluble Aitken mode are transferred to the soluble accumulation mode. In grid boxes that contain ISCCP derived low level clouds, SO_2 dissolves in cloud droplets and gets oxidised to increase the size and mass of sulphate aerosol in the clouds. This additional sulphate mass is then partitioned between the soluble accumulation and coarse modes based on the fractional contribution of each of the modes to the total activated particle number concentration. In-cloud processing is a more efficient growth process for aerosols than condensation or coagulation and defines the minimum in particle size distribution between Aitken and accumulation modes.

2.2.6 Ageing

Ageing converts non-hydrophilic aerosol particle (for example, freshly emitted BC) to hydrophilic. Ageing occurs by condensation of sulphuric acid and secondary organic compounds on insoluble particles and by accumulation of soluble particles due to inter-modal coagulation between an insoluble and a smaller soluble mode. At every time step the total flux of soluble material is calculated based on condensation

and coagulation routines. Once sufficient soluble matter has been accumulated (corresponding to 10 monolayers of soluble material) a fraction of particles from the insoluble mode is transferred to the corresponding soluble mode.

2.2.7 Hygroscopic growth

Particles in each mode grow by uptake of water (Zdanovskii, 1948; Stokes and Robinson, 1966) using data from Jacobson et al. (1996). Any POM present in the non-hydrophilic Aitken mode is primary and assumed to be non-hygroscopic. POM in the 4 soluble modes are either secondary or aged primary particles and are assigned a moderate hygroscopicity Mann et al. (2010).

2.2.8 Aerosol removal processes in GLOMAP

Mechanisms that remove aerosols in GLOMAP-mode are dry deposition, sedimentation, nucleation scavenging and impact scavenging. Dry deposition accounts for gravitational settling, Brownian motion, impaction interception, particle rebound and predominantly removes particles smaller than 50 nm. Processes represented under wet deposition are nucleation scavenging and impact scavenging. GLOMAP-mode treats nucleation scavenging (i.e. formation of a droplet around an aerosol nucleus) of in-cloud activated aerosol in grid boxes that are, according to ECMWF reanalyses, precipitating. Impaction scavenging is the process by which aerosols are collected by falling rain drops and is a fairly minor deposition process.

2.2.9 Sequence of operations in GLOMAP

In GLOMAP the change in aerosol mass and number concentrations with time - as a result of advective transport, gaseous phase chemistry and microphysical processes - is governed by a set of non-linear, coupled partial differential equations (PDEs) which are solved by the operator splitting method. This method, apart from being

computationally feasible, allows the breaking down of the PDEs into smaller sub-problems representing each process, solving for each in separate time steps and then bringing together the changes resulting from each of the separate calculations. Accuracy of the operator split method depends on the length of timestep used (Spracklen et al., 2005a). Figure 2.1 taken from Spracklen et al. (2005a) describes the sequence of microphysical operations in GLOMAP and the length of each timestep.

Large-scale advection, sub grid scale transport are performed by TOMCAT with a dynamical time-step of 1800 seconds. Each advection time step is divided into two sub-steps when emissions and chemistry are solved (NCTS). Each NCTS is further divided into two sub steps when aerosol microphysics (nucleation, condensation, coagulation) is solved (NMTS). To best capture the competition between nucleation and condensation processes NMTS is further split into five steps, NNTS, each of 90 seconds when the model alternates between a short step of nucleation (45 seconds) followed by condensation (45 seconds). Thus particles are produced and grown in the model by condensation within the NMTS sub step where they compete for gaseous phase condensables.

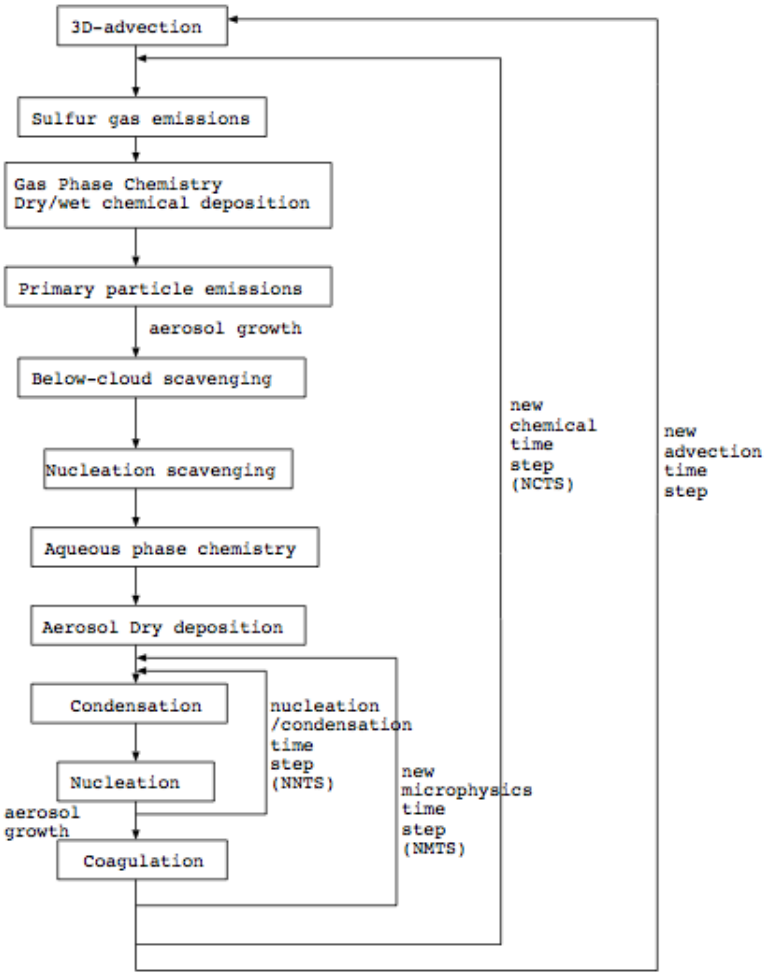

Figure 2.1: Flowchart from Spracklen et al. (2005a) showing sequence of processes in GLOMAP.

Chapter 3

Climate impact of pure biogenic nucleation in the atmosphere

3.1 Introduction

Accurate estimation of the top of the atmosphere first aerosol indirect forcing (AIF) due to anthropogenic aerosols depends largely upon accurate estimation of the number concentrations of aerosol particles in global models which can act as seeds for cloud formation both in pre-industrial and present-day atmosphere. The number concentrations of cloud condensation nuclei (CCN) simulated by a global model is determined by a number of factors (Merikanto et al., 2009; Pierce and Adams, 2009; Wang and Penner, 2009; Gordon et al., 2017) including primary emissions and the representation of new particle formation or nucleation in the model. Evidence of new particle formation in the atmosphere is abundant including observations made in the upper troposphere (Lee et al., 2003; Lovejoy et al., 2004), in continental boundary layer (Birmili and Wiedensohler, 2000; Boy and Kulmala, 2002; Kulmala, 2003), in marine boundary layer (Hoppel et al., 1994), in coastal regions (O'Dowd et al., 1999), in forests (Mäkelä et al., 1997; Vehkamäki et al., 2004), in remote regions (Weber et al., 1996) and in polluted regions (Woo et al., 2001; Mönkkönen et al.,

2005), to name a few. Nucleation accounts for almost half of the global low-level CCN (calculated at 0.2 % supersaturation; Merikanto et al., 2009; Gordon et al., 2017). Spracklen et al. (2006) showed boundary layer nucleation is an important contributor to total particle number concentrations (N3) increasing N3 by a factor of 2 (in polluted regions) to a factor of 8 (in relatively clean remote regions). Spracklen et al. (2006) suggested that nucleation is the dominant source of particles in remote continental regions. Spracklen et al. (2008) showed boundary layer nucleation (BLN) increases global CCN (calculated at 0.2 % supersaturation) concentrations by 3−20 % and global CCN (calculated at 1 % supersaturation) concentrations by 5−50 %. Wang and Penner (2009) showed including BLN in a global aerosol model increases global mean CCN concentrations by 31.4 % without primary sulphate particle emission and by 5.3 % with primary sulphate particle emission. Wang and Penner (2009) showed estimated AIF vary from -1.22 to -2.03 W m^{-2} due to various treatments of nucleation in the model, emphasizing the need for better representation of nucleation in global aerosol models.

It is likely that different nucleation mechanisms involving different precursor molecules are at play at different parts of the globe or at different altitudes, depending on the relative abundance of these precursor molecules. Atmospheric observations (Kulmala et al., 2004; McMurry et al., 2005) and laboratory studies (Benson et al., 2008; Berndt et al., 2005; Sipilä et al., 2010; Young et al., 2008) have identified a few such precursor molecules and possible chemical pathways that lead to particle formation. The primary vapour essential for atmospheric nucleation is established to be sulphuric acid produced from oxidation of SO_2 (Weber et al., 1996; Kulmala et al., 1998; Sipilä et al., 2010). Later studies identified the roles of amines (Kurtén et al., 2008; Almeida et al., 2013), ammonia (Napari et al., 2002; Benson et al., 2009; Berndt et al., 2010), organic compounds (Zhang et al., 2004) and ions (Laakso et al., 2002) - all of which enhance nucleation rates through stabilisation of the

sulphuric acid cluster. While the importance of organic compounds in nucleation has been established by several studies (Zhang et al., 2004; Leck and Bigg, 2010; Riccobono et al., 2014), given the large number of organic compounds found in the atmosphere and their varying physical and chemical properties, there are still huge gaps in understanding how they take part in aerosol formation or at what stage of aerosol growth do they contribute to (Riipinen et al., 2012). Consequently the representation of nucleation processes in global models and the simulated atmospheric particle number concentrations are, to date, largely impacted by the incompleteness of the existing knowledge on the mechanisms of particle formation in the atmosphere.

One of the challenges in understanding and quantifying the effects of atmospheric nucleation from organic compounds is identifying the relevant precursor molecules from a wide range of plausible trace gases found in the atmosphere. Key determinants of a species' role in nucleation (regardless of whether the species is emitted from biogenic or anthropogenic sources into the atmosphere) are their saturation vapour pressure and chemical reactivity in the gaseous phase. Typically the precursor molecules are biogenic (Kanakidou et al., 2005). After being emitted into the atmosphere the precursor molecules are oxidised by common atmospheric oxidants such as $OH^{\cdot}$, $NO_3^{\cdot}$ and O_3 to yield products of lower saturation vapour pressure. How saturation vapour pressure of gaseous phase species affects aerosol formation is discussed in detail in Chapter 4. Here it suffices to know that oxidation reactions of precursor gases typically produce molecules with a lower saturation vapour pressure than the reactants. A lower saturation vapour pressure favours the transfer from gaseous to the aerosol phase - making the oxidation products more capable of aerosol formation (than the reactant precursor molecules).

Model estimated particle number concentration is sensitive not only to the implementation of nucleation but also the choice of nucleation mechanism (Makkonen

et al., 2008). As a result several nucleation mechanisms have been implemented in global aerosol models reflecting the advances in the understanding of atmospheric nucleation (see Chapter 2 for a list of nucleation mechanisms implementd and used in GLOMAP-mode). The most widely used nucleation mechanism is the binary homogeneous water-sulphuric acid nucleation mechanism proposed by Kulmala et al. (1998). In GLOMAP this mechanism produces reasonable particle number concentration in the free troposphere (Spracklen et al., 2005a) but fails to simulate sufficient particles in the boundary layer (Merikanto et al., 2009). A second nucleation scheme involving the same molecules - water and sulphuric acid - uses an empirically derived mechanism for the activation of clusters containing one sulphuric acid molecule in the boundary layer (Kulmala et al., 2006). The activation nucleation mechanism of Kulmala et al. (2006) is based on the assumption that a single sulphuric acid molecule activates pre-existing clusters and therefore the nucleation rate is linearly dependent on atmospheric sulphuric acid concentration. A third mechanism, the kinetic nucleation mechanism (McMurry and Friedlander, 1979), is based on the assumption of a 'barrierless' nucleation that occurs when two sulphuric acid molecules collide with each other. In the kinetic mechanism the nucleation rate is proportional to the square of sulphuric acid concentration and the nucleation rate constant takes into account the collision frequency and the probability of the two sulphuric acid molecules sticking together after collision.

With increasing evidence of the involvement of vapours other than sulphuric acid in atmospheric nucleation (Weber et al., 1997; Birmili et al., 2003; Boy et al., 2005), large emissions of potentially nucleating organic vapours (Kesselmeier and Staudt, 1999; Rinne et al., 2009) and evidence of a large contribution of secondary processes to the organic aerosol load (Hallquist et al., 2009; Jimenez et al., 2009), Paasonen et al. (2010) suggested a nucleation parameterisation including sulphuric acid and low volatile organic compounds. Metzger et al. (2010) formulated a pa-

rameterisation based on smog chamber experiments involving oxidation products of an anthropogenic precursor of secondary organic aerosol (SOA). Riccobono et al. (2014) formulated a nucleation mechanism based on oxidation of pinanediol, a first-generation oxidation product of α-pinene, by $OH^{\cdot}$ in the CLOUD chamber. Implementing the nucleation scheme of Riccobono et al. (2014) in GLOMAP-mode significantly improved the seasonal cycle of monthly mean total particle number conentrations at ground-level simulated at 19 locations. Scott et al. (2015) reported, including nucleation of secondary organic compounds in GLOAMP-mode (boundary layer nucleation as in Metzger et al., 2010) increased estimated radiative effect in the present-day by 0.59 W m^{-2} (from -0.07 W m^{-2} estimated with activation scheme to -0.66 W m^{-2} estimated with organically mediated nucleation scheme).

This chapter is motivated from the experimental findings of Kirkby et al. (2016) that show for the first time that nucleation can occur in absence of sulphuric acid. Kirkby et al. (2016) finds that volatile organic compounds emitted from biogenic sources can initiate and sustain particle formation in absence of sulphuric acid in a chamber experiment based on ozonolysis of α-pinene. Until Kirkby et al. (2016) it was generally accepted that nucleation requires the presence of sulphuric acid (Kuang et al., 2008; Pierce et al., 2012; Kulmala et al., 2013). This means in the pre-industrial atmosphere when SO_2 emissions were much lower than present-day, nucleation still provided CCN particles in the atmosphere. The aim of this chapter is to implement a new nucleation mechanism based on the experimental results of Kirkby et al. (2016) in GLOMAP-mode and assess its implications on the first indirect aerosol radiative forcing.

3.2 Pure biogenic nucleation mechanism

3.2.1 Experimental set up

The findings of Kirkby et al. (2016) are based on the CLOUD (Cosmics Leaving OUtdoor Droplets) chamber experiment at CERN. The experiments are conducted in a 26.1 m^3 electro-polished stainless steel chamber, 3 m in diameter, under carefully monitored experimental conditions. The chamber is ultra-clean at technologically possible limits with very stable temperature control and has a large array of state-of-the-art instruments from international partner institutions, which continuously sample and analyse the contents of the chamber.

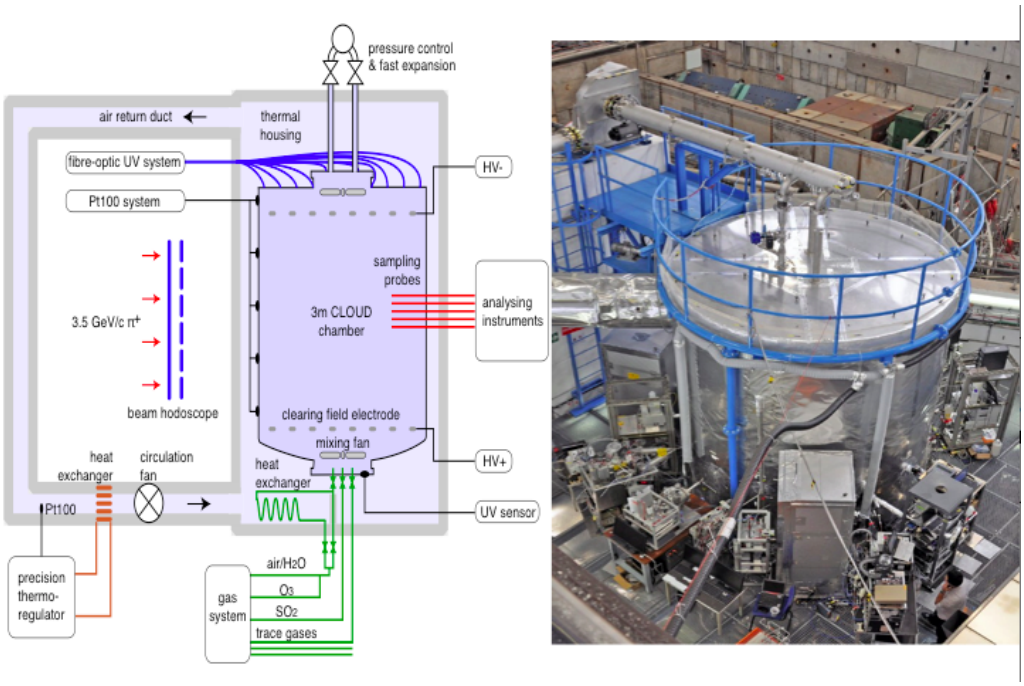

Figure 3.1: A schematic describing the chamber for the CLOUD Experiment at CERN (left) and the real stainless steel chamber used by the CLOUD Experiment at CERN (right).

For pure biogenic nucleation experiments during the 8^{th} CLOUD campaign in 2013, the chamber was set at relative humidity of 38 % and temperature of 278 K, contaminants levels were below the detection limit for SO_2 (<15 pptv) and H_2SO_4 (<5×10^4 cm^{-3}) and the total concentration of organic compounds (largely compris-

ing high volatility compounds) were below 150 pptv. A detailed description of the instruments used and experimental conditions can be found in Kirkby et al. (2016).

Nucleation rates (in $cm^{-3}s^{-1}$) were measured under 3 conditions:

1. Neutral condition i.e. conducting the experiment in an ion free condition using an electric clearing field of ±30 kV. Under this condition all ions are swept out of the chamber in about 1 second, suppressing all effects of ions on the measured nucleation rate.

2. Ground level or GCR condition when equilibrium ion pair concentrations in the chamber are around 700 cm^{-3} corresponding to atmospheric ion concentrations at surface-level.

3. A π^+ beam condition in which ion pair concentrations is increased up to 3000 cm^{-3} corresponding to upper (around 15 km altitude) atmospheric ion concentrations. The π^+ beam condition is achieved by using a adjustable particle beam from the CERN Proton Synchrotron.

For each experiment the concentration of α-pinene was within the range $0.1-2$ ppbv and O_3 within the range $20-40$ ppbv. Within minutes of coming in contact with ozone, α-pinene got oxidised to form extremely low volatility organic compounds. These compounds are referred to as highly oxygenated molecules or HOMs in Kirkby et al. (2016). The chemical ionization atmospheric pressure interface time-of-flight (CI-APi-TOF) mass spectrometers detected HOMs to be mixture of (a) $C_{8-10}H_{14,16}O_{6-12}$ species with an oxygen to carbon ratio (O:C) above about 0.6, also called HOM monomers, (b) HOM dimers which are two covalently bound monomers and (c) organic peroxy radicals ($RO_2^{\cdot}$) formed in the initial stages of alphapinene oxidation. Molar yield of HOM from ozonolysis of α-pinene was measured to be 1.2 % per hydroxyl radical ($OH^{\cdot}$) reaction with α-pinene, 3.2 % per ozone reaction with α-pinene and 2.9 % from pure ozonolysis, the uncertainty in HOM yields

being +80 %/−45 %. Shortly after their formation, HOMs were found to nucleate to produce particles.

Figure 3.2 (from Kirkby et al., 2016) shows CLOUD nucleation rates against sulphuric acid concentrations at varying concentrations of HOM. The shapes of symbols reflect the ion concentration during the experiment, the colors of symbols reflect the HOM concentration during the experiment and the shaded grey dots correspond to observations of nucleation rate made in the atmospheric boundary layer (Kuang et al., 2008; Paasonen et al., 2010; Kulmala et al., 2013).

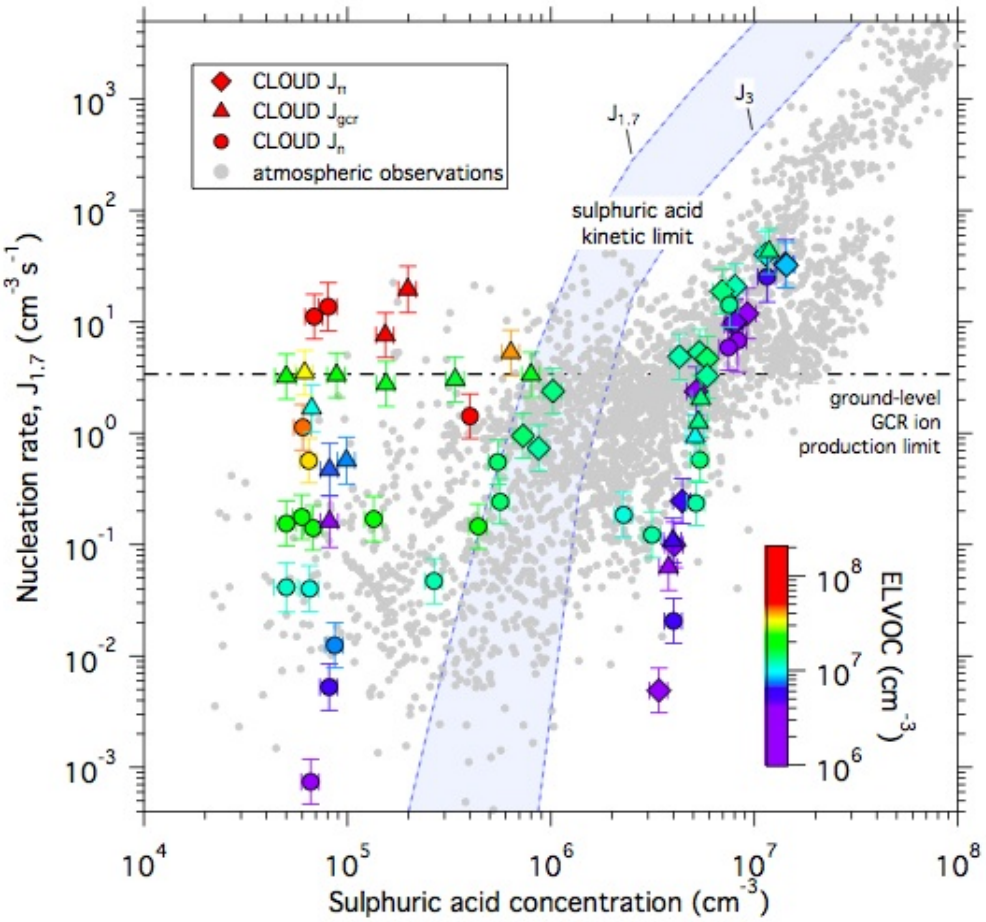

Figure 3.2: Experimental and observed nucleation rates ($J_{1.7}$) against sulphuric acid concentrations from Kirkby et al. (2016). The observed nucleation rates are shown as gray dots. CLOUD measured nucleation rates are shown using diamonds, triangles and circle symbols indicative of the concentration of ions during each experiment. Colours in symbols indicate the HOM concentrations for each experiment.

The figure shows two distinct regimes when the experiments produce atmospherically relevant nucleation rates.

- At $[H_2SO_4]$ $<10^6$ cm^{-3}, experimentally observed nucleation rates are independent of $[H_2SO_4]$ and show a strong dependence on [HOM]. It is in this regime, only to be found in very pristine regions in the present-day, that pure biogenic nucleation can explain particle formation rates.

- When $[H_2SO_4]$ $>10^6$ cm^{-3}, dependence of nucleation rate on [HOM] decreases

and sulphuric acid and other vapours are required to explain observed nucleation rates.

Tröstl et al. (2016) found HOMs comprise of compounds with a wide range of volatility and classified HOMs into extremely low volatility (ELVOC), low volatility (LVOC) and semi-volatile (SVOC) organic compounds - of which only ELVOC contributes to nucleation. This implies the yield of ELVOC should be less than that measured for HOMs in Kirkby et al. (2016). Tröstl et al. (2016) and Gordon et al. (2016) combined the *pure* ozonolysis yield of 2.9 % from O_3 with 1.2 % yield from $OH^{\cdot}$ (Kirkby et al., 2016) to represent ELVOC in GLOMAP-mode. In this chapter and throughout this thesis, the HOM yields as given in Kirkby et al. (2016) are used to produce ELVOC in the model (i.e. 3.2 % from O_3 and 1.2 % yield from $OH^{\cdot}$). The slightly higher yield for α-pinene and O_3 reaction, than that used in Tröstl et al. (2016) or Gordon et al. (2016), lie well within the uncertainty range (+80 %/−45 %) of ELVOC concentrations specified in Tröstl et al. (2016). Further, Jokinen et al. (2015) estimated ELVOC yields from α-pinene ozonolysis to be 3.4±1.7 % which is higher than the yields of HOM estimated by Kirkby et al. (2016). Jokinen et al. (2015) also reported efficient production of ELVOC from endocyclic monoterpene other than α-pinene, limonene and small amounts of ELVOC production from exocyclic monoterpenes such as β-pinene, myrcene and isoprene - which when quantified is likely to add to the ELVOC yield used in this thesis. The yields of nucleating-HOMs (or ELVOCs) and the nucleation mechanism remain the same throughout this thesis.

3.2.2 Nucleation rate parameterisation

Nucleation rates at 1.7 nm is determined by fitting time-dependent particle number concentrations measured by particle size magnifier (PSM1.8) and condensation particle counter (CPC2.5) within a simplified numerical model, AEROCLOUD, which

treats nucleation and growth of particles at a molecular level. AEROCLOUD and the parameterisation used for pure biogenic nucleation were developed by Jo$\widetilde{a}$o Almeida (CERN). AEROCLOUD uses ELVOC monomer, dimer and H_2SO_4 production rates derived from CI-APi-TOF experimental data. As ELVOC clusters have been found to be unstable (Kirkby et al., 2016), 1.7 nm is thought to be a reasonable approximation of the critical cluster size when growth rates equal evaporation rates. A cluster reaching the 1.7 nm size threshold is therefore considered to be thermodynamically stable growing at kinetic limit. The 1.7 nm size cluster is equivalent to roughly 5 ELVOC monomer units.

In AEROCLOUD clusters are formed due to kinetic collision between gaseous molecules. Once formed the model does not allow clusters to evaporate. Instead, to account for the loss of small unstable clusters through evaporation, the model uses a reduced clustering probability upon collision. Particle growth rate between PSM1.8 and CPC2.5 is treated as kinetically limited growth by molecular coagulation and condensation of ELVOC and H_2SO_4 vapours. Particles grow through size bins that are linearly spaced for small sizes and logarithmically spaced from 2 to 400 nm. The time for clustering is set to be between $0.9-10$ seconds while time step for all other processes (such as update of gas concentrations, high-voltage clearing field changes, fan changes and particle losses due to dilution of the chamber and diffusion to walls) is set to be 10 seconds.

To determine the nucleation rates, five free parameters of the model are fitted to the experimental particle concentrations in the PSM1.8 and CPC2.5 versus time. (Equations 3.1 and 3.2). The model successfully reproduces the time development of the particle number concentrations in both counters throughout all of the nucleation events in the data set. After fitting the data with the model, the nucleation rate $J_{1.7}$ is determined as the number of particles that grow to a mobility diameter of 1.7

nm or larger in any time step divided by the time increment. A full description of AEROCLOUD can be found in Kirkby et al. (2016).

The neutral ($J_{n,1.7,PB}$) and ion-induced ($J_{iin,1.7,PB}$) pure biogenic nucleation rates are parametrised as

$$J_{n,1.7,PB} = a_1[ELVOC]^{(a_2+a_5)/[ELVOC]} \tag{3.1}$$

$$J_{iin,1.7,PB} = 2[n\pm]a_3[ELVOC]^{(a_4+a_5)/[ELVOC]} \tag{3.2}$$

where $n\pm$ denotes ion concentration, a denotes free parameters such that a_1 = 0.04001, a_2 = 1.848, a_3 = 0.001366, a_4 = 1.566, and a_5 = 0.1863, with [ELVOC] expressed in units of 10^7 molecules cm^{-3}. The terms a_{1-4} describe simple power laws, while the term a_5 accounts for the steepening of the nucleation rate at low ELVOC concentrations. All organic nucleation rates are assumed to be independent of temperature.

3.2.3 Model set up

GLOMAP-mode as used in this study has been described in detail in Chapter 2. The modifications made to the model for this work, besides implementation of the pure biogenic nucleation mechanism, are:

1. All particles are allowed to grow by irreversible condensation of H_2SO_4 and (assumed non-volatile) gaseous phase secondary organic compounds (derived from oxidation of monoterpene at 13 % fixed yield) - unlike previous model versions where particles smaller than 3 nm grow by condensation of sulphuric acid only. This was implemented in the model by Kirsty Pringle (School of Earth and Environment, University of Leeds). Tests for the implementation were carried out by the candidate.

2. Prescribed oxidant concentrations ($OH^{\cdot}$, $NO_3^{\cdot}$, O_3) for the present-day and pre-industrial atmospheric conditions were updated to reflect advances in modelling atmospheric chemistry in the host CTM, TOMCAT. The new oxidant fields were provided by Nigel Richards (School of Earth and Environment, University of Leeds). Implementation of the new oxidant fields in the model and subsequent tests were carried out by the candidate.

For simulations performed in this chapter, nucleation in GLOMAP is represented using either the first two or all three of the following mechanisms:

1. Binary homogeneous nucleation of sulphuric acid and water according to Kulmala et al. (1998).

2. Ternary biogenic nucleation of H_2SO_4-BioOxOrg according to Riccobono et al. (2014) - representing the $[H_2SO_4]>10^6$ cm^{-3} regime in Figure 3.2.

3. Binary nucleation of ELVOC and water or pure biogenic nucleation, as implemented in this study according to Kirkby et al. (2016) - representing the $[H_2SO_4]<10^6$ cm^{-3} regime in Figure 3.2.

All three nucleation mechanisms are allowed to occur at every altitude although mechanism 1 produces more particles in the free troposphere while mechanisms 2 and 3 produce more particles in the boundary layer. BioOxOrg in mechanism 2 and ELVOC in mechanism 3 are both oxidised organic compounds participating in nucleation but the former refers to the parameterised oxidation products derived from pinanediol, a first-generation oxidation product of α-pinene, its concentration being

$$[BioOxOrg] = \frac{k_{MT*OH^{\cdot}}[MT][OH^{\cdot}]}{CS} \tag{3.3}$$

where

$$k_{(MT*OH^{\cdot})} = 1.2 \times 10^{-11} exp(444/T) \tag{3.4}$$

in units of cm^3 $molecule^{-1}$ s^{-1} (Atkinson et al., 2006) and CS represents the condensation sink in s^{-1} calculated from the reduced condensation sink and vapour diffusion coefficient (full description can be found in Kerminen and Kulmala, 2002; Spracklen et al., 2006).

The nucleation rate of mechanism 2 involving BioOxOrg is calculated as

$$J_{1.7,BioOxOrg} = k_1[H_2SO_4]^2[BioOxOrg] \tag{3.5}$$

The parameterisation to calculate nucleation rate for mechanism 3 involving ELVOCs has been described in Section 3.2.2 (Equations 3.1 and 3.2). Concentrations of ELVOC (that take part in pure biogenic nucleation) are derived from oxidation of monotepene by O_3 and $OH^{\cdot}$ and is given by

$$[ELVOC] = \frac{Y_{ELVOC*O_3}k_{MT*O_3}[MT][O_3] + Y_{ELVOC*OH\cdot}k_{MT*OH\cdot}[MT][OH]}{CS} \tag{3.6}$$

where $k_{(MT*O_3)} = 1.01 \times 10^{-15}exp(-732/T)$ $cm^3molecule^{-1}s^{-1}$, $k_{(MT*OH\cdot)} = 1.2 \times 10^{-11}exp(444/T)$ $cm^3molecule^{-1}s^{-1}$, $Y_{ELVOC*O_3} = 3.3$ % , $Y_{ELVOC*OH\cdot} = 1.2$ %.

Nucleation rates given by Equations 3.1, 3.2 and 3.5 determine the formation of clusters of 1.7 nm diameter i.e. $J_{1.7} = J_{n,1.7,PB} + J_{iin,1.7,PB} + J_{1.7,BioOxOrg}$. The growth of 1.7 nm clusters up to 3 nm sizes in the model is determined using the equation of Kerminen and Kulmala (2002) which takes into account the losses during initial growth of clusters.

$$J_{app} = J_{crit}exp\left(0.23\frac{CS'}{GR}\left(\frac{1}{D_{app}} - \frac{1}{D_{crit}}\right)\right) \tag{3.7}$$

where J_{crit} is the cluster formation rate in cm^{-3} s^{-1} and D_{crit} the diameter of the critical cluster which is taken to be 1.7 nm throughout the thesis, D_{app} is the diameter of the measured particle i.e. 3 nm. CS' is the reduced condensation sink in m^{-2}

calculated by integrating over all aerosol modes according to Kulmala et al. (2001). GR is the constant growth rate of particles from 1.7 to 3 nm in nm hr^{-1}. The existent approach in GLOMAP is to grow clusters by kinetic condensation of sulphuric acid up to 3 nm sizes (Spracklen et al., 2006) following Kerminen and Kulmala (2002).

$$GR = \frac{3.0 \times 10^{-9}}{\rho_{nuc}} c_{H_2SO_4} M_{H_2SO_4} C_{H_2SO_4} \tag{3.8}$$

where ρ_{nuc} is the cluster density in kg m^{-3}. $C_{H_2SO_4}$ is the gaseous phase concentration in molecules cm^{-3} of sulphuric acid, $c_{H_2SO_4}$ is the molecular speed of sulphuric acid in m s^{-1} and $M_{H_2SO_4}$ is the molecular weight of sulphuric acid in kg mol^{-1}. Once the clusters reach a size of 3 nm, they enter into the nucleation mode in the model.

With the discovery of organic compounds that are capable of initiating particle formation in Kirkby et al. (2016), it is evident that some organic compounds in the atmosphere are also capable of contributing to the subsequent growth of the nucleated clusters. Kulmala et al. (2013) establishes the dominant role of organic molecules in stabilisation of growing clusters between $1.5-1.9$ nm that largely determines the number concentration of 3 nm size particles. Hence in this thesis oxidised biogenic organic compounds, along with sulphuric acid, are used to grow sub-3 nm clusters in the model.

$$GR = \frac{3.0 \times 10^{-9}}{\rho_{nuc}} \sum_i c_i M_i C_i \tag{3.9}$$

where ρ_{nuc} is the cluster density in kg m^{-3}. i denotes each condensable vapour (sulphuric acid and oxidised biogenic organic compounds). C_i is gaseous phase concentration in molecules cm^{-3}, c_i is the molecular speed in m s^{-1} and M_i is the molecular weight in kg mol^{-1} of the corresponding condensable vapour. Thus the sub-3 nm growth rate is proportional to concentrations of gaseous sulphuric acid

and oxidised biogenic organic compounds in the model.

To estimate the anthropogenic aerosol indirect forcing, simulated aerosol-cloud interaction in the present-day (PD) is contrasted against that simulated in the pre-industrial (PI) atmosphere. The PI and PD simulations are identical except for anthropogenic emissions. To simulate the PI atmosphere (Dentener et al., 2006), SO_2 emissions from industries, powerplants, international shipping, off-road, road transport and domestic sources are removed - allowing only the domestic source of SO_2 in the model. Further, biofuel and fossil fuel emission sources of carbonaceous aerosols are scaled down (based on population and crop production statistics) to reflect PI emissions. Biomass burning, DMS, sea salt, dust and volcanic SO_2 emissions are assumed to be the same in PI and PD.

Simulations for this study are carried out for the years 1750 and 2000, with three months model spin-up, to represent the PI and PD atmospheres respectively. All simulations are first performed with aerosol production involving primary emitted particles together with secondary particles from mechanisms 1 and 2 (control simulations). A further set of simulations (perturbed simulations) is then performed under identical conditions except with pure biogenic nucleation (mechanism 3) added. The impact of pure biogenic nucleation on climate is then evaluated by comparing the control and perturbed simulations. Number concentrations of all particles greater than 50 nm dry diameter (N50) are taken as proxy for CCN.

3.2.3.1 Offline estimation of CDNC

In GLOMAP cloud droplet number concentrations (CDNC) are calculated as a post-processing step. Estimates of CDNC are based on the the assumption that clouds consist of 'activated' droplets that grow continuously after they reach a critical size corresponding to a critical value of the supersaturation of water vapour (Charlson

et al., 2001). Before the critical diameter is reached particles are considered to be in equilibrium with the ambient (supersaturated) water vapour concentrations. The number of cloud droplets formed can therefore be calculated by estimating the number of activated CCN at the maximum supersaturation in a cloud updraft (Nenes et al., 2001).

Simulating the activation of aerosol particles to act as cloud droplets requires a resolution on scales of tens of meters which is computationally not feasible for a global aerosol model. GLOMAP-mode relies on the parameterisation of Nenes and Seinfeld (2003) and Fountoukis and Nenes (2005) to calculate CDNC. The parameterisation was found to predict observed CDNC with good accuracy when evaluated against aircraft data collected in low-level cumuliform and stratiform clouds formed in marine and continental air masses (Meskhidze et al., 2005). When implemented in GLOMAP-bin with aerosol components restricted to sulphate and sea-salt by Pringle et al. (2009), this scheme predicted realistic CDNC concentrations (Pringle et al., 2009; Merikanto et al., 2010) and since then have been used in several studies to calculate CDNC from GLOMAP-mode simulations (Spracklen et al., 2011b; Schmidt et al., 2012; Lee et al., 2013; Scott et al., 2014; Regayre et al., 2014; Gordon et al., 2016).

The parameterisation of Nenes and Seinfeld (2003) and Fountoukis and Nenes (2005) firstly involves calculating the number concentration of droplets that can potentially form at a certain level of supersaturation. In principle any particle with a critical supersaturation less than the maximum supersaturation encountered within the parcel activates. But as pointed out by Nenes et al. (2001) the time for which a particle is exposed to a critical supersaturation level must be sufficient for it to reach its critical diameter. Nenes and Seinfeld (2003) introduced the concept of 'population splitting' by which particles that have diameters close to their critical supersatura-

tion and those that do not, are separated. This approach addresses the errors that result from assuming that activation process is not kinetically limited and that CCN particles grow to their critical diameter instantly when their critical supersaturation equals parcel supersaturation (Nenes and Seinfeld, 2003). This is important as the aerosol activation scheme not only influences CDNC but also influences the mean cloud droplet size, which in turn influences cloud reflectivity (Abdul-Razzak and Ghan, 2000).

Secondly, the CCN spectrum is included within the framework of an adiabatic cloud parcel model, with a constant updraft velocity, to compute the maximum supersaturation of cloud parcel. A rising air parcel with weaker velocity achieves lower maximum supersaturation compared to a parcel with strong updraft velocity. A lower maximum supersaturation implies only particles with very small critical supersaturation can be activated. In GLOMAP-mode a constant updraft value of 0.15 ms^{-1} is prescribed over the oceans and 0.3 ms^{-1} over the land (see Schmidt et al., 2012 for more detail).

Calculating the number concentration of droplets that may be activated necessitates the estimation of the soluble fraction of aerosol particles. The scheme currently used in GLOMAP takes into account the fraction of soluble material in the particles and number of ions each component releases in the solution to predict CDNC. The latter is represented by the van't Hoff factor, which is an emperically determined correction factor to account for the dissociation of the solute and the non-ideal behaviour of the solution. The van't Hoff factors for inorganic salts are well-known while van't Hoff factor for complex organic compounds are highly variable due to the high variability of the response of organic compounds to water (Sun and Ariya, 2006).

Only particles with some water soluble species can act as CCN. The solubility of

commonly found atmospheric inorganic species and hence their ability to act as CCN are well known. However presence of organic compounds internally mixed with inorganic species alter the CCN activity of aerosol particles (Corrigan and Novakov, 1999). Measurements show terpene oxidation products can act as CCN (Yu, 2000; Engelhart et al., 2008). The ability of organic compounds to act as CCN depends on their solubility (which spans a wide range) and is further complicated by the surfactant activity of organic molecules. By acting as surfactants organic compounds reduce surface tension of aerosol particles which significantly reduce the critical supersaturation (Shulman et al., 1996). Consequently as the droplet grows and the mass of organic component increases, the soluble fraction increases. Sorjamaa et al. (2004) shows organic compounds acting as surfactants can increase the growth of larger droplets and lead to less dense clouds. Thus from a global modelling point of view, assigning a single van't Hoff factor to the organic component (POM) in GLOMAP-mode to contribute to the soluble fraction of aerosol particles is extremely challenging. Consequently in previous studies no contribution from POM was included in the estimation of CDNC (Spracklen et al., 2011a; Schmidt et al., 2012; Scott et al., 2014).

Petters and Kreidenweis (2007) proposed the hygropscopicity parameter, kappa (κ), to model the composition-dependence of the solution water activity. The hygropscopicity parameter is a quantitative measure of the aerosol water uptake characteristics and CCN activity, which can be measured in laboratory experiments. It may also be understood as the volume of water associated with a dry particle (Rissler et al., 2006). For multicomponent particles such as the particles simulated in GLOMAP-mode, Petters and Kreidenweis (2007) shows kappa can be derived by weighting the best fit kappa values of individual constituents to their volume fractions in the mixture. The hygroscopicity approach has been shown to be adequate, within experimental uncertainties, for estimating critical supersaturation for mixed

particles containing a surfactant (Petters and Kreidenweis, 2007). Thus together, the hygroscopicity approach and the activation parameterisation - used to calculate CDNC from the soluble fraction of simulated aerosol particles - are suitable to treat aerosol mixtures including slightly soluble surface-active organic compounds (Nenes and Seinfeld, 2003). The kappa values assigned to aerosol components in GLOMAP-mode are: 0.61 for sulphate, 1.28 for sea-salt, 0.0 for black carbon and 0.1 for particulate organic matter (including both primary and secondary aerosol).

The same hygroscopicity parameters have previously been used in GLOMAP-mode to calculate CCN concentrations (Spracklen et al., 2011a; Scott et al., 2014). However as mentioned earlier, in those studies POM was not allowed to contribute to the soluble fraction of aerosol particles that can be activated to constitute CDN. The implementation of the hygroscopicity parameter to calculate CDNC was done by Hamish Gordon (School of Earth and Environment, University of Leeds Gordon et al., 2016; Dunne et al., 2016) in collaboration with Athansios Nenes (California Institute of Technology). Comparison between the old and new methods were made by the candidate and shown in Section 3.3.3.3.

3.2.3.2 Estimation of the first AIF

Higher CDNC increases cloud albedo, which in turns reflects more incoming SW radiation producing additional top of the atmosphere cooling. This constitutes the first aerosol indirect effect or AIE. The radiative forcing by anthropogenic aerosols due to the first indirect effect (first AIF) at any region is directly controlled by the *relative change* in CDNC over the industrial period. A higher CDNC implies smaller cloud droplet sizes, the liquid water content of the cloud being fixed. Throughout this thesis the term **radiative forcing** (or first AIF) is used to denote change in the top of the atmosphere radiative balance from PI to PD conditions and **radiative effect** (or first AIE) is used to denote the impact of an perturbation (in this chap-

ter, pure biogenic nucleation) in the present-day or in the pre-industrial atmospheric conditions.

The first AIF is calculated using an offline version of the radiative transfer model of Edwards & Slingo (Edwards and Slingo, 1996). The radiative transfer model has a resolution of 144 (longitude) × 72 (latitude) × 23 (altitude) and uses monthly mean climatology from ECMWF reanlysis and cloud fields from the International Satellite Cloud Climatology (ISCCP). The method used to calculate cloud droplet effective radius is the same as described in Schmidt et al. (2012); Scott et al. (2014) and is briefly described here:

For each perturbed simulation, the cloud droplet effective radius $r_e^{perturbed}$ is calculated in μm based on the equation:

$$r_e^{perturbed} = r_e^{control} \times \left(\frac{CDNC^{control}}{CDNC^{perturbed}} \right)^{\frac{1}{3}} \tag{3.10}$$

where $\text{CDNC}^{control}$ and $\text{CDNC}^{perturbed}$ are monthly mean number concentrations of cloud droplets in cm^{-3}, calculated from GLOMAP-mode control and perturbed simulations (as described in the last section). The cloud droplets in control simulation is given a mean effective radius ($r_e^{control}$) value of 10 μm.

The first AIE is then estimated by comparing the net change in (SW+LW) flux between the control and perturbed simulations for either the present-day or the pre-industrial atmosphere. For example, to calculate the radiative perturbation attributable to the inclusion of pure biogenic nucleation in the model in the present-day atmosphere, $\text{CDNC}^{control}$ corresponds to a simulation without ELVOC nucleation and $\text{CDNC}^{perturbed}$ corresponds to an identical simulation but with ELVOC nucleation. The first AIF between 1750 and 2000 is calculated by comparing simulations

for 1750 and 2000 i.e. $CDNC^{control}$ corresponds to PD simulation and $CDNC^{perturbed}$ corresponds to pre-industrial simulation. The calculations of first AIE and first AIF, from CDNC concentrations derived from GLOMAP-mode simulations, are done by Alex Rap (School of Earth and Environment, University of Leeds).

3.3 Results

3.3.1 The effect of pure biogenic nucleation on modelled N50

The minimum dry diameter required for a particle to act as a CCN is 50 nm. Figure 3.3 shows the global distribution of particles with dry diameter greater than 50 nm, N50, for simulations with and without pure biogenic nucleation and the change in N50 as a result of including pure biogenic nucleation.

A notable feature of Figure 3.3 is the larger increase in pre-industrial N50 (Figure 3.3g) when pure biogenic nucleation is used compared to the increase in the present-day (Figure 3.3h). The change in PI is expected to have significant climatic implication as the anthropogenic aerosol radiative forcing is more sensitive to changes in pre-industrial particle number concentrations (Carslaw et al., 2013). The larger increase of N50 in PI (compared to PD) as a result of pure biogenic nucleation lowers the relative change in N50 over the industrial period. Figure 3.3i shows the lowering of $N50_{1750-2000}$ in shades of blue.

Overall pure biogenic nucleation changes surface-level N50 concentrations in the model between -2 and $+256$ % in PI with more than half the globe experiencing a change above 21 %. In the PD atmosphere pure biogenic nucleation changes surface-level N50 concentrations between -2.5 and $+211$ % with more than half the globe experiencing a change above 4 %. The global mean relative change when pure

biogenic nucleation is included is 36 % (56 % for the Northern Hemisphere, NH and 16 % for the Southern Hemisphere, SH) in PI and 13 % (17% for NH and 8 % for SH) in PD. Change in the global mean N50 is about 47 % (from 170 to 252 cm^{-3}) in the PI and 14 % (from 310 to 354 cm^{-3}) in the PD. Pure biogenic nucleation increases N50 particularly over the boreal forests in the northern latitudes and over the tropical rain forest regions.

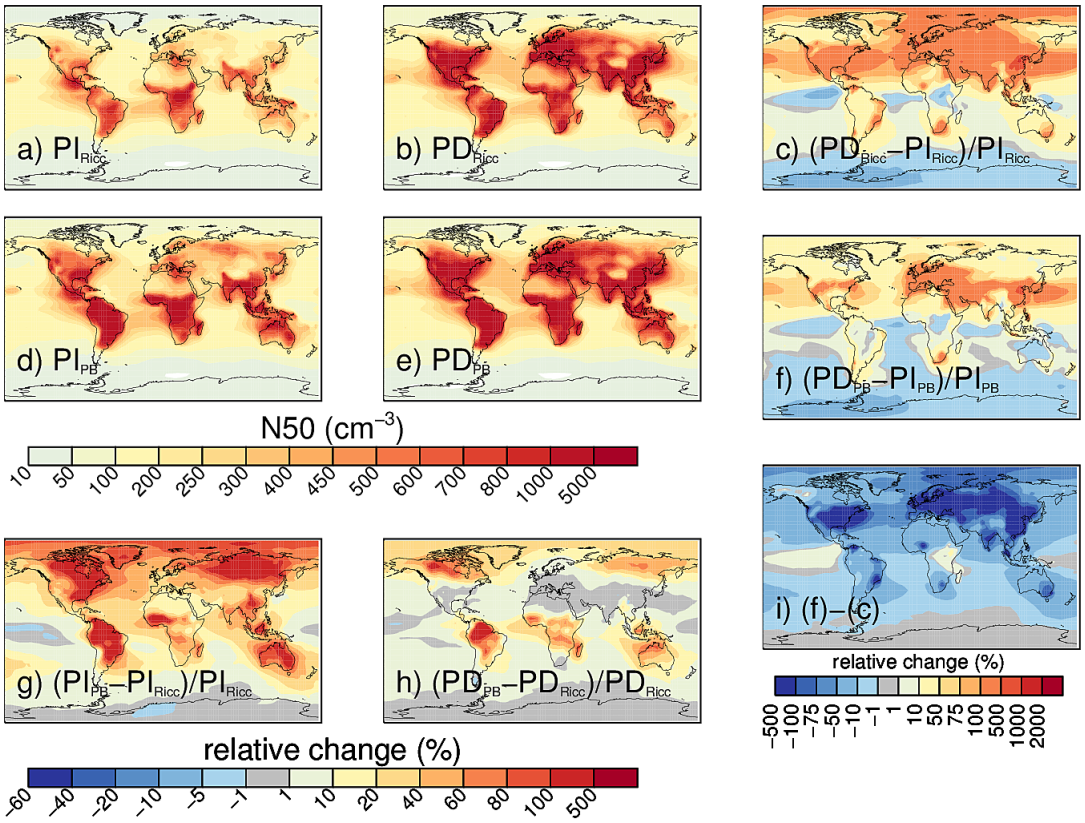

Figure 3.3: Annual mean number concentrations of surface-level particles with dry diameter above 50 nm (N50) for a) pre-industrial atmosphere without pure biogenic nucleation, b) present-day atmosphere without pure biogenic nucleation, d) pre-industrial atmosphere with pure biogenic nucleation, e) present-day atmosphere with pure biogenic nucleation. The relative change in annual mean N50 from pre-industrial to present-day is shown in c) without pure biogenic nucleation, d) with pure biogenic nucleation. The absolute difference between c) and f) is shown in i). Relative change in annual mean N50 due to pure biogenic nucleation is shown in g) for pre-industrial and h) for present-day atmospheres.

Boreal forests and tropical rain forests have the highest emissions of biogenic

VOCs, including monoterpene which is used in GLOMAP-mode to generate oxidised organic compounds (Guenther et al., 1995; Mann et al., 2010). Observations at several boreal forest sites at Northern and Central Europe such as the Finnish SMEAR II station at Hyytiala (Kulmala et al., 2001), stations located in the Finnish Lapland, Pallas and Varrio (Vehkamäki et al., 2004), stations in the Scandinavian rim of the boreal region, Aspvreten (Tunved et al., 2006) show evidence of boundary layer nucleation being a significant source of particles. Regional nucleation events occur 25−40 % of days (Lyubovtseva et al., 2010), the frequency peaking in spring with highest growth rates observed in summer in association with increased biogenic activity. On the other hand Siberian boreal forest nucleation is considered to be more sulphuric acid and ammonia dependent (Lyubovtseva et al., 2010).

By contrast nucleation events in tropical rain forests are relatively less studied and less observed. In the Amazon basin, which represents more than half of the Earth's rainforests in the present day, boundary layer nucleation events have been less commonly reported (Zhou et al., 2002; Rizzo et al., 2006, 2010), although biogenic aerosols are known to dominate the particle composition over this region during the wet seasons (Andreae and Crutzen, 1997; Echalar et al., 1998). Pöschl et al. (2010) reports low abundance of nucleation mode particles in the Amazon and infers the high concentrations of SOA are a result of entrainment of nucleated particles from the free troposphere. Martin et al. (2010) reports the smallest particles in the Amazon typically have size between 10−20 nm and continuous growth to larger sizes is rarely observed.

The enhanced nucleation predicted by the model over the Amazon basin when pure biogenic nucleation is introduced and the lack of direct atmospheric observations validating the same raises the question: *Is pure biogenic nucleation relevant in the real atmosphere?*

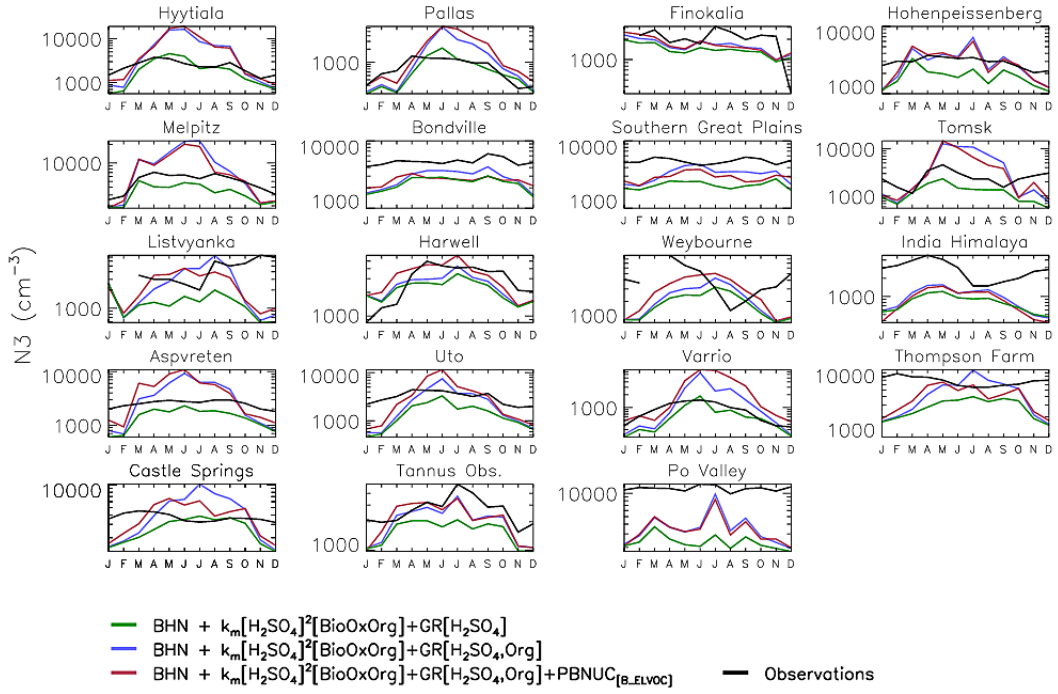

Figure 3.4: Comparison of modelled and observed monthly mean surface-level total particle number concentration (N3) at 19 ground-based locations. The black line shows N3 from atmospheric observations. The green line shows N3 simulated with boundary layer nucleation of BioOxOrg only (as in Riccobono et al., 2014). The blue line shows N3 simulated with growth of nucleated particles from organic compounds, added to the simulation in green line. The red line shows N3 simulated with pure biogenic nucleation added to the simulation in blue line. All simulations include binary homogeneous nucleation (BHN) of sulphuric acid in the free troposphere.

Figure 3.4 compares monthly mean observations of surface-level total particle number concentrations (N3) at 19 sites in the NH (Spracklen et al., 2010; Riccobono et al., 2014). The figure compares three simulations: the green line showing N3 from a simulation involving BioOxOrg nucleation, identical to that published in Fig 3 of Riccobono et al. (2014); the blue line showing N3 from a simulation with BioOxOrg nucleation with oxidised organic compounds (in addition to sulphuric acid) growing freshly nucleated particles; the red line showing N3 from a simulation with pure biogenic nucleation with oxidised organic compounds (in addition to sulphuric acid)

growing freshly nucleated particles.

The simulation with pure biogenic nucleation predicts a reasonable seasonal cycle in Figure 3.4. However an overestimation in particle number concentration in the summer is evident. Riccobono et al. (2014) showed nucleation of BioOxOrg generated from biogenic monoterpenes in the model corrected the problem of a summer dip in particle number concentrations, which had been a robust feature associated with nucleation schemes dependent only on sulphuric acid. Herein it is seen that including oxidised organic compounds from monoterpene oxidation to *grow* freshly nucleated clusters to 3 nm size, leads to an overestimation of N3 at many sites (blue line). Consequently adding pure biogenic nucleation (to blue line) which *additionally produces* particles further overestimates particle number concentrations.

It may be noted here that the increase in particle number concentration is dominated by organic compounds taking part in the *growth* of freshly nucleated particles rather than pure biogenic nucleation itself (increase from green to blue line is much bigger than increase from blue to red line in Figure 3.4). The overall overestimation of particles as a result of pure biogenic nucleation is therefore, to a large extent, a result of overestimating the organic contribution to growth of freshly nucleated particles. The initial growth of nucleated particles is an area of active research. While it has been shown that organic compounds are largely responsible for the growth of particles up to detectable sizes (Ehn et al., 2014), no study to date has characterised or quantified the source of such organic compounds (Tröstl et al., 2016).

It is suggested here that the striking increase of annual mean N50 concentration over the Amazon basin, with pure biogenic nucleation mechanism in the present-day atmosphere (Figure 3.3h), could partly be associated with the one or both of the following factors:

1. Prior to pure biogenic nucleation mechanism, all nucleation mechanisms were entirely or heavily sulphuric acid-dependent (Kulmala et al., 1998; Vehkamäki et al., 2004; Paasonen et al., 2010; Metzger et al., 2010; Riccobono et al., 2014). In the model sulphuric acid concentrations are controlled by emissions of anthropogenic SO_2 and DMS (from marine phytoplanktons that produce SO_2). Concentrations of SO_2 are low in the Southern Hemisphere (see Figure 1, Mann et al., 2010), especially over the Amazon basin where ambient conditions approach those of the pristine pre-industrial during the wet season (Pöschl et al., 2010). With low SO_2 concentrations, the model predicted lower concentrations of CCN-sized particles in Amazon basin in previous GLOMAP studies (Mann et al., 2010; Riccobono et al., 2014).

   In contrast to the low levels of sulphuric acid, monoterpene emissions in the model peaks in the Southern Hemisphere tropical rainforest regions (Figure 1, Mann et al., 2010). Emission of biogenic VOCs show a low seasonality in the Amazon because of consistent high temperatures, particularly over the Amazon basin. As a result a nucleation scheme such as pure biogenic nucleation, that is solely dependent on biogenic monoterpene oxidation, produces particles all year round in the model over the Amazon basin.

2. The pre-existing aerosol concentration in the model is underestimated. For a nucleation scheme to increase particle number concentrations, the production rate of freshly nucleated particles must exceed the loss rate due to coagulation with pre-existing particles (condensation sink). When pure biogenic nucleation is implemented, the significant increase in N50 over the Amazon basin (Figure 3.3h), where atmospheric nucleation events are hardly observed, suggests the concentration of pre-existing particles in the region may be underestimated in the model. Such underestimation of ambient aerosol concentrations are not

uncommon in global models (Hallquist et al., 2009). It is thought that the underestimation arises from using laboratory measured yields to simulate the conversion of gaseous phase oxidised organic compounds to SOA. Such yields may significantly underestimate the conversions that occur on longer time-scales in the atmosphere (Goldstein and Galbally, 2007). Further, laboratory studies are free from any pre-existing aerosol concentrations. Pre-existing aerosol concentrations in the atmosphere may cause the measured nucleation rates to be lower in some parts of the globe (Kanakidou et al., 2005) - which cannot be captured by a model that underestimates the pre-existing aerosol concentrations. The potential impact of an increased pre-existing particle concentration is seen in Chapter 4.

3.3.2 The effect of pure biogenic nucleation on modelled CDNC

Figure 3.5 shows the effect of including pure biogenic nucleation in the model on estimated CDNC. Including pure biogenic nucleation in the model changes CDNC between 0.2 and 81 % in the pre-industrial with more than half the globe experiencing a change above 15 %. In the present day CDNC changes are between -0.5 and 38 % with more than half the globe experiencing a change above 5 %. The mean relative change globally is 20 % (30 % in NH and 13 % in SH) in PI and 7 % in PD (8 % in NH and 7 % in SH). The global annual mean CDNC increases by 19 % (98 to 117 cm^{-3}) in PI and 6 % (155 to 165 cm^{-3}) in PD.

The change in CDNC is controlled by the change in N50 (Figure 3.3), following similar spatial pattern, though the magnitude of the change is far less compared to that in N50. Pure biogenic nucleation increases the aerosol number concentration by adding more particles to the nucleation mode. But freshly nucleated particles need a longer time to grow to CDNC sizes and have higher loss probability than

larger particles. Only the fraction of nucleated particles that can reach accumulation mode size ranges may activate to CDNC. As a result the change in CDNC, when pure biogenic nucleation is added to the model, is much smaller than the change in N50 (compare Figures 3.3h and 3.5h). For example, the Amazon basin which shows a striking increase (> 500 %) in N50 concentration when pure biogenic nucleation is added to the model, shows a modest $20-40$ % increase in CDNC. An additional factor that comes into play in regions of high primary emissions (such as the Amazon basin with high biomass burning emissions) is that the primary (carbonaceous and sulphate) particles emitted to the higher modes increase the competition for water vapour, further limiting the number of smaller particles that can grow to cloud droplet sizes.

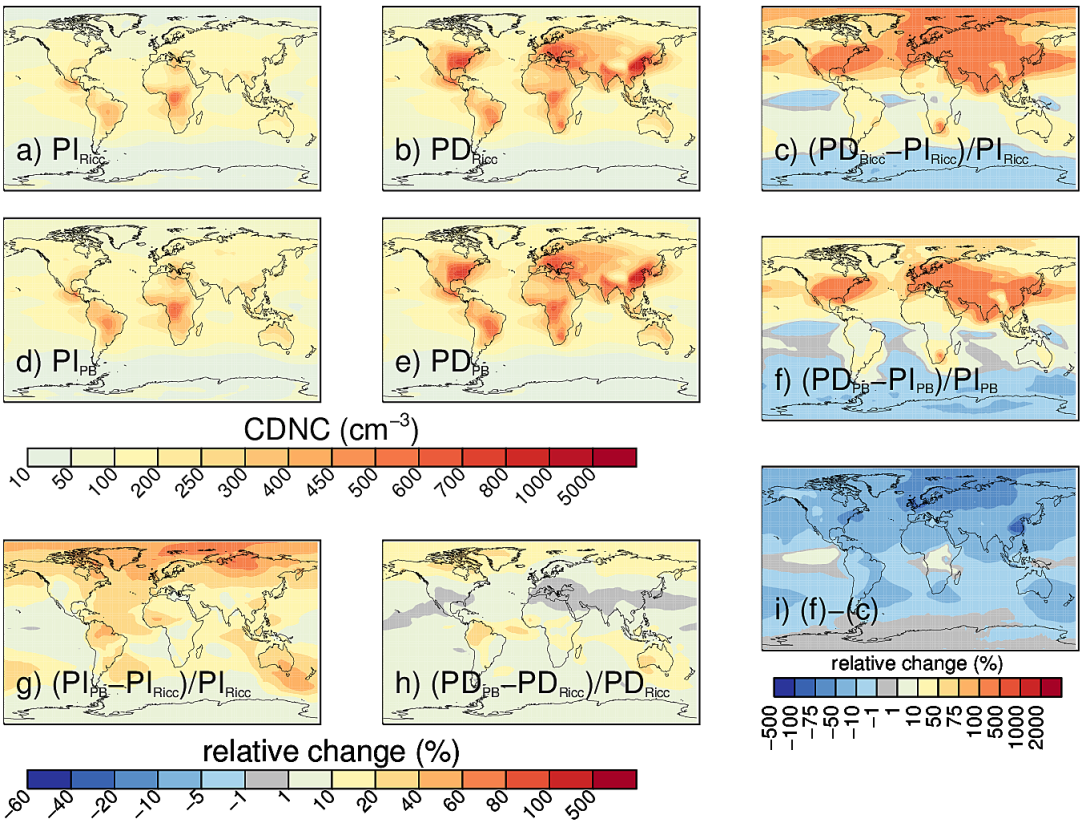

Figure 3.5: Annual mean surface-level cloud droplet number concentration (CDNC) for a) the pre-industrial atmosphere without pure biogenic nucleation, b) the present-day atmosphere without pure biogenic nucleation, d) the pre-industrial atmosphere with pure biogenic nucleation, e) the present-day atmosphere with pure biogenic nucleation. The relative change in annual mean CDNC from the pre-industrial to present-day is shown in c) without pure biogenic nucleation and d) with pure biogenic nucleation. The absolute difference between c) and f) is shown in i). Relative change in annual mean CDNC due to pure biogenic nucleation is shown in g) for the pre-industrial and h) for the present-day atmospheres.

There is a greater increase in CDNC in the PI (Figure 3.5g) than in the PD (Figure 3.5h) with pure biogenic nucleation. The enhanced increment of CDNC in PI (with pure biogenic nucleation) lowers the contrast in CDNC between PI and PD (compared to simulation without pure biogenic nucleation) which is reflected in Figure 3.5i. A small increase in CDNC in a pristine region with low CDNC causes a large relative change. The same increase in CDNC over a polluted region results in a smaller relative change. Hence most of the relative increase in CDNC from PI to PD in Figure 3.5f occurs in the NH where more pristine conditions prevailed in

the PI.

3.3.3 Estimation of the first indirect aerosol radiative forcing

Figure 3.6 shows the annual mean top of the atmosphere first AIF due to anthropogenic aerosols, as after pure biogenic nucleation is implemented in the model. Figure 3.7 shows the change in top of the atmosphere first AIF due to anthropogenic aerosols, as a result of implementing pure biogenic nucleation. The positive changes in first AIF due to pure biogenic nucleation (Figure 3.7) closely follow the negative changes in the relative change in CDNC due to pure biogenic nucleation (Figure 3.5i) and vice versa. Positive change in first AIF indicates a lowering of the previously estimated cooling by anthropogenic aerosols and are therefore associated with regions of lower relative change in CDNC.

The global annual mean **radiative forcing** due to anthropogenic aerosols with pure biogenic nucleation is estimated to be -0.54 W m^{-2} and the change due to pure biogenic nucleation estimated to be $+0.25$ W m^{-2} which is a 32.5 % reduction in the negative forcing. Over the boreal forests in the NH, first AIF lies between -0.01 to -0.5 W m^{-2} and over the Amazon basin between -0.01 to -0.1 W m^{-2}. Figure 3.6 shows radiative cooling due to anthropogenic aerosols occurs preferentially over the NH, where anthropogenic activities between 1750 and 2000 has been most significant.

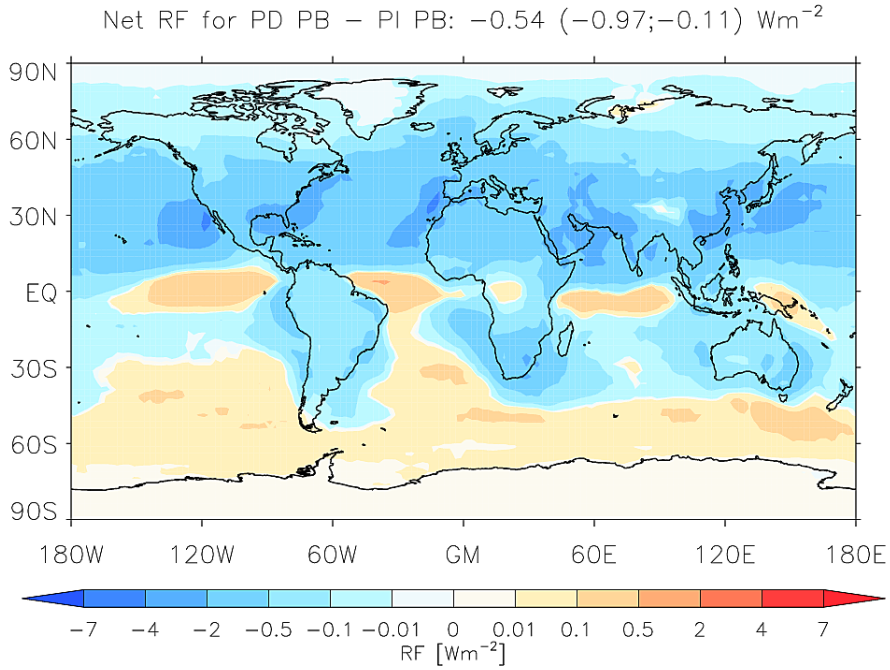

Figure 3.6: Annual mean top of the atmosphere first aerosol indirect forcing (AIF) between 1750 and 2000 after including pure biogenic nucleation in GLOMAP-mode. The first AIF is calculated at the top of the atmosphere for low and mid-level clouds (upto 600 hPa) for pre-industrial and present-day atmospheres. The magnitude of global annual mean net AIF is specified at the top of the plot. Numbers in brackets denote the annual mean AIF for the Northern and Southern Hemispheres respectively.

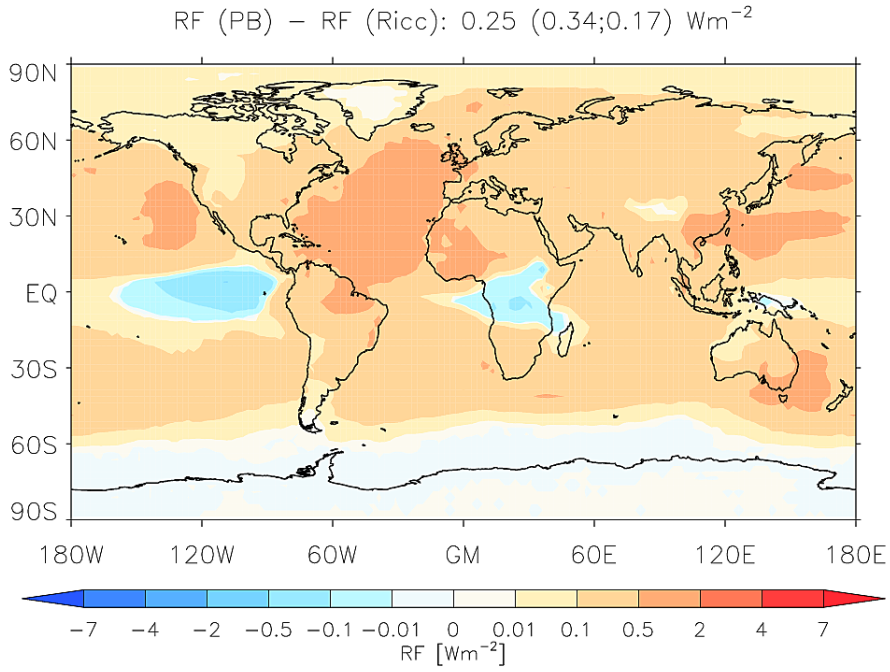

Figure 3.7: Change in annual mean top of the atmosphere first aerosol indirect forcing (ΔAIF) between 1750 and 2000 after including pure biogenic nucleation in GLOMAP-mode. The magnitude of global annual mean ΔAIF is specified at the top of the plot. Numbers in brackets denote annual mean ΔAIF for the Northern and Southern Hemispheres respectively.

In a study comparing 168 GLOMAP-mode simulations in the PI and PD, covering the full uncertainty range for 28 model parameters that encompass uncertainties in processes, emissions, parametric and structural uncertainty, Carslaw et al. (2013) estimated a global mean AIF uncertainty range between -0.7 W m^{-2} to -1.6 W m^{-2}. All simulations in Carslaw et al. (2013) produced boundary layer particles using a sulphuric acid based nucleation mechanism. Scott et al. (2014) showed the sensitivity of the first AIF to biogenic SOA is greatly increased when organic compounds take part in nucleation. Scott et al. (2014) estimated a decrease of $+0.12$ W m^{-2} in first AIF when organic compounds participate in nucleation (global mean AIF of -1.04 W m^{-2}, with nucleation scheme based on smog chamber experiment involving 1,3,5-trimethylbenzene - following Metzger et al., 2010 - compared to global mean AIF of -1.16 W m^{-2}, when nucleation proceeds by activation of sulphuric acid clusters - following Kulmala et al., 2006). With a different nucleation parameterisation involving biogenic organic compounds but derived from an experiment involving pinanediol (a first generation oxidation product of α-pinene) Riccobono et al. (2014) estimated a first AIE of -1.15 W m^{-2}. This shows the estimates of AIF is dependent not just on the species participating in the nucleation mechanism but also on the differing dependencies of each mechanism on the species (Riccobono et al., 2014). The first AIF estimated in this study (-0.54 W m^{-2}) is significantly lower i.e. less negative (by $+0.61$ W m^{-2}) than that estimated in Riccobono et al. (2014) - of which $+0.25$ W m^{-2} is explained by pure biogenic nucleation. Between the publication of Riccobono et al. (2014) and inclusion of pure biogenic nucleation, the model has undergone a few changes. A detailed list of all the changes and how each change has affected the model estimate of first AIF, is provided in the next sections.

The global annual mean **radiative effect** in the present day (first AIE) due to pure biogenic nucleation is estimated to be -0.23 W m^{-2} (shown in Figure 3.9 and

in the pre-industrial -0.40 W m^{-2} (shown in Figure 3.8). The above numbers show that the impact of pure biogenic nucleation on the first AIF - i.e. the reduction in the estimated negative forcing by anthropogenic aerosols over the industrial period - is largely attributable to a higher perturbation of the Earth's radiative balance in the pre-industrial atmosphere.

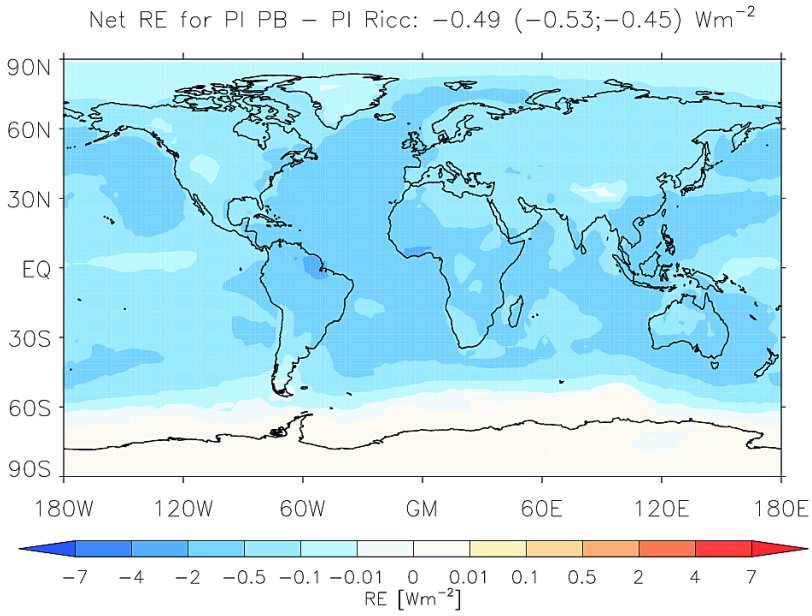

Figure 3.8: Annual mean top of the atmosphere first aerosol indirect effect (AIE) after including pure biogenic nucleation in GLOMAP-mode for the pre-industrial atmosphere. The magnitude of global annual mean net AIE is specified at the top of the plot. Numbers in brackets denote the annual mean AIE for the Northern and Southern Hemispheres respectively.

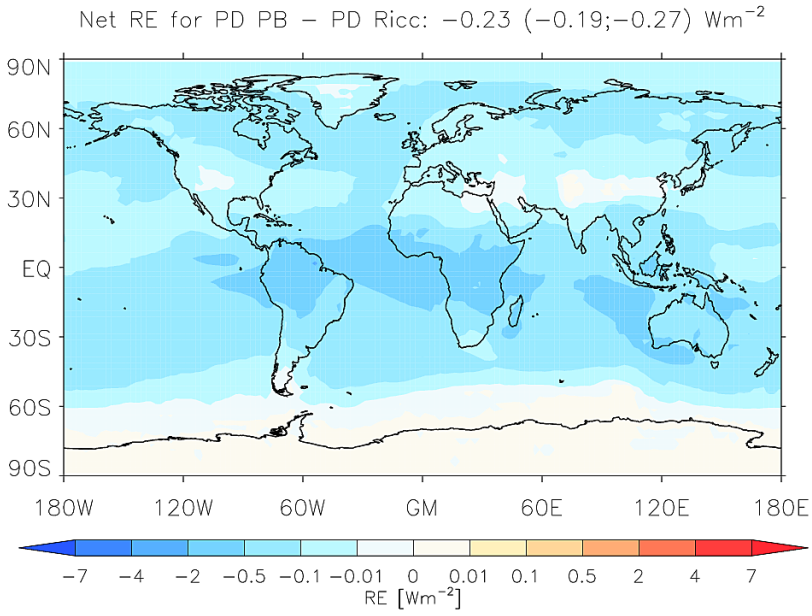

Figure 3.9: Annual mean top of the atmosphere first aerosol indirect effect (AIE) after including pure biogenic nucleation in GLOMAP-mode for the present-day atmosphere. The magnitude of global annual mean net AIE is specified at the top of the plot. Numbers in brackets denote the annual mean AIE for the Northern and Southern Hemispheres respectively.

3.3.3.1 Sensitivity of estimated first AIF to uncertainty in ELVOC yield

Kirkby et al. (2016) estimates the uncertainty in HOM yields to be +80 %/−45 %. From the same experiments, Tröstl et al. (2016) assess an overall scaling uncertainty for nucleating HOMs or ELVOC to be +80 %/−45 %. Here the effect of a +100 %/−50 % perturbation in the yields of ELVOC on model estimates of first AIF is assessed.

When ELVOC yields are increased by +100 % in the model, the global mean AIF estimated is −0.52 W m^{-2} (−0.93 W m^{-2} in NH and −0.11 W m^{-2} in SH). The change in global mean AIF as a result of pure biogenic nucleation (shown in Figure 3.10) is +0.28 W m^{-2} (+0.38 W m^{-2} in NH and +0.18 W m^{-2} in SH).

When ELVOC yields are decreased by −50 %, the global mean AIF from 1750−2000 is estimated to be −0.6 W m^{-2} (−1.06 W m^{-2} in NH and −0.15 W m^{-2} in SH). The change in global mean AIF as a result of pure biogenic nucleation (shown in Figure 3.11) is +0.19 W m^{-2} (+0.25 W m^{-2} in NH and +0.14 W m^{-2} in SH).

Thus with pure biogenic nucleation the first AIF is estimated to be −0.54 W m^{-2}, with an uncertainty range between −0.52 to −0.6 W m^{-2}, for the uncertainty associated with HOM measurements. This AIF estimate is within the uncertainty range (−0.3 to −1.8 W m^{-2}) estimated by Forster et al. (2007) but outside the uncertainty range resulting from uncertainty in 28 model parameters Carslaw et al. (2013). However it should be noted that Carslaw et al. (2013) did not include particle formation from organic compounds which has been shown to affect first AIF significantly (Scott et al., 2014).

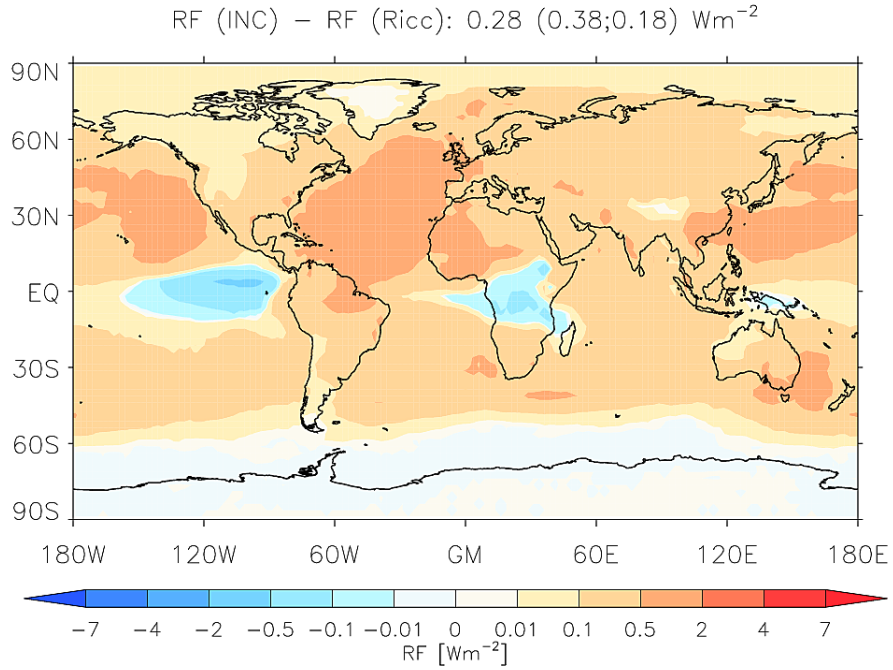

Figure 3.10: Change in annual mean top of the atmosphere first aerosol indirect forcing (AIF) between 1750 and 2000 after including pure biogenic nucleation with 100% increased ELVOC yields in GLOMAP-mode. The magnitude of global annual mean net AIF is specified at the top of the plot. Numbers in brackets denote the annual mean AIF for the Northern and Southern Hemispheres respectively.

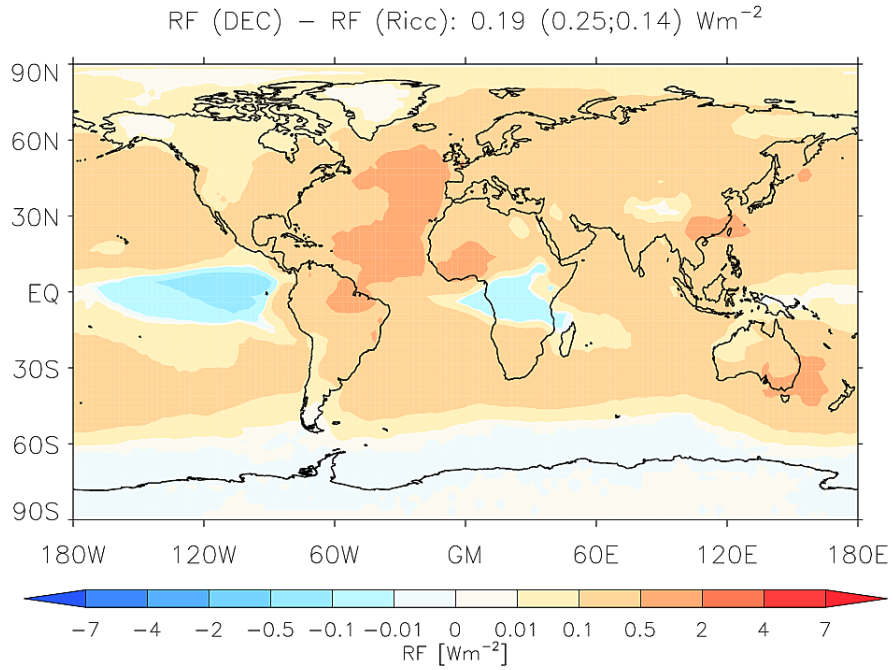

Figure 3.11: Change in annual mean top of the atmosphere first aerosol indirect forcing (AIF) between 1750 and 2000 after including pure biogenic nucleation with 50% decreased ELVOC yields in GLOMAP-mode. The magnitude of global annual mean net AIF is specified at the top of the plot. Numbers in brackets denote the annual mean AIF for the Northern and Southern Hemispheres respectively.

3.3.3.2 Sensitivity of estimated first AIF to nucleation in the tropics

Given the large increase in total particle number concentrations (Figure 3.4) and N50 (Figure 3.3) with pure biogenic nucleation, it may be questioned to what extent the above estimate of first AIF is affected by the overestimation of nucleated particle concentrations in the tropical boundary layer? To test the sensitivity of first AIF (estimated with pure biogenic nucleation) to the enhanced particle production in the tropics (30 N to 30 S), two sensitivity tests are performed:

- 'NoNucTrop' with no boundary layer nucleation in the tropics and pure biogenic nucleation in the rest of the globe (simulation performed for both PI and PD) and
- 'RiccTrop' with only nucleation of sulphuric acid and BioOxOrg in the tropics (as in Riccobono et al., 2014) and pure biogenic nucleation implemented to the rest of the globe (simulation performed for both PI and PD).

The global mean first AIF with 'NoNucTrop' is -0.7 W m^{-2} (Figure 3.12). The increase in the negative radiative forcing by anthropogenic aerosols when no nucleation occurs in the tropical boundary layer is evident in the NH (-1.22 W m^{-2}), particularly over the oceans along the equator. The global mean first AIF with 'RiccTrop' is -0.65 W m^{-2} (Figure 3.13). The weaker negative forcing estimated with simulation RiccTrop, compared to simulation NoNucTrop, indicates a smaller relative change in CDNC between PI to PD in simulation RiccTrop (compared to simulation NoNucTrop). Similarly the stronger negative forcing estimated with simulation RiccTrop, compared to the simulation with pure biogenic nucleation globally (-0.54 W m^{-2}, Figure 3.6), indicates a larger relative change in CDNC between PI to PD in simulation RiccTrop (compared to simulation pure biogenic).

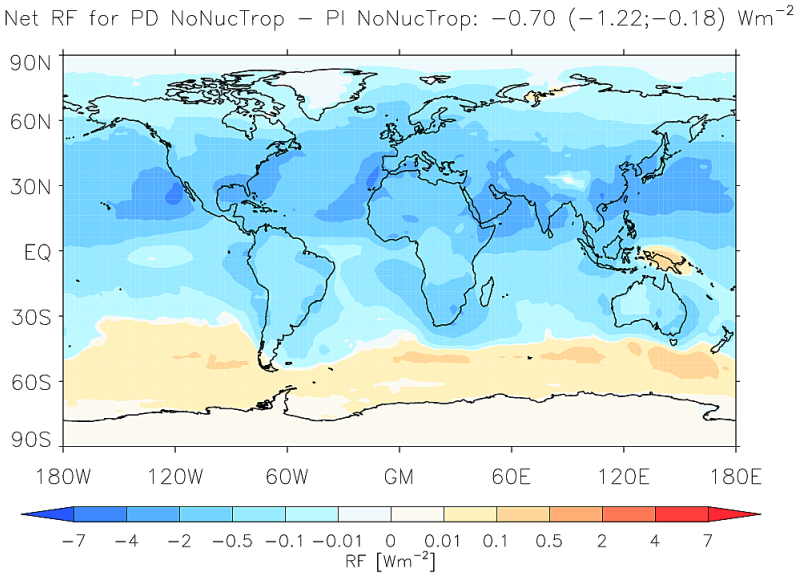

Figure 3.12: Annual mean top of the atmosphere first aerosol indirect forcing (AIF) between 1750 and 2000 after including pure biogenic nucleation in GLOMAP-mode such that between 30 N−30 S no nucleation occurs in the boundary layer. Elsewhere sulphuric acid-dependent and sulphuric acid-independent nucleation of organic compounds occur. The magnitude of global annual mean net AIF is specified at the top of the plot. Numbers in brackets denote the annual mean AIF for the Northern and Southern Hemispheres respectively.

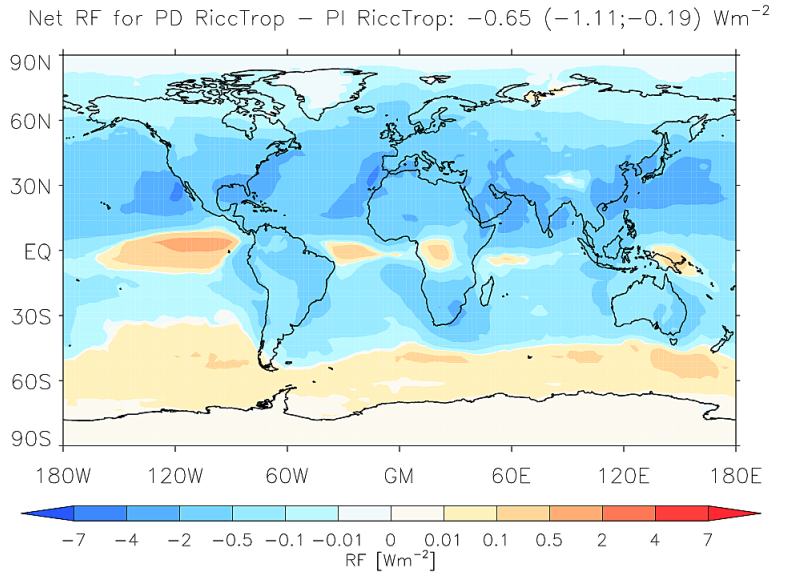

Figure 3.13: Annual mean top of the atmosphere first aerosol indirect forcing (AIF) between 1750 and 2000 after including pure biogenic nucleation in GLOMAP-mode such that between 30 N−30 S only BioOxOrg + sulphuric acid nucleation occurs in the boundary layer. Elsewhere additionally sulphuric acid-independent nucleation of organic compounds occur. The magnitude of global annual mean net AIF is specified at the top of the plot. Numbers in brackets denote the annual mean AIF for the Northern and Southern Hemispheres respectively.

Nucleation is a major contributor to CCN sized particle number concentrations in the model (Spracklen et al., 2008; Merikanto et al., 2009). In absence of nucleation the only source of particles is primary particles emitted locally or transported from other regions. Restricting pure biogenic nucleation in tropics (RiccTrop) lowers particle number concentrations in the PI and PD atmospheres. Particle number concentrations are lowered further when all boundary layer nucleation is restricted in the tropics (NoNucTrop).

Carslaw et al. (2013) shows natural aerosols contribute most significantly to the uncertainty in AIF estimates. Carslaw et al. (2013) cites the primary causes of such uncertainty as a) high response of CCN to DMS emissions due to increased nucleation, b) the greater sensitivity of CDNC to low concentrations of CCN typical of PI and c) a greater susceptibility of cloud reflectivity to CDNC concentrations in the PI. Restricting all boundary layer nucleation or pure biogenic nucleation leads to a significant change in first AIF estimate due to enhanced sensitivity of the estimated AIF to low PI concentrations.

The above tests show overestimation of tropical nucleation, especially in the PI, can potentially lead to an enhanced reduction (less negative) in the first AIE, when pure biogenic nucleation is included in the model. As discussed earlier the enhanced particle formation in the tropics may potentially result from a structural deficiency in the model - such as underestimation of pre-existing aerosols. On the other hand, it is also worth remembering that the CERN CLOUD experiment is the first of its kind to discover and quantify pure biogenic nucleation based on ozonolysis of one particular monoterpene. Oxidation products of other biogenic compounds such as sesquiterpenes (Jokinen et al., 2015; Richters et al., 2016) may play similar atmospheric roles increasing the estimated reduction in first AIF.

3.3.3.3 Dependence of estimated first AIF to method adopted to model composition-dependent CCN activity of aerosol particles

Using two different methods to quantify the contribution of the simulated organic component to the fraction of soluble aerosol in each mode results in a difference of -0.04 W m^{-2} in the estimate of the global annual mean radiative forcing due to anthropogenic aerosols. In one method a van't Hoff factor (vhf) of 0.5 is assigned to the organic component and in the other, a kappa value of 0.1 is assigned to the organic component. In both simulations, boundary layer nucleation includes sulphuric acid-dependent BioOxOrg nucleation and sulphuric acid-independent ELVOC nucleation.

As described in Section 3.2.3.1, the kappa approach allows the calculation of activated number of particles within an aerosol population without explicitly resolving the density, molecular mass and van't Hoff factor for each component - which is particularly challenging to determine for organic aerosol in global models. Figures 3.14 and 3.15 show the change in CDNC calculation method from assigning vhf to assigning kappa to the organic fraction does not produce any appreciable change in the spatial variability of the annual mean first AIF.

However although studies have found that using a value of 0.1 for the hygroscopicity parameter can adequately represent CCN activity of the organic component (Wang et al., 2008; Gunthe et al., 2009), there is considerable uncertainty associated with the same. Petters and Kreidenweis (2007) estimates the hygroscopicity parameter for organic component to lie between 0.01 and 0.5. Chang et al. (2010) finds kappa for oxygenated organic fraction to be 0.22 ± 0.04. The effect of varying this parameter on estimated CDNC and first AIF has not been examined in this study.

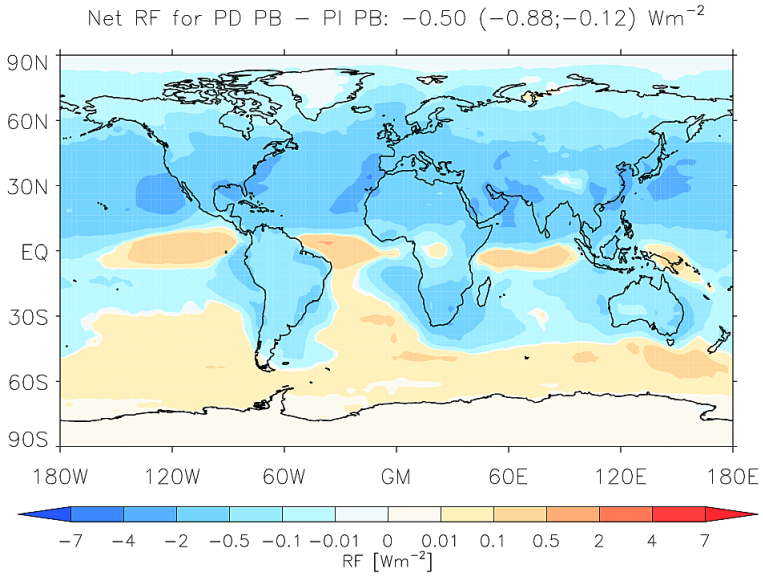

Figure 3.14: Annual mean top of the atmosphere first aerosol indirect forcing (AIF) between 1750 and 2000 after including pure biogenic nucleation in GLOMAP-mode. The soluble fraction of aerosols potentially growing to cloud droplets is calculated using a van't Hoff factor value of 0.5 assigned to the organic component POM. The magnitude of global annual mean net AIF is specified at the top of the plot. Numbers in brackets denote the annual mean AIF for the Northern and Southern Hemispheres respectively.

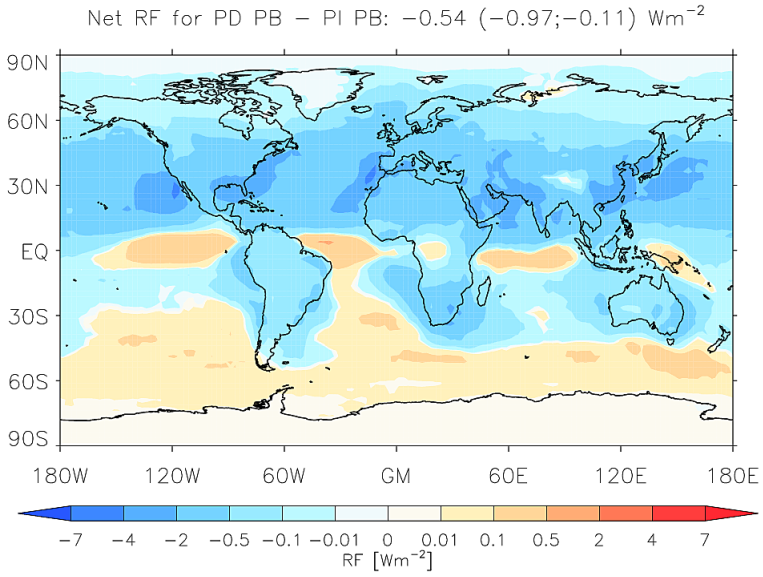

Figure 3.15: Annual mean top of the atmosphere first aerosol indirect forcing (AIF) between 1750 and 2000 after including pure biogenic nucleation in GLOMAP-mode. The soluble fraction of aerosols potentially growing to cloud droplets is calculated using a kappa value of 0.1 assigned to the organic component POM. The magnitude of global annual mean net AIF is specified at the top of the plot. Numbers in brackets denote the annual mean AIF for the Northern and Southern Hemispheres respectively.

3.3.4 Summary of the effects of additional model developments to estimated first AIF

This study started with the model version as used in Riccobono et al. (2014) wherein the top of the atmosphere first AIF was estimated to be -1.15 W m^{-2}. The first AIE estimated in this study is -0.54 W m^{-2} i.e. there has been a change of $+0.61$ W m^{-2} from the forcing reported in Riccobono et al. (2014). As seen in earlier sections, including pure biogenic nucleation in the model results in a $+0.25$ W m^{-2} change in the first AIE. This section quantifies the change in first AIF after each model development starting from the model version used in Riccobono et al. (2014) - to account for the remaining $+0.36$ W m^{-2} change. It should be borne in mind that the estimated AIF is the consequence of many complex interactions within the model triggered by each new development and hence not additive. The aim of this section is to simply get an idea of the magnitude and direction in which each model development affects the first AIF. The model developments in chronological order are:

1. **MUP_GR:** Permit oxidation products of biogenic organic compounds to condense irreversibly on nucleated sub-3 nm clusters which previously only grew by condensation of sulphuric acid.
2. **MUP_kappa:** Implement the kappa approach with a value of 0 for the organic component to calculate CDNC.
3. **MUP_orgCDN:** Assign a value of 0.1 to kappa for the OA (POA+SOA) component to account for the contribution of organic component to CDNC.
4. **MUP_oxidants:** Change the offline oxidant (O_3, $OH^{\cdot}$, $NO_3^{\cdot}$) fields used to generate oxygenated VOCs from monoterpene emissions for both pre-industrial and present-day simulations.
5. **MUP_PBnucl:** Add sulphuric acid-independent nucleation of ELVOC or pure biogenic nucleation.

	Model development					
	A MUP_GR	B MUP_kappa	C MUP_orgCDN	D MUP_oxidants	E MUP_PBnucl	First AIF W m^{-2}
1	None	Vhf	None	Old	BHN+BioOxOrg	−1.15*
2	Yes	Vhf	None	Old	BHN+BioOxOrg	−0.99
3	Yes	Kappa	None	Old	BHN+BioOxOrg	−1.01
4	Yes	Kappa	yes	Old	BHN+BioOxOrg	−0.95
5	Yes	Kappa	yes	New	BHN+BioOxOrg	−0.8
6	Yes	Kappa	yes	New	BHN+BioOxOrg+PBnucl	−0.54

Table 3.1: Summary of changes in the estimate of global annual mean top of the atmosphere first $AIF_{1750-2000}$ as a result of model developments. The reference model/starting point (row 1) is the model used in Riccobono et al. (2014). The final model (row 6) is the model used in this chapter. The change implemented in each step is highlighted in yellow. After each model development (represented by each column in table) the model estimate of first AIF was calculated (tabulated in last column). The effect of pure biogenic nucleation as presented in earlier sections was assessed by comparing model as described in rows 5 and 6. *as reported in Riccobono et al. (2014)

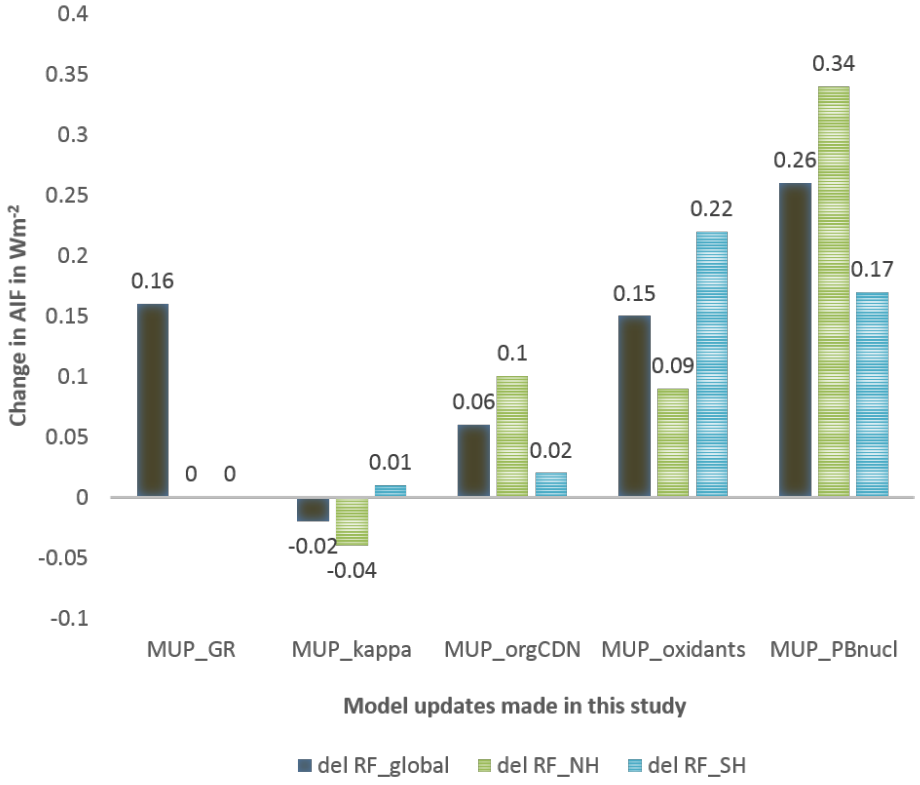

Figure 3.16: Change in global and hemispheric annual mean top of the atmosphere first aerosol indirect forcing (AIF) due to successive model developments. The dark green bar represents global annual mean first AIF, the green bar represents annual mean first AIF for the Northern Hemisphere and the blue bar represents annual mean first AIF for the Southern Hemisphere.

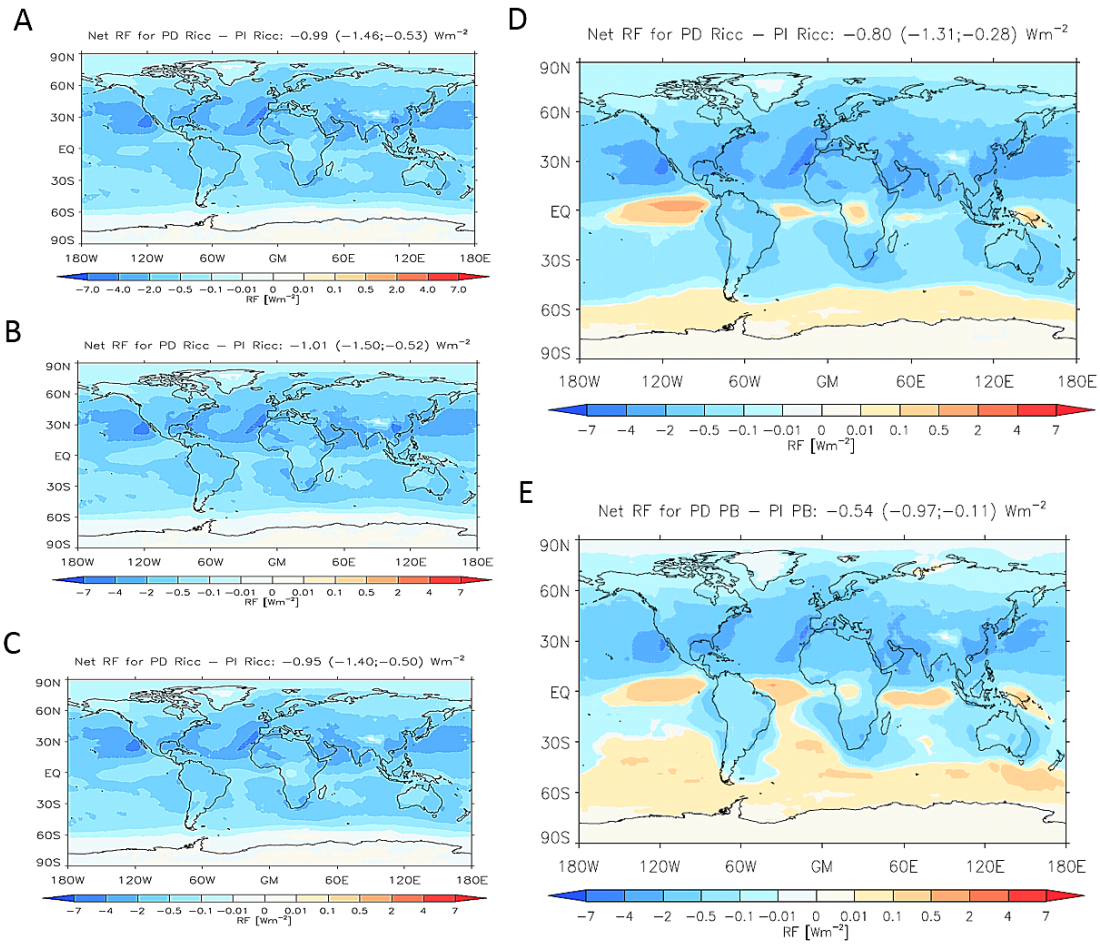

Figure 3.17: Global maps of annual mean top of the atmosphere first first aerosol indirect forcing (AIF) after each model development. A) MUP_GR - after permitting organic compounds to grow sub-3 nm nucleated clusters. B) MUP_kappa - after implementing the kappa approach instead of van't Hoff factor for calculating CDNC in the model. C) MUP_orgCDN - after assigning a value of 0.1 to kappa for organic component in calculation of CDNC D) MUP_oxidants - after changing the offline oxidant concentrations. E) MUP_PBnucl - after including sulphuric acid-independent pure biogenic nucleation.

For all the model developments a greater change in the Northern Hemispheric first AIF is seen, except for MUP_oxidants. Previously GLOMAP-mode used the same oxidant fields for PI and PD atmospheres. The new oxidant fields used in this study reflect a more detailed representation of hydrocarbon chemistry in TOMCAT (Monks et al., 2017) *and* is different for the PD and PI atmospheres.

Change in the offline oxidant fields results in a reduction in the negative first AIE,

the reduction being most prominent in the Southern Hemisphere (Figure 3.17 D). The Southern Hemispheric mean first AIF changes from -0.5 to -0.28 W m^{-2} (an increase of -44 %) due to change in oxidant fields. Areas of positive radiative forcing appear in Figure 3.17D which is indicative of a smaller change in cloud-aerosol interaction over the industrial period. To investigate the above the global distribution of old and new oxidant fields for PI and PD, the global distribution of N50 with old and new oxidant fields in PI and PD and the relative change in N50 with old and new oxidant fields were looked into. The main finding of the investigation is described here.

Of the three oxidant fields updated, the contrast with the older version is most prominent for OH$^{\cdot}$ fields. OH$^{\cdot}$, apart from producing oxidised organic compounds that grow particles by kinetic condensation, is the only oxidant (before pure biogenic nucleation was added) that produces oxidised organic compounds which take part in nucleation (BioOxOrg + sulphuric acid nucleation). As a result any change in OH$^{\cdot}$ significantly affects particle number concentration via its effect on particle formation and growth processes in the model. In the pre-industrial atmosphere the effect of increased OH$^{\cdot}$ on particle number concentration is additionally supported by a low condensation sink, resulting in a larger increase in particle number concentration.

Figure 3.18 shows a significant decrease in OH$^{\cdot}$ concentration over the continents, especially in the Southern Hemisphere and a significant increase over tropical oceans - for both PI and PD (Figure 3.18 a and b) with the new oxidant fields. Over the Southern Hemispheric tropical oceans, the increase in OH$^{\cdot}$ concentrations is more in the PI than in the PD atmosphere. The larger increase in the PI reduces the contrast in OH$^{\cdot}$ concentrations between PI and PD and additionally reduces the *relative* change in OH$^{\cdot}$ concentration. This reduced relative change of OH$^{\cdot}$ concentration (between PI and PD) impacts the relative change in CDNC concentrations (between PI and PD) for reasons explained earlier. The reduction in the relative change in

CDNC from PI to PD over the tropical oceans becomes extremely consequential for the first indirect effect (Figure 3.17D) because this region has predominantly high stratocumulus cloud cover all year through.

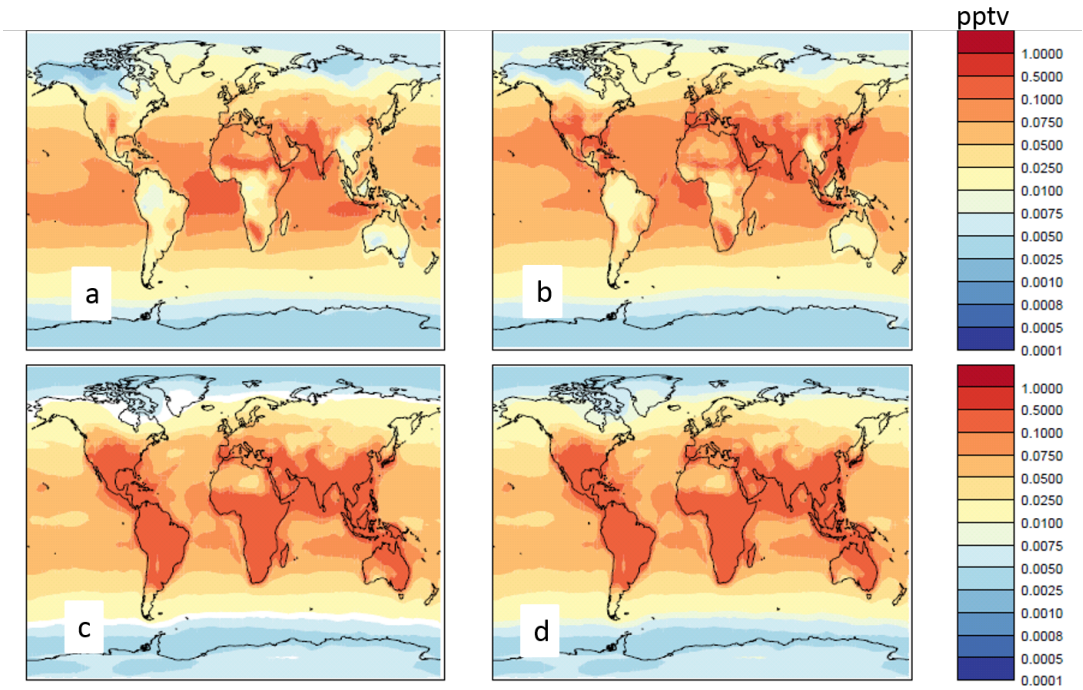

Figure 3.18: Surface-level concentrations of offline oxidant $OH^{\cdot}$ in GLOMAP-mode after being updated from a new TOMCAT simulation (Monks et al., 2017) for (a) the pre-industrial and (b) the present-day. c) and d) show previous $OH^{\cdot}$ concentrations in GLOMAP-mode (Arnold et al., 2005) which were identical for pre-industrial and present-day atmospheres.

To obtain a fuller understanding of the relationship between each model development undertaken for this chapter and changes seen in first AIF (Figure 3.17) further work is required.

3.4 Conclusion

A new nucleation parameterisation, based on the experimental findings of the CERN CLOUD experiment (Kirkby et al., 2016), is implemented in GLOMAP-mode to assess its climatic implications. The CLOUD experiment at CERN has, for the first time, found evidence of nucleation initiated by highly oxidised organic compounds in the atmosphere. Sulphuric acid, whenever present, takes part in the process. The pure biogenic nucleation mechanism increases particle production in the model - increasing global annual mean N50 by 47 % in the PI and 14 % in the PD. Global annual mean CDNC increases by 19 % in the PI and 6 % in the PD.

With the pure biogenic nucleation mechanism, the calculated first AIF is -0.54 W m^{-2} (-0.52 to -0.6 W m^{-2} - due to uncertainty in experimental measurements of highly oxidised organic compounds, Kirkby et al., 2016). The global annual mean change in first AIF as a result of pure biogenic nucleation is estimated to be $+0.25$ W m^{-2}, driven by the change in the pre-industrial. Inclusion of pure biogenic nucleation mechanism increases particle number concentrations in the pre-industrial atmosphere when sulphuric acid concentrations were low because the mechanism permits particle formation in absence of sulphuric acid. Model estimates of first AIF are highly sensitive to the natural aerosols (Carslaw et al., 2013; Rap et al., 2013; Spracklen and Rap, 2013) and hence pure biogenic nucleation leads to a large reduction in the estimated cooling by anthropogenic aerosols.

Pure biogenic nucleation is hard to decouple from sulphuric acid nucleation in the polluted present-day atmosphere (Gordon et al., 2016). As a result direct evidence for pure biogenic nucleation is sparse in the real atmosphere. Laboratory studies, such as those in the CERN CLOUD chamber, therefore play a pivotal role in understanding the mechanisms by which atmospheric species of biogenic nature affected

aerosol concentrations in the pristine pre-industrial atmosphere. Such understanding is invaluable for modellers in their model extrapolation to the pre-industrial atmosphere, which is one of the largest source of uncertainty in determining forcing due to anthropogenic aerosols and climate sensitivity (Carslaw et al., 2013; Stocker et al., 2013).

Pure biogenic nucleation shifts the entire probability distribution of model estimates of cloud albedo forcing, re-emphasizing the findings of Carslaw et al. (2013). Regardless of the uncertainty associated with the nucleation mechanism and its implementation in the global model, the chain of processes that lead to the reduced first AIF in this study is expected to produce similar effects in other global models. Following Hamilton et al. (2014), it is suggested that more observations must be made in the pristine regions in the Southern Hemisphere (that best represent the pre-industrial atmosphere) in order to understand the effects of anthropogenic aerosols in the Northern Hemisphere.

It is well known that several sources of uncertainties compensate each other in a global model, making it difficult to apportion the total uncertainty (Lee et al., 2011, 2012, 2013). It is therefore possible that overestimation in particle concentrations at the 19 sites (Figure 3.4) when pure biogenic nucleation is included in the model, is indicative of a completely different model limitation - such as a poorly represented condensation sink in the model. Such an overestimation in the model could be caused by, for example, an underestimation of other biogenic species that have high reactivity towards $OH^{\cdot}$ and can suppress nucleation (such as isoprene; Kiendler-Scharr et al., 2009). This possibility is revisited in the next chapter where a new scheme of secondary organic aerosol formation, bringing together recent findings related to the role of oxygenated organic molecules in the atmosphere (in addition to pure biogenic nucleation), is introduced to the model.

Chapter 4

Volatility treatment of atmospheric VOCs and the implication for estimating anthropogenic climate change

4.1 Introduction

Simulating the dynamics of atmospheric volatile organic compounds (VOCs) in space and time to produce secondary organic aerosol (SOA) in a global aerosol model is challenged hugely by the vast number of organic compounds present in the atmosphere, the uncertainty associated with the few compounds that have been studied and the complexity of their chemical interactions. As a result models tend to base their treatment of VOC to SOA conversion on classes of VOCs rather than specific compounds (Donahue et al., 2006).

The extent to which an organic species contributes to atmospheric SOA is determined by the species' volatility. Additionally, volatility of a species also controls the

size range of particles it contributes to the growth of - which is of great significance when estimating the climate relevance of VOCs. The top of the atmosphere first aerosol indirect effect (AIE) is determined by the number concentration of cloud condensation nuclei (CCN) particles. A number of conditions have to be satisfied for an aerosol population to act as CCN (for example, their hygroscopicity, updraft velocity) but of primary importance is their size. A particle has to attain at least a 50 nm diameter, before it can act as CCN (Mikkonen et al., 2011). Given the abundance of organic compounds in the atmosphere and the various processes that scavenge particles before they can grow upto 50 nm, the size range at which VOCs contribute to particle growth is therefore of critical importance in determining their climatic impact.

The Volatility Basis Set (VBS) based on volatility (measured by the saturation concentration) and average oxidation state of the carbon in an organic compound was proposed by Donahue et al. (2012) as a basis to classify organic molecules in aerosol models. Several modelling studies (such as Farina et al., 2010; Pye and Seinfeld, 2010; Jathar et al., 2011) have implemented the VBS framework for the description of organic partitioning and chemical ageing. Pye and Seinfeld (2010) treated primary organic aerosol (POA) as semi-volatile and reactive (such that POA evaporate, get oxidised and condense onto particle phase as SOA) and additionally considered the role of intermediate volatility compounds, IVOC (which is emitted entirely in the gaseous phase), in contributing to SOA after undergoing gaseous phase oxidation. This approach estimated global organic aerosol production between $60-100$ Tg yr^{-1} which is close to the lower range of top-down estimates (140 Tg yr^{-1}; Goldstein and Galbally, 2007). Jathar et al. (2011) reported treating POA as reactive and contributing to SOA, brought the model predicted POA/SOA split to better agreement with observations. Jathar et al. (2011) also emphasized the contribution of IVOCs to SOA and suggested global models that do not include the contribution of IVOCs

could be underestimating SOA by 50 %. Farina et al. (2010) reported chemical ageing of anthropogenic SOA nearly doubles the annual average total SOA burden, challenging the assumption that anthropogenic VOCs do not contribute significantly to SOA.

In GLOMAP-mode the gaseous phase oxygenated molecules that condense irreversibly on aerosol particles (referred to as SEC_ORG in the model) are biogenic, produced from oxidation of monoterpenes. The reactivity of monoterpene is assumed to be the same as that of α-pinene, a biogenic VOC widely accepted to contribute to atmospheric SOA. Considering a fixed molar yield of 13 % following Tunved et al. (2006) for all oxidation reactions (by $OH^{\cdot}$, O_3 and $NO_3^{\cdot}$) and assuming the oxidation products to be non-volatile, this produces about 18.5 Tg yr^{-1} of SEC_ORG (Mann et al., 2010). Such representation of SOA production performs reasonably well when compared against observations of particle number concentrations (Spracklen et al., 2006; Merikanto et al., 2009; Mann et al., 2010; Spracklen et al., 2010). However in Spracklen et al. (2011b) effects of additional SOA sources were assessed for the first time and the best match between modelled and observed organic aerosol was found when a large (100 Tg yr^{-1}) anthropogenic source of SOA was considered along with SOA from biogenic sources, ageing and biomass burning. The best estimate of SOA source given by Spracklen et al. (2011b) is 140 Tg yr^{-1}, with an uncertainty range 50−380 Tg yr^{-1}, which is much higher than typical GLOMAP estimates of SOA (Mann et al., 2010).

In Lee et al. (2013) Gaussian process emulators and variance-based sensitivity analysis were applied to study the sensitivity of modelled CCN particles that determine radiative forcing due to anthropogenic aerosol, to 28 model parameters covering all essential aerosol processes, emissions and representations of aerosol size distribution in GLOMAP. Lee et al. (2013) showed that estimates of CCN are much less sensi-

tive to the huge uncertainties in biogenic VOC emissions, SOA formation process and boundary layer nucleation compared to other model parameters and processes. The results of Lee et al. (2013) were based on simulations using binary homogeneous nucleation throughout the troposphere and using an activation scheme based on sulphuric acid concentrations for the boundary layer, both of which had been found to capture nucleation events in the free troposphere reasonably well (Spracklen et al., 2010; Mann et al., 2010) and in the boundary layer (Spracklen et al., 2006, 2008; Merikanto et al., 2009). The study found a greater sensitivity of CCN to SO_2 emissions and suggested that one possible reason for the increased sensitivity to SO_2 emissions is due to the role of SO_2 oxidation products in particle formation as well as particle growth (in contrast to BVOC oxidation products that only contributed to particle growth). Further anthropogenically controlled SOA was found to have more effect on the CCN uncertainty than biogenic, and the widespread hemispheric effect was particularly enhanced in winter. The study concluded that a greater participation of oxidised BVOC in nucleation and hence CCN production could potentially make the uncertainties associated with biogenic SOA one of the biggest contributors to CCN uncertainty. Since then our understanding of organic compounds in the atmosphere has increased considerably.

Metzger et al. (2010), Riccobono et al. (2014) and Kirkby et al. (2016) found nucleation of organic compounds can explain observed nucleation rates better than mechanisms involving only sulphuric acid. Heald et al. (2005) reported a large source of SOA in the free troposphere from an aircraft measurement campaign over the NW Pacific - possibly from successive chemical oxidation products of insoluble VOCs transported from the boundary layer. Recent studies (Pöschl et al., 2010; Robinson et al., 2011) suggest a significant fraction of the global aerosol budget, especially in the vast tropical rainforest regions, could be due to SOA formation from isoprene, the most abundantly emitted biogenic organic compound (Claeys et al.,

2004; Carlton et al., 2009). In parallel with the growing evidence of BVOCs being the drivers of particle formation and growth in many rural and urban sites (Riipinen et al., 2012), studies such as Volkamer et al. (2006); Weber et al. (2007); Hoyle et al. (2011); Spracklen et al. (2011b); Ding et al. (2012); Gentner et al. (2012); Ehn et al. (2017) demonstrate the significance of anthropogenic VOCs in SOA formation and the enhancement of SOA formation from BVOCs in presence of anthropogenic emissions such as NO_x. The findings of Marais et al. (2016, 2017) show biogenic SOA yield from isoprene strongly declines as a result of SO_2 emission control.

In a modelling study (Riipinen et al., 2011) based on observed data from Hyytiala in Finland and Egbert in Canada, it was found that growth due to addition of organic compounds is a vital link to observed growth of ultrafine particles (<100 nm). Several studies (Donahue et al., 2011; Pierce et al., 2011; Zhao et al., 2013) infer on the possibility of involvement of organic vapours in supporting the initial growth of freshly nucleated particle. Tröstl et al. (2016) found evidence that growth following nucleation is primarily driven by atmospheric organic vapours, in absence of which the nucleated particles are lost by coagulation with pre-existing particles.

In addition to the effect of organic compounds on CCN number concentration due to their role in nucleation and growth, Liu and Wang (2010) found changing the hygroscopicity of SOA from 0.14 to 0.07 and 0.21 changes the CCN number concentration in pre-industrial and present-day disproportionaley causing a reduction in global annual mean anthropogenic aerosol indirect forcing (AIF). Gordon et al. (2016) found a reduction in estimated AIF when nucleation from pure biogenic organic compounds was considered. Scott et al. (2014) showed the direct and first indirect aerosol effects in the present-day atmosphere are highly sensitive to the role of organic compounds in SOA formation in a study based on SOA formation from biogenic precursors. Such recent experimental breakthroughs (in particular Ehn

et al., 2014; Riccobono et al., 2014; Jokinen et al., 2015; Kirkby et al., 2016; Tröstl et al., 2016) emphasizing the significance of organic compounds in the atmosphere, make it imperative to reassess the mechanism of SOA formation in GLOMAP-mode and quantify the climatic implication.

In this chapter a more complex representation of SOA production, that brings together SOA formation pathways from Spracklen et al. (2011b); Scott et al. (2014) and Gordon et al. (2016), is implemented in GLOMAP-mode. However compared to the full VBS approach, the modified scheme implemented here is simple and computationally less expensive. The aim of this chapter is to develop a modified SOA scheme that is necessary to reflect the advances in our understanding of the role of VOCs of different volatilities on particles of different sizes and assess the importance of such a modification on a global scale. The impact of the modified scheme on particle number concentrations, aerosol size distribution and anthropogenic aerosol indirect radiative forcing is quantified.

4.2 Modelling the gas to aerosol phase transfer of organic compounds

There are about 10^{19} molecules cm^{-3} in the atmospheric boundary layer, 10^{17} molecules cm^{-3} of water, the most condensable vapour, and less than 10^{10} molecules cm^{-3} of trace gases, all of which continuously collide and exchange energy. The process of mass transfer from gaseous to condensed phase is simply dependent on the frequency of collisions that involve molecules of a condensable gas and a particle surface such that the gaseous molecule 'sticks' to the particle surface (Donahue et al., 2012).

The simplest model to understand the principles of aerosol growth due to influx of gaseous molecules is a two-phase system (gaseous and condensed) in thermodynamic equilibrium (Odum et al., 1996; Donahue et al., 2006; Vehkamäki and Riipinen, 2012). Equilibrium between a condensed and a gaseous phase is a balance between condensation (flux into condensed phase) and evaporation (flux out to gaseous phase) of molecules such that there is no net molecular flux between the two phases. At any given time whenever the equilibrium is disturbed due to addition of molecules to the gaseous phase or to the condensed phase, the system regains equilibrium by redistributing molecules within its condensed and gaseous phases. Once the gaseous phase reaches saturation (the concentration at saturation is called the saturation concentration, C^0, which is the maximum the gaseous phase can hold at any given temperature; an increase in concentration after saturation results in supersaturation), any additional increase in the vapour phase should lead to its irreversible condensation on the particle phase. If VOCs emitted in the atmosphere constituted a closed system with no exchange of matter and energy with its surrounding, all gaseous phase VOCs whose ambient concentrations exceed their saturation concentration would add irreversibly to the aerosol phase.[1]

An open system (such as VOCs in the atmosphere) can experience changes after the gaseous phase saturation concentration has been reached - that lower the concentration of the species in concern below C^0. The lowering of the gaseous phase concentration below C^0 disturbs the equilibrium established between the gaseous and condensed phases and drives molecules from the condensed to the gaseous phase. Consequently a corresponding amount of the species is returned to the gaseous phase

[1]It is worth making the distinction between saturation and equilibrium clear. Saturation refers to the maximum concentration of a solute in a solvent at any given temperature. Equilibrium refers to zero net movement of molecules between the solute and solvent. While every solution tends towards equilibrium, a solution in equilibrium may or may not be saturated. The tendency of a gaseous species to transfer to aerosol phase is dependent on how quickly its ambient concentration can surpass its saturation concentration irrespective of whether or not it has attained equilibrium before that time-scale.

to re-establish equilibrium. Most atmospheric VOCs therefore exist in both gaseous and condensed phase, the amount in each being determined by the amount that maintains equilibrium between the two phases at any given instant.

For any species either the vapour pressure exerted by the gaseous phase at saturation (saturation vapour pressure) (Pankow, 1994) or C^0 can be used as a measure of volatility (Donahue et al., 2011). A highly volatile species is one that has a high C^0 (indicating a high concentration of the species is required to saturate the gaseous phase thereby driving more molecules of the species to the gaseous phase) and a high saturation vapour pressure (indicating the pressure exerted by molecules at saturation is higher thereby driving more molecules of the species to the gaseous phase). Thus volatility determines what fraction of a species would partition onto the particle phase, in principle, by determining the tendency of molecules which have arrived in the condensed phase, to evaporate back into the gaseous phase.

Modelling the gaseous to aerosol phase transfer assuming instant equilibrium: gas/particle partitioning absorption model

Modelling how oxidation products of VOCs lead to atmospheric SOA therefore means modelling a gaseous phase species that distributes a part of its mass in the condensed phase once its ambient concentration exceeds its C^0. Pandis et al. (1992) pointed out that a model allowing partitioning of gaseous phase organic species, say i, *only* when its C^0 is exceeded underestimates the gaseous-to-particle-phase conversion. Later a partitioning model was proposed by Pankow (1994), where SOA production by partitioning was allowed to occur when the gaseous phase concentration of i was below its ${C_i}^0$. Pankow (1994) reasoned that either adsorption of i onto the particle surface or absorption (dissolution) of i into a particle phase made of organic compounds would allow some partitioning to occur even before the saturation

concentration ${C_i}^0$ is reached. With time the amount of i in the condensed phase would influence the partitioning of more gaseous i onto the condensed phase. Including the role of pre-existing organic aerosols in modelling absorption partitioning of organic compounds proved to be an important step towards understanding and modelling the role of semi-volatile organic compounds in SOA formation (Carlton et al., 2009). The partitioning models (Pankow, 1994; Odum et al., 1996) assume an instantaneous equilibrium between the gaseous and condensed phase of i such that i co-exists in two phases and there is no net exchange of molecules between the two phases. For such a species, i, the amount that gets distributed onto the condensed phase is an important quantity as that contributes to the global SOA budget. Donahue et al. (2011, 2012) expressed this fraction of i in the condensed phase as a function of its effective saturation concentration (C_i^*) and total mass concentration of organic aerosol (C_{OA}) in the condensed phase such as

$$\xi_i = (1 + {C_i}^*/C_{OA})^{-1} \tag{4.1}$$

The effective saturation concentration includes the activity coefficient[2], γ, in a mixture such that, $C_i^* = \gamma\ C_i^0$, where C_i^0 is the saturation concentration of a species over a pure liquid. As compounds that are highly volatile have a higher C^* than compounds that are less volatile, it follows from the above expression that at equilibrium, a highly volatile compound will have a higher proportion of its mass in the gaseous state than a lower volatility compound and the contribution of i to OA is dependent on thermodynamic properties of i, ${C_i}^*$ and existing mass of OA.

What happens if a species does not reach instant equilibrium upon its emission or

[2]In a non-ideal solution with significant molecular interactions, the chemical activity of a component is determined by the *active* concentration of the component as opposed to the total measured concentration. Activity coefficient is the ratio of the effective concentration of the component to the measured concentration i.e. it determines the chemical activity for a substance in a real solution under non-ideal conditions.

production in the atmosphere - irreversible condensation

Although the assumption of equilibrium is justified for some systems, particularly for semi-volatile compounds in the atmosphere, in reality atmospheric systems are much more complex, multi-phase systems that may not reach equilibrium (Perraud et al., 2012; Barsanti et al., 2017). The saturation concentrations of some organic compounds are so low that their ambient concentrations far exceed $C_i{}^*$. For such compounds the time-scale of reaching equilibrium between the gaseous and particle phase approaches infinity as the molecules have no drive to leave the particle phase and return to the ambient gaseous phase (Donahue et al., 2012). With extremely low C^* resulting in a low drive to be in the gaseous state, molecules of these compounds condense on freshly nucleated particles at kinetic rates (Tröstl et al., 2016) i.e. for such molecules transfer to the condensed phase is entirely dependent on collision with the condensed phase. As frequency of collisions is proportional to the surface area of the particles (here the gas molecules and the aerosol particle), such growth is modelled as being proportional to aerosol surface area (Mann et al., 2010). Such a growth via condensation is dependent on the concentration of the gaseous phase species and occurs irreversibly until the species is entirely depleted in the gaseous phase and been added to the condensed phase.

In GLOMAP, the existing approach to produce SOA from biogenic organic compounds is to assume irreversible kinetic condensation of gaseous phase vapours on particles (here we refer to it as the kinetic approach; Mann et al., 2010). All organic compounds that can condense onto the gaseous phase are lumped together in a single tracer (called SEC_ORG in the model). SEC_ORG is generated from monthly monoterpene emissions after oxidation by O_3, $OH^{\cdot}$, NO_3, following reaction rates of α-pinene.

Scott et al. (2015) introduces the partitioning approach in GLOMAP (referred to

as the mass-based approach) and assesses the climatic implications of the scheme chosen to represent SOA formation in a global aerosol microphysics model. Instead of considering a range of representative organic compounds with varying C^*, Scott et al. (2015) uses the lumped gaseous phase organic SEC_ORG and 'mimics' the gaseous-to-aerosol phase partitioning behaviour. Scott et al. (2015) compares three model simulations: one with the kinetic approach, second with the mass-based approach and a third where half of the available gaseous phase organic compounds follow each approach (combined scheme).

In the kinetic approach, the mass of SEC_ORG entering the aerosol phase across the aerosol modes (M_{SOA_m}) is governed by the equation:

$$\frac{dM_{SOA_m}}{dt} = \frac{Cond_m N_m}{\sum_{m=1,5} Cond_m N} \times \frac{dS_{org}}{dt} \tag{4.2}$$

where dS_{org}/dt is the rate of SEC_ORG condensation. $Cond_m$ is the condensation coefficient for each mode m and N_m the number concentration of particles for the mode. $Cond_m$ is calculated using the diffusion coefficient (D_s) for a typical gaseous-phase oxidation product of α-pinene in air, the condensation sink radius ($\bar{r}_{m,cond}$) for the mode m and is corrected for molecular effects and limitations in interfacial mass transport using the terms F(Kn) and A(Kn). A full description of the above can be found in Mann et al. (2010).

$$Cond_m = 4\pi D_s \bar{r}_{m,cond} F(Kn_m) A(Kn_m) \tag{4.3}$$

$$F(Kn_m) = \frac{1 + Kn_m}{1 + 1.71Kn_m + 1.33(Kn_m)^2} \tag{4.4}$$

$$A(Kn_m) = \frac{1}{1 + 1.33Kn_m F(Kn_m)(\frac{1}{s} - 1)} \tag{4.5}$$

$$Kn_m = \frac{\lambda_{gas}}{\bar{r}_{m,cond}} \tag{4.6}$$

where s is the accommodation coefficient or sticking coefficient set to 1 for soluble modes and set to 0.3 for insoluble modes. Kn_m is the Knudsen number for mode m calculated using the mean free path of the relevant condensable gas in air λ_{gas}. In the kinetic approach the mass of SEC_ORG adding to the aerosol phase is thus proportional to the surface area (diameter squared) of particles.

In the mass-based approach SEC_ORG adding to the aerosol phase is proportional to the pre-existing mass of organic aerosol in each mode, M_{OA_m}.

$$\frac{dM_{SOA_m}}{dt} = \frac{M_{OA_m}}{\sum\limits_{m=1,5} M_{OA_m}} \times \frac{dS_{org}}{dt} \tag{4.7}$$

Aerosol mass scales with diameter cubed. Therefore in the mass-based approach the mass of SEC_ORG adding to the aerosol phase is proportional to the cube of particle diameter.

The kinetic approach results in a 24 % higher estimate of aerosol indirect effect (-0.66 W m^{-2}) than the mass-based approach (-0.5 W m^{-2}) by facilitating the growth of smaller particles. When the mass-based approach is used, growth of particles smaller than 10 nm is limited by sulphuric acid availablity. The slower growth rate results in fewer particles reaching CCN-relevant size and gives a lower estimate of the aerosol indirect effect. The simulation with the combined scheme leads to a very similar result as the kinetic approach. Scott et al. (2015) suggests since only a small amount of gaseous phase organic compounds is required to grow smaller particles, allowing a small fraction of gaseous phase condensables to follow the kinetic approach in the combined scheme produces similar results between the kinetic approach and the combined scheme.

Scott et al. (2015) gives an useful first estimate of the impact of considering different pathways of SOA formation. However adopting either one of the kinetic or mass-based approach or splitting SEC_ORG in two equal pathways in the combined approach is too simplistic to capture the non-linear interactions between atmospheric organic compounds following different pathways to produce SOA. The atmosphere is a huge reservoir of gaseous phase organic compounds whose spatial patterns, production rates and chemical reactivities widely vary. This can potentially influence the aerosol size distribution in a different way as compared to splitting the same tracer (SEC_ORG) across the two schemes.

In this work four completely independent gaseous phase advected tracers are used to represent oxidised organic compounds of different volatilities that eventually produce SOA. Of the parent VOCs, some are biogenic (from monoterpene and isoprene, Mann et al., 2010; Spracklen et al., 2011b) and some are anthropogenically controlled (Spracklen et al., 2011b). In GLOMAP these gases are oxidised by $OH^{\cdot}$, NO_3 and O_3 and the gaseous phase oxidation product is then added to the aerosol phase. Although technically all the organic compounds in the atmosphere fall under volatile organic compounds - whose definition spans a large range of volatility - for clarity in this work, we reserve the term 'VOC' for the parent VOCs i.e. monoterpene, isoprene, anthropogenically controlled VOCs and refer to their oxidation products as 'ox-VOC's.

In the atmosphere a highly volatile species may undergo successive oxidation reactions in the gaseous phase that lower its volatility. Such chemical pathways may eventually lead to reaction products that are capable of forming SOA. An apt example of such a species is isoprene, which has a large global emission estimated to be between $500-750$ Tg yr^{-1} (Guenther, 2006). Isoprene is highly reactive and

gets easily oxidised by atmospheric oxidants. However because oxidation of isoprene produces volatile compounds (with high C^*) laboratory (Pandis et al., 1991) studies found SOA formation occurs only at high isoprene conditions (>120 ppb). As these concentrations used in the laboratory are several times higher than that typically found in atmospheric conditions (a few ppb), it had been generally accepted that SOA formation from isoprene is not atmospherically relevant (Carlton et al., 2009). Recent re-examinations (Matsunaga et al., 2003; Paulot et al., 2009) have found that second (and later generation) isoprene oxidation products are semi-volatile which means they can contribute to aerosol phase by absorptive partitioning. These later stage oxidation products may also undergo further oxidation reactions lowering their volatility even further (Carlton et al., 2009). Multi-stage oxidation therefore has an important effect on determining the amount of condensable gases available for aerosol growth at any given instant. GLOMAP does not simulate multi-stage oxidation reactions. In this study VOCs are lumped in three categories based on their volatility. The difference in volatility is manifested in the pathway they follow to add to aerosol particles. Whether these products are born from single or multi-stage oxidation products is not relevant for the aim of this study. In the next sections we describe the basis on which we classify VOCs into different categories.

4.3 Current understanding of SOA producing organic compounds

Of the thousands of organic molecules in the atmosphere only a few have been identified to date. Volatility of the identified organic compounds span several orders of magnitude making their interactions complex and difficult to model. As a result they have to be studied in aggregates (Donahue et al., 2006) in global models.

Donahue et al. (2011, 2012) presented the 2D Volatility Basis Set (VBS) as a means to classify atmospheric organic compounds based on ranges of saturation concentration (C^*) and oxygen content (O:C ratio). In order of increasing volatility they are,

- Extremely Low Volatility Organic Compounds or ELVOC
  with $C^*<10^{-4}$ μg m^{-3}
- Low Volatility Organic Compounds or LVOC
  10^{-4} μg m$^{-3}<C^*<10^{-1}$ μg m^{-3}
- Semi Volatile Organic Compounds or SVOC
  10^{-1} μg m$^{-1}<C^*<10^{2}$ μg m^{-3}
- Intermediate Volatility Organic Compounds or IVOC
  with 10^{2} μg m$^{-3}<C^*<10^{6}$ μg m^{-3}
- Volatile Organic Compounds or VOC
  with $C^*>10^{6}$ μg m^{-3}

The principle of the VBS classification is to categorise thousands of organic compounds based on their C^* and oxygen content, O:C ratio. As discussed in previous sections, a low C^* of any species implies its ambient concentrations can easily surpass the C^* making it a low volatility species. A higher O:C in a species is indicative that the species is highly oxygenated and hence of lower volatility. From a study based on the α-pinene ozone system and SOA formation from experiments involving ageing of non-traditional sources (usually associated with POA), woodsmoke and diesel via OH oxidation, Donahue et al. (2012) suggested ELVOCs remain in the particle phase under any ambient condition, LVOCs remain dominantly in the particle phase, SVOCs have a considerable fraction of their mass in both the condensed and gaseous phase while IVOCs almost exclusively reside in the gaseous phase.

Ehn et al. (2012) reported observations of high-molecular weight (300-650 Da) naturally charged molecules, monomers and dimers in the boreal forest of Hyytiala, which were also reproduced in the Julich Plant Atmosphere Chamber from α-pinene ozone reactions under low OH conditions. These molecules termed HOMs or highly oxygenated molecules were found to retain a 10 carbon structure (monomers) while attaining a O:C ratio of $0.7-1.3$ through oxidation. Their dimers consist of units of two covalently-bonded monomers with lower O:C ratio but larger mass (about 500 Da) and volatility. The study speculated that these compounds take part in nucleation as their ambient concentrations were estimated to be similar to sulphuric acid, a key molecule for nucleation, and they have a mass roughly three times that of sulphuric acid.

Ehn et al. (2014) coined the compounds described above as ELVOC. It was proposed that formation of ELVOC take place when a fraction of the initial peroxy radical formed from VOC oxidation rapidly undergoes H-shift followed by addition of a O_2 molecule at the formed alkyl radical site. Such oxidation reactions produced ELVOC at $6-8$ % molar yield, with an uncertainty of ± 50 %. ELVOCs were found to condense irreversibly on particles and could explain observed particle growth rate between $5-50$ nm in the boreal forest of Hyytiala. Ehn et al. (2014) also reported ELVOC yields from other common biogenic endocyclic alkenes - 4 % yield from Cyclohexene, 17 % yield from Limonene and less than 0.1 % from β-pinene. The yields estimated in Ehn et al. (2014) were considered to be a lower limit of the estimate of ELVOC concentrations.

Kirkby et al. (2016) observed particle formation occurring solely from α-pinene oxidation products produced at a yield of 3.2 % from ozone and 1.2 % from $OH^{\cdot}$ radical oxidation in the CLOUD facility at CERN. The nucleating species in Kirkby

et al. (2016) were reported to be the same compounds as described in Ehn et al. (2012, 2014), with less than half the yields. Kirkby et al. (2016) reverted back to calling these nucleating species highly oxygenated molecules or HOMs rather than ELVOCs, citing that HOMs span a huge range of volatility of which only a subset (ELVOC) can drive nucleation.

Tröstl et al. (2016) classified HOMs using the Volatility basis set (VBS) into ELVOC (same as ELVOC or HOMs in Kirkby et al., 2016; Ehn et al., 2014), LVOC and SVOC of which only ELVOCs have the ability to overcome the Kelvin barrier at the smallest sizes and produce relatively stable clusters smaller then 2 nm. Beyond 2 nm with increasing size the Kelvin effect diminishes and LVOCs dominate the growth of particles. The most efficient source of ELVOC is the α-pinene+ozone system as described in Ehn et al. (2014) and Kirkby et al. (2016), with an uncertainty of +80 %/−45 %. LVOCs are likely to be produced from first generation oxidation products like the above as well as from ageing of compounds in the atmosphere through multi-stage oxidation. SVOCs are also formed in abundance from α-pinene oxidation and do not take part in the observed growth rate in the experiments. The ELVOC, LVOC, SVOCs defined in Tröstl et al. (2016), have C* values as follows: $C^*<10^{-4.5}$ μg m^{-3}, LVOC $10^{-4.5}$ μg m^{-3}$<C^*<10^{-0.5}$ μg m^{-3}, SVOC $10^{-0.5}$ μg m^{-1}$<C^*<10^{2.5}$ μg m^{-3}. To help the reader, Table 4.1 lists the progression of studies as described above and the different terminologies used over the years for organic compounds with very low volatility.

Publication	Precursor Gas	% SOA yield	Identified Molecular Structure	O:C ratio	Terminology used for oxidation products
Donahue et al. (2012)	α-pinene	6−8			ELVOC when C^* $<10^{-4}$ μg m^{-3}
Ehn et al. (2012)	α-pinene	6−8	$C_{10}H_{14-16}O_{7-11}$ and $C_{19-20}H_{2832}O_{10-18}$	0.7−0.13	HOM
Ehn et al. (2014)	α-pinene	6−8	"	0.7−0.13	ELVOC
Ehn et al. (2014)	Cyclo-hexane	4	-	-	ELVOC
Ehn et al. (2014)	Limonene	17	-	-	ELVOC
Ehn et al. (2014)	β-pinene	0.1	-	-	ELVOC
Kirkby et al. (2016)	α-pinene	2.9	$C_{8-10}H_{14,16}O_{6-12}$ and dimer	>0.6	HOM
Tröstl et al. (2016)	α-pinene	2.9	$C_{8-10}H_{14,16}O_{6-12}$ and dimer	>0.6	HOM of which 36% are ELVOC*

Table 4.1: Summary of experimental and observational studies, described in Section 4.3, showing the progression in current understanding of the role of SOA-producing organic compounds in the atmosphere. Several independent studies have found evidence of compounds, with extremely low volatility and characterised by high O:C ratio, which readily condense on aerosol particles. *Saturation concentrations (C^*) of ELVOCs in Tröstl et al. (2016) are $<10^{-4.5}$ μg m^{-3}

To summarise the above, various experimental and observational studies conducted independently at different laboratory/atmospheric conditions, point towards the existence of at least three classes of organic compounds:- compounds that nucleate, compounds that stabilise freshly nucleated particles and compounds that account for observed growth rates of particles in the atmosphere. Few of these organic molecules have been detected but overall there is huge uncertainty in the quantification of organic compounds in each of those pathways.

In this study GLOMAP's existing treatment of SOA-producing ox-VOC (SEC_ORG), as non-volatile organic compounds produced at a fixed yield from monoterpene oxidation, is changed to represent three ox-VOC groups of different volatility in the model - ELVOC, LVOC and SVOC - that contribute to SOA via three distinct pathways - nucleation, growth by kinetic condensation and growth by mass-based partitioning. Each of LVOC and SVOC is further divided into two categories, biogenic and anthropogenic, based on the source of their precursor VOCs. The prefix 'A' for anthropogenic and 'B' for biogenic are added to LVOC and SVOC to denote the nature of their sources. Replacing SEC_ORG, the ox-VOCs in this new scheme of SOA formation are, B_ELVOC, B_LVOC, B_SVOC_M, B_SVOC_I, A_LVOC and A_SVOC. More details on each ox-VOC are provided in next section. The following diagram from Ehn et al. (2014) shows, in principle, the scheme implemented in this chapter to produce SOA from ox-VOCs.

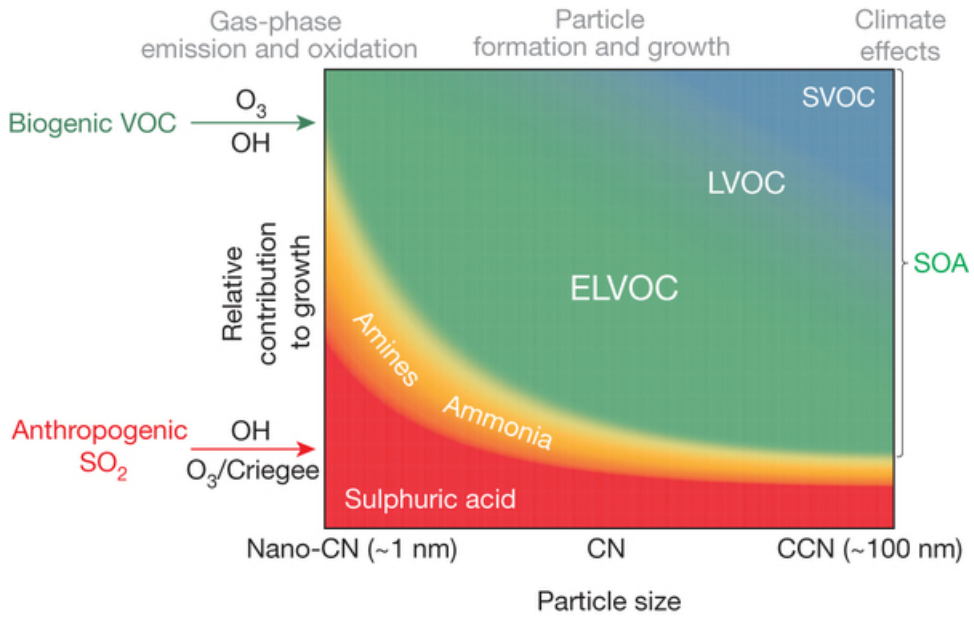

Figure 4.1: Schematic from Ehn et al. (2014) showing the relative contribution of atmospheric volatile organic compounds (VOCs) of different volatilities on particles of different sizes. Extremely low-volatility organic compounds or ELVOCs contribute to the growth of all particles, while low-volatility and semi-volatile organic compounds (LVOCs and SVOCs respectively) contribute to the growth of larger particles making them climate-relevant.

4.4 VOC implementation in GLOMAP

This section describes each ox-VOC, their source, their role in SOA production as implemented in GLOMAP-mode in this work. It may be noted here that although the different ox-VOCs represent atmospheric organic compounds with different volatilities, the study does not use saturation concentration of surrogate compounds to represent each category. Rather the difference in volatility of each ox-VOC category is manifested in the pathway they follow to contribute to SOA. An advantage of having three separate *pathways* for gaseous-aerosol phase transfer instead of tracking three separate surrogate *compounds* in the model is that, as more sources of ox-VOCs that nucleate or condense or partition to produce atmospheric SOA are identified, or new reaction yields of ELVOC, LVOC, SVOC are quantified in laboratories, these additional sources can be lumped together in the corresponding ox-VOC

tracer to follow the corresponding pathway of SOA formation thereby minimising computational costs. Further, the model does not simulate transfer of molecules from aerosol to gaseous phase or potential chemical reactions of the ox-VOCs in the aerosol phase. Thus a simpler approach that estimates the total gaseous to aerosol phase transfer via each pathway and their potential interaction suffices.

1. B_ELVOC:

   This category of ox-VOC in the model represents atmospheric organic compounds with extremely low volatility that take part in nucleation. B_ELVOC includes ox-VOCs that can initiate nucleation (Kirkby et al., 2016) as well as those which take part in nucleation in presence of sulphuric acid (Riccobono et al., 2014). A nucleation scheme involving B_ELVOC was introduced in Chapter 3. Throughout this thesis the nucleation scheme remains unchanged.

2. B_SVOC and A_SVOC:

   A huge number of organic compounds in the atmosphere fall in the category of SVOC. Donahue et al. (2006) defines SVOC as any organic compound in the atmosphere which distributes more than 1 % of its mass between the gaseous and particle phase. A major fraction of SOA is known to comprise of SVOCs, which partition between the condensed and gaseous phase (Pöschl, 2005; Robinson et al., 2011; Grieshop et al., 2009).

   In the atmosphere saturation concentrations of SVOCs can range between $10^{-0.5}$ μg m^{-1}<C^*<$10^{2.5}$ μg m^{-3} (Tröstl et al., 2016). Saturation concentration for oxidation products of α-pinene range from $1-10^7$ μg m^{-1} (see Figure 4.2 from Jimenez et al., 2009) well encompassing the range of SVOCs determined by Tröstl et al. (2016) - implying potential contribution of α-pinene oxidation products to atmospheric SVOCs. Later stage oxidation products of isoprene are known to be semi-volatile (Carlton et al., 2009) contributing to

SOA (Surratt et al., 2010; Matsunaga et al., 2003). Laboratory studies quantify SOA yields from isoprene to be 1−2 % at high NO_x level (Kroll et al., 2005) and about 3 % at low NO_x level (Kroll et al., 2006). Global SOA production from isoprene has previously been estimated to be between 2 Tg yr^{-1} (Claeys et al., 2004) to 10−120 Tg yr^{-1} (Matsunaga et al., 2005). Henze and Seinfeld (2006) shows including SOA formation from partitioning of isoprene oxidation products in a global aerosol model leads to substantial increase in predicted SOA concentrations. The authors suggest such an increase could potentially help explain previously underestimated observations by global models. Gentner et al. (2012) quantifies SOA formation from anthropogenic VOCs such as gasoline and diesel fuel, which produce VOCs at the higher end of the volatility spectrum.

In this study, oxidation products of α-pinene and isoprene are produced with yields of 13 % and 1.5 % yields respectively - based on previous studies (Spracklen et al., 2006; Mann et al., 2010; Spracklen et al., 2011b; Scott et al., 2014) and personal communication. These oxidation products are considered to constitute B_SVOC, producing about 24 Tg yr^{-1} of SOA. A source of anthropogenically controlled VOC is generated using MACCity (Granier et al., 2011) CO emissions that are produced from anthropogenic activities and therefore have a similar spatial pattern as anthropogenic VOCs. The CO emissions are scaled and optimised (using a constant $scalingfactor$ throughout the globe) to reproduce the global sum of VOC emissions from the Emissions Database for Atmospheric Research (EDGAR) for anthropogenic and biomass burning sources. The approach is adopted from Spracklen et al. (2011b) and a full description can be obtained therein. Oxidation products of the reaction between anthropogenically controlled VOC and $OH^{\cdot}$ are divided to produce equal amounts of A_LVOC and A_SVOC (about 34 Tg yr^{-1} of each).

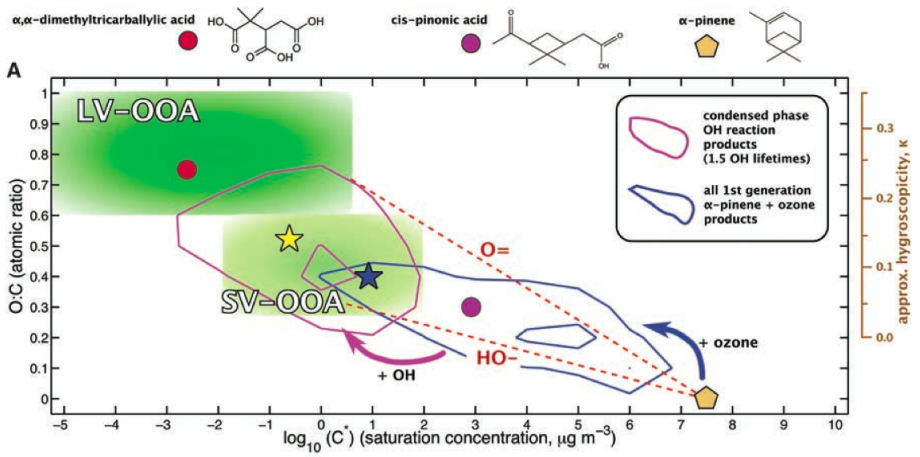

Figure 4.2: A 2-D framework for organic aerosol ageing from Jimenez et al. (2009). The x-axis represents volatility ($\log_{10}C^*$ at 298 K) and the y-axis represents the oxidation state, approximated by the O:C ratio. All products from ozonolysis of α-pinene are distributed across the blue contours. The products with lower C^* and higher O:C ratio form SOA, their mean properties depicted by the blue star.

3. B_LVOC and A_LVOC:

   These are Low Volatility Organic Compounds representing atmospheric ox-VOCs whose volatilities are higher than B_ELVOC and hence they do not take part in nucleation but lower than SVOCs and hence are not limited to partitioning onto the aerosol phase. Instead LVOCs in the model irreversibly condense on the aerosol phase.

Riipinen et al. (2011) shows the thermodynamic approach adopted by most models (one exception being GLOMAP; Spracklen et al., 2005a,b; Mann et al., 2010) to produce SOA from VOCs, is insufficient to model organic contribution to particle number concentrations. According to Riipinen et al. (2011), the typical mass ratio between the semi- and low-volatility aerosol components described by Jimenez et al. (2009) (see Figure 4.2) in Hyytiala is 50 %−50 % - demonstrating the need to model gaseous to aerosol phase transfer of ox-VOCs with low C^* via irreversible condensation. Indeed studies using GLOMAP-mode (Spracklen et al., 2006; Mann et al., 2010; Riccobono

et al., 2014; Gordon et al., 2016) producing SOA with the kinetic approach only, show reasonable agreement with observed particle number concentrations. Scott et al. (2015) in a study assessing the significance of kinetic and thermodynamic approaches in GLOMAP-mode further demonstrates the need to model size-dependent growth by kinetic condensation based on estimates of the first AIE.

Recently Tröstl et al. (2016) emphasized the role of oxidation products of α-pinene in initial growth after nucleation although no quantification of such compounds in the atmosphere have been made to date. O'Dowd et al. (2002) also found freshly nucleated particles with diameters between $3-5$ nm to be primarily composed of oxidation products of biogenic terpenes.

Based on the above B_LVOCs are considered to be oxidation products of α-pinene at yields typically used in GLOMAP i.e. 13 % from $OH^{\cdot}$, O_3 and $NO_3^{\cdot}$. B_LVOCs produce about 14 Tg yr^{-1} of SOA annually. Half of the oxidation products (about 34 Tg yr^{-1}) generated from oxidation of anthropogenic VOCs constitutes A_LVOC.

The extent to and mechanism by which anthropogenic VOCs form SOA is still very much an open question. A_LVOC in this study is permitted to grow particles by kinetic condensation only after they enter the nucleation mode (that is A_LVOC is not permitted to grow freshly nucleated clusters which have less than 3 nm diameter).

The ox-VOCs, their source and role in SOA formation is tabulated in Table 4.2. The bimolecular reaction rates used to produce the ox-VOCs are listed in Table 4.3. The new SOA-scheme is schematically described in Figure 4.3.

ox-VOC	Volatility	Nature of source	Role	Parent VOC	Oxidants
B_ELVOC	Extremely Low	biogenic	nucleation	MT	O_3, OH·
B_LVOC	Low	biogenic	kinetic condensation	MT	O_3, OH· , $NO_3^·$
B_SVOC_M	Semi	biogenic	mass-based partition	MT	O_3, OH· , $NO_3^·$
B_SVOC_I	Semi	biogenic	mass-based partition	IP	O_3, OH· , $NO_3^·$
A_LVOC	Low	anthropogenic	kinetic condensation	CO	OH·
A_SVOC	Semi	anthropogenic	mass-based partition	CO	OH·

Table 4.2: List of ox-VOCs implemented in this study, the volatility bin they represent, whether produced from biogenic or anthropogenic sources, how they take part in atmospheric SOA formation, parent VOC and oxidants which react to produce each ox-VOC. MT stands for monoterpene, IP stands for isoprene and CO stands for carbon monoxide indicating anthropogenically sourced VOC.

Reaction	Product(s)	Rate constant
		cm^3 $molecule^{-1}$ s^{-1}
α-pinene + OH·	B_ELVOC, B_LVOC, B_SVOC_M	$1.2 \times 10^{-11} exp(444/T)$
α-pinene + O_3	B_ELVOC, B_LVOC, B_SVOC_M	$1.01 \times 10^{-15} exp(-732/T)$
α-pinene + $NO_3^·$	B_ELVOC, B_LVOC, B_SVOC_M	$1.19 \times 10^{-12} exp(490/T)$
IP + OH·	B_SVOC_I	$2.7 \times 10^{-11} exp(390/T)$
IP + O_3	B_SVOC_I	$1.0 \times 10^{-14} exp(-1995/T)$
IP + $NO_3^·$	B_SVOC_I	$3.15 \times 10^{-12} exp(-450/T)$
AVOC + OH·	A_LVOC, A_SVOC	$5 \times 10^{-12} \times scalingfactor$

Table 4.3: List of bimolecular oxidation reactions in the model involving biogenic and anthropogenic VOCs that produce ox-VOCs, as implemented in this study. α-pinene is used as a representative monoterpene, IP stands for isoprene and AVOC stands for anthropogenically sourced VOC derived from CO emissions (Spracklen et al., 2011b) using the $scalingfactor$. Above reaction rates (Atkinson et al., 2006) have been used in previous GLOMAP studies (Spracklen et al., 2006; Mann et al., 2010; Scott et al., 2014).

.

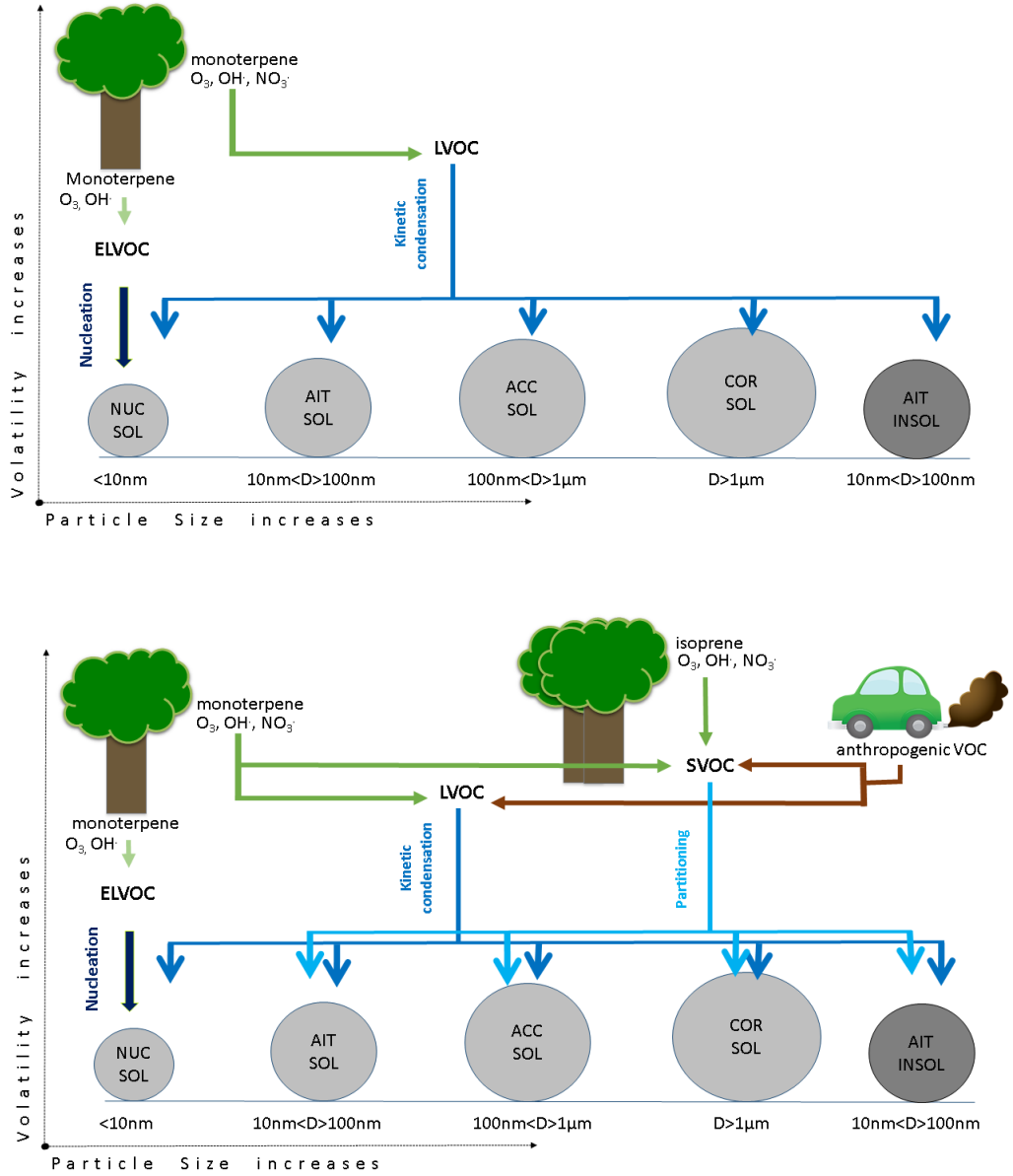

Figure 4.3: Schematic showing the existing SOA production scheme in GLOMAP-mode as described in Mann et al., 2010; Gordon et al., 2016 (top panel) and the modified SOA formation scheme introduced in this study (bottom panel).

4.4.1 Model set-up

The following developments are made in the model version used in Chapter 3, besides introducing the modified scheme for SOA production.

- Monthly mean emissions of SO_2, BC and OC for the year 2008 from the

MACCity inventory (Granier et al., 2011) replace AEROCOM emissions for 2000 (Dentener et al., 2006).

- Monthly mean emissions of CO for the year 2008 from MACCity inventory is added to represent VOC from anthropogenic sources (Spracklen et al., 2011b).

- Monthly mean emissions of monoterpene for the year 2007 generated from the Community Land Model by Sarah Monks (MEGANv2.1; Guenther et al., 2012) replaces monoterpene emissions for the year 2000 from the GEIA database (Guenther et al., 1995).

- Monthly mean emissions of isoprene for the year 2007 generated from the Community Land Model by Sarah Monks (MEGANv2.1; Guenther et al., 2012) is added.

- Large-scale atmospheric transport is driven by ERA-Interim reanalysis for 2008, produced by the European Centre for Medium-Range Weather Forecasts (ECMWF) at 6 hourly intervals replaces ERA 40 (which is available until 2001).

4.4.2 Model Simulations

After implementing the changes described above the model has been tested extensively. To assess the effect of ox-VOCs on aerosol number concentration in the present-day as well as pre-industrial atmospheres, the model is run for 1750 and 2008. Further a set of twelve one-at-a-time sensitivity tests are performed in which the yields of each ox-VOC is varied from 0 to a factor of 10 to assess the effects of each ox-VOC on the simulated size distribution. Table 4.4 lists all simulations.

Number	Simulation Name	year	Perturbed parameter	Perturbation Range
1	OMOD PD	2008		
2	OMOD PI	1750		
3	ORG PD	2008		
4	ORG PI	1750		
5	B_ELVOC_LO	2008	B_ELVOC	0
6	B_ELVOC_HI	2008	B_ELVOC	10 times higher
7	B_LVOC_LO	2008	B_LVOC	0
8	B_LVOC_HI	2008	B_LVOC	10 times higher
9	B_SVOC_M_LO	2008	B_SVOC_M	0
10	B_SVOC_M_HI	2008	B_SVOC_M	10 times higher
11	B_SVOC_I_LO	2008	B_SVOC_I	0
12	B_SVOC_I_HI	2008	B_SVOC_I	10 times higher
13	A_LVOC_LO	2008	A_LVOC	0
14	A_LVOC_HI	2008	A_LVOC	10 times higher
15	A_SVOC_LO	2008	A_SVOC	0
16	A_SVOC_HI	2008	A_SVOC	10 times higher

Table 4.4: List of simulations performed in this chapter. Simulation OMOD PD includes all six ox-VOCs described in Table 4.2 for the present-day atmosphere. Simulation OMOD PI includes ox-VOCs except A_LVOC and A_SVOC for the pre-industrial atmosphere. Simulation ORG represents the model before implementing the modified SOA scheme. 12 one-at-a-time sensitivity tests (listed from 5-16) are performed to assess the model sensitivity to the six ox-VOCs. The suffix 'HI' is added to indicate an increase in ox-VOC yields by a factor of 10. The suffix 'LO' is added to indicate an absence of that particular ox-VOC type.

4.5 Results

4.5.1 Change in SOA production from ox-VOC

	(a) OMOD PI					(b) OMOD PD				
ox-VOC	Nuc sol	Aitken sol	Accum sol	Coarse Sol	TOTAL_{ox-VOC}	Nuc sol	Aitken sol	Accum sol	Coarse Sol	TOTAL_{ox-VOC}
	Tg yr^{-1}	Tg yr^{-1}	Tg yr^{-1}	Tg yr^{-1}	Tg yr^{-1}	Tg yr^{-1}	Tg yr^{-1}	Tg yr^{-1}	Tg yr^{-1}	Tg yr^{-1}
B_LVOC	0.23	2.8	11.4	0.09	14.52	0.12	2.89	11.6	0.06	14.67
B_SVOC	-	2.8	23.2	0.09	26.09	-	3.10	23.04	0.06	26.2
A_LVOC	-	-	-	-		0.16	8.8	22.72	0.13	31.65
A_SVOC	-	-	-	-		-	6.5	25.2	0.04	31.74
TOTAL_{mode}	**0.23**	**5.6**	**34.6**	**0.18**		**0.28**	**21.29**	**82.56**	**0.29**	-
$\text{TOTAL}_{Allmodes}$	40.61					104.42				-
	(c) ORG PI					(d) ORG PD				
ox-VOC	Nuc sol	Aitken sol	Accum sol	Coarse Sol	TOTAL_{ox-VOC}	Nuc sol	Aitken sol	Accum sol	Coarse Sol	TOTAL_{ox-VOC}
	Tg yr^{-1}	Tg yr^{-1}	Tg yr^{-1}	Tg yr^{-1}	Tg yr^{-1}	Tg yr^{-1}	Tg yr^{-1}	Tg yr^{-1}	Tg yr^{-1}	Tg yr^{-1}
B_LVOC	0.3	3.16	10.6	0.09	14.15	0.22	3.1	10.7	0.07	14.09
B_SVOC	-	-	-	-	-	-	-	-	-	-
A_LVOC	-	-	-	-	-	-	-	-	-	-
A_SVOC	-	-	-	-	-	-	-	-	-	-
TOTAL_{mode}	**0.3**	**3.16**	**10.6**	**0.09**		**0.22**	**3.1**	**10.7**	**0.07**	-
$\text{TOTAL}_{Allmodes}$	14.15					14.09				-

Table 4.5: Global annual mean mass flux (in Tg yr^{-1}) of each ox-VOC adding (via kinetic condensation or mass-based partitioning) to the aerosol phase in each of the four soluble modes, the mass flux of all ox-VOCs in each soluble mode (TOTAL_{mode}) and the mass flux of all ox-VOCs in all soluble modes ($\text{TOTAL}_{Allmodes}$) for (a) simulation OMOD for pre-industrial (b) simulation OMOD for present-day (c) simulation ORG for pre-industrial (b) simulation ORG for present-day. The global distribution of TOTAL_{mode}, highlighted in bold within the table, is shown in Figure 4.4.

Table 4.5 summarises the effects of the implemented changes on SOA produced from ox-VOCs for pre-industrial (a and c) and present-day (b and d) atmospheres

in GLOMAP. With the existing approach in GLOMAP (simulation ORG) about 14 Tg yr^{-1} SOA is produced from kinetic condensation of SEC_ORG (lumped monoterepene oxidation products) for both present-day asnd pre-industrial atmosphere. The modified treatment of SOA formation (simulation OMOD) introduced in this chapter includes additional SOA sources such as isoprene and anthropogenically controlled VOCs. Under this treatment, the total global flux of gaseous phase organic compounds into the aerosol phase is about 40 Tg yr^{-1} in the pre-industrial atmosphere and about 104 Tg yr^{-1} in the present-day atmopshere. The present-day production of SOA from VOC condensation under the modified scheme lies within the SOA uncertainty range 50−380 Tg yr^{-1} (and close to the best estimate of 140 Tg yr^{-1}) given by Spracklen et al. (2011b) .

Comparing the mass fluxes of A_LVOC and A_SVOC in the Aitken and accumulation modes (Table.4.5b) gives insight to the effect of kinetic and thermodynamic approaches used for SOA production in the model. Equal amounts of A_LVOC and A_SVOC are produced in the model as a result of oxidation reactions between the same precursor VOC and oxidant. Once formed condensable A_LVOC is distributed in the particle phase using the kinetic approach and condensable A_SVOC is distributed in the particle phase using the mass-based approach. Mass transfer in the kinetic scheme scales to particle surface area i.e. square of the particle diameter (Equation 4.2). Mass transfer in the thermodynamic approach scales to particle mass (Equation 4.7) which is proportional to volume or the cube of the particle diameter. The above implies relatively larger particles get a greater fraction of total A_SVOC than A_LVOC, which leaves more A_LVOC for the growth of smaller particles. In other words, the distribution of A_SVOC is more strongly skewed towards larger particles compared to A_LVOC. This behaviour is in agreement with that reported in Scott et al. (2015) where two model simulations, one producing SOA using the kinetic approach only and another producing SOA using the ther-

modynamic approach only, were compared.

Together the particles in the Aitken and accumulation modes get about 99 % ox-VOCs in simulation OMOD (increased from about 97 % in simulation ORG). About 79 % of the total gaseous phase organic compounds contribute to the growth of particles bigger than 100 nm (accumulation mode) while about 20 % contributes towards the growth of Aitken mode particles ($10-100$ nm) in simulation OMOD. Majority of the gaseous phase ox-VOCs distribute on particles in the Aitken and accumulation modes because these two modes :

1. have highest particle number concentration including large contributions from primary particles.

   The soluble Aitken mode has the highest number concentration of particles as a result of primary emission of aerosol particles (from fossil fuel, biofuel burning and primary sulphate) in this mode in addition to the secondary particles transferred from the nucleation mode via mode-merging. The soluble accumulation mode contains primary particles from biomass burning sources. The nucleation mode on the other hand only contains secondary particles formed from nucleation in the model. The coarse mode is dominated by large sea-salt aerosol particles (as dust is not treated in the model version used in this thesis) and the transfer of particles from accumulation to coarse mode is the slowest. As the distribution of ox-VOCs to the aerosol modes largely depends on the number concentration of aerosol particles, more ox-VOCs get distributed in the Airken and accumulation modes.

2. have particles which are less efficiently removed from the atmosphere.

   Particle number concentration in the nucleation mode is greatly reduced by intra-modal coagulation due to small size of the particles. Particles in the coarse mode are efficiently removed by sedimentation due to their large sizes.

By contrast in Aitken and accumulation mode, which as stated above have steady particle sources, particles are less prone to loss by removal mechanisms. Thus Aitken and accumulation mode particles have a longer atmospheric lifetime (than nucleation or coarse mode particles) causing greater condensation of ox-VOCs on particles in these modes.

The greater distribution of ox-VOCs to accumulation mode compared to the Aitken mode may be attributed to cloud processing in the model. Particles at the larger end of the Aitken mode (with dry diameter $>$ 50 nm following Spracklen et al., 2005b) are transferred to the accumulation mode as 'activated particles' causing a reduction in the number of Aitken mode particles. Once in accumulation mode these activated particles are additionally grown by aqueous phase oxidation of SO_2. Such growth further increases their mass and surface area, attracting more ox-VOCs for their growth compared to particles in other modes.

A large fraction (61 % of total SOA from VOCs) of SOA is produced by VOCs from anthropogenically controlled sources in the current model set up. Anthropogenically controlled SOA has been known to make a significant difference when simulating observed SOA (Spracklen et al., 2011b). Including VOCs from anthropogenically controlled sources sets the pre-industrial and present-day simulation apart not only in terms of primary emissions but also the available gaseous phase organic compounds to produce secondary aerosol particles in the model (Figure 4.4). The radiative impact of aerosols is dependent on relative change in their number concentration from pre-industrial to present-day. Whether the above changes lead to a significant change in particle number concentrations and affect aerosols indirect forcing due to anthropogenic aerosols is examined in following sections.

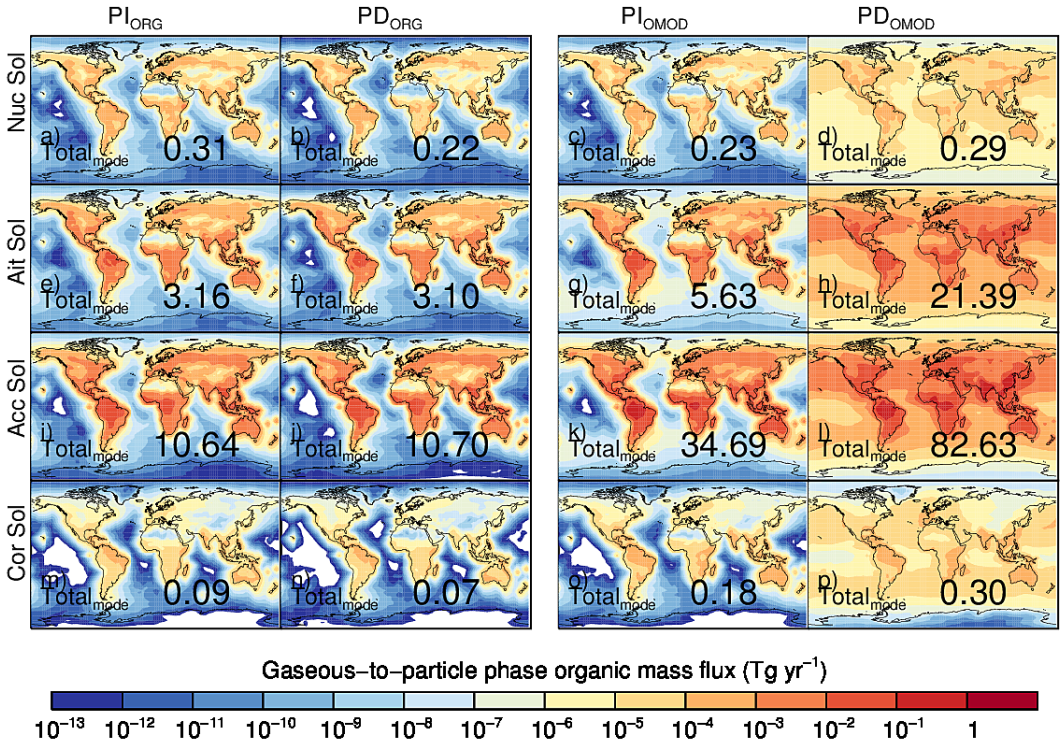

Figure 4.4: Annual mean surface-level mass flux (Tg yr^{-1}) of gaseous phase ox-VOCs to the nucleation mode for (a) simulation ORG in the pre-industrial (b) simulation ORG in the present-day (c) simulation OMOD in the pre-industrial (d) simulation OMOD in the present-day; to the Aitken soluble mode for (e) simulation ORG in the pre-industrial (f) simulation ORG in the present-day (g) simulation OMOD in the pre-industrial (h) simulation OMOD in the present-day; to the accumulation soluble mode for (i) simulation ORG in the pre-industrial (j) simulation ORG in the present-day (k) simulation OMOD in the pre-industrial (l) simulation OMOD in the present-day; to the coarse soluble mode for (m) simulation ORG in the pre-industrial (n) simulation ORG in the present-day (o) simulation OMOD in the pre-industrial (p) simulation OMOD in the present-day. The number printed represents the global annual mean for each subplot.

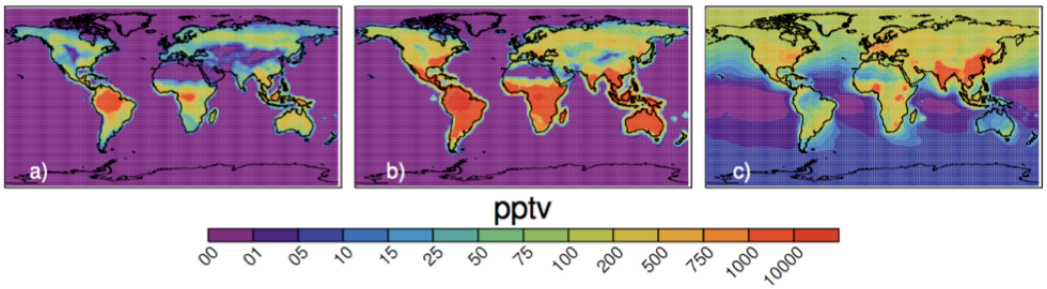

Figure 4.5: Global distribution of annual mean mixing ratio (in pptv) of (a) terpenes (b) isoprene and (c) anthropogenically controlled VOC at surface-level in the model.

4.5.2 Changes in particle number concentrations in pre-industrial and present-day atmospheres

Figures 4.6 and 4.7 show the global distribution of particles with diameter greater than 3 nm, N3, and those with diameter greater than 50 nm, N50, for simulations ORG and OMOD. The plots also depict the relative difference in particle number concentrations between the two simulations for pre-industrial and present-day atmospheres. N3 is synonymous with CN (total particles or condensation nuclei) in our model as any particle entering the nucleation mode has at least 3 nm dry diameter. N50, as in Chapter 3, is the number concentration of particles with potential to act as CCN in the atmosphere.

Global annual mean N3 changes by -15.8 % in the present-day (-20 % in NH and -11 % in SH) and -9 % (-13 % in NH and -4.8 % in SH) in the pre-industrial atmosphere. Global annual mean N50 changes by $+14$ % ($+17.7$ % in NH and $+11.9$ % in SH) in the present-day and by $+2.8$ % ($+3.9$ % in NH and $+1.7$ % in SH) in the pre-industrial atmosphere.

The bigger change in NH is expected as most of the precursor gas emissions are continental. The stronger sensitivity shown by N3 (as compared to N50) is in agreement with the findings of Merikanto et al. (2009). In the present-day the reduction in N3 is strongest over NH mid-latitude (Figure 4.6f), particularly over North America (where the decrease is between $100-500$ %) and boreal forest zone across Europe and America. The reduction continues for N50 (Figure 4.7f) at tropical forest regions over South America, central Africa and Australia ($5-25$ %). There is an increase in N50 over the rest of the world, particularly in the pristine regions of the northern high-latitudes (upto 75 %).

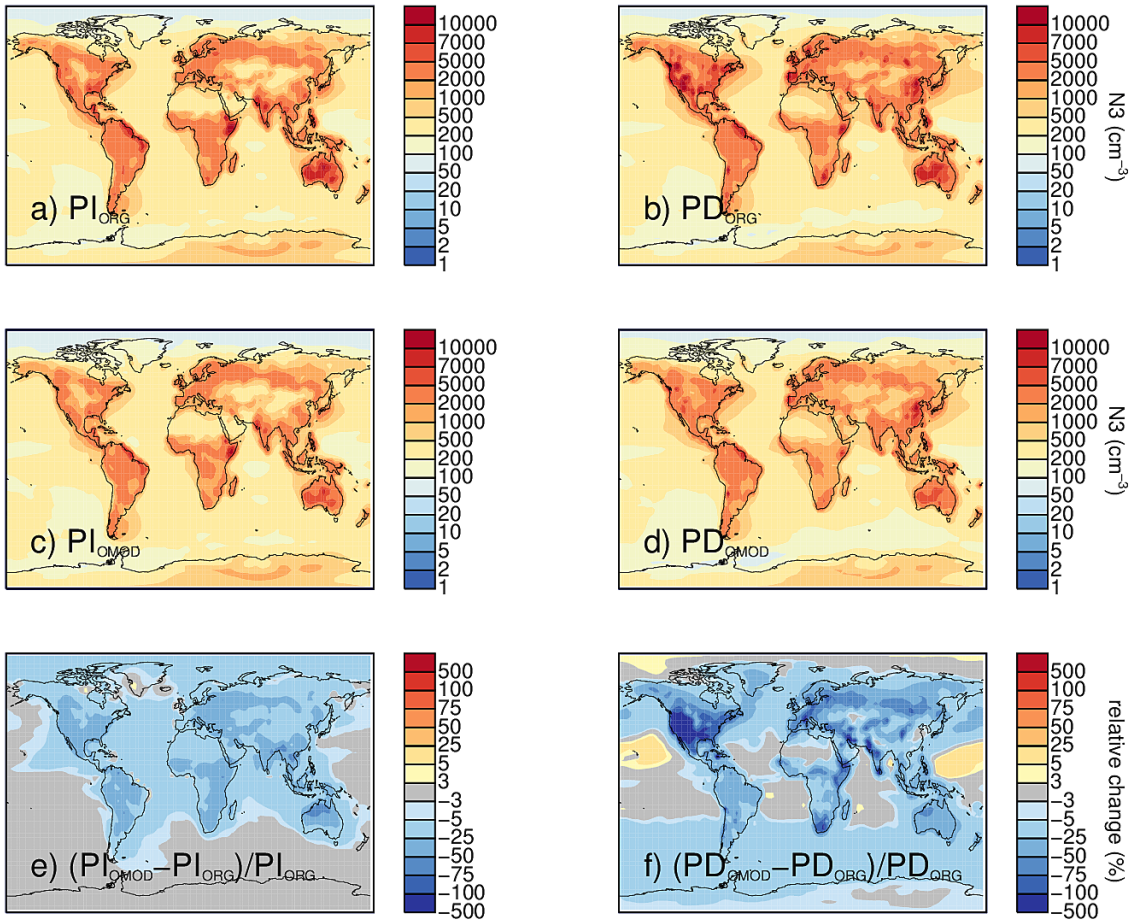

Figure 4.6: Annual mean number concentration of surface-level particles with dry diameter above 3 nm (N3) for a) simulation ORG in the pre-industrial atmosphere b) simulation ORG in the present-day atmosphere c) simulation OMOD in the pre-industrial atmosphere d) simulation OMOD in the present-day atmosphere. The relative change in annual mean N3 as a result of introducing the modified SOA formation scheme are shown in e) for the pre-industrial and f) for the present-day atmospheres.

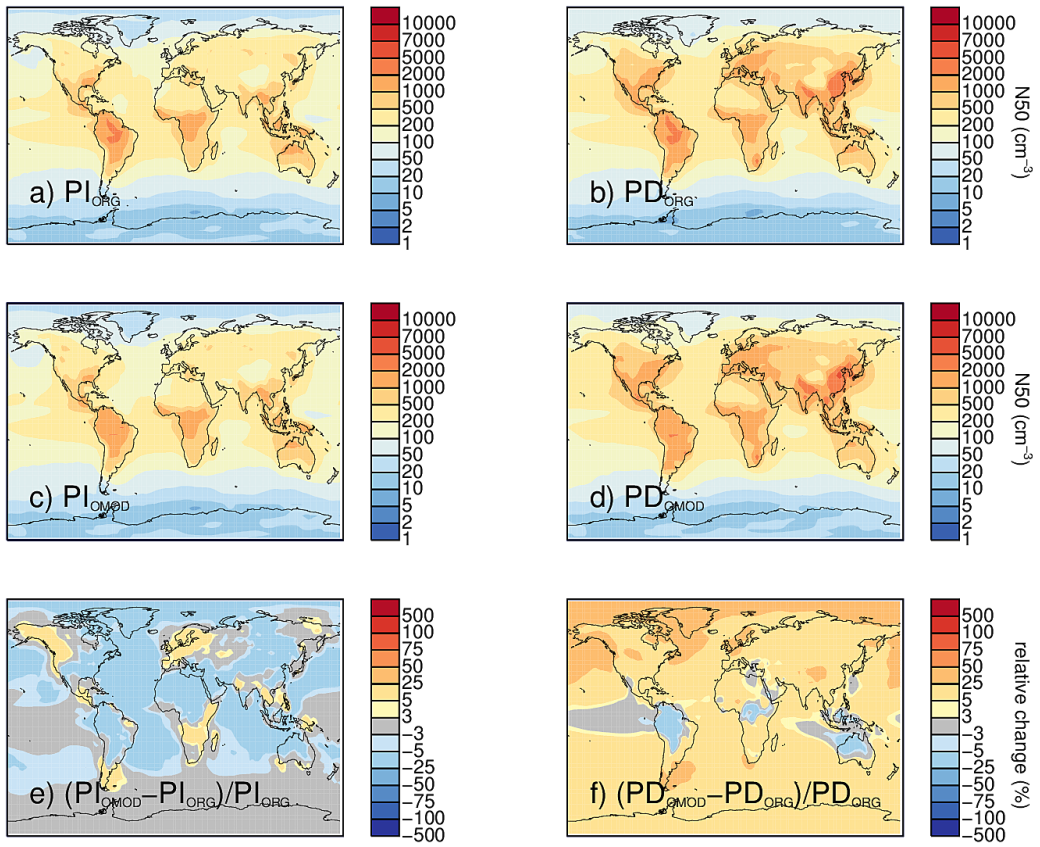

Figure 4.7: Annual mean number concentration of surface-level particles with dry diameter above 50 nm (N50) for a) simulation ORG in the pre-industrial atmosphere b) simulation ORG in the present-day atmosphere c) simulation OMOD in the pre-industrial atmosphere d) simulation OMOD in the present-day atmosphere. The relative change in annual mean N3 as a result of introducing the modified SOA formation scheme are shown in e) for the pre-industrial and f) for the present-day atmospheres.

The response of N3 and N50 to the changes made in SOA formation scheme in this study can be understood from considering the aerosol microphysical processes in the model. Particle number is known to vary non-linearly with changes in particle sources (Stier et al., 2006; Spracklen et al., 2006). In the model three sources contribute to surface-level N3 and N50:

- Primary particles including sea-salt, particulate carbonaceous emissions (EC and OC), and sulphate emissions from wild- fires, biofuels, fossil fuels and volcanoes.

- Secondary particles formed in the free troposphere from binary sulphuric acid

nucleation and entrained into boundary layer.

- Secondary particles formed as a result of nucleation in the boundary layer.

Merikanto et al. (2009) shows globally these sources may contribute 27 %, 26 % and 48 % respectively of the total particles at ground level and constitute 55 %, 35 %, 10 % respectively of the particles that can act as CCN at 0.2 % supersaturation. The modifications in the treatment of SOA made in this study has no effect on particles sourced from primary emissions. A decrease in surface level N3 is therefore a result of suppressed nucleation in the free troposphere and/or boundary layer.

Nucleation in the model is a result of two competing processes: production of particle clusters and their loss. Cluster production and their subsequent growth upto 3 nm size, in the model, is directly facilitated by two of the six ox-VOCs: B_ELVOC and B_LVOC. The total concentrations of both these ox-VOCs and the mechanism by which they transfer to the particle phase are identical in simulations ORG and OMOD. Thus in principle, the processes governing the production of nucleation mode particles are the same in both simulations. Therefore in simulation OMOD with lower N3, processes that scavenge particles must be stronger leading to a lower *net* production of particles and lowering of the total particle number concentration.

The primary scavenging mechanism for nucleated clusters is loss by coagulation on bigger particles that constitute the condensation sink. Once formed survival of clusters is dependent upon the availability of low volatility vapours to grow the clusters as well as a sufficiently low background aerosol concentration or condensation sink that allows small particles to grow without getting scavenged (Equation 3.7). Increase in the concentrations of condensable gaseous phase organic compounds favours growth via condensation thereby increasing SOA formation. The increased growth leads to an increase in the number of bigger particles which in turn provides

additional surface area for small clusters to collide and get scavenged, eventually suppressing nucleation. This may account for a lower contribution of boundary layer nucleation to simulated N3 in simulation OMOD.

Whether increased scavenging of clusters and small particles in the boundary layer is the only cause for the decrease in particle number concentrations or, entrainment from upper atmosphere has a role to play is investigated by plotting the vertical variation of N3 from surface to 10 hPa, averaged longitudinally. Particle concentrations reduce above the boundary layer and reaches a maxima at around 100 hPa (around 16-17 km) for both simulations ORG and OMOD (Figure 4.8 a, b, c and d). The minimum above the boundary layer is attributed to scavenging of aerosols by the low level clouds while the maxima at the free troposphere to upper atmospheric nucleation (Schröder et al., 2002).

Figures 4.8e and f show the difference in the vertical profiles of N3 between simulations ORG and OMOD. The reduction in ground level N3 seen in surface maps (Figure 4.6f) is found to have propagated to higher altitude levels, particularly in the present-day. Over the equator N3 has decreased by 500-1000 cm^{-3} at about 100 hPa (16 km). At a lower altitude this reduction belt extends to the tropics and mid-latitudes in the NH. As nucleation is a significant source of particles in the free troposphere (favoured by low background particle concentrations and low temperature), this could indicate a suppression of free tropospheric (binary sulphuric acid) nucleation. In simulation OMOD increased condensation and coagulation increases the average size of particles in the boundary layer thereby increasing the amount of gaseous phase sulphuric acid contributing to their growth. The increased amounts of sulphuric acid required to support the growth of boundary layer particles in OMOD in turn reduces the amount of sulphuric-acid available for the production of free-tropospheric particles.

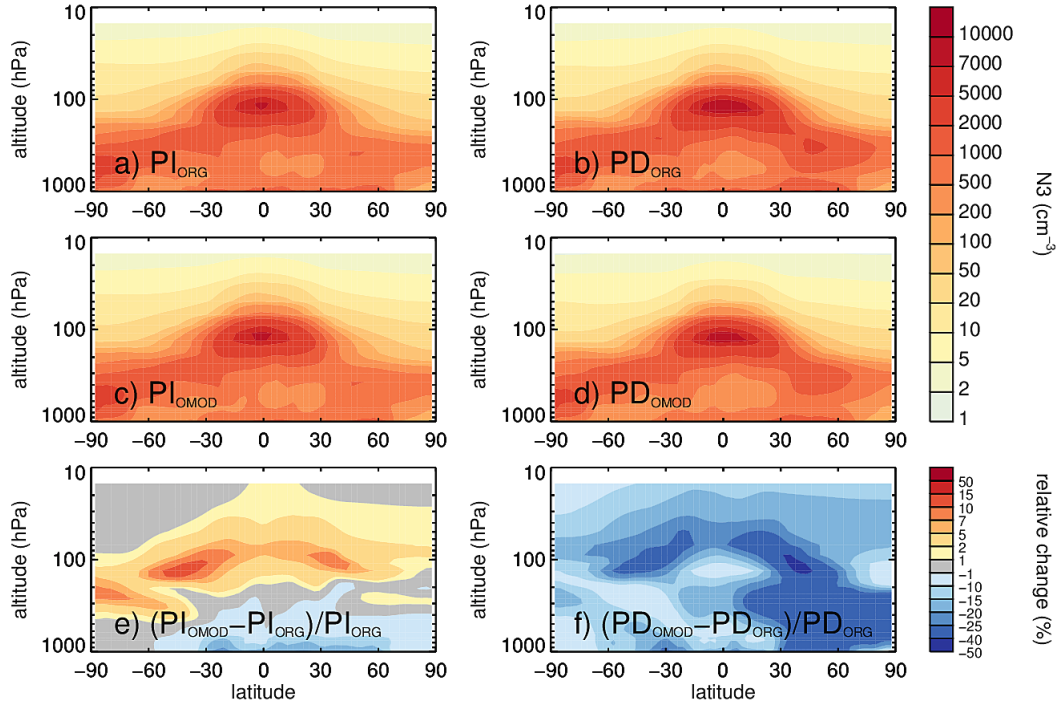

Figure 4.8: Meridional annual mean vertical distribution of particles with dry diameter above 3 nm (N3) for a) simulation ORG in the pre-industrial atmosphere b) simulation ORG in the present-day atmosphere c) simulation OMOD in the pre-industrial atmosphere d) simulation OMOD in the present-day atmosphere. The relative change in meridional annual mean vertical distribution of N3 as a result of introducing the modified SOA formation scheme are shown in e) for the pre-industrial and f) for the present-day atmospheres.

In the following sections the aerosol size distribution simulated by ORG and OMOD are compared, monthly mean simulated N3 is compared against monthly mean global N3 observations and the climatic relevance of the new treatment assessed.

4.5.3 Changes in aerosol size distribution

Figure 4.10 shows the aerosol size distribution in 33 locations across the globe for simulations ORG and OMOD. The locations (shown in Figure 4.9) chosen are those that have N3 data (used in Section 4.5.4) and includes free tropospheric (FT) sites, continental boundary layer (CBL) sites and marine boundary layer (MBL) sites.

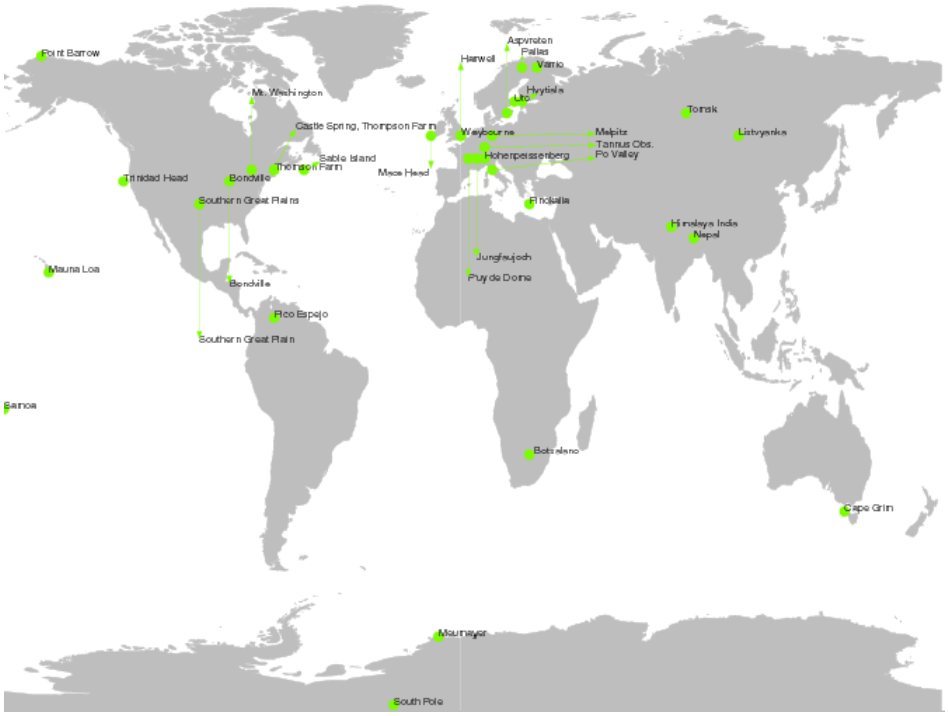

Figure 4.9: Map showing 33 ground-based locations at which the surface-level aerosol number size distribution simulated by the model under various conditions are inter-compared (Figures 4.10, 4.11 and 4.12) and the monthly mean total aerosol number concentration is compared against observations (Figures 4.13, 4.14).

Figure 4.10 shows a decrease in the number concentration of particles in the nucleation mode (yellow in Figure 4.10) and an increase in particle diameter of Aitken and accumulation modes (green and blue in Figure 4.10) particles with simulation OMOD (solid line). This is in agreement with Table 4.5 which shows most of the added ox-VOCs in OMOD are distributed in the Aitken and accumulation modes. As a result the particles in these modes grow bigger in simulation OMOD than in simulation ORG.

Implementing the new treatment for SOA formation has resulted in up to an order of magnitude decrease in the number of sub-10 nm particles in almost all locations. With increasing size, particle number concentration becomes less sensitive to the changed SOA production treatment (OMOD) and a relatively small increase in

number concentration is observed beyond 50 nm (as previously seen in the global maps - Figures 4.6 and 4.7).

Possible reasons for the reduction of particle number concentration in the nucleation mode and the increase in larger modes are:

- 99 % of the total available ox-VOCs in simulation OMOD contribute to the growth of larger particles in Aitken and accumulation modes (Table 4.5), which is a 2 % increase from simulation ORG.
- Suppression of nucleation due to larger sizes of Aitken and accumulation mode particles in OMOD which enhances sulphuric acid condensation (Figure 4.8).
- Increased loss of freshly nucleated sub-3 nm clusters to the increased condensation sink in simulation OMOD (Figure. 4.6.
- Increased loss of nucleation mode ($>$ 3 nm) particles by intra and inter-modal coagulation with larger particles in OMOD, since particles in Aitken and accumulation have greater diameter in simulation OMOD than in simulation ORG (Figure 4.10).

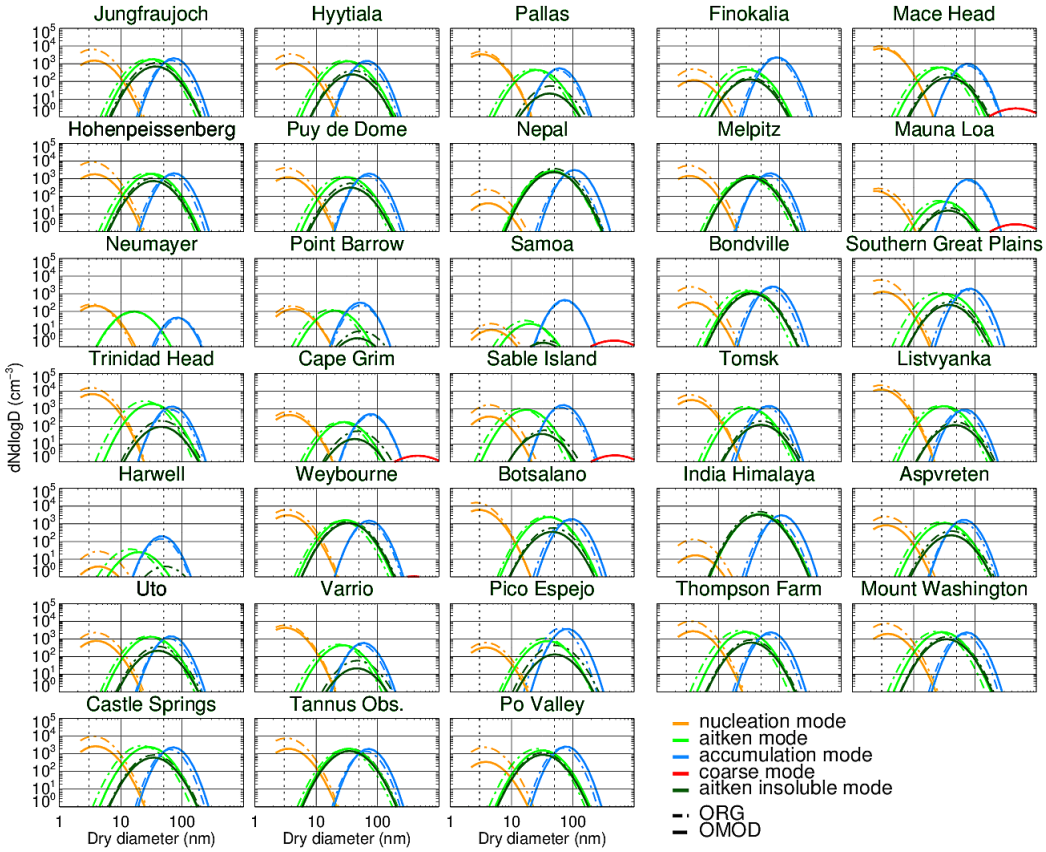

Figure 4.10: Aerosol number size distribution at 33 ground-based locations (as shown in Figure 4.9) for simulation ORG (dotted line) and simulation OMOD (solid line). Each color represents a size mode: yellow represents the nucleation mode, green represents the Aitken mode, blue represents the accumulation mode and red represents the coarse mode.

It should be noted here that in most locations, the modified SOA treatment (solid line in Figure 4.10) shifts the size distribution to the larger particle sizes. However the increase in diameter for larger particles is not as striking as the decrease in number of smaller particles. Whether the decrease in the number concentrations of nucleation mode particles or the increase in mean particle dry diameter of Aitken and accumulation mode particles has a more significant climate impact, is assessed later in Section 4.5.5.

To investigate the role of each ox-VOC on the aerosol size distribution in simulation OMOD a set of one-at-a-time sensitivity tests are performed with the yields of each of ox-VOC (from their parent VOC) perturbed from 0 to a factor of 10 higher (as listed in Table 4.4. In GLOMAP-mode the amount of condensable vapours available to form SOA can be controlled by controlling the yields for the bimolecular reaction between precursor gases and oxidants in the model. Changing the yields of condensables from precursor gases has the same effect as changing emissions of these precursor gases, for example. The simulations for which the parameters are set to 0, provide an insight to the role each of these parameters play.

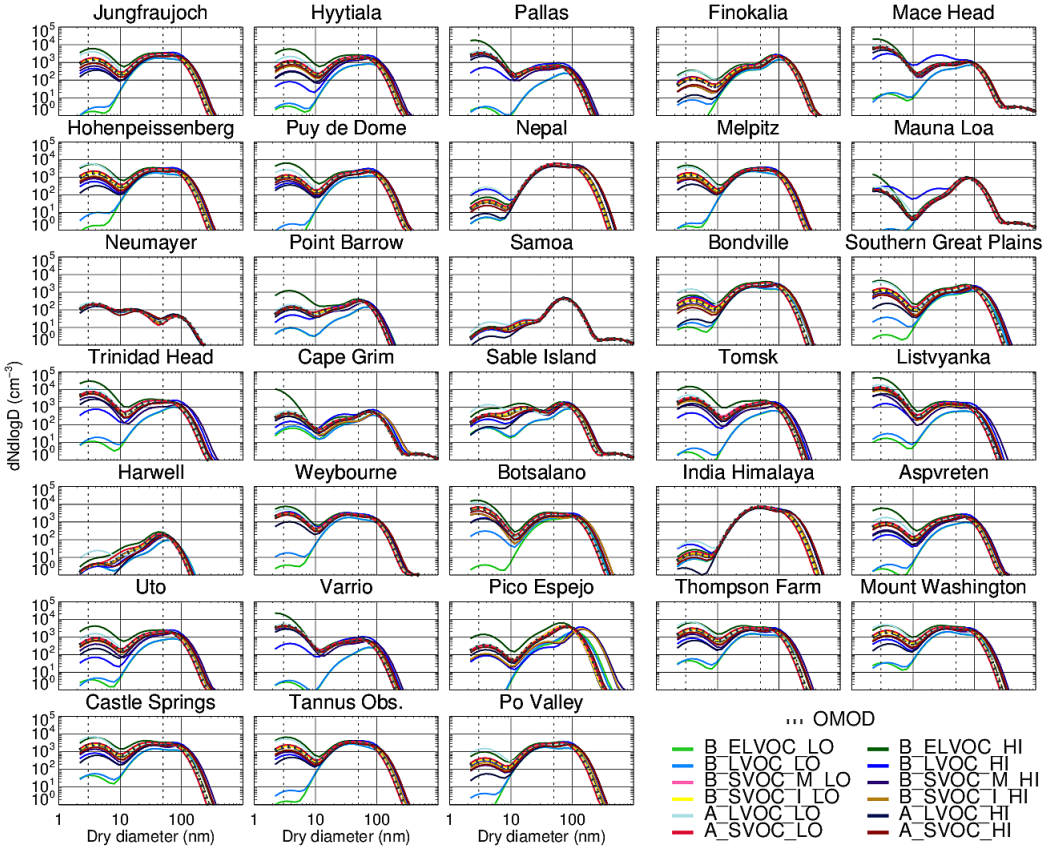

Figure 4.11: Aerosol number size distribution in GLOMAP-mode at 33 ground-based locations (as shown in Figure 4.9) for simulation OMOD and 12 one-at-a-time sensitivity tests, perturbing the concentrations of each of the six ox-VOCs implemented in this chapter. Details of the perturbations in the 12 simulations are tabulated in Table 4.4.

The common feature among all the sites in Figure 4.11 is that the aerosol size distribution is most sensitive to the variations in concentrations of B_ELVOC and B_LVOC. B_ELVOC and B_LVOC directly contribute to new particle formation and their subsequent growth. Consequently these two parameters are critical modulators of the total particle number concentration. Perturbations to all other VOC parameters cause the modelled N3 to vary within a much narrower range compared to perturbations in B_ELVOC and B_LVOC .

In almost all the sites B_ELVOC_HI (dark green line) produces the maximum number of 3 nm sized particles while in B_ELVOC_LO (light green line) N3 concentrations drop to the lowest. This shows of all the ox-VOCs, B_ELVOC plays the most important role in modulating particle number concentration in the nucleation mode and by tuning B_ELVOC alone, the model can be made to produce a range of nucleation mode particles and N3.

The availability of B_LVOC ensures rapid growth of clusters upto 3 nm sizes before they can be scavenged via coagulation. This is a critical parameter in the model as in absence of B_LVOC (simulation B_LVOC_LO) particle number concentrations drop significantly. In some sites (such as in Hyytiala, Pallas, Varrio, Mace Head, Melpitz and Mt Washington) the reduction in the nucleation mode particle number concentrations in absence of B_LVOC is similar to that in seen in absence of B_ELVOC, implying growth of clusters by organic compounds is critical in these locations. This is in agreement with previous studies (Asmi et al., 2011; Lyubovtseva et al., 2010) that have shown that nucleation and subsequent particle growth in Finnish boreal forests are strongly dependent on non-volatile oxidation products of biogenic organic compounds. Such organic compounds are estimated to contribute to one-third of particle growth in Melpitz according to Wehner et al. (2005). O'Dowd et al. (2004) reports significant contribution from organic compounds to aerosols in

marine boundary layer regions such as Mace Head. Thus B_ELVOC and B_LVOC prove to be the most critical parameters in determining and maintaining model particle concentrations.

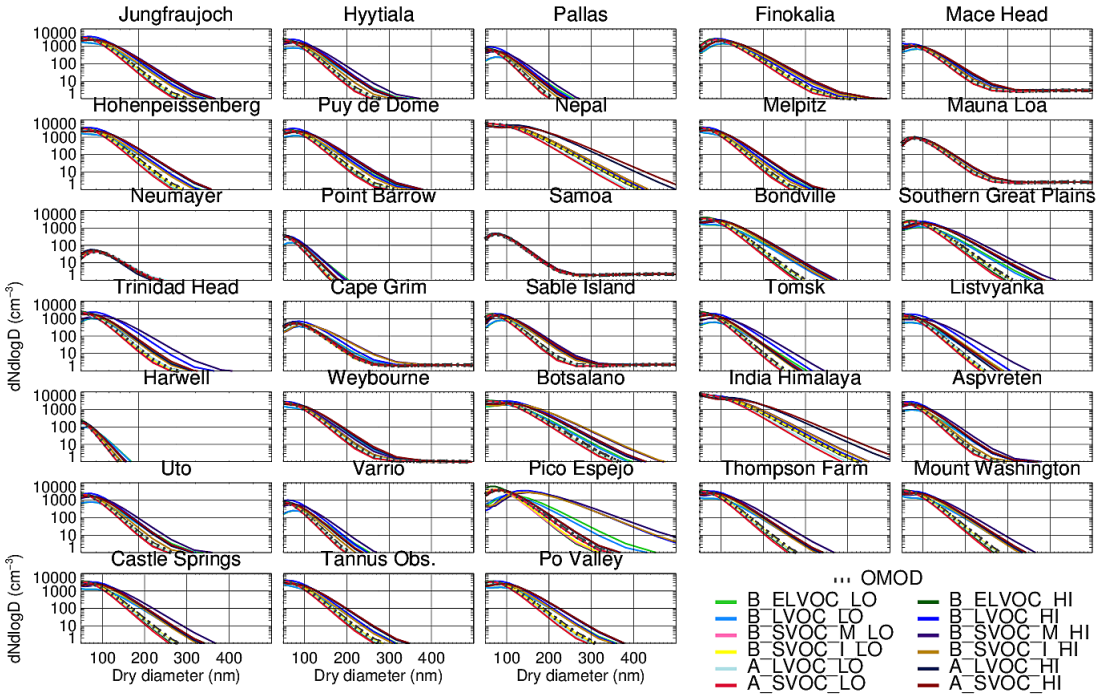

Figure 4.12: Aerosol number size distribution (above 50 nm particle diameter) in GLOMAP-mode at 33 ground-based locations (as shown in Figure 4.9) for simulation OMOD and 12 one-at-a-time sensitivity tests, perturbing the concentrations of each of the six ox-VOCs implemented in this chapter. Details of the perturbations in the 12 simulations are tabulated in Table 4.4.

Some locations, such as Neumayer and Samoa, stand out in their non-responsiveness to changes in the SOA production mechanism in the model. In Samoa, which shows a relatively small change in N3 due to the modifications in SOA treatment (Figure 4.10), the condition most conducive for a high N3 is absence of anthropogenic LVOCs (Figure 4.11). This further indicates that the dip in particle number concentration is a result of an increased condensation sink and the sites that respond the least to the changes made in simulation OMOD (such as Neumayer and Samoa) represent

regions where background aerosol concentrations are low.

In some locations, such as Harwell and India Himalaya, absence of A_LVOC (pale blue line A_LVOC_LO Figure 4.11) leads to the production of maximum aerosol number concentration in the nucleation mode. The effect of A_LVOC_LO in increasing nucleation mode particle number concentration is also clearly seen at continental sites such as Aspvreten, Bondville and Puy de dome. In all these sites anthropogenic air masses from nearby regions influence the aerosol size distribution. Thus including kinetically condensing anthropogenic ox-VOCs in the model causes a noticeable decrease in nucleation mode number concentration in regions highly effected by anthropogenic activities, possibly through suppressed boundary layer nucleation due to enhanced condensation sink.

Table 4.6 summarises the absolute and the change in global annual mean total particle number concentration and dry diameter for each mode for each simulation ORG and OMOD in pre-industrial and present-day. In the present-day the modified SOA scheme causes a 20 % decrease in nucleation mode particle number concentration globally while increasing Aitken mode particle number concentration by 11 %. Particle mean dry diameter for the Aitken and accumulation modes are increased by 16 % and 10 % respectively in simulation OMOD. In the pre-industrial atmosphere the changes are relatively smaller with 7 % and 3 % increase in the particle mean dry diameter for the Aitken and accumulation modes respectively.

It is interesting to note that in the pre-industrial atmosphere the modified SOA production scheme (including B_ELVOC, B_LVOC, B_SVOC_M and B_SVOC_I) increases nucleation mode particles by 2 % globally (compared to the 20 % reduction in present-day). This is because a larger fraction of B_LVOC is available in the pre-industrial OMOD simulation (1.5 % of 14.67 Tg yr^{-1} compared to 0.8 %

in the present-day, Table. 4.5) for growth of nucleation mode particles, in addition to the condensation sink being lower in the pre-industrial atmosphere. This indicates in the pristine pre-industrial atmosphere much of the low-volatility oxidation products of biogenic gases would have contributed to the growth of small particles. In the present-day atmosphere with the increase in primary particles, the competition for such low volatility compounds has increased. Consequently in the present-day atmosphere B_LVOCs increasingly contribute to the higher end of the size distribution resulting in faster production of climate relevant particles (than in the pre-industrial).

To summarise: nucleating B_ELVOC is critical for the production of sufficient small particles. The competing effects of B_LVOC (that grows all nucleated particles via kinetic condensation) and A_LVOC (that grows particles above 3 nm via kinetic condensation) is an important controller of nucleation mode/small particle number concentration. SVOCs in the model increase the mean diameter of larger particles i.e. addition of SVOCs increases the number of molecules per particle in each mode without increasing the number of particles in the mode. SVOCs therefore contribute significantly to the total mass of SOA produced. The right combination of these parameters may therefore be able to produce a model that simulates the right particle number concentration and SOA. This question is revisited in Chapter 5, where the entire uncertainty parameter space of SOA-producing ox-VOCs is explored.

Soluble Mode All numbers are global annual mean	ORG_PI	OMOD_PI	diff_PI (%)	ORG_PD	OMOD_PD	diff_PD (%)
Nucleation sol						
number concentration (cm^{-3})	663	675	2	854	682	-20
mean dry diameter (nm)	6.6	6.6	0.3	6.5	6.4	-1
Aitken sol						
number concentration (cm^{-3})	83	77	-6	88	97	11
mean dry diameter (nm)	53	57	7.7	59	68	16
Accumulation sol						
number concentration (cm^{-3})	37	29	-21	37	37	-0.4
mean dry diameter (nm)	105	108	3	110	120	10
Coarse sol						
number concentration (cm^{-3})	0.06	0.06	-	0.06	0.06	-
mean dry diameter (nm)	1814	1814	-	1814	1814	-

Table 4.6: Global annual mean number concentration of particles (in cm^{-3}) and global annual mean particle mean dry diameter (in nm) in each soluble mode, tabulated for simulations ORG and OMOD for present-day and pre-industrial atmospheres. The coloured columns show the % difference between OMOD and ORG simulations. Positive changes with OMOD are highlighted in red and negative change with OMOD are highlighted in blue.

4.5.4 Comparison with observed N3

Figure 4.13 compares simulated monthly mean total particle number concentrations (N3/N7/N10 depending on the cut-off diameter at observed sites) from 3 simulations (OMOD, ORG and ORG_BioOxOrg) with observed data from 33 sites (data

from Spracklen et al., 2010). In simulation ORG_BioOxOrg, nucleation is dependent on sulphuric acid plus oxidation products of monoterpene and $OH^{\cdot}$ and sub-3 nm particles grow only by addition of sulphuric acid (as in Riccobono et al., 2014). The Pearson correlation coefficient (R) and normalised mean bias factor (NMBF; Yu et al., 2006) are calculated for each of the simulations indicating the extent of agreement between modelled and observed seasonal cycle and are presented in 4.15.

NMBF is an unbiased and symmetric metric with a range from -∞ to +∞ with a score of 0 meaning best agreement. NMBF is calculated as follows:

$$NMBF = \begin{cases} \frac{\sum_{i=1}^{N}(M_i - O_i)}{\sum_{i=1}^{N} O_i}, if \bar{M} \geq \bar{O} \\ \frac{\sum_{i=1}^{N}(M_i - O_i)}{\sum_{i=1}^{N} M_i}, if \bar{M} < \bar{O} \end{cases} \tag{4.8}$$

NMBF is free from the following issues statistical metrics commonly have:

- it is proportionate for overprediction and underprediction. Some metric, for example mean normalised bias, ranges up to infinity for overprediction but only up to -100 % for underprediction. This means the interpretation of the same score is different for underestimation and overestimation.

- undue influence of one or two small observation points in the denominator is avoided by using the concept of a factor.

Positive NMBF, for example NMBF = 1.5, indicates the model is biased towards overestimating observations by a factor of 2.5 (NMBF+1). Negative values of NMBF, for example NMBF = -1.5, indicates the model is biased towards underestimating observations by a factor of -2.5 (NMBF-1).

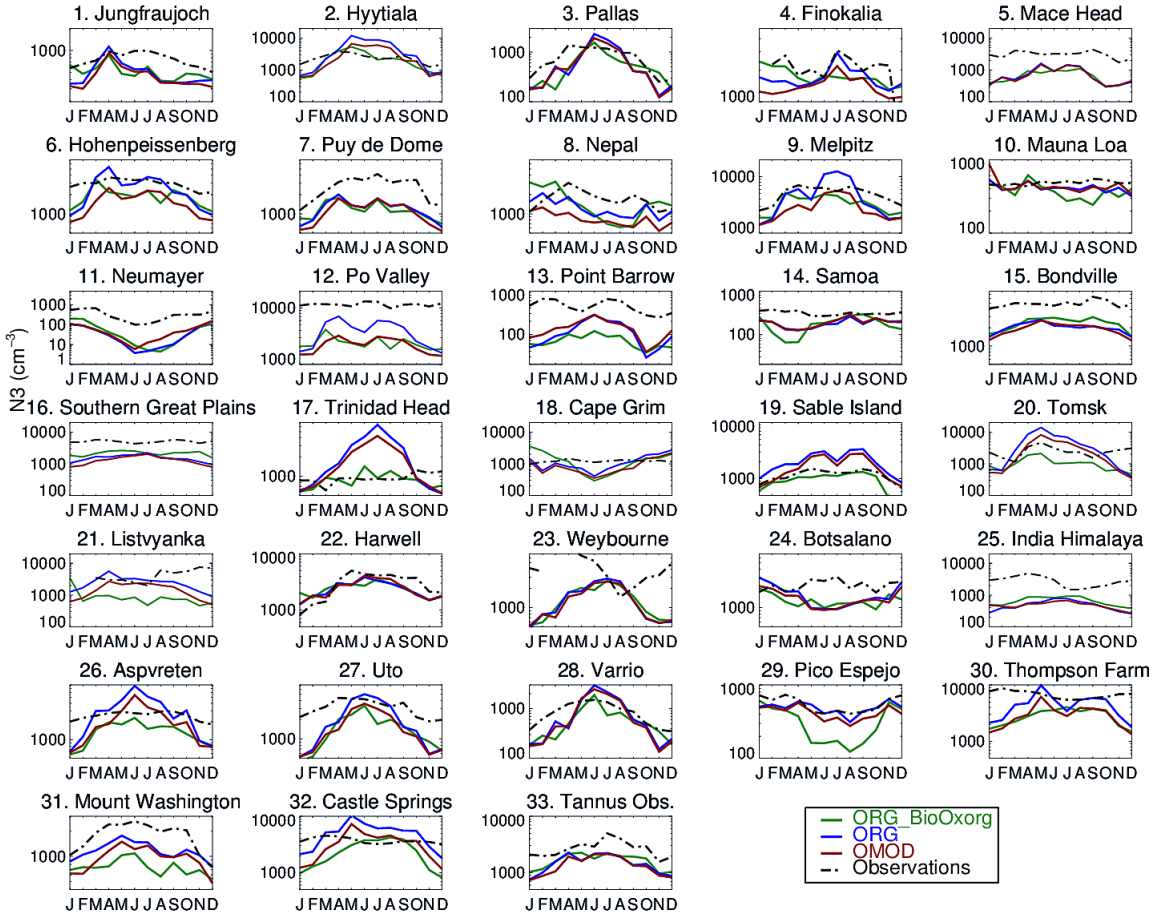

Figure 4.13: Comparison of observed and modelled monthly mean total aerosol number concentration (N3) at 33 ground-based locations (as shown in Figure 4.9). Cut-off diameters at sites range from 3 nm to 10 nm. The red line shows N3 from simulation OMOD, the blue line shows N3 from simulation ORG and the green line shows N3 from simulation ORG_BioOxOrg. The black dotted line shows data from atmospheric observations. Simulation ORG_BioOxOrg includes nucleation of sulphuric acid and biogenic oxidised organic compounds following Riccobono et al. (2014). In addition to that in ORG_BioOxOrg, simulation ORG includes pure biogenic nucleation of B_ELVOC following Kirkby et al. (2016) and cluster growth by B_LVOC. In addition to that in ORG, simulation OMOD includes particle growth by A_LVOC and SVOC.

In most locations, for most of the year, all three model simulations underestimate particle number concentrations. The simulation without pure biogenic nucleation of B_ELVOC (BioOxOrg) produces the least number of particles (green line in Figure 4.13). Including B_ELVOC and B_LVOC causes the maximum aerosol number concentration (ORG, blue line). The presence of additional SOA sources produces aerosol concentration in-between (OMOD, red line). In simulation OMOD

A_LVOCs and SVOCs which partition onto bigger particles, suppress particle formation. But clearly the suppression due to SVOCs (change from blue to red line) is less than the enhancement in particle concentration due to ELVOC and LVOC (increment from green to blue line). The figure demonstrates that the total particle number concentration in the model reaches a saturation point beyond which increasing non-nucleating, SOA-producing organic vapours decreases total aerosol number or at best has no effect (for example, at Varrio where the red and the blue lines nearly superimpose).

The annual average underestimation by the model (irrespective of how organic compounds are treated in the model) is within a factor of 3 except in Mace Head, Neumayer, Po Valley, Point Barrow and India Himalaya (Figure 4.14). The underestimation of observed aerosol concentrations at Mace Head, Point Barrow and Po Valley has previously been noted in Riccobono et al. (2014); Gordon et al. (2016); Dunne et al. (2016) and was attributed to missing sources of nucleated particles from anthropogenic molecules, iodine or amines. In Dunne et al. (2016) including ammonia ternary nucleation to produce particles along with nucleation from sulphuric acid and oxidised organic compounds (BioOxOrg as in Riccobono et al., 2014) considerably improved aerosol number concentration in high altitude stations such as Nepal, India Himalaya and Puy de Dome. In this study we expect the model performance to slightly degrade at free tropospheric sites compared to Dunne et al. (2016) since free-tropospheric nucleation involves only sulphuric acid. However this is not a serious limitation as the aim of this study is to intercompare different representations of SOA formation from ox-VOCs and assess the potential difference it could make on model estimates of first AIF.

Figure 4.13 shows in addition to the underestimation of aerosol number concentration, particularly in the winter months at several sites, introducing B_ELVOC

and B_LVOC (simulation ORG) results in an overestimation in the summer months. This is most pronounced in Trinidad Head, a coastal MBL site and also seen in a number of rural and polluted continental mid-latitude sites such as Hyytiala, Pallas, Varrio, Trinidad Head, Castle Spring, Aspvreten and Tomsk. Thus a stronger seasonal cycle is simulated in the model than that observed in the above mentioned sites. In Neumayer (site 11 in Figure 4.13) for example, the simulations with best to worst NMBF (see Figure 4.14) are - BioOxOrg, OMOD and ORG (i.e. simulation with no B_ELVOC or B_LVOC, followed by simulation with B_ELVOC, B_LVOC and with their effects dampened by increased condensation sink, followed by simulation including B_ELVOC and B_LVOC). This suggests that the contribution of biogenic organic compounds to aerosol formation via nucleation is overestimated at this site with simulation ORG. Yet the particle number at Neumayer is underestimated by a factor of 5 at best (simulation ORG_BioOxOrg), which indicates adding more particles from nucleation of biogenic organic compounds is unlikely to rectify the underestimation.

A part of the underestimation in N3 may be explained by missing nucleation pathways involving inorganic components such as iodides, amines and ammonia or nucleation of organic compounds from marine phytoplankton sources and anthropogenic sources, nucleation of iodides and amines. Under-represented background aerosol concentrations at many sites from primary emissions may also account for considerable part of the model underestimation of aerosol number. It is important to note that none of the simulations stand out when compared against available N3 observation. Figure 4.15 shows the R and NMBF at each site for the model simulation that performs best at that site. Out of 33 sites, simulation ORG_BioOxOrg gives the best model-observation agreement in 11 sites and best captures the seasonal cycle in 13 sites. Simulation ORG gives the best model-observation agreement in 15 sites and best captures the seasonal cycle in 7 sites. Simulation OMOD gives the best

model-observation agreement in 7 sites and best captures seasonal cycle in 9 sites.

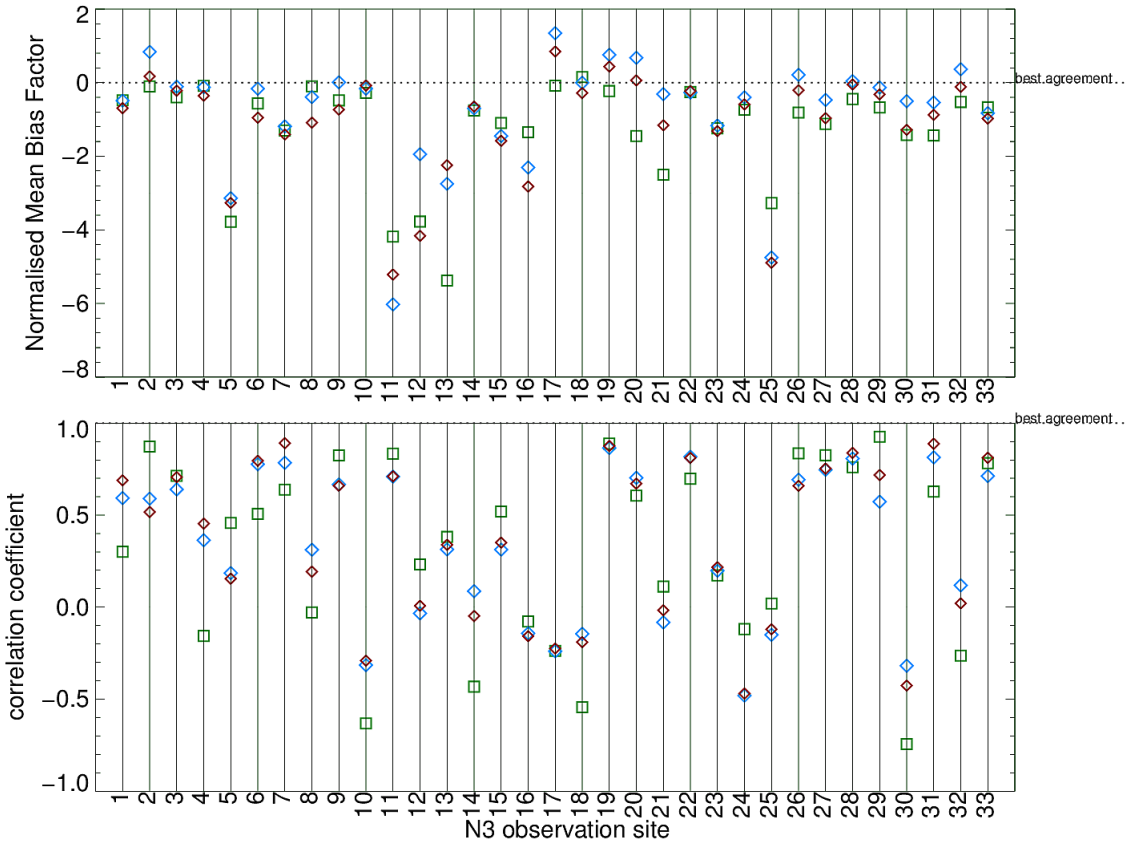

Figure 4.14: Graphical representation of the Pearson correlation coefficient (R) and Normalised Mean Bias Factor (NMBF) calculated at 33 ground-based locations (as shown in Figure 4.9) on comparison between observed and modelled monthly mean surface-level N3. Green squares represent skill score for simulation ORG_BioOxOrg, blue diamonds for simulation ORG and red diamonds for simulation OMOD. Each number in the x-axis corresponds to an observation site, as numbered in Figure 4.13.

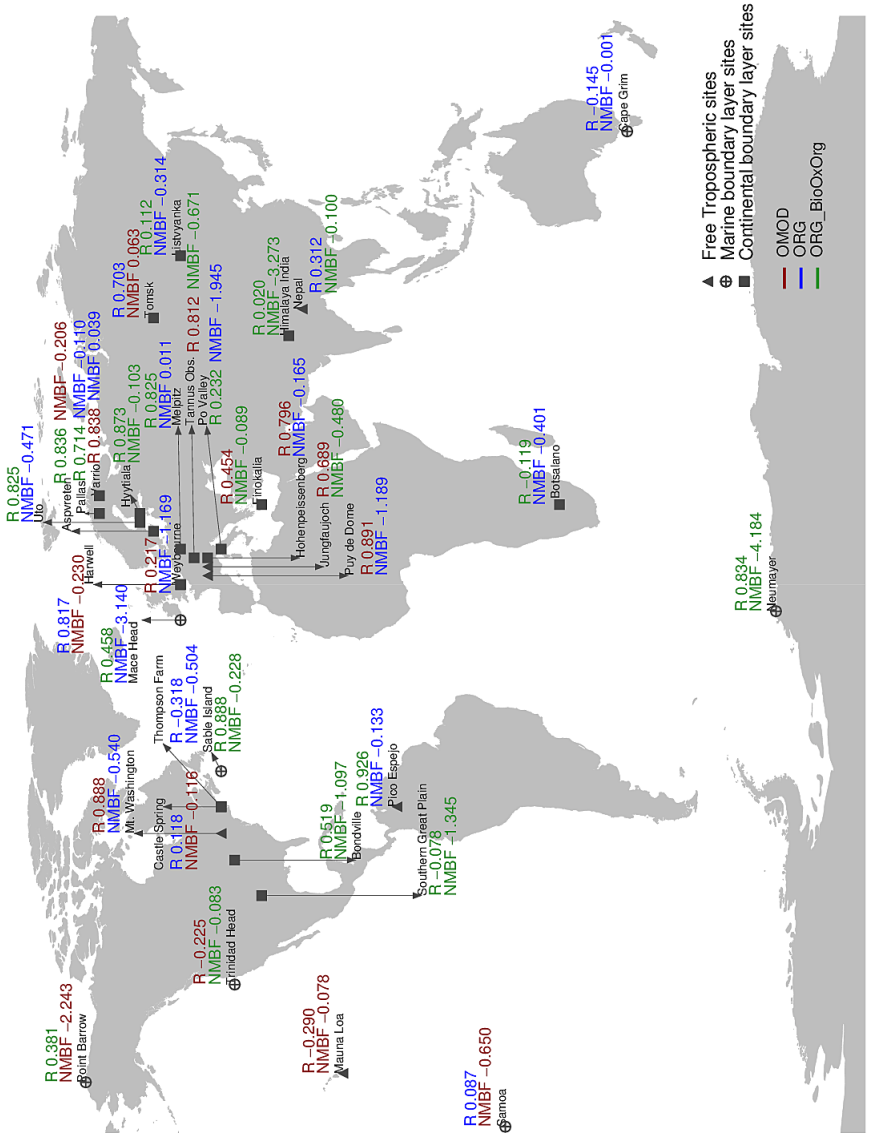

Figure 4.15: Map showing the best model performance against ground-based observations, based on 3 simulations ORG _BioOxOrg, ORG and OMOD at 33 locations (as shown in Figure 4.9). The best skill scores (R and NMBF) between simulation and observation are printed on plot. The colour of printed R or NMBF for each location indicates the best performing simulation for the location: red for simulation OMOD, blue for simulation ORG and green for simulation BioOxOrg.

To summarise the key points so far: modified treatment of SOA production in the model increases the total SOA budget from about 14 Tg yr $^{-1}$ to about 104 Tg yr $^{-1}$ (Section 4.5.1), reduces the number of small particles while favouring the growth of large particles (Section 4.5.3). The changes implemented in this study (simulation OMOD) does not significantly improve or degrade the model's capability to reproduce observed aerosol number concentration (Figure 4.15). However the requirement to represent semi-volatile and anthropogenic ox-VOCs in GLOMAP may not be ruled out yet. With a large fraction of atmospheric organic compounds being semi-volatile (Donahue et al., 2006) and with evidence of their contribution to SOA (Kanakidou et al., 2005), it must be remembered it is the aerosol size distribution rather than the aerosol number concentration at any given time that determines potential climate impact of aerosols. Figures 4.10, 4.13 emphasize the point that adequate representation of particle sink (pre-existing aerosol particles) is as important as representation of nucleation, to simulate the right aerosol size distribution. In the next section the climatic impact of implementing the modified SOA scheme is investigated.

4.5.5 Change in CDNC and aerosol radiative forcing

Figure 4.16 shows the cloud droplet number concentrations (CDNC) in pre-industrial and present-day atmospheres calculated from simulation ORG (a and b) and simulation OMOD (d and e). Global annual mean CDNC changes by +15 % (+19 % in NH and +12 % in SH) in the present-day atmosphere (Figure 4.16h) and by +0.5 % (+0.7 % in NH and +0.4 % in SH) in the pre-industrial atmosphere (Figure 4.16g). In the pre-industrial atmosphere CDNC decreases over the oceans and Saharan region by up to 10 % and increases by up to 16 % over the continents (Figure 4.16g). In the present-day atmosphere except over a few oceanic pockets in the tropics (where CDNC decrease by up to 2 %), there is an overall increase in CDNC

(Figure 4.16h). The increase in present-day CDNC is particularly prominent in the northern high latitudes.

The changes in CDNC broadly follow the same spatial pattern as the changes in N50 (Figure 4.7). The biggest increments of CDNC in the present-day atmosphere are seen over the northern high latitudes. The northern high latitudes are characterised by low primary emissions at the ground level (Merikanto et al., 2009) and moderately high concentrations of anthropogenically controlled VOCs (Figure 4.5c). The relatively cleaner environment in the northern high latitudes lowers particle loss by coagulation and lowers the competition for water vapour for the activation of CCN-sized particles to cloud droplets, which in turn results in more particles growing into cloud droplets. By contrast over the Amazon rainforest, highly affected by biomass burning emissions, the increment in CDNC in simulation OMOD is highly limited.

In the pre-industrial simulations the only difference between simulations ORG and OMOD is the inclusion of B_SVOC_M and B_SVOC_I i.e. biogenic semi-volatile compounds. Consequently increments of CDNC due to enhanced growth by biogenic SVOCs (Figure 4.16g) follow same regional patterns with high concentrations of BVOCs (Figure 4.5a and b).

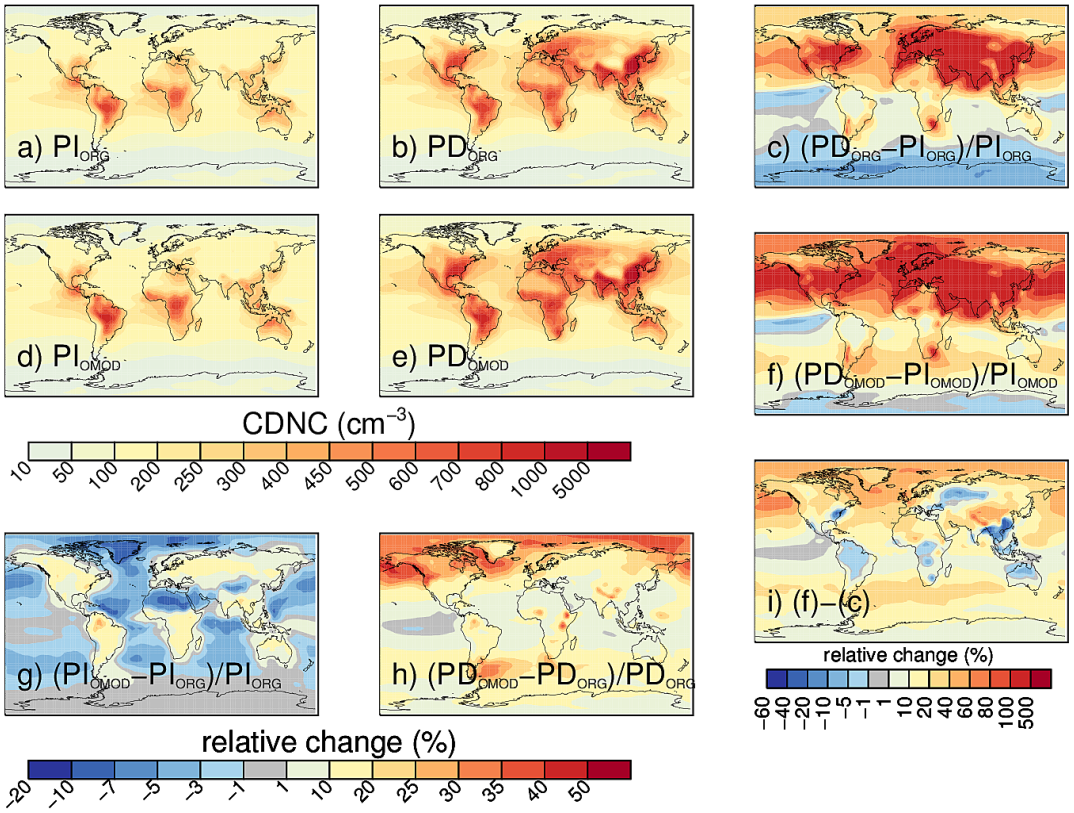

Figure 4.16: Annual mean surface-level cloud droplet number concentrations (CDNC) for a) simulation ORG in the pre-industrial atmosphere, b) simulation ORG in the present-day atmosphere, d) simulation OMOD in the pre-industrial atmosphere and e) simulation OMOD in the present-day atmosphere. The relative change in annual mean CDNC from the pre-industrial to present-day is shown in c) with simulation ORG and f) with simulation OMOD. The absolute difference between c) and f) is shown in i). Relative change in annual mean CDNC due to implementation of the new SOA-scheme is shown in g) for the pre-industrial and h) for the present-day atmospheres.

Calculations of CDNC reinforces the climatic significance of representing SVOCs in global models. Although SVOCs suppress nucleation and consequently reduces the number of small particles, they contribute to the growth of particles at the higher end of the aerosol size spectrum. Due to enhanced particle growth in areas of high SVOCs, a larger number of particles grow up to the activation diameter in simulation OMOD (compared to simulation ORG). When some of these larger particles get advected to SVOC-free regions (where there is no 'enhanced growth')

an increase in coagulation sink occurs and cause a reduction in CDNC in those regions (such as the Saharan desert and the oceans, Figure 4.16g).

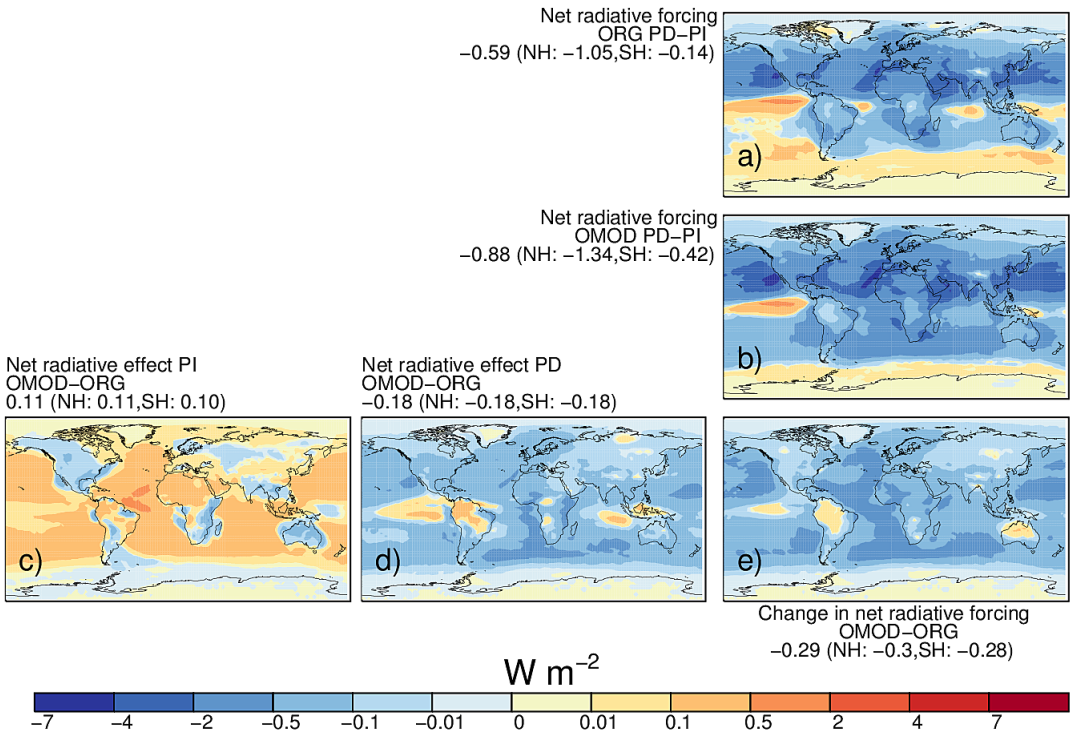

Figure 4.17: Annual mean top of the atmosphere first aerosol indirect forcing (AIF) from 1750 to 2008 after including the new SOA-scheme in GLOMAP-mode for a) simulation ORG and b) simulation OMOD. e) shows the absolute difference between a) and b) i.e. ΔAIF. Annual mean top of the atmosphere first aerosol indirect effect (AIE) after including pure biogenic nucleation in GLOMAP-mode is shown in c) for the pre-industrial and d) for the present-day atmospheres. Forcing plots correspond to the ΔCDNC plots shown in Figure 4.16. The magnitude of global annual mean AIF/AIE/ΔAIF is specified at the top of the plot. Numbers in brackets denote the annual mean values for the Northern and Southern Hemispheres respectively.

The climatic impact of the changes implemented in this study is assessed by estimating the first AIE for simulations OMOD and ORG. The +15 % change in global annual mean CDNC (in OMOD) in the present-day atmosphere translates to a radiative effect (first AIE) of -0.18 W m^{-2} (Figure 4.17d). The +0.5 % change in global annual mean CDNC (in OMOD) in the pre-industrial atmosphere translates

to a radiative effect (first AIE) of +0.11 W m^{-2} (Figure 4.17c).

Figures 4.16c and f show the relative change in CDNC between 1750 and 2008 in simulations ORG and OMOD respectively. The global annual mean CDNC change between 1750 and 2008 is 33 % with simulation ORG and 52 % with simulation OMOD. The difference in change in CDNC from 1750 to 2008 between the two simulations is shown in Figure 4.16i. Global annual mean CDNC increases by 19 % more in OMOD during the industrial period with a substantially larger increase over the NH (27 % compared to 11 % in the SH) due to greater concentrations of both biogenic and anthropogenic ox-VOCs in the continental NH. The change is driven by the 15 % increase in CDNC in the present-day (Figure 4.16h). The relative change in CDNC has a significant impact on the estimated first AIF due to anthropogenic aerosols as shown in Fig.4.17c and f.

After implementing the new scheme of SOA treatment, which includes contributions from ELVOC, LVOC and SVOC, the global annual mean first AIF due to anthropogenic aerosols is estimated to be −0.88 W m^{-2}. The change in the estimated AIF with simulation OMOD is −0.29 W m^{-2} (or a 49 % increment in negative forcing compared to simulation ORG) implying more radiative cooling by anthropogenic aerosols. The cooling is maximum in the Northern Hemisphere - particularly over the marine stratocumulus decks - where the persistent cloud cover coupled with the longitudinally transported cloud droplets from the continents result in the strongest cloud-aerosol interactions. The estimated global mean first AIF of −0.88 W m^{-2} is within the uncertainty range of the Effective Radiative Forcing due to aerosol cloud interaction (ERFaci) given by Boucher et al. (2013) (−1.2 to 0 W m^{-2}) and that given by Carslaw et al. (2013) (−0.7 to −1.6 W m^{-2}).

Introducing pure biogenic nucleation to GLOMAP-mode causes a change of +0.25

W m^{-2} in Chapter 3 (+0.22 W m^{-2} in Gordon et al., 2016). In Chapter 3 based on the high N50 concentrations simulated in the tropics, particularly over the Amazon basin, it was suggested that the estimated reduction in cooling due to anthropogenic aerosols with pure biogenic nucleation may have been overestimated. In this chapter it is shown that including SOA formation from SVOCs and anthropogenic LVOC along with pure biogenic nucleation causes a change of -0.29 W m^{-2} i.e. *offsets the reduction in cooling observed when only pure biogenic nucleation is added to the model.* The reduction in cooling with pure biogenic nucleation is driven by an increase in particle number in the pre-industrial atmosphere. By itself pure biogenic nucleation tells one side of the story about the climatic impact of SOA-producing organic compounds in the atmosphere. The other side of the story includes LVOCs and SVOCs which do not take part in nucleation but because of their high volatility affect the aerosol size distribution at larger sizes. This means in theory the contribution of LVOCs and SVOCs, however little, can produce climate-relevant particles faster (than ELVOCs can via nucleation). Thus along with nucleating ELVOCs, representation of particle growth from LVOCs and SVOCs on a global scale is a necessity when modelling the contribution of atmospheric organic compounds in producing climate-relevant particles.

4.6 Conclusion

This chapter implements and assesses the climatic impact of a SOA production scheme, devised on recent advances made in the understanding of SOA production from VOCs. The study includes extremely low volatility organic compounds that can initiate nucleation (B_ELVOC), low volatility organic compounds from biogenic sources that grow particles (including sub-3 nm clusters) via kinetic condensation (B_LVOC), low volatility organic compounds from anthropogenic sources that grow particles larger than 3 nm via kinetic condensation (A_LVOC) and semi-volatile organic compounds from isoprene, monoterpene and anthropogenic sources (B_SVOC_M, B_SVOC_I and A_SVOC) that grow particles by mass-based addition to aerosol particles. Results from this chapter show:

- In the present-day atmosphere implementing the new SOA scheme produces about 104 Tg yr^{-1} of SOA in the present-day and about 40 Tg yr^{-1} of SOA in the pre-industrial (compared to 14 Tg yr^{-1} of SOA produced both in the present-day and pre-industrial without the new SOA scheme). Of the total SOA produced in the present-day atmosphere, 61 % (about 63 Tg yr^{-1}) is anthropogenic.

- With the new SOA scheme fewer nucleation mode particles and more Aitken mode particles reach climate-relevant sizes, due to growth by ox-VOCs. In the present-day atmosphere implementing the new SOA scheme changes the global annual mean particle number concentration in the nucleation mode (including all particle with diameter < 10 nm) by -20 % and changes the number concentration of particles in the Aitken mode (including all particles with diameter between $10-100$ nm) by $+11$ %. This is also reflected in the reduction of total particle number concentration (simulated global annual mean N3 changes by -15.8 %) but the increase in number of particles above 50 nm (simulated N50 changes by $+15$ %) and increase in CDNC by $+15$ % in the present-day

atmosphere.

- In the pre-industrial atmosphere implementing the new SOA scheme changes the global annual mean particle number concentration in the nucleation mode (including all particles with diameter < 10 nm) by +2% and changes the number concentration of particles in the Aitken mode (including all particles with diameter between $10-100$ nm) by -6%. The changes to the growth of smaller particles are relatively modest in the pre-industrial atmosphere due to fewer primary particles (which are larger than nucleation mode particles) taking up the available ox-VOCs for their growth. Consequently the changes in particle number concentrations are modest compared to the present-day. Simulated global annual mean N3 changes by -9 %, N50 changes by +2.8 % and CDNC changes by +0.5 % in the pre-industrial atmosphere.

- Nucleation of B_ELVOC and initial particle growth by kinetic condensation of B_LVOC are extremely critical for production of nucleation mode particles. Aerosol number concentrations are most sensitive to the amount of nucleating B_ELVOC and tuning the concentrations of this ox-VOC alone can produce a wide range of total aerosol number concentrations in the model.

SVOCs contribute to the growth of larger particles, increasing primarily the average diameter of particles. Introducing SVOCs and anthropogenic LVOC in the model causes the mean dry diameter of the Aitken mode particles to change by +16 % and that of the accumulation mode to change by +10 %. In contrast the nucleation mode mean dry diameter changes by -1 %. Thus the new SOA scheme favours the growth of larger particles. The loss of nucleated particles with the new SOA scheme are attributed to increased condensation sink due to more particle growth, lack of available vapours to condense on smaller particles due to competition from larger particles or to increased loss

by coagulation with larger particles.

- Comparing the monthly mean modelled and observed total particle number concentration (Figure 4.13) shows the variation in modelled N3 between 3 simulations (ORG_BioOxorg, ORG, and OMOD) having different representation of processes leading to SOA production is less than the difference between model and observation. Based on the consistent underestimation at some sites (such as at Puy De Dome, Mace Head and Neumayer) especially in the winter months, the exaggerated seasonal pattern simulated by the model (such as at Hyytiala) and the overestimation by simulation ORG (such as at Trinidad Head and Po Valley) it is suggested that the model-observation agreement may be improved by better representing pre-existing aerosol particles, which peak in the winter months characterised by low temperatures and reduced convection.

- The net radiative forcing from pre-industrial to present-day due to first AIF is -0.88 W m^{-2}. The change in net AIF is -0.29 W m^{-2}, driven by a +15 % change in present-day CDNC. Thus implementing the new SOA scheme exerts a larger and opposite change in AIF than that exerted by including *only* pure biogenic nucleation in the model (+0.25 W m^{-2} in Chapter 3). This means including ELVOCs, LVOCs and SVOCs offsets the estimated reduction in radiative cooling by anthropogenic aerosols which results when only ELVOCs are included in GLOMAP-mode.

  The large negative change in AIF with simulation OMOD implies alongside the contribution of ELVOCs in nucleation, global models need to account for the contribution of the non-nucleating organic compounds (LVOCs and SVOCs) to atmospheric SOA. In particular models need to account for the differential contribution of ox-VOCs to aerosol particles of various size ranges in the atmo-

sphere which is governed by the volatility of the ox-VOCs. Nucleation accounts for small particles in the atmosphere which have to survive for a longer time in order to grow to CCN sizes, increasing their loss probability. Thus simulating the right number of particles produced from nucleation becomes irrelevant for estimating the climatic impact if the growth at larger sizes is not realistically accounted for in models. Similarly simulating the right total particle number concentration (which is most sensitive to nucleating ELVOC and as seen in Figure 4.11 can be made to span a wide range by tuning B_ELVOC) is irrelevant from a climatic impact perspective if the aerosol size distribution is not simulated realistically.

In conclusion atmospheric organic compounds of higher volatility that do not nucleate can affect the aerosol size distribution at larger size ranges and thereby make a significant difference to the net production of climatically relevant particles both in the pre-industrial and present-day atmospheres. This study approximates LVOCs to be oxidation products of terpenes producing about 14 Tg yr^{-1} of SOA globally, SVOCs to be oxidation products of terpene and isoprene producing about 26 Tg yr^{-1} SOA globally and assumes oxidation products of anthropogenic VOCs to produce equal amounts of LVOCs and SVOCs (total about 63 Tg yr^{-1} of SOA globally annually). These estimates are likely to be at the lower end of the range. Future observational and laboratory studies need to be directed towards understanding and quantifying particle growth from the low and semi-volatile organic compounds in the atmosphere. However given the vast number of organic compounds present in the atmosphere, most of them SVOCs, it is extremely difficult if not impossible to achieve a realistic estimate of LVOCs and SVOCs from bottom-up laboratory measurements. The next chapter explores a large uncertainty space for each of the ox-VOCs introduced in this chapter with the aim to identify plausible parameter space for each in the current SOA production scheme.

Chapter 5

Perturbed parameter ensemble study on secondary organic aerosol formation

5.1 Introduction

Nearly 20−50 % of lower tropospheric fine aerosol mass in the continental mid latitudes and almost 90 % in the tropics is organic in nature (Kanakidou et al., 2005). The major fraction of organic aerosol has been found to be secondary (Zhang et al., 2007; Jimenez et al., 2009) formed as a result of atmospheric oxidation of volatile organic compounds (VOC). A comprehensive characterisation of atmospheric VOCs and hence their reaction pathways leading to SOA formation and products has not been possible due to tens of thousands of VOCs that have been identified in the atmosphere and yet more that still remain to be detected (Goldstein and Galbally, 2007). For those precursor gases that have been identified, questions remain as to the extent of their conversion to SOA, accurate characterisation of their emission sources, the critical concentrations and conditions at which SOA formation takes place. The picture is further complicated by the interaction between VOC

precursor gases, availability of oxidants, chemistry of the products under different atmospheric conditions, transport from surrounding regions, topography and meteorological conditions all of which impact the formation processes of SOA.

From a modelling perspective, in addition to the uncertainty in SOA formation cited above, a further challenge is to adequately parameterise laboratory and observational results, experimental uncertainties and incorporate them in a complex global model. Studies like Heald et al. (2005); Johnson et al. (2006); Spracklen et al. (2011b) show models have consistently and significantly underestimated SOA concentrations in different parts of the atmosphere and different regions of globe compared to measurements. Models traditionally use experimentally observed reaction rate constants and yields to produce highly oxidised VOCs from reactions between precursor VOCs (usually monoterpene) and common atmospheric oxidants. These highly oxidised VOCs in turn undergo a series of microphysical processes and produce a global SOA field in the model. This approach of estimating global SOA budget is referred to as 'bottom-up' and to date models using the bottom-up approach predict a SOA budget ranging between $12-70$ Tg yr^{-1}, at the lower end of the total SOA uncertainty range (Kanakidou et al., 2005). In a study evaluating 31 chemical transport models and general circulation models, Tsigaridis et al. (2014) found the simulated global SOA source strength covers a range of $13-120$ Tg yr^{-1} with 50 % of models simulating less than 19 Tg yr^{-1} SOA. A second, 'top-down' approach to estimate the total atmospheric SOA is based on the eventual fate of total known precursor emissions (Goldstein and Galbally, 2007) and are between $120-1820$ Tg yr^{-1} (Hallquist et al., 2009). The basis of top-down estimates is that all emitted atmospheric VOCs must eventually be removed from the atmosphere by either dry deposition, oxidation to CO and CO_2 or conversion to SOA. Thus the top-down estimate of SOA is a mass-balance estimate depending on estimates of total emission of VOCs, mass of VOC removed by dry-deposition and mass of

VOC removed by oxidation to CO and CO_2. The huge difference in estimates using these two approaches suggest laboratory experiments are unable to capture the full oxidative pathways that precursor gases undergo in the atmosphere and as a result underestimate SOA yields (Hallquist et al., 2009). Further, global models usually rely upon terrestrial sources of VOCs to produce SOA whereas several studies have reported significant emissions of VOCs from oceans (Kettle and Andreae, 2000, Meshkhidze and Nenes, 2007). With potential missing sources of VOCs that produce SOA and the inability of laboratory experiments to capture the full oxidative chemistry in the atmosphere, global models using the bottom-up approach will continue to underestimate SOA in comparison to other methods of SOA estimation.

In Chapter 4 a modified scheme was implemented to produce SOA from VOCs in the model. The scheme is based on the recent advances in the understanding of the roles that oxidation products of biogenic and anthropogenic VOCs (ox-VOCs) play in producing SOA. The new scheme (called OMOD in Chapter 4) essentially includes semi-volatile organic compounds in the model (B_SVOC_M, B_SVOC_I and A_SVOC) which undergo mass-based partitioning, along with low volatility compounds that condense kinetically (B_LVOC and A_LVOC) and extremely low volatility compounds that nucleate (B_ELVOC). OMOD increased the number concentration of CCN-sized aerosol particles (preferentially over smaller particles), resulting in an increase in the net radiative cooling over the industrial period by -0.29 W m^{-2}, showing the representation of SVOCs is important to quantify in global models.

However often increasing the complexity of a model or tuning a model to finer details observed in laboratory experiments is not desirable. A frequently asked question is therefore, how much of the complexity of SOA formation processes is necessary to represent in global models (Shrivastava et al., 2016). The SOA scheme described in

Chapter 4, though relatively simple, has resulted in including 3 additional gaseous phase advected tracers and 32 extra diagnostics to the model used in Chapter 3. While this does not slow down the model appreciably, it is still important to to know which of the ox-VOCs are more important than others from a modelling perspective. Firstly, increasing model complexity inevitably requires more computational resources, more runtime, all of which need to be considered carefully by modellers. Secondly, GLOMAP is used as a part of the chemistry-aerosol-climate model UKCA (United Kingdom Chemistry and Aerosols) which is a sub-model within the numerical model UM (Unified model). The UM is used for predictions over a range of spatial systems starting from convective scale to Earth system modelling and temporal timescales including nowcasting to centennial. Structural and process based uncertainties related to a large number of aspects are an integral part of large models that inherently make it impossible for the model to be right for the right reasons. Thus (potential) addition of more complex chemistry to the aerosol scheme (GLOMAP) within such a large scale model might not be always be optimum in the long run when the bigger picture is considered.

Further every added complexity increases the problem of equifinality in the system (Lee et al., 2016). Equifinality refers to multiple paths of reaching the same end state. The model's estimate of particle number (and anthropogenic aerosol forcing which is dependent on simulated particle number) is an outcome of several model parameters and their associated uncertainties, some of which compensate for each other. Fine-tuning any one aspect of the model (for example, the nucleation scheme in the model) to greater details to get the best model-observation comparison for any one output (for example, the simulated total particle number concentration) while keeping the other aspects unchanged might therefore make the model more wrong than right (with respect to other outputs such as mass of aerosol simulated). Such fine-tuned observationally constrained models give the impression of low aerosol un-

certainty and model robustness but predict a large range of aerosol forcing (Lee et al., 2016). Lee et al. (2016) concluded equifinality is less consequential if the model is used to explore conditions that are similar to what it has been constrained to (such as, simulating the present-day atmosphere using inputs from present-day inputs) but reduces its ability to make robust predictions. In other words, added complexities in models lower the confidence with which models can reproduce the pre-industrial atmosphere and thereby introduce more uncertainty in the quantification of the effect of anthropogenic aerosols.

With new discoveries of particle formation and SOA production pathways, as global models move towards more complexity, it is important to ask the questions,

1. Are we moving any closer to the reduction in anthropogenic aerosol forcing uncertainty by increasing the complexity of SOA formation pathways in the model?

2. Atmospheric organic molecules from single or multi-stage oxidation reactions of precursor VOCs (i.e ox-VOCs) are known to span a large range of volatility. From a global modelling perspective, which ox-VOC interactions are necessary to simulate a realistic number concentration of particles along with the mass concentration of SOA? Which SOA production pathways (from ox-VOCs) are not crucial to account for?

3. How do additional complexities in chemical pathways of particle formation (which aim towards better model-observation agreement of particle number concentration), affect the model estimate of atmospheric SOA mass?

The aim of this study is to find answers to questions 2 and 3. The study explores the effect of varying amounts of ox-VOCs on modelled aerosol number and mass using an ensemble of model runs. These oxidised organic compounds are produced from oxidation of traditional precursor gases and contribute to different size

regimes of aerosol formation and growth processes via nucleation, growth by kinetic condensation and growth by partitioning (as described in Chapter 4). In this work a large uncertainty space associated with ox-VOCs - that could be attributed to uncertainties in emissions, chemical pathways and interactions - is explored and the significance of each ox-VOC **and** their combined effect on modelled mass and number concentrations are assessed. The primary aim is to understand the responses of N3, N50 and OA to different ox-VOC parameter combinations and identify parts of parameter space that give the best (or plausible) agreement with currently available observations and to identify parameter combinations which are likely give a range of equifinal models with respect to either number or mass concentrations.

5.2 Perturbed Parameter Ensemble

The modelled number and mass concentrations of particles resulting from the condensation of ox-VOCs depend on the concentration of each ox-VOC as well as the competing and compensating effect of different ox-VOCs. In Chapter 4, the effect of increasing the concentrations of each category of ox-VOC and their absence were studied through one-at-a-time sensitivity tests. To remind the reader, the six categories of ox-VOCs implemented in Chapter 4 are: B_ELVOC which are biogenic compounds of extremely low volatility and take part in nucleation, B_LVOC which are biogenic compounds of low volatility and take part in growth of all particles including sub-3 nm clusters by kinetic condensation, B_SVOC_M which are semi-volatile biogenic compounds derived from monoterpenes and take part in particle growth by mass-based partitioning, B_SVOC_I which are semi-volatile biogenic compounds derived from isoprene and take part in particle growth by mass-based partitioning, A_LVOC which are anthropogenic compounds of low volatility and take part in the growth of all particles by kinetic condensation, A_SVOC which are semi-volatile anthropogenic compounds and take part in particle growth by mass-based partitioning. In Chapter 4 it was noted that by tuning B_ELVOC alone, the model can account for a large range of total particle number concentrations (N3). However Chapter 4 also showed that accounting for the contribution of SVOCs to particle growth in the atmosphere is important as SVOCs have a significant impact on the budget of climate-relevant sized particles (N50).

In order to capture the effect of each ox-VOC as well as the effect of their interaction on the simulated aerosol field, a perturbed parameter ensemble (PPE) is designed and the uncertainty space for atmospheric SOA explored. Several PPEs of GLOMAP-mode have been extensively used to analyse model uncertainty (Lee et al., 2012, 2013; Carslaw et al., 2013; Hamilton et al., 2014; Regayre et al., 2015;

Lee et al., 2016). In this study within each PPE member (PPEM) six parameters are perturbed simultaneously. The simultaneous perturbations allow us to study the effects of the ox-VOC interactions on modelled outputs.

The steps followed to produce the PPE in this chapter are as follows:

1. Selection of parameters:-

   The aim of this chapter is to find the best parameter setting for the six ox-VOC categories implemented as a part of the modified SOA scheme in Chapter 4. Therefore, the yields of bimolecular oxidation reactions in the model which generate the ox-VOCs (B_LVOC, B_SVOC_M, B_SVOC_I, A_LVOC and A_SVOC) constitute the perturbed parameters. Perturbing the yield of ox-VOCs from VOC oxidation reactions is essentially same as perturbing VOC emissions for some ox-VOC such as B_SVOC_I, the only ox-VOC produced from isoprene. The advantage in perturbing the yield of ox-VOCs instead of total emissions of VOCs is that it makes each ox-VOC independent of the other. This is particularly useful when ox-VOCs are produced from oxidation of the *same* VOC (such as A_LVOC and A_SVOC or B_LVOC and B_SVOC_M). By varying the yield of ox-VOCs rather than the emission of VOCs, any perturbation applied to one ox-VOC does not affect the production or loss of the others. The perturbations applied to the 5 ox-VOCs mentioned above are absolute i.e. the absolute values of yields are changed in each PPEM. For B_ELVOC, a scaling factor is introduced that scales the concentrations of oxidised compounds taking part in biogenic nucleation. The parameters and their respective roles in SOA formation in the model are depicted in Figure 5.1.

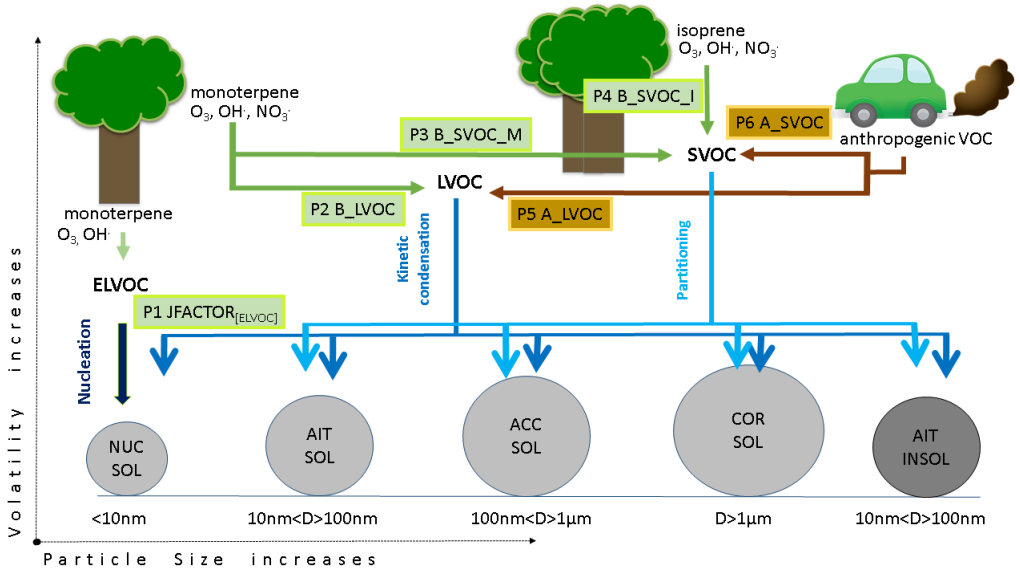

Figure 5.1: Schematic showing the SOA formation scheme in GLOMAP-mode (as implemented in Chapter 4) and the six ox-VOCs (products of photochemical oxidation of emitted VOCs that eventually produce SOA) whose yields from precursor VOCs are perturbed in this study. B_ELVOC, B_LVOC, B_SVOC_M and B_SVOC_I are ox-VOCs produced from the oxidation of biogenic VOCs and highlighted in green. A_LVOC and A_SVOC are ox-VOCs produced from the oxidation of anthropogenic VOCs and highlighted in yellow. The schematic shows the precursor gases and oxidants that react to produce these ox-VOCs, their relative volatility (ELVOC<LVOC<SVOC) and the mechanism (nucleation for ELVOC, kinetic condensation for LVOCs and mass-based partitioning for SVOCs) by which they add to the condensed phase (represented here by the five modes:- nucleation soluble, Aitken soluble, accumulation soluble, coarse soluble and Aitken insoluble modes).

2. Determining the range of perturbation for each parameter:-

   To explore a wide range of SOA production scenarios in the model, the fixed global yield of each ox-VOC is perturbed from zero to an upper range of 20 times the default for biogenic parameters B_LVOC, B_SVOC_M, B_SVOC_I and 5 times the default for anthropogenic parameters A_LVOC and A_SVOC. The concentrations of B_ELVOC participating in nucleation are varied with a factor of 0 to 10. These ranges are chosen after comparing results of one-at-a-time tests to observations. The range is chosen to encompass emission uncertainties such as uncertainties in estimates of precursor gas emission (such as monoterpene or isoprene for biogenic sources), uncertainties in the estimates of anthropogenic VOC, structural uncertainty such as omission of VOCs that

are known to have similar SOA producing capabilities as traditional precursor gases (such as sesquiterpenes), parameter uncertainty such as yields of production of the ox-VOCs from the precursor gases, process based uncertainty such as uncertainty in nucleation mechanism, potential contribution to SOA by multi-stage oxidation products of VOCs (in GLOMAP-mode only single stage oxidation products are represented), uncertainty in SOA due to the representation of mass-based partitioning in the model (which does not involve feedback from the aerosol phase i.e. there is no evaporation of partitioned ox-VOC back to gaseous phase). Overall while selecting the parameter ranges preference is given to overestimation of the the range to encompass any identified/unidentified uncertainty related to a specific pathway of SOA formation rather than to shrink the parameter space down and omit an useful part.

It should be noted here that the yields of the bimolecular reactions producing the 5 ox-VOCs are specified via the ASAD chemical integration package (Carver et al., 1997) that GLOMAP uses to solve time-dependent chemical equations (Spracklen et al., 2005a). The yield of a product from a chemical reaction is specified to ASAD as the fraction of reactants that contribute to the particular reaction product. For example, for a bimolecular reaction $A + B = C + D$ that proceeds with the rate k, the rate of production of C is $dC/dt = fraction \times k \times A \times B$. Although setting a value to $fraction$ is a way to specify the yield of a particular product, ASAD deals with the fractions set for multiple products (C and D in the above example) independent of each other. Therefore setting $fraction$ to be more than 1 (or 100 %) is an effective way of varying not just the yield of the product (ox-VOC) but also the total reactant (VOC) concentration. A yield above 100 % in the bimolecular reactions should be interpreted as an increase in the total concentration of reactants. The parameters and chosen ranges are tabulated below.

		Perturbed Parameter	Perturbation Range		
ox-VOC	Produced from	Default yield value (in %)	minimum	maximum	Perturbation
B_ELVOC	Monoterpene, O_3	3.3	0	10×default	scaled
	Monoterpene, $OH^{\cdot}$	1.2	0	10×default	scaled
B_LVOC	Monoterpene, O_3	13	0	20×default	absolute
	Monoterpene, $OH^{\cdot}$	13	0	20×default	absolute
	Monoterpene, $NO_3^{\cdot}$	13	0	20×default	absolute
B_SVOC_M	Monoterpene, O_3	13	0	20×default	absolute
	Monoterpene, $OH^{\cdot}$	13	0	20×default	absolute
	Monoterpene, $NO_3^{\cdot}$	13	0	20×default	absolute
B_SVOC_I	Isoprene, O_3	1.5	0	20×default	absolute
	Isoprene, $OH^{\cdot}$	1.5	0	20×default	absolute
	Isoprene, $NO_3^{\cdot}$	1.5	0	20×default	absolute
A_LVOC	Anthropogenic VOC, $OH^{\cdot}$	50*	0	5×default	absolute
A_SVOC	Anthropogenic VOC, $OH^{\cdot}$	50*	0	5×default	absolute

Table 5.1: List of six ox-VOCs whose productions are simultaneously perturbed to produce the ensemble of model simulations used in this study, the precursor gases that take part in the binary reactions producing ox-VOCs, default values of ox-VOC yields in the binary reactions and the range of perturbation used for each ox-VOC. The last column indicates how the perturbation for each parameter is implemented in the model: 'absolute' indicates the default yield value is replaced by the perturbed value, 'scaled' indicates the default yield value is scaled by the perturbed value. *For AVOCs, the 'yield' is a scaling factor applied to divide the total AVOC into A_LVOC and A_SVOC.

3. Design of experiments:-

   The aim of this study is to explore the entire 6-D space defined by the ranges of the six ox-VOC parameters tabulated above. To sample the space sufficiently an ensemble of 60 simulations (10 for each dimension) is produced. The parameter combinations for each PPEM is generated using the maximin Latin Hypercube Sampling (LHS) method. The effectivity of LHS as a method to create sampling design has been discussed in Lee et al. (2011), Lee et al. (2013). LHS samples the entire 6-D parameter space and creates a space-filling

design of 60 combinations of parameter setting such that the distance between any two points in the 6-D space is maximised. The design of experiments used in study is shown in Figure 5.2.

Figure 5.3 shows the relative variation of ox-VOCs in each simulation. Each subplot in the figure describes the parameter values for an ensemble member. The relative position of each axis represents the relative proportion of each ox-VOC in the parameter setting for that PPEM. The centre of the radar plot is the range minima for each of the six parameters or axes. The periphery represents the maxima of the parameter range. The shape of the hexagon indicates which parameter values lie towards the low end of their range and which ones lie towards the higher end.

4. Running GLOMAP-mode:-

   Sixty model simulations each with a different combination of the six parameters (Figure 5.3) is produced for the year 2008. Except for the perturbations applied to the six ox-VOCs, the model is identical to that described in Chapter 4. Three model outputs, the number concentration of particles with diameter greater than 3 nm (N3 in cm^{-3}), the number concentrations of particles with diameter greater than 50 nm (N50 in cm^{-3}) and total mass concentration of organic aerosol produced (OA in $\mu g\ m^{-3}$) are analysed from the PPE to compare the 60 simulations against each other and against available observations.

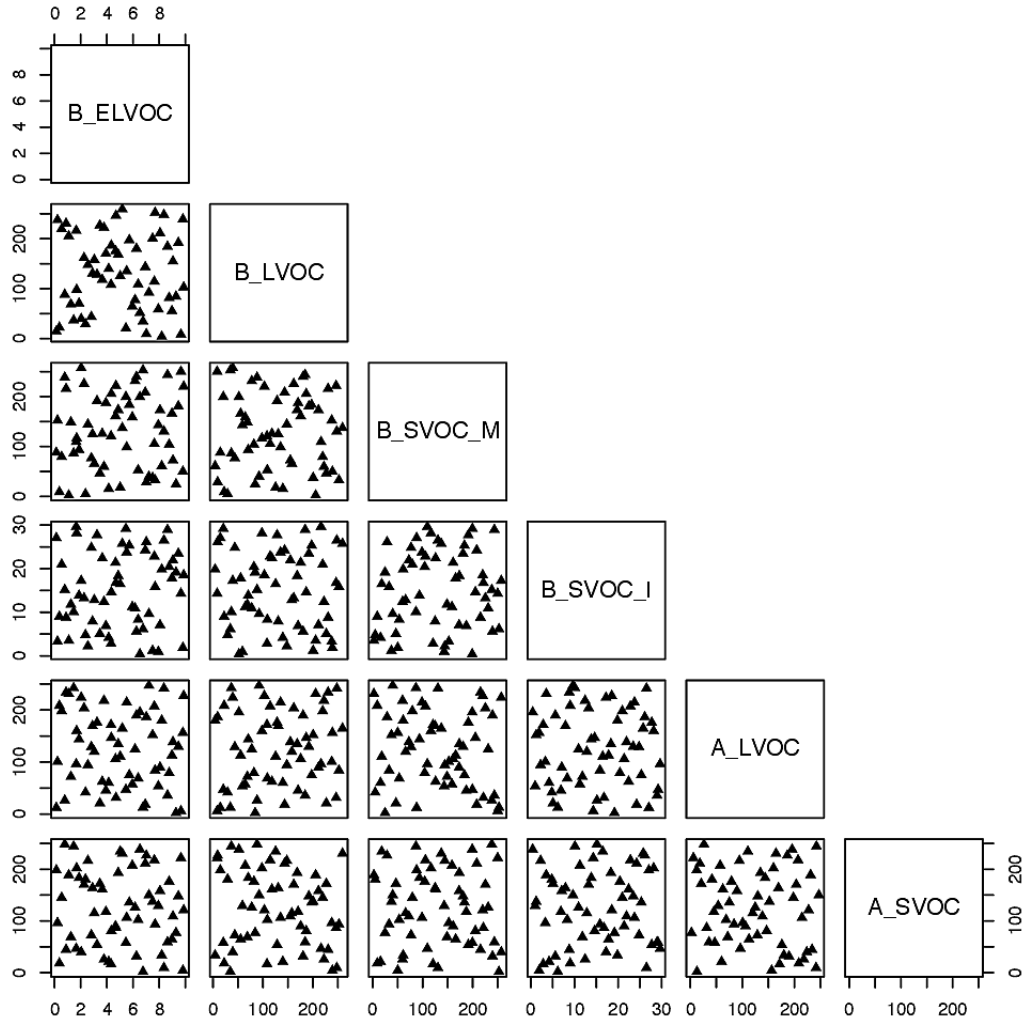

Figure 5.2: The 6-D space-filling design generated by the maximin Latin Hypercube Sampling (LHS) depicted in 2-D. Each ox-VOC constitutes a dimension of the parameter space explored in this study. Each subplot in the scatter plot matrix shows the position of the 60 simulations in a 2-D parameter space i.e. shows a 2-D slice of the 6-D parameter space. The x- and y-axes for a subplot show the total range of reaction yields (in %) over which each of the two parameters (as indicated by the plot labels at the top and right for each subplot respectively) is perturbed in the ensemble. The LHS maximises the distance between any two points in a multi dimensional parameter space, ensuring the best coverage of the 6-D parameter space by the ensemble. Each point represents a simulation within the ensemble and the plot shows the combination of parameters used to produce the ensemble, fills all corners of the parameter space.

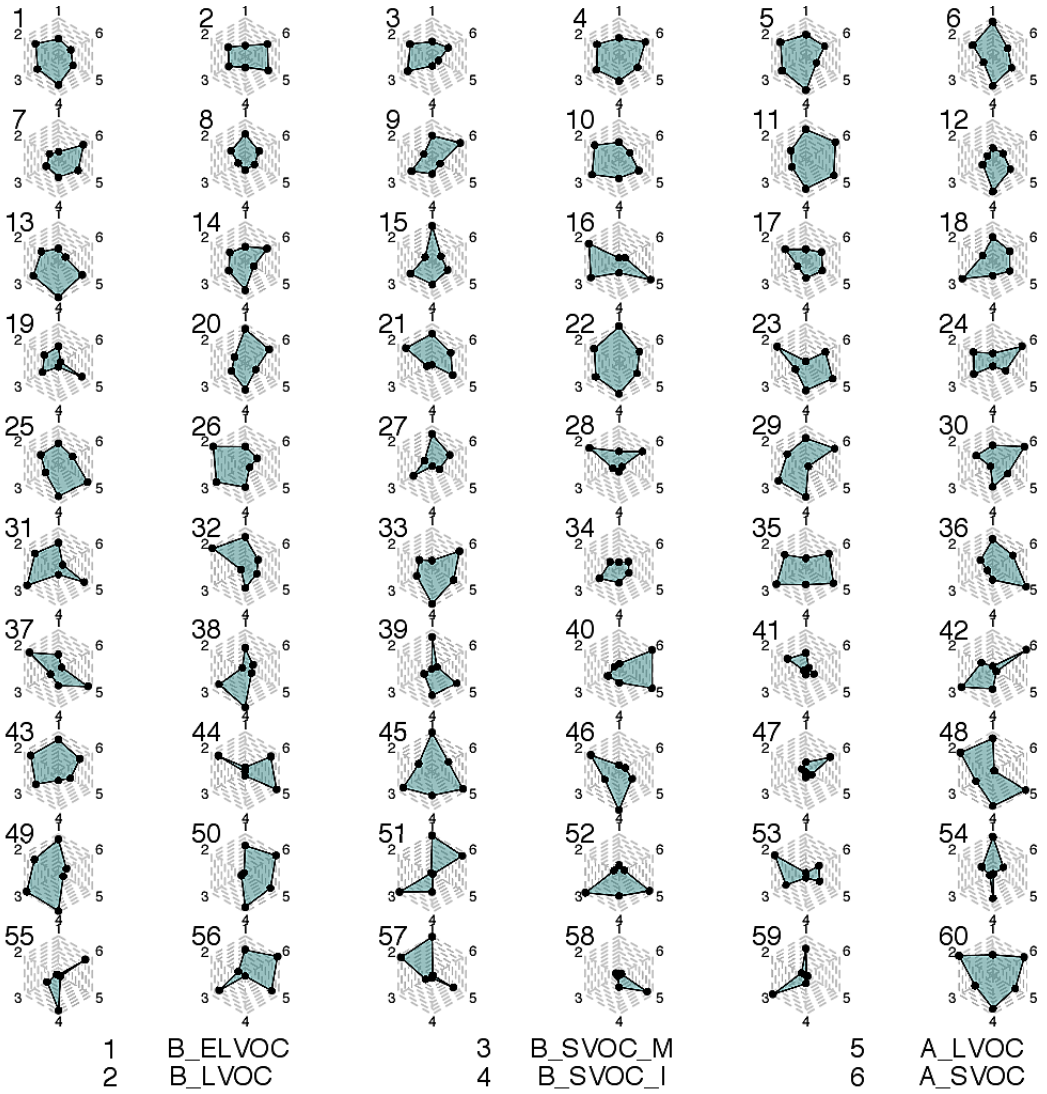

Figure 5.3: The relative variation of the six perturbed parameters (in %) for each ensemble member (numbered 1 to 60). Each hexagon (gray dashed area) represents the entire 6-D parameter space and the position of the black dots show the position of each parameter within its range for the specific ensemble member. The dots are joined and shaded green for easy identification of explored parameter space in each ensemble member. Counter clockwise from top, the black dots represent parameter settings for B_ELVOC, B_LVOC, B_SVOC_M, B_SVOC_I, A_LVOC and A_SVOC respectively. Example interpretation: in simulation 19 (fourth row, 1st hexagon) B_SVOC_I and A_SVOC concentrations are towards the lower ends of the respective ranges being explored for each of them while concentrations of A_LVOC is towards the high end of the A_LVOC range.

5.3 Results

5.3.1 Variation of SOA mass across the ensemble

Figure 5.4 depicts the total global mass of SOA produced from the addition of VOCs (by kinetic condensation or mass-based partitioning) in each ensemble member. As a result of simultaneously perturbing the six ox-VOCs within their pre-defined uncertainty range (as specified in Table 5.1), the mass of SOA produced from ox-VOCs ranges from 220−850 Tg yr^{-1}. In Chapter 4 the inclusion of additional sources of ox-VOCs in the model led to an increase in simulated SOA from 14 Tg yr^{-1} (typical GLOMAP-mode estimate, Mann et al., 2010) to 104 Tg yr^{-1} showing the low estimates of simulated SOA is a result of underestimated contributions from ox-VOCs. In this study, the parameter combinations for ox-VOC yields are prescribed after evenly exploring the entire 6-D parameter space. As a result ox-VOC yields within the ensemble members are not limited by laboratory-derived yields resulting in higher (compared to 104 Tg yr^{-1}) SOA production across the ensemble. That all of the ensemble members simulate more SOA than that simulated with experimental yields in Chapter 4, is a result of the random space-filling experimental design used to build the ensemble and does not impact the conclusions of this study (which are based on the competing and contrasting effects of individual ox-VOCs).

The minimum mass of SOA from ox-VOCs is produced in PPEM 47 and the maximum in PPEM 60. In PPEM 47 contribution from B_LVOC, B_SVOC, A_LVOC and A_SVOC are, 13 %, 18.2 %, 12.9 % and 55.8 % respectively. In PPEM 60 the contributions are 30 %, 38.2 %, 13.2 %,18.5 % respectively. The range of produced SOA covered by the ensemble is within the uncertainty range of SOA (12−1820 Tg yr^{-1}) and higher than the bottom-up estimates given by model based on laboratory-derived yields (12−70 Tg yr^{-1}). 50 % of the ensemble members produce more than

535.5 Tg yr^{-1}. Within the ensemble, the median contribution of biogenic ox-VOCs to SOA is 69 % and the median contribution of anthropogenically controlled ox-VOCs to SOA is 31 %. In 7 simulations (PPEMs 1, 3, 17, 24, 28, 30 and 34) anthropogenically controlled VOCs produce more than 50 % of SOA as a result of condensation or partitioning. In the rest of the ensemble, SOA from biogenic ox-VOCs dominate (contributing upto 97 % of the total SOA in PPEM 7). Figure 5.4 shows that several different combinations of ox-VOC yields can produce similar mass of SOA and although the yields are varied over a factor of 20, the total global mass of SOA produced varies only by a factor of 4 for the entire parameter space explored.

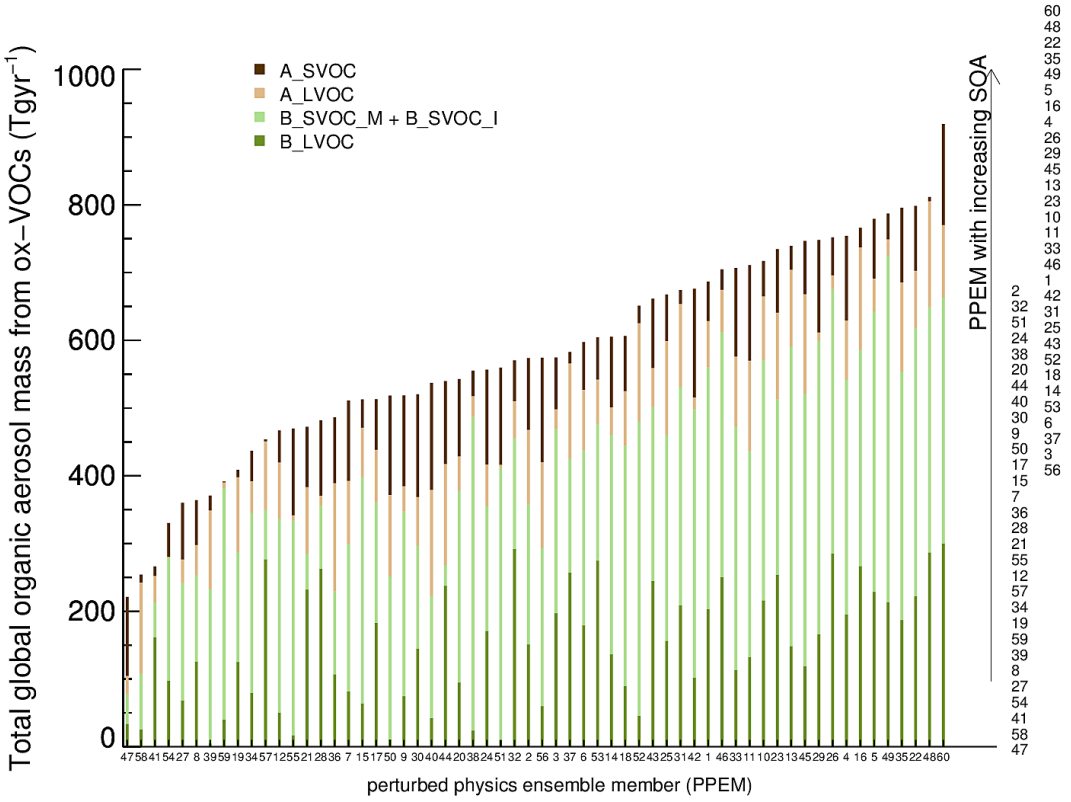

Figure 5.4: Total global SOA produced by each of the ensemble member. The ensemble members on the x-axis are ordered according to increasing values of total global SOA and the order is re-printed on the right hand side of the plot. The minimum contribution of ox-VOCs to SOA is 220 Tg yr^{-1} produced by PPEM 47 and the maximum contribution is 850 Tg yr^{-1} produced by PPEM 60.

Within the ensemble maximum SOA is produced from biogenic semi-volatile ox-VOCs (B_SVOC_M + B_SVOC_I) which are formed from monoterpene and isoprene oxidation (light green bars in 5.4). However in PPEM 44, where B_SVOC contributes the least (5 % of total SOA from ox-VOCs), total global SOA production is still considerable (517 Tg yr^{-1}). This shows B_SVOC is an important but not a limiting factor for SOA production. The relative contribution of low and semi-volatile biogenic ox-VOCs (B_LVOC + B_SVOC) lie between 31 % (PPEM 47) to 97 % (PPEM 59) of total SOA within the ensemble producing 220.6 and 338.6 Tg yr^{-1} of SOA respectively.

As seen in Figure 5.4 several combinations of parameter setting can lead to similar estimates of total global mass of SOA. Similar magnitudes of any particular ox-VOC can be associated with a high or low production of SOA within the ensemble. The simulated SOA mass in any ensemble member is therefore a result of the co-variation of all six ox-VOCs rather than the effect of any one ox-VOC. The next section looks into the global distribution of particle number and mass concentrations of total organic aerosol simulated by each combination of parameter setting (i.e. each ensemble member).

5.3.2 Variation in the global distribution of modelled N3, N50 and total OA across the ensemble

The impact of gaseous ox-VOCs on atmospheric aerosol concentrations varies across the globe depending on the spatial distribution of the precursor VOCs and meteorological conditions. This section looks at the spatial variability in N3, N50 and OA simulated by the 60 parameter combinations. The reader may be reminded here

that in the model set-up used in this study only the amount of each gaseous phase ox-VOC, condensing or partitioning to the aerosol phase to form SOA, is tracked. Once in the aerosol phase SOA sourced from ox-VOCs is not tracked separately from primary organic matter (POM). We refer to the total organic component in the aerosol phase (POM+SOA) as organic aerosol (OA). Since all the perturbed simulations have identical primary emissions (POM) and identical ageing mechanism to produce SOA from POM, any change in OA can be attributed to changes in SOA from ox-VOCs and in turn can be attributed to the changes changes in the parameter combinations in this study.

Figure 5.5 shows the anomaly in global distribution of total OA concentration within the ensemble with respect to the ensemble mean. The subplots are arranged in order of increasing global mean OA and labelled according to their simulation number (numbered 1 to 60) within the ensemble. As the primary sink for ox-VOCs is addition to the particle phase, the different combination of yield parameters for the production of ox-VOCs are reflected in the amount of SOA produced from their condensation or partitioning. Figure 5.6 (Figure 5.3 rearranged in the same order as simulations in Figure 5.5) depicts the combination of parameter values that have resulted in the global distributions.

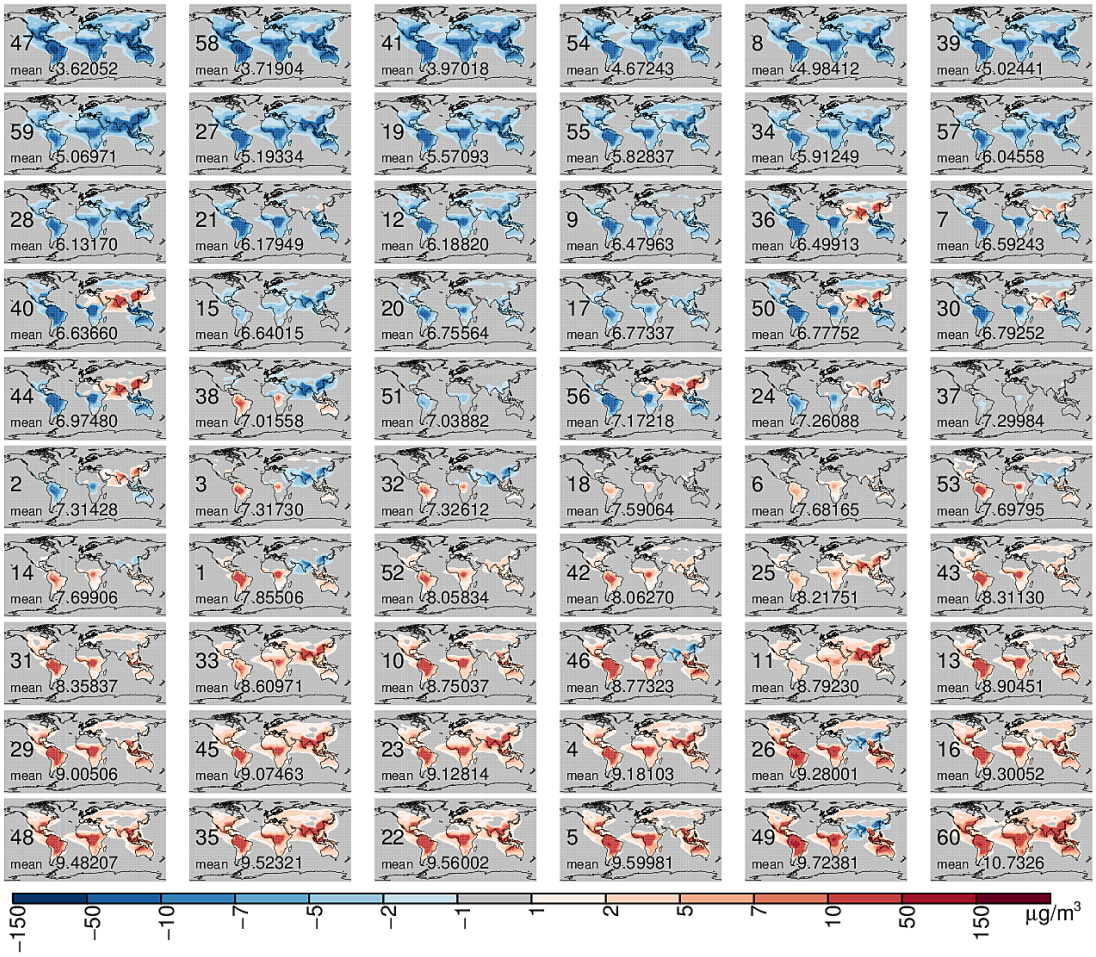

Figure 5.5: Anomaly of global organic aerosol mass (OA in μg m^{-3}) produced within the ensemble. Each subplot shows the anomaly of an ensemble member (numbered between 1 and 60) from the ensemble mean OA. The global mean OA for each subplot is printed. The subplots are arranged in order of increasing global mean OA with PPEM 47 producing the least mass of organic aerosol and PPEM 60 producing the maximum.

Figures 5.5 and 5.6 show, within the parameter space explored in this study, for global models to simulate higher (than the typical 12−70 Tg yr^{-1}; Kanakidou et al., 2005) mass of SOA, significant contribution from most (if not all) ox-VOCs (representing different sources and volatility groups of organic compounds) are necessary. Within the parameter space explored in this study global mean OA concentration varies by a factor of 3 ranging from 3.6 to 10.7 μg m^{-3}. The ensemble member producing the highest mass concentration of organic aerosol (PPEM 60 with global mean OA = 10.7 μg m^{-3}) has moderate to high yields of all the ox-VOCs: nucleat-

ing B_ELVOC is produced at about 15 % yield with B_LVOC at 259 % producing 255 Tg yr^{-1} of SOA, B_SVOC_I at 25 % and B_SVOC_M at 137 % together producing 324 Tg yr^{-1} of SOA, A_LVOC at 164 % producing 112 Tg yr^{-1} of SOA and A_SVOC at 230 % producing 157 Tg yr^{-1}) of SOA. With all the ox-VOCs contributing significantly to total SOA, the model produces 850 Tg yr^{-1} which just about reaches the middle of the SOA uncertainty range estimate of $12-1820$ Tg yr^{-1} (Spracklen et al., 2011b). Whether or not PPEM 60 simulates a *realistic* SOA mass is assessed in later sections where the ensemble is compared to observations. Here PPEM 60 may be used as an example to understand what magnitude of yields of ox-VOCs is required to produce 850 Tg yr^{-1} in the same model that simulates 14 Tg yr^{-1} (model without anthropogenic and semi-volatile organic compounds as in Chapter 3) and 140 Tg yr^{-1} (model with default parameter settings as in Chapter 4). Figure 5.6 demonstrates that within the 6-D parameter space explored, contributions from multiple ox-VOC categories (as implemented in Chapter 4) is necessary in GLOMAP-mode to simulate higher (than current) SOA production.

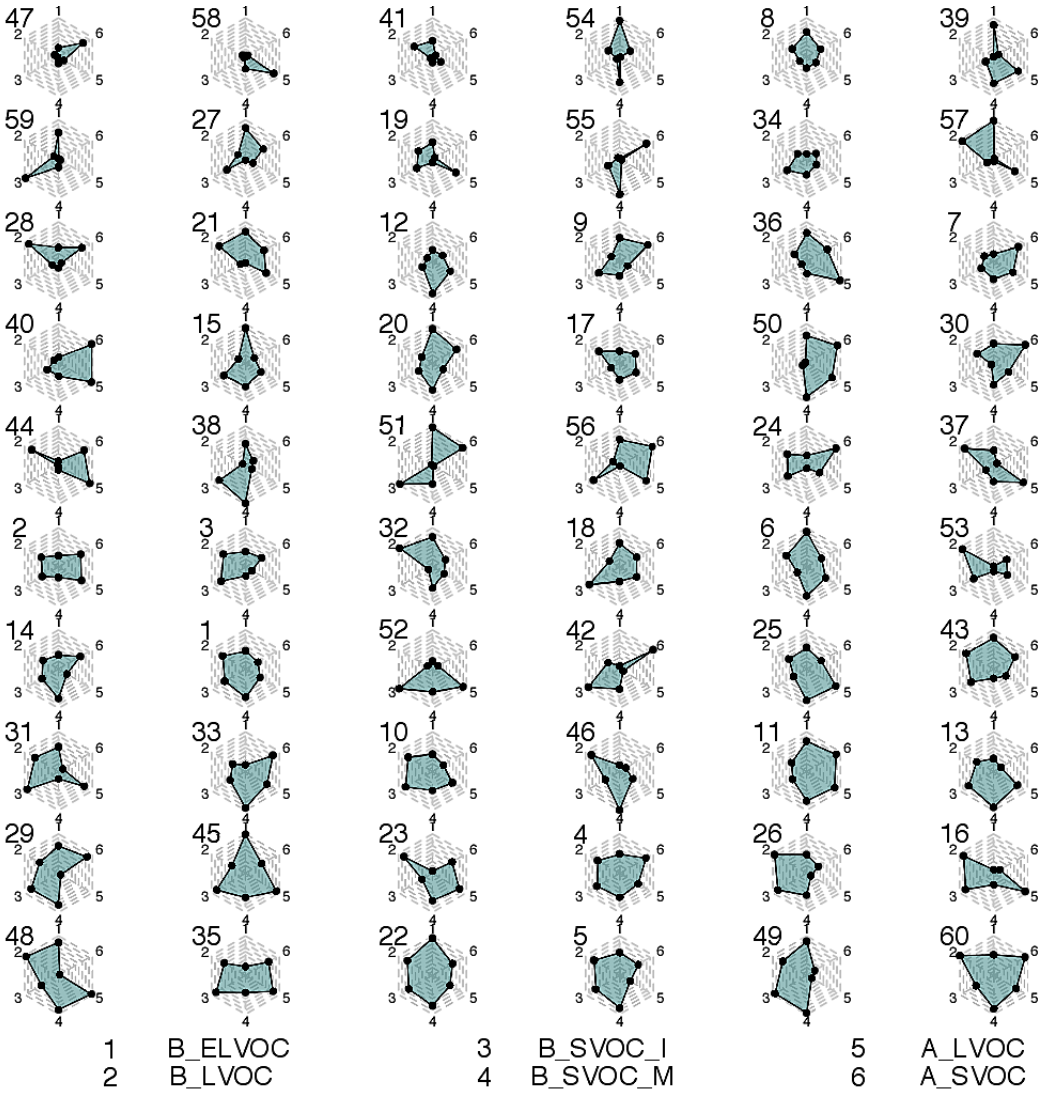

Figure 5.6: Figure 5.3 resorted. The relative variation of six perturbed parameters for each of the 60 ensemble members ordered in increasing order of global mean OA for easy comparison with Figure 5.5.

Figure 5.5 highlights that the contribution of different sources of ox-VOCs to OA varies regionally and is dependent on the competition and compensation between them. For example in PPEM 36, where relative contribution of A_LVOC is 15.32 %, more than 10 μg m^{-3} OA is simulated in the highly polluted SE Asian region. In PPEM 21 which has a very similar contribution from A_LVOC (15.14 %), OA concentrations simulated in the SE Asian region is $<$2 μg m^{-3}. Globally, the difference between the total SOA production from ox-VOCs simulated by PPEM 36

and PPEM 21 is 0.1 % (compared to a 150 % uncertainty in SOA estimates). This demonstrates that a model that simulates the "right" amount of total global SOA may not be necessarily right in simulating regional level aerosol mass concentrations. Two simulations from the same model with very similar concentrations of one ox-VOC, estimating very similar global SOA production can significantly under or over estimate organic aerosol mass concentration in particular regions depending on the parameter settings of the other ox-VOCs. The important aspect to constrain in models is therefore the relationship between different ox-VOCs and how their covariation affects model outputs.

Next the particle number concentrations simulated by each ensemble member are investigated. Figures 5.7 and 5.8 show the global map of N50 and N3 anomaly within the ensemble respectively. Subplots for each ensemble member are arranged in order of increasing global mean N3 in both figures. The parameter combination design for each simulation is re-ordered likewise and shown in Figure 5.9. Across the parameter range spanned in this study, global mean N50 varies by a factor of 2.39 within the ensemble (from 377 per cc to 903 per cc). As seen in Chapter 4, modelled N50 is much less sensitive to changes in ox-VOCs than modelled N3 which varies by a factor of 3.5 across the 60 ensemble members (from 531 to 1889 cm^{-3}).

Figure 5.7 helps in the identification of those combination of parameters which inhibit the growth of smaller particles to CCN-relevant sizes in the model. In most ensemble members, N50 concentrations increase proportionally with N3, thereby maintaining the order of subplots. In some cases the order is reversed (example, between PPEM 37 and 14 in row 4 Figure 5.7) when N50 does not increase proportionate to N3. This is likely due to enhanced condensation sink in the PPEM 14 that favours loss of small particles and thus a reduction in particle number of bigger sizes. The parameter combination for PPEM 14 (Figure 5.9) shows the simulation

has higher concentrations of B_SVOC and A_SVOC which, as seen in Chapter 4, increasingly favour the growth of bigger particles at the expense of smaller particles. Figure 5.9 shows all of the PPEMs (PPEMs 14, 39, 47, 56, 50, 38, 9, 15, 15, 59, 51) where N50 concentrations are low despite N3 concentrations being high have very low yields of B_LVOC. Particularly striking are the low N50 simulated in PPEMs 51 and 59, which are the second and fourth highest in N3 respectively. Both have very high yields of B_ELVOC (about 31 % and 22 % respectively) which significantly enhance particle formation but coupled with a low yields of B_LVOC (8.34 % and 34.6 % respectively), there is not enough ox-VOCs to support initial growth of the sub-3 nm clusters and small particles to CCN-relevant size. Several studies have investigated nucleation capability and nucleation pathways of atmospheric molecules (Kulmala et al., 1998, 2004; Kirkby et al., 2011; Kurtén et al., 2008; Almeida et al., 2013; Riccobono et al., 2014; Kirkby et al., 2016) whereas the contribution of organic molecules to sub-3 nm cluster growth is relatively recent knowledge and the molecules largely unidentified (Tröstl et al., 2016). The findings of this study suggests B_LVOC is a key class of SOA-producing organic compounds for understanding atmospheric CCN production. Without adequate representation of B_LVOCs in models, including new nucleation pathways puts global aerosol models at a risk of underestimating N50 which is a highly relevant parameter for estimation of climate relevant aerosol-cloud interactions.

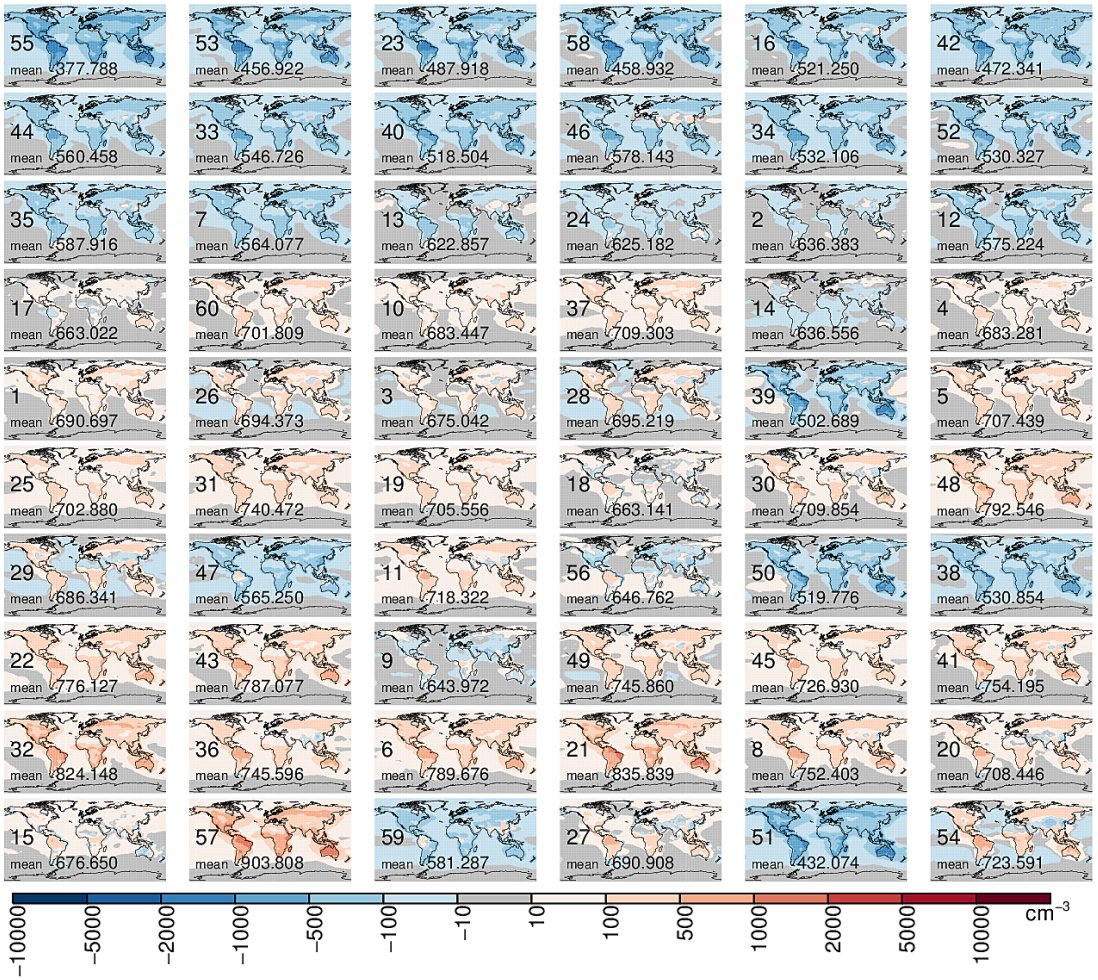

Figure 5.7: Anomaly of global N50 number concentration (cm^{-3}) produced within the ensemble. Each subplot shows the anomaly of an ensemble member (numbered between 1 and 60) from the ensemble mean N50. The global mean N50 for each subplot is printed. The subplots are arranged in order of increasing global mean N3 with PPEM 55 producing the least global mean N3 and PPEM 54 producing the maximum.

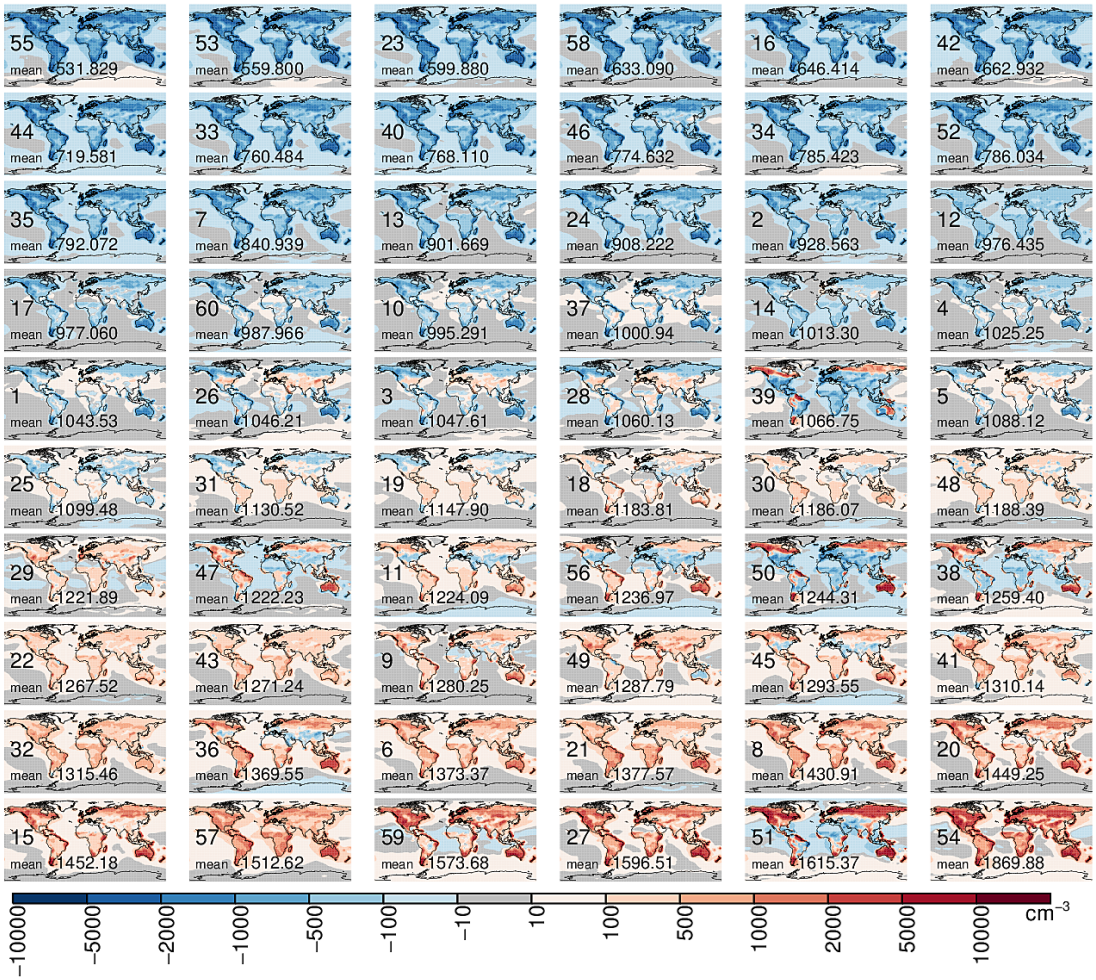

Figure 5.8: Anomaly of global N3 number concentration (cm^{-3}) produced within the ensemble. Each subplot shows the anomaly of an ensemble member (numbered between 1 and 60) from the ensemble mean N3. The global mean N3 for each subplot is printed. The subplots are arranged in order of increasing global mean N3 with PPEM 55 producing the least global mean N3 and PPEM 54 producing the maximum.

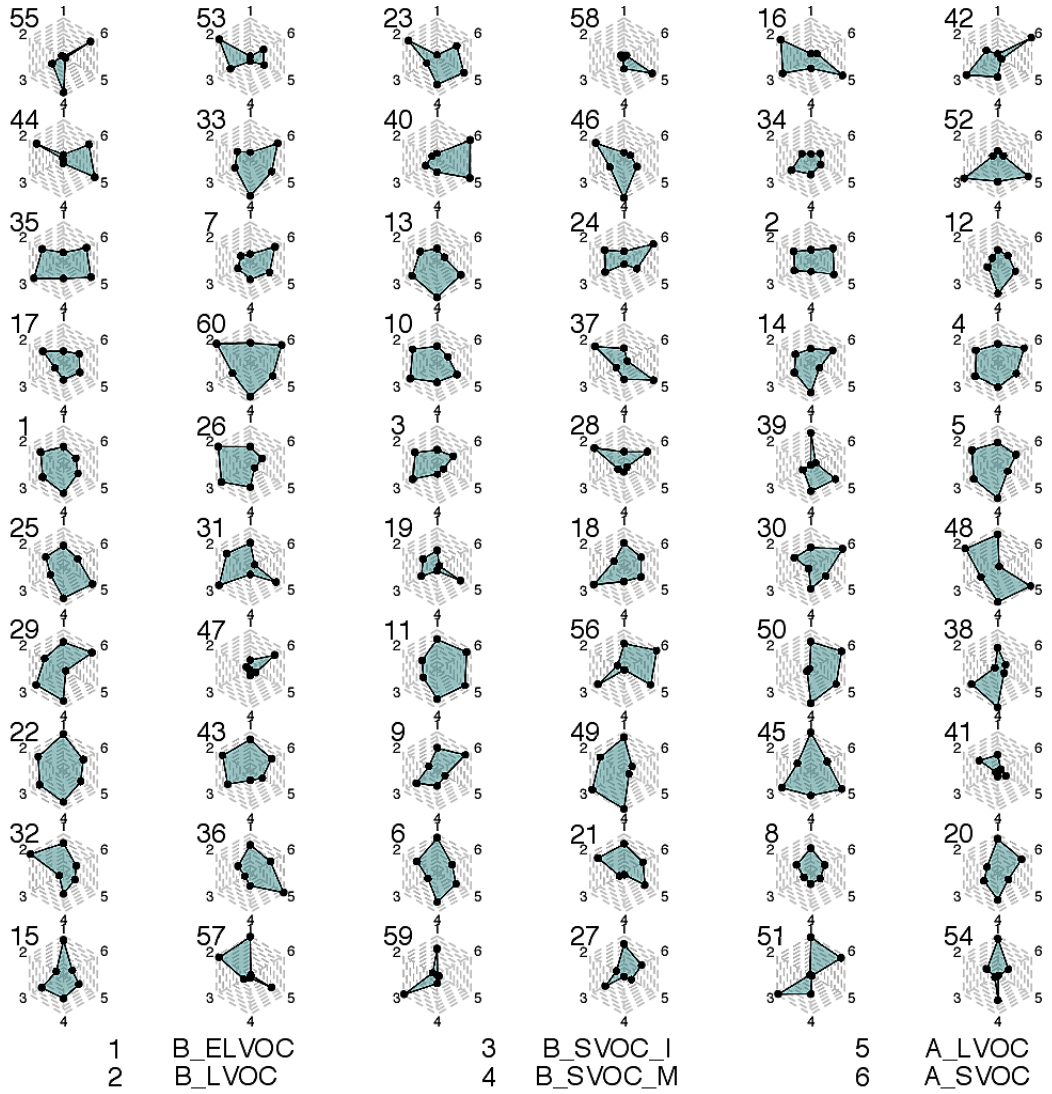

Figure 5.9: Figure 5.3 resorted. The relative variation of six perturbed parameters for each of the 60 ensemble members ordered in increasing order of global mean N3 for easy comparison with Figures 5.7 and 5.8.

Table 5.2 divides the ensemble in three groups based on their global mean N3, N50 and OA. Simulations with global mean values of N3 (or N50 or OA) in the lower quartile are in group 'Low' designated with 'L', those with values in the upper quartile are in group 'High' designated with 'H' and those with values in the interquartile range are in group 'Medium' designated with 'M'. The high and low simulations for each category are shaded red and blue respectively. In the text, characteristics of groups of PPEMs are looked into to infer upon patterns in their behaviour. Each group consists of multiple PPEMs and each PPEM may have been allotted multiple groups. The group names are based on the output they are being compared on (N3, N50 or OA) and their rank in the said output (H/M/L). For example, a group termed L_{OA} refers to all PPEM with low global mean OA. A group termed $H_{N3}H_{N50}L_{OA}$ refers to a group of all PPEMs that produce high global mean N3, high global mean N50 and low global mean OA and so on.

	Global mean				Global mean		
PPEM	N3	N50	OA	PPEM	N3	N50	OA
1	M	M	M	31	M	H	M
2	M	M	M	32	H	H	M
3	M	M	M	33	L	L	M
4	M	M	H	34	L	L	L
5	M	M	H	35	L	M	H
6	H	H	M	36	H	H	M
7	L	L	M	37	M	M	M
8	H	H	L	38	M	L	M
9	M	M	L	39	M	L	L
10	M	M	M	40	L	L	M
11	M	H	H	41	H	H	L
12	M	M	L	42	L	L	M
13	L	M	H	43	M	H	M
14	M	M	M	44	L	L	M
15	H	M	M	45	H	H	H
16	L	L	H	46	L	M	H
17	M	M	M	47	M	M	L
18	M	M	M	48	M	H	H
19	M	M	L	49	H	H	H
20	H	M	M	50	M	L	M
21	H	H	L	51	H	L	M
22	M	H	H	52	L	L	M
23	L	L	H	53	L	L	M
24	L	M	M	54	H	H	L
25	M	M	M	55	L	L	L
26	M	M	H	56	M	M	M
27	H	M	L	57	H	H	L
28	M	M	L	58	L	L	L
29	M	M	H	59	H	M	L
30	M	H	M	60	M	M	H

Table 5.2: Classification of ensemble members (PPEM) based on their simulated global mean N3, N50 and OA in categories High (or H), Medium (or M) and Low (or L). PPEM with global mean values in the lower quartile are designated with L (and shaded blue) and those with values in upper quartile are designated with H (and shaded red). PPEM with values in the inter-quartile range are all marked M. The first, second and third quartile values for OA are 6.5, 7.3, 8.8 μg m^{-3} respectively, for N3 are 908, 1099, 1280 cm $^{-3}$ respectively and for N50 are 564, 676, 709 cm $^{-3}$ respectively.

Simulations with low N3 and low N50 (group $L_{N3}L_{N50}$) consist of PPEMs 7, 16, 23, 33, 34, 40, 42, 44, 52, 53, 55, 58 and those with high N3 and high N50 (group

$H_{N3}H_{N50}$) consist of PPEMs 6, 8, 21, 32, 36, 41, 45, 49, 54, 57. The common feature among all the simulations in group $L_{N3}L_{N50}$ is low concentrations of one or both of B_ELVOC and B_LVOC and that in group $H_{N3}H_{N50}$ is the relative dominance of either or both of these two ox-VOCs. The importance of these ox-VOCs in modulating modelled number concentrations is explained by their respective roles in aerosol formation and growth. B_ELVOC is the only ox-VOC capable of nucleating and B_LVOC, the only ox-VOC that grow clusters (along with sulphuric acid in the model) before they attain 3 nm dry diameter. Consequently, for the model to simulate a high total number concentration of particles, high yields of B_ELVOC and B_LVOC are needed.

The relationship between total particle number concentration and mass concentration of organic aerosol produced is not straightforward and is strongly dependent on the interaction between different ox-VOCs. Simulations that produce OA within the lower quartile (group L_{OA}) are PPEM 8, 9, 12, 19, 21, 27, 28, 34, 39, 41, 47, 54, 55, 57, 58 and 59. Simulations that produce OA within the upper quartile (group H_{OA}) are PPEM 4, 5, 11, 13, 16, 22, 23, 26, 29, 35, 45, 46, 48, 49 and 60.

All simulations with low B_ELVOC concentrations have low N3. However out of these simulations, some produce higher mass of OA than others. 9 out of 16 PPEMs in group L_{OA} with low OA have low or medium N3. 4 out of 15 PPEMs in group H_{OA} with high OA have low N3. The main difference in simulations that produce high amount of OA when particle concentrations are low (PPEM 16, 23, 35, 46) and those who do not (PPEMs 34, 55, 58) is the relative concentrations of B_LVOC which grow freshly nucleated clusters before they are scavenged by coagulation.

Further the parameter designs for all three of PPEM 34, 55, 58 in group $L_{N3}L_{N50}L_{OA}$ have extremely high values of one or two ox-VOCs (B_SVOC_I in PPEM 34,

B_SVOC_M and A_SVOC in PPEM 55, A_LVOC in PPEM 58). High estimates of SVOCs coupled with very low values of B_ELVOC and B_LVOC result in these PPEM simulating the lowest mass as well as number concentrations.

PPEMs in group L_{OA} that have a high particle number concentration ($H_{N3}H_{N50}L_{OA}$) are PPEMs 8, 21, 41, 54, 57. Simulations in group H_{OA} with low particle number concentrations are, PPEM 16 and 23 (group $L_{N3}L_{N50}H_{OA}$). In $H_{N3}H_{N50}L_{OA}$, the relative contributions of B_ELVOC and/or B_LVOC dominate significantly over the the rest of the ox-VOCs. High yields of B_ELVOC and/or B_LVOC increase particle number concentrations and the competition for ox-VOCs to grow to larger sizes. Low yields of all the other ox-VOCs enhance the competition and the available ox-VOCs distribute on a larger number of particles, causing smaller increase in the particle mass. On the other hand, $L_{N3}L_{N50}H_{OA}$ have low B_ELVOC, which is responsible for the low global mean particle number concentrations but high B_LVOC, to minimise the loss of the freshly nucleated particles and significant contributions from A_LVOC and SVOCs, to add to the mass of these particles. As a result $L_{N3}L_{N50}H_{OA}$ have fewer particles with heavier mass. Thus organic compounds such as SVOC and A_LVOC that do not take part in formation or initial growth of particles contribute significantly to the mass of aerosol produced and their underrepresentation leads to underestimation of modelled OA.

PPEM 45 and 49 of group $H_{N3}H_{N50}$ simulate some of the highest OA within the ensemble (group $H_{N3}H_{N50}H_{OA}$) i.e. for PPEM 45 and PPEM 49, the simulated global mean N3, N50 and OA are all in the upper quartile. Both these simulations have high concentrations of B_ELVOC which promote nucleation and moderate to high B_LVOC which help freshly formed particles to survive. However in PPEM 45 all six ox-VOC yields contribute significantly with B_ELVOC, B_SVOC_I and A_LVOC concentrations being predominant (Figure 5.3). In PPEM 49 contributions to SOA

are predominantly biogenic as the yields of anthropogenically controlled ox-VOCs are much smaller (Figure 5.3). Although the global mean number and mass concentrations are similar in these two simulations, the difference in parameter design is reflected in the global distributions. In absence of anthropogenic ox-VOCs PPEM 49 simulates less OA concentrations (compared to PPEM 45) in the highly polluted SE Asian region and simulates more OA concentrations (compared to PPEM 45) in tropical rain forest regions which have the maximum biogenic VOC emissions.

The climatic implications of under-representing SOA from anthropogenic sources can be more significant than under-representing biogenic SOA sources as the former affects the pre-industrial and present-day atmospheres differently (Carslaw et al., 2013). PPEM 21 and PPEM 36 were cited earlier in this chapter as examples to demonstrate that simulations predicting similar mass of global OA with similar anthropogenic contributions to total SOA do not necessarily predict similar regional distribution. PPEM 21 and PPEM 36 differ most significantly in yields of biogenic and anthropogenic LVOCs. PPEM 49, on the other hand, strikingly differs from PPEM 45 in having very low anthropogenic ox-VOC yields. The poor representation of anthropogenic sources of SOA in PPEM 49 (compared to PPEM 45) leads to a decreased condensation sink in polluted regions which favours particle formation and growth, resulting in higher total particle number concentration over the polluted east coast of USA and SE Asia (Figure 5.8). However these simulated particles in the polluted regions in PPEM 49 are likely to be small particles because of which they do not add substantial mass, as is evident from the lower OA concentrations simulated in these regions (Figure 5.5). This re-emphasises the need to represent anthropogenic sources of SOA and to ensure that the spatial variability of total organic aerosol is realistic. Under-representing SOA formation from anthropogenic VOCs in the model leads to underestimation of aerosol mass and overestimation of aerosol numbers in polluted regions which impact estimates of first aerosol indirect

forcing.

Number concentrations of CCN-relevant sized particles in the atmosphere is the **combined** effect of the presence of B_ELVOC which can nucleate and low volatility organic compounds which are able to condense on freshly nucleated particles i.e. B_LVOC. To demonstrate the above, simulations are divided based on their ranks (H/M/L) in simulated N3 and N50.

- Group $H_{N3}M_{N50}$

  Simulations that rank high in global mean N3 and medium in global mean N50 - PPEMs 15, 20, 27, 59

- Group $H_{N3}L_{N50}$

  Simulations that rank high in global mean N3 and low in global mean N50 - PPEMs 38, 39, 51

- Group $L_{N3}M_{N50}$

  Simulations that rank low in global mean N3 and medium in global mean N50 - PPEMs 13, 24, 35, 46

- Group $L_{N3}H_{N50}$

  Simulations that rank low in global mean N3 and high in global mean N50 - No PPEM fall under this category

Simulations in groups $H_{N3}M_{N50}$ and $H_{N3}L_{N50}$ stand out in Figure 5.7. As discussed previously, all simulations in these two groups have negligible yields of B_LVOC. The high concentrations of nucleating B_ELVOC in these PPEMs initially facilitate the formation of particles but extremely low yields of B_LVOC especially when coupled with high B_LVOC_I and A_LVOC suppresses further growth and the particles are lost.

In contrast, despite the low B_ELVOC concentrations, the relatively higher concentration of B_LVOC in group $L_{N3}M_{N50}$ ensures survival of more clusters to reach 3 nm size range in these PPEMs, as a result of which they rank 'M' when ordered according to global mean N50. Thus survival of clusters below 3 nm diameter is extremely critical step in determining particle number concentrations and in GLOMAP-mode, B_LVOC is the most important controller of total particle number concentrations.

That no PPEM falls in the category $L_{N3}H_{N50}$ shows a minimum particle number concentration is required before B_LVOC can grow all particles optimally to produce CCN-relevant size particles and B_ELVOC is essential to produce that baseline number of particles. Simulation such as PPEM 16 which has a high concentration of B_LVOC but very low concentrations of B_ELVOC (group $L_{N3}L_{N50}$) proves the point.

In this study, A_LVOC does not take part in growth of particles less than 3 nm in diameter as evidence of such contribution of A_LVOC to particle growth is yet to be established in experimental and observational studies. However, based on the above, it is suggested that if found to play a role in growth of sub-3 nm particles, anthropogenically controlled VOCs will have a greater impact in determining simulated particle number concentrations in areas dominated by anthropogenic activities.

5.3.3 Ensemble comparison to observations

Figure 5.10 shows a map of ground-based observation stations used in this study where sites marked with green, blue and red denote data sites for N3, N50 and OA respectively. There are some overlap of sites between observed variables - for example, Pallas, a site in northern Finland, has data for both N3 and N50 and Mace Head, off west coast of Ireland, has data for all three.

N3 observations covering 34 ground-based stations worldwide were compiled by Dr. Dominick Spracklen (University of Leeds; Spracklen et al., 2010) from online portals, published articles and personal communications. Measurements of N3 were made between 1994 and 2009 using either condensation particle counters (CPCs), scanning mobility particle sizers (SMPS), differential mobility particle sizers (DMPS) or Diffusion Aerosol Spectroscopes (DAS). The N3 data set is fully described in Spracklen et al. (2010) and has been used in previous studies such as Riccobono et al. (2014), Gordon et al. (2016) and Dunne et al. (2016).

N50 observations covering 31 ground-based stations worldwide were compiled by Dr. Jo Browse (University of Exeter; manuscript in preparation). The data comprise of sites in Europe as described in Asmi et al. (2011) along with data from additional African, Indian, Canadian and polar sites obtained from individual projects and online data portals (such as the International Arctic Systems for Observing the Atmosphere, IASOA and the World Data Center for Aerosol, WDCA). Measurements of N50 were made between 1990 and 2015 using DMPS or SMPS instruments. A full description of the N50 data set can be found in Browse et al., (in preparation).

OA observations covering 41 ground-based stations worldwide were taken from the Global Aerosol Synthesis and Science Project (GASSP) database compiled by Dr.

Carly Reddington (University of Leeds; Reddington et al., 2017). OA measurements were made between 1990 and 2015 using the Aerosol Mass Spectrometer (AMS) and the associated Aerosol Chemical Speciation Monitor (ACSM) that characterise the mass and chemical composition of particulate matter (Canagaratna et al., 2007; Ng et al., 2011). A full description of the OA data set can be found in Reddington et al. (2017)

All ground-based station data are averaged for each month and gridded to the model resolution. Station heights were matched to model pressure level for each month using barometric altitude. Stations cover a wide range of atmospheric conditions such as continental boundary layer (CBL e.g. Hyytiala, Harwell, Botsalano), marine boundary layer (MBL e.g. Mace Head, Trinidad Head, Sable Island) and free tropospheric (FT e.g. Nepal, Jungfraujoch, Pico Espejo, Mauna Loa) sites. Errors in measurements is estimated to be around 30 % on average, depending strongly on the spatial heterogeneity of sources (Reddington et al., 2017).

This section compares the seasonal cycle of N3 and N50 simulated by each ensemble member to observations from ground-based observation stations. Figures 5.11 and 5.13 show the annual N3 and N50 timeseries for 60 ensemble members compared to monthly mean observations in 34 and 31 locations respectively.

Despite spanning a large part of the plausible parameter space for each ox-VOC, the ensemble is able to encompass observations at only 3 sites for N3 (Cape Grim, Pico Espejo and Sable Island) and 2 sites for N50 (Schauinsland and Alert). In most locations the model underestimates observed N3 and N50 concentrations (except in Trinidad Head and Whistler Mountain on the west coast of North America. The entire ensemble overestimates N3 upto a factor of 5 in Trinidad Head and overestimates N50 by a factor of 2 or more in Whistler Mountain). In most locations the model

bias ranges between a factor of 3 underestimation to a factor of 2 overestimation (shown by dotted lines in Figures 5.11 and 5.13) for both N3 and N50. The monthly timeseries for both N3 and N50 show that the principal contributor to the low bias in the model is the low particle numbers simulated in winter whereas the high bias in some ensemble members is caused by the overestimation in the summer. The exaggeration of the seasonal cycle by the model (compared to observed seasonal cycle) was also observed in Chapter 4. Modelled N3 and N50 concentrations are primarily driven by B_ELVOC and B_LVOC. After exploring 60 combinations of parameter setting in this study, we suggest the inability of the model to simulate the seasonal variability is not caused and hence cannot be addressed by changing how biogenic organic compounds contribute to particle formation and growth in the model.

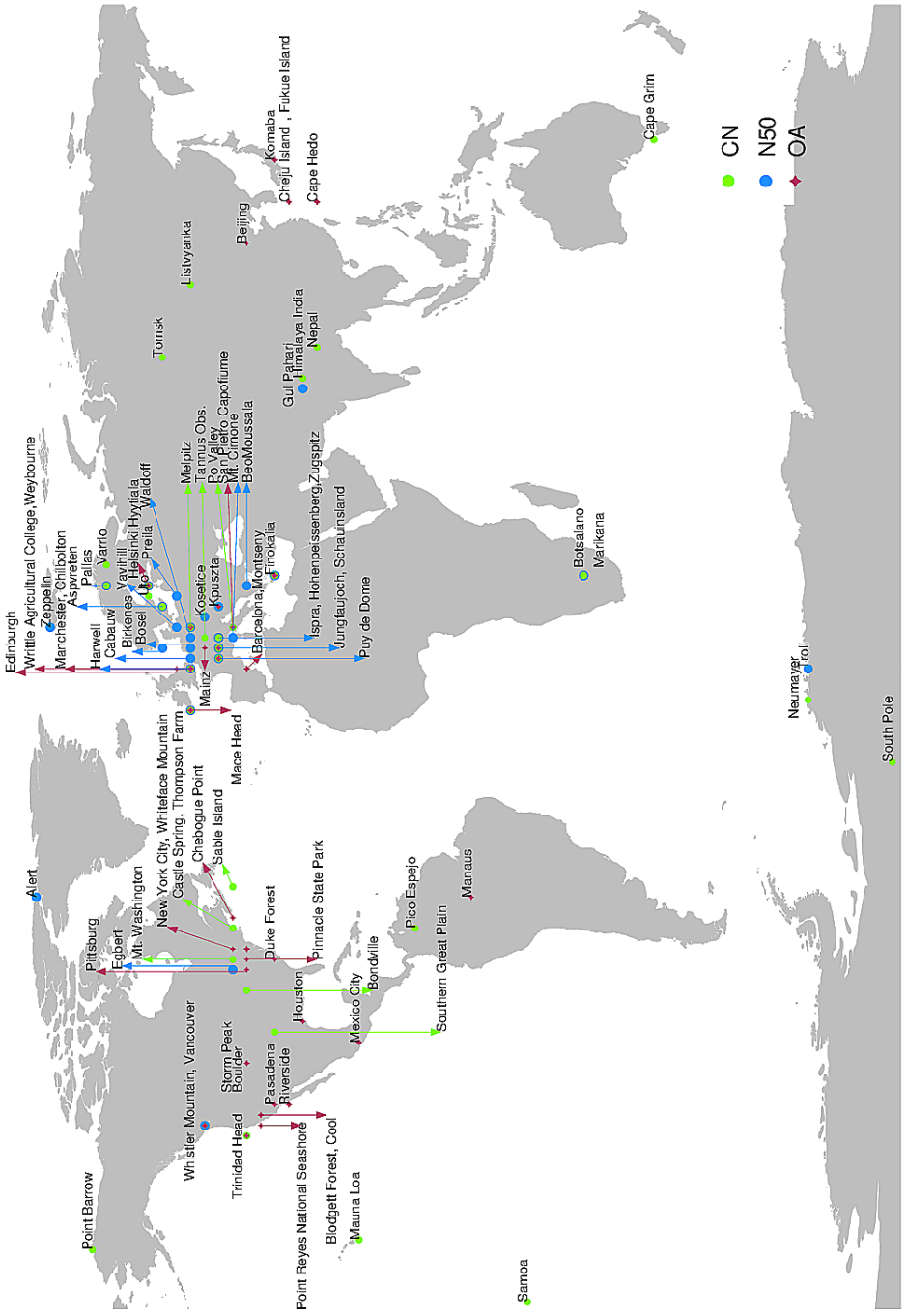

Figure 5.10: Locations of ground-based sites where model-observation match is compared for N3 (symbols in light green), N50 (symbols in blue) and OA (symbols in red).

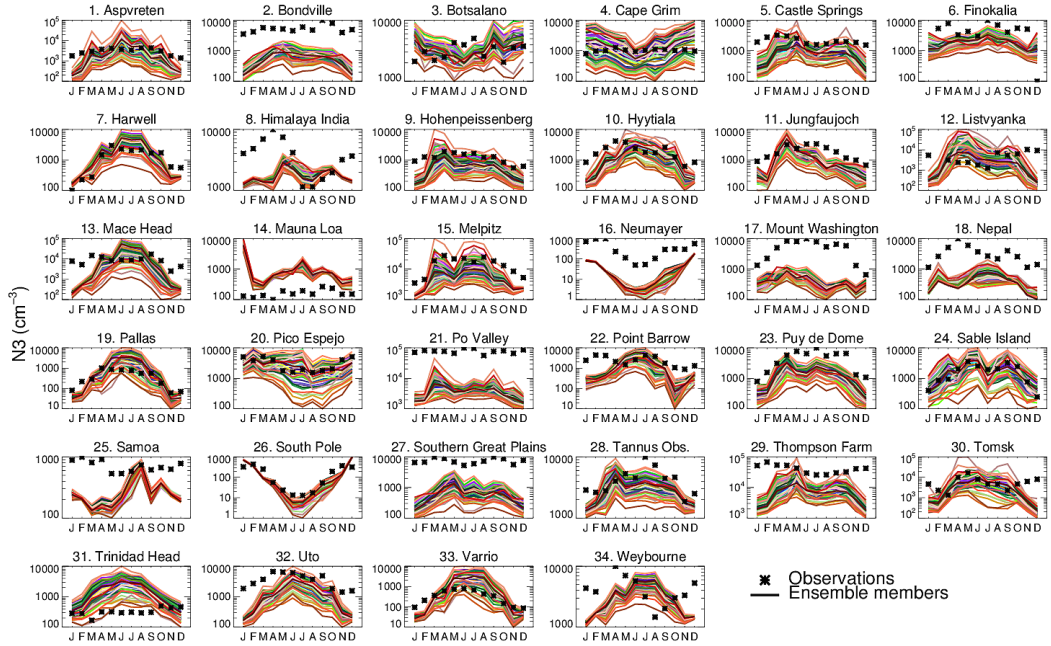

Figure 5.11: Annual cycle of simulated (solid coloured lines) and observed (black stars) monthly mean surface-level N3 concentrations at 34 ground-based sites. Each coloured line is an ensemble member.

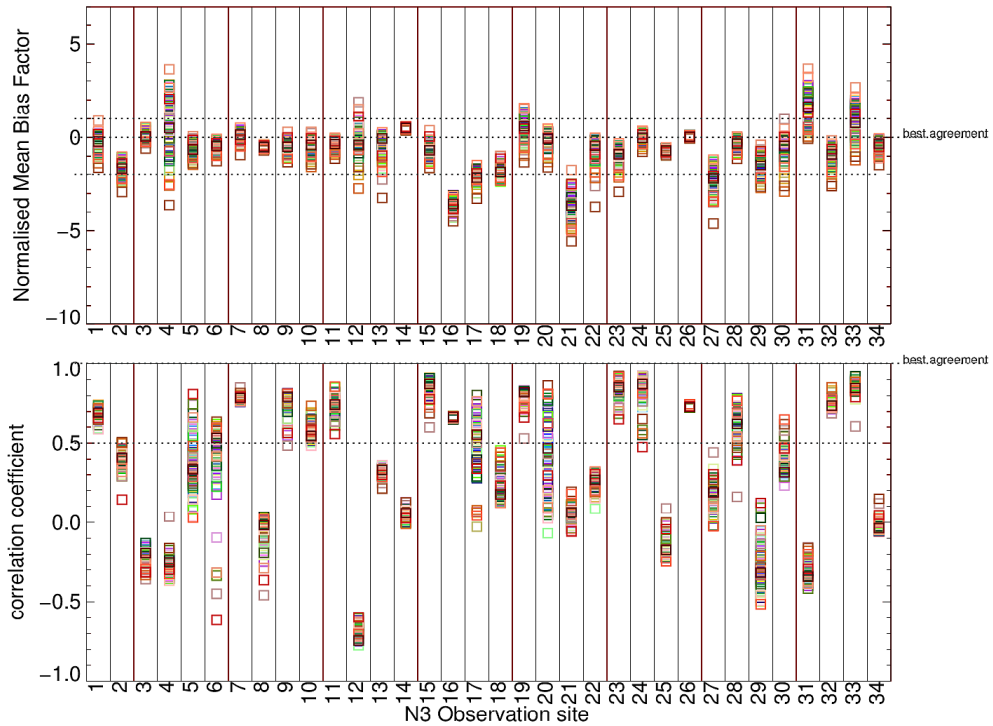

Figure 5.12: Normalised Mean Bias Factor (NMBF) and Pearson correlation coefficient (R) calculated from monthly mean surface-level simulated and observed N3 for each PPEM at each ground-based location. Each number on the x-axis represents an observation site, as numbered in Figure 5.11. The best agreement values for both NMBF and R are shown in the plot. Additional dotted lines represent an overestimation of a factor 2 (NMBF = 1), underestimation of a factor of 3 (NMBF = 2) and a Pearson correlation coefficient of 0.5.

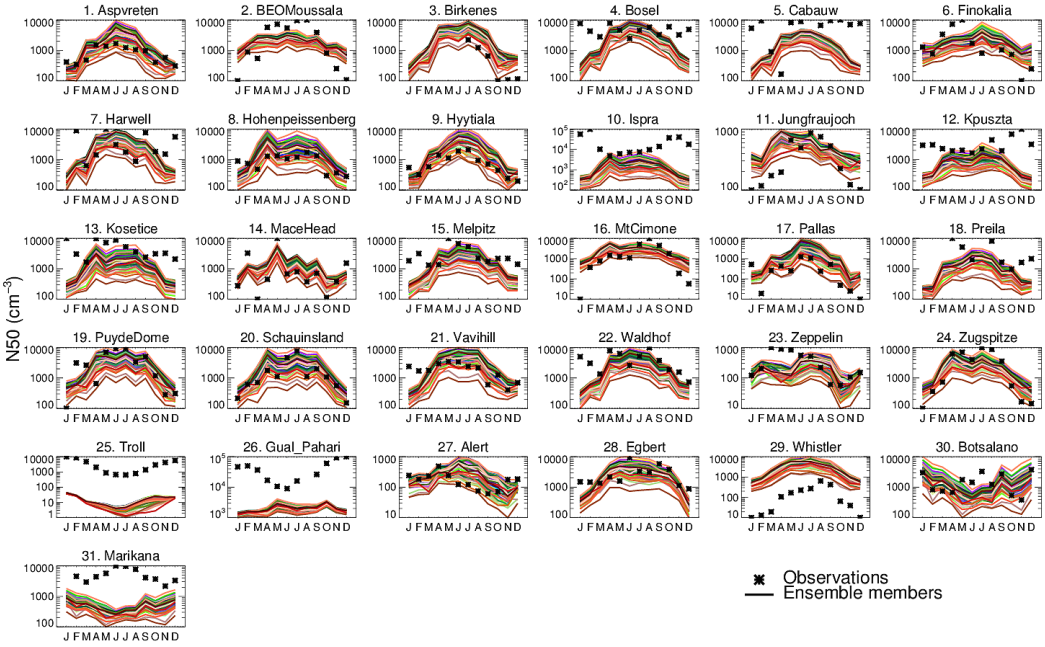

Figure 5.13: Annual cycle of simulated (solid coloured lines) and observed (black stars) monthly mean surface-level N50 concentrations at 31 ground-based sites. Each coloured line is an ensemble member.

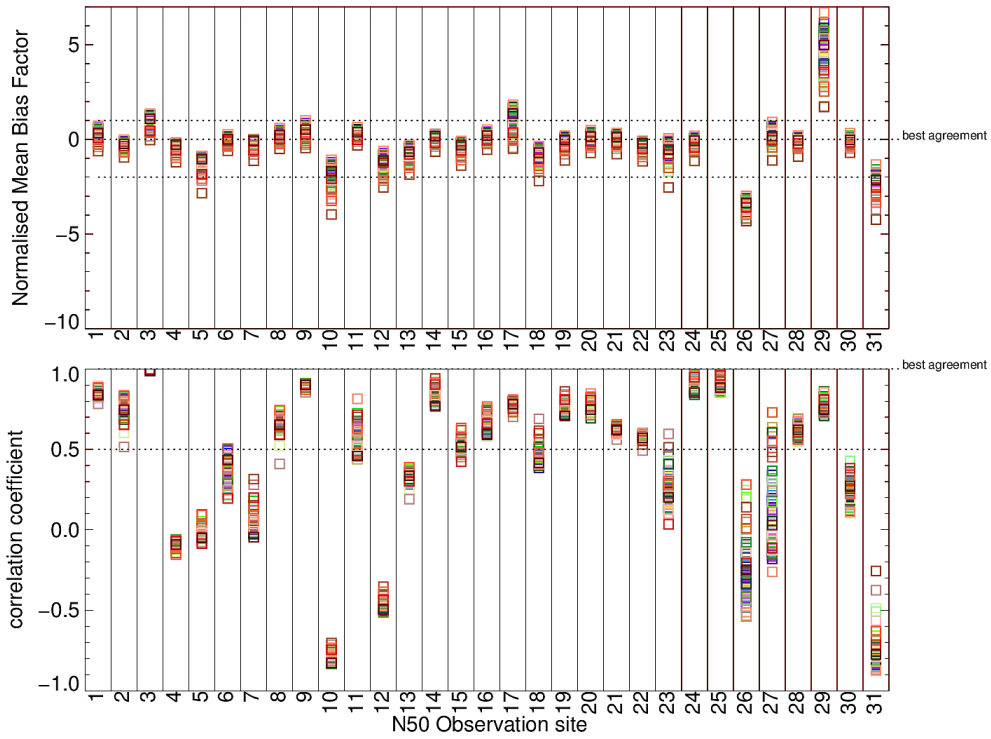

Figure 5.14: Normalised Mean Bias Factor (NMBF) and Pearson correlation coefficient (R) calculated from monthly mean surface-level simulated and observed N50 for each PPEM at each location. Each number on the x-axis represents an observation site, as numbered in Figure 5.13. The best agreement values for both NMBF and R are shown in the plot. Additional dotted lines represent an overestimation of a factor 2 (NMBF = 1), underestimation of a factor of 3 (NMBF = 2) and a Pearson correlation coefficient of 0.5.

The sensitivity of modelled N3 to the applied perturbations is maximum in Botsalano, Cape Grim, Castle Springs whereas in locations such as Mauna Loa, Neumayer and Samoa (remote marine sites) the model shows the least sensitivity to perturbations. There are 5 sites for which both N3 and N50 concentrations are compared, Finokalia, Hohenpeissenberg, Hyytiala, Jungfraujoch and Pallas. The sensitivity of simulated N50 is less than that of N3 at all locations except Hohenpeissenberg. Simulated N50 is least sensitive at Troll, a station close to Neumayer, where the model underestimation is maximum (Figure 5.13). At some sites, such as Bondville, India Himalaya, Mt. Washington, Nepal, Po Valley, Samoa, Southern Great Plains and Thompson Farm, the ensemble completely fails to reach the observed N3 values (Figure 5.11). The ensemble underestimation is maximum at Po Valley reaching upto a factor of 6. The same is observed in Troll and Marikana for N50 (Figure 5.13). The inability of the ensemble to simulate N3 values close to those observed confirms that the uncertainty in aerosol formation from organic compounds is not the primary cause of underestimation of aerosol concentration in these regions. Sites such as Bondville, Thompson Farm, Mount Washington are heavily affected by SO_4^{2-}, NH_4^+ and to a lesser extent NO_3^- (Fischer et al., 2007). As seen in Dunne et al. (2016) including the role of ammonia in particle formation improved model-observation agreement in India Himalaya and Nepal. It is suggested here that including the influence of ammonium and nitrate ions in aerosol formation and growth in the boundary layer could improve particle number concentrations predicted in these locations (Yu and Luo, 2009; Dunne et al., 2016).

For N50, correlation coefficients (calculated for each PPEM at each location using monthly mean simulated and observed N50 concentrations) in 22 out of 31 sites are higher than 0.5 (Figure 5.13). Locations where ensemble members reach a correlation coefficent >0.8 for the simulated seasonal cycle are, Aspvreten, Birkenes, Hyytiala, Jungfraujoch, Mace Head, Pallas, Puy de Dome, Schauchinland, Zugspitz,

Troll and Whistler for N50. For N3, correlation coefficent >0.8 occurs in Castle Springs, Harwell, Hohenpeissenberg, Jungfraujoch, Melpitz, Mount Washington, Pallas, Pico Espejo, Puy de Dome, Sable Island, Tannus Observatory, Uto and Varrio. These are all non-urban sites including FT, MBL and CBL stations. In Ispra and Marikana, both locations highly influenced by anthropogenic activities, the ensemble correlation worsens lowering to values upto -0.9. Aerosol concentrations at sites affected by anthropogenic sources are closely linked with simultaneous occurrence of low-mobility atmospheric conditions that trap pollutants (Strader et al., 1999; Bigi and Ghermandi, 2011), local emissions and regional transports. As a result contributions to aerosol concentrations from local anthropogenic sources are difficult to capture by large global models (which inevitably have coarser resolution than small-scale models).

The maximum underestimation and worst correlation coefficient for N50 are observed at Ispra and Marikana. The ensemble performs significantly better at Hohenpeissenberg and Zugspitz which are sites located close (about 458 km) to Ispra and at Botsalano which is close (150 km) to Marikana. Hohenpeissenberg and Zugspitze are both high altitude sites and free from influence of nearby anthropogenic sources while Ispra is one the most polluted European sites (Asmi et al., 2011). Similarly Botsalano presents a semi-clean environment with no local anthropogenic activities but affected by plumes form nearby megacity and surrounding industry (Vakkari et al., 2013). Marikana is a polluted site, where aerosol seasonality is dominated by domestic heating and cooking practises in residential area (Vakkari et al., 2013). Gual Pahari, also like Marikana, is heavily affected by biomass burning from cooking and domestic heating (Hyvärinen et al., 2010). It is worth noting that at all three polluted sites, Ispra, Gual Pahari and Marikana, the model underestimation ranges from more than a factor of 5 to a factor of 4 (Gual Pahari) or 2 (Ispra, Marikana). Such a range is also observed in the correlation coefficient for Gual Pahari and

Marikana. Similar range (from a factor of 6 to less than a factor of 2 underestimation) for model predicted N3 is seen in Po Valley, another heavily polluted European site within the ensemble range. The response of model performance at these polluted sites to the perturbations implemented in this study indicates that model performance at heavily polluted sites (such as Marikana, Ispra, Gual Pahari and Po Valley) can be significantly improved by including additional or better characterised sources of anthropogenic ox-VOCs (A_LVOC or A_SVOC), which contribute significantly to atmospheric aerosol number concentrations in these regions. The next section compares the simulations individually to identify those combinations of ox-VOCs that produce the best agreement between observed and modelled N3, N50 and OA.

5.3.4 Ensemble member intercomparison and comparison with observed N3, N50 and OA

Figures 5.15, 5.17 and 5.18 show scatter plots for model-observation comparison of monthly mean N3, N50 and OA observed in 34, 31 and 57 sites respectively. Each PPEM is shown in a subplot with the subplots ordered according to an increasing order of global mean N3 for Figures 5.15, 5.17 and an increasing order of global mean OA for Figure 5.18. Each subplot also shows the correlation coefficient (printed top left) and NMBF (printed bottom left) for each PPEM based on modelled and observed N3 (or N50 or OA) for all 34 (or 31 or 57) stations. In addition to R, which is a score of how well the data variability is captured and NMBF, which gives a measure of the systematic bias within the model, the Taylor Skill Score (TSS) for each PPEM is calculated following Taylor (2001):

$$TSS = \frac{4(1+R)^4}{(\hat{\sigma_f} + \frac{1}{\hat{\sigma_f}})^2(1+R_0)^4} \tag{5.1}$$

where $\hat{\sigma}$ is the normalised standard deviation ($\sigma_{model}/\sigma_{observation}$) and R_0 is the maximum correlation attainable by the model, given the internal variability in the system (here R_0 is assumed to be 1). As the model variance approaches the variance in observation and R approaches R_0, TSS approaches unity. TSS approaches zero as the model variance approaches zero or the correlation becomes more and more negative. TSS thus takes into account both how well the model simulates the observed pattern (correlation coefficient) as well as how close model observation agreement is (root-mean-square error). The full statistics (TSS, NMBF and R) calculated for each PPEM is presented in Table. 5.3.

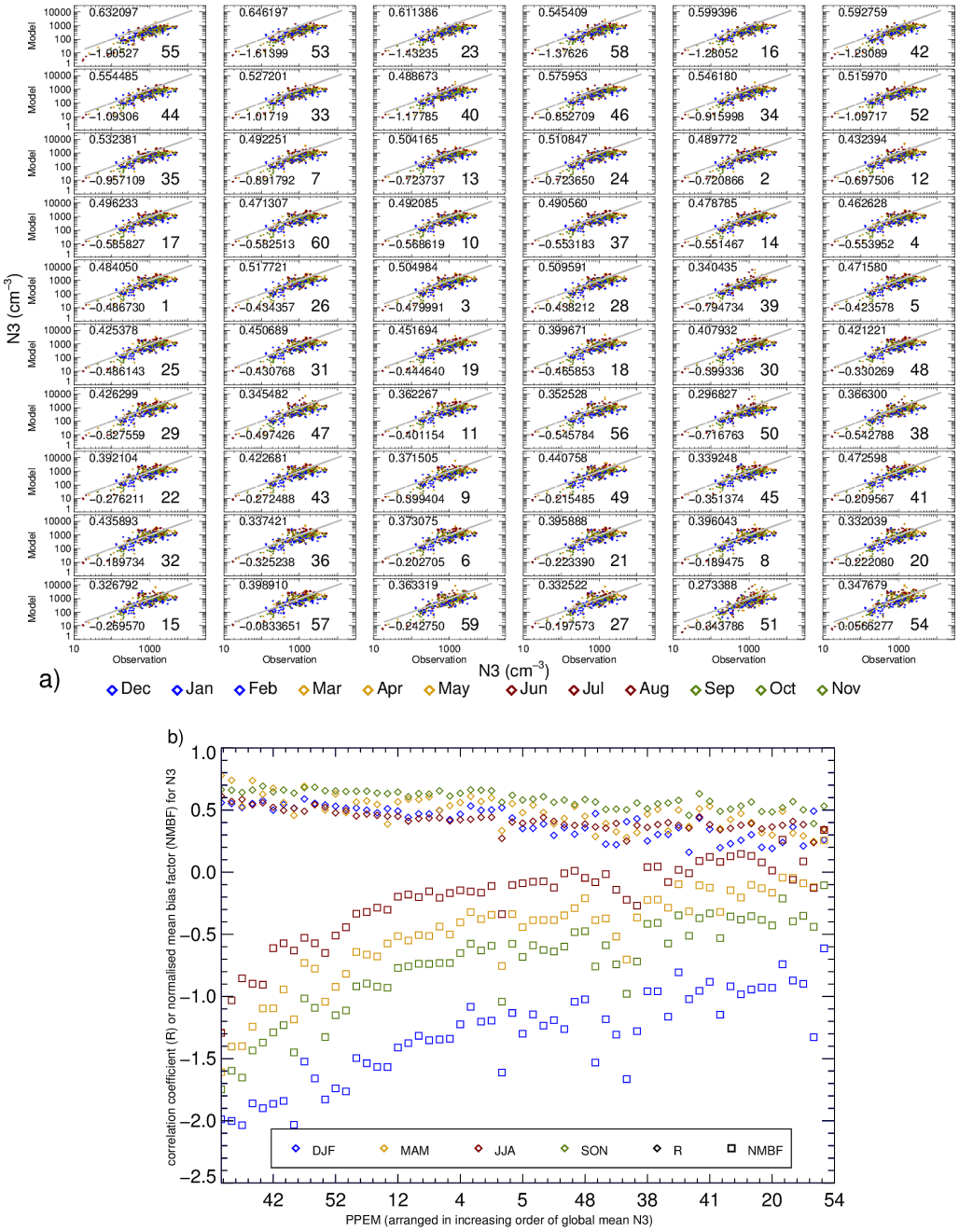

Figure 5.15: Comparison of simulated monthly mean and seasonal surface-level N3 against observations. a) Comparison of the monthly mean surface-level N3 simulated by each ensemble member (subplots numbered between 1 to 60) to observed N3 at 34 sites. The subplots of 60 ensemble members are arranged in order of increasing global mean surface-level N3 (as in Figure 5.8). Each point within a subplot represents monthly mean surface-level N3 at one site. Months are color coded according to the season they represent - blue, yellow, red and green for winter, spring, summer and autumn respectively. The Pearson correlation coefficient (R) for each PPEM-observation match is shown on the top left and the normalised mean bias factor (NMBF) for each PPEM-observation match is shown on the bottom left of each subplot. b) Seasonal R (diamonds in blue for winter, yellow for spring, red for summer and green for autumn) and seasonal NMBF (squares in blue for winter, yellow for spring, red for summer and green for autumn) plotted against each PPEM. The order of PPEM in the x-axis is the same as in a) with every sixth PPEM (last column of subplots in panel a) labelled.

The minimum bias (NMBF closest to zero) between the model and observation is given by PPEM 54 (overestimating observations by a factor of 1.05) for N3, PPEM 57 (underestimating observations by a factor of 1.27) for N50 and PPEM 47 (overestimating observations by a factor of 1.13) for OA. The worst model-observation bias is given by PPEM 55 (underestimating observations by a factor of 2.9) for N3 , PPEM 55 (underestimating observations by a factor of 2.8) for N50 and PPEM 60 (overestimating observations by factor of 4.04) for OA.

The model suffers from an overall low bias in most locations (Figures 5.11 and 5.13). The bias therefore improves in PPEMs associated with higher global mean N3 (Figure 5.15a) which as discussed earlier have high yields of B_ELVOC and B_LVOC. B_ELVOC and B_LVOCs contribute especially towards the formation of particle clusters and their subsequent growth. Therefore any increase in B_ELVOC or B_LVOC concentrations in the model reduces the model error. However an important aspect to note is, with increasing global mean N3 as the negative bias (NMBF) reduces, the model becomes worse in capturing the observed seasonal variability in N3 (indicated by the decreasing R in Figure 5.15b). This happens because the response of particle number concentration to increased B_ELVOC and B_LVOC are different in different seasons. The highest increase in N3 in response to increase in B_ELVOC and B_LVOC is seen in the warmer months while N3 in colder months are least sensitive to changes in these two ox-VOCs. The uneven response of particle number concentration in different seasons to these ox-VOCs results in a worse prediction of the seasonal cycle. An indication of this behaviour was seen in Chapter 4 when the seasonal cycles of N3 predicted by three simulations with different SOA formation schemes were compared against observed N3 (Chapter 4, Figure 4.13). Therein it was noted, including B_ELVOC and B_LVOC in the model (blue line in Figure 4.13) resulted in overestimation of particle number concentrations in summer (compared to green line in Figure 4.13) and implementation of the modified

SOA scheme (i.e. adding SVOCs; red line) brought the overestimation in the summer down without significantly affecting the winter particle concentrations. A low model bias in winter was also noted in Riccobono et al. (2014). However in Figure 5.11 several PPEMs overestimate summer-time N3 concentrations showing the issue is not so much as that the underprediction in winter but the simulation of a largely exaggerated seasonality in total aerosol number concentrations. To validate the above, two simulations from the ensemble (Figure 5.11) - PPEM 55 with the lowest global mean N3 and PPEM 54 with the highest global mean N3 are shown in 5.16. Figure 5.16 clearly shows with increasing B_ELVOC and B_LVOCs the model increasingly overestimates particle concentrations in summer with little change in particle concentrations in winter, thereby reducing the model-observation (negative) bias but worsening the model-observation correlation coefficient.

For N50 although the model bias reduces in PPEMs with higher global mean N3, the response to increase in B_ELVOC and B_LVOC is much less and the improvement in bias occurs without much worsening of R. This is a further indication that the overall low bias of particle number concentrations that the model exhibits at most locations, particularly in winter, is linked with processes that affect smaller particles more than larger ones (hence the higher sensitivity of N3) such as nucleation or stabilisation of sub-3 nm clusters.

The exaggerated seasonal cycle of particle number concentrations simulated by the model compared to the observed cycle could potentially be linked with the absence of a nucleation mechanism involving anthropogenic ox-VOCs or the absence of anthropogenic contribution to the growth of sub-3 nm clusters. Recent studies (Volkamer et al., 2006; Weber et al., 2007) point towards a higher impact of anthropogenic VOCs in SOA formation than previously estimated, independent of the place of origin of the condensing VOCs. Studies such as Strader et al. (1999) esti-

mate as much as 15−20 μgC m^{-3} of SOA in the winter from aromatic compounds favoured by low mixing heights, low winds and clear sky conditions. With new and more sophisticated nucleation schemes involving biogenic organic compounds being implemented in the model, the summer months overestimate particle number concentrations while winter months remain largely unaffected - in accordance with the annual cycle of biogenic terpenes which peak during the spring and summer months and dip to lowest in winter (Staudt et al., 2000). In contrast, VOCs emitted from anthropogenic sources have higher concentrations in the winter than in summer and hence their oxidation products could compensate the current effect of B_ELVOC and B_LVOC. It is suggested here that much of the exaggeration in the simulated seasonality will be addressed by including better characterisation of anthropogenic sources of SOA (which peak in the winter), their effects on nucleation and cluster stabilisation.

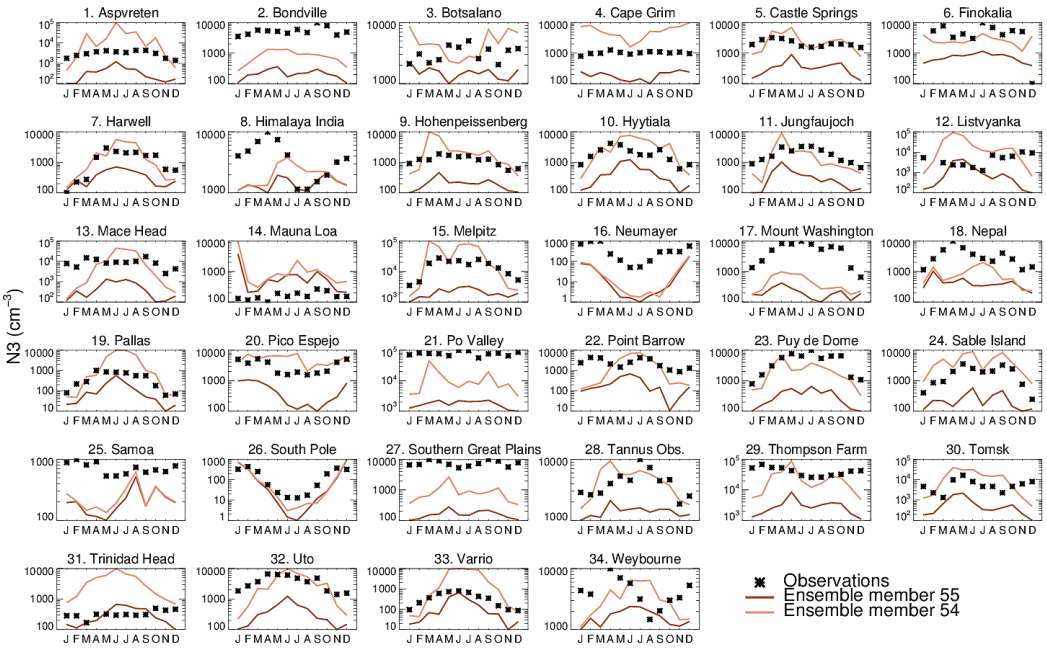

Figure 5.16: Annual cycle of simulated (solid lines) and observed (black stars) monthly mean surface-level N3 concentrations at 34 ground-based sites. The PPEMs shown are those with the lowest and highest number concentration of global mean surface-level N3 from Figure 5.11.

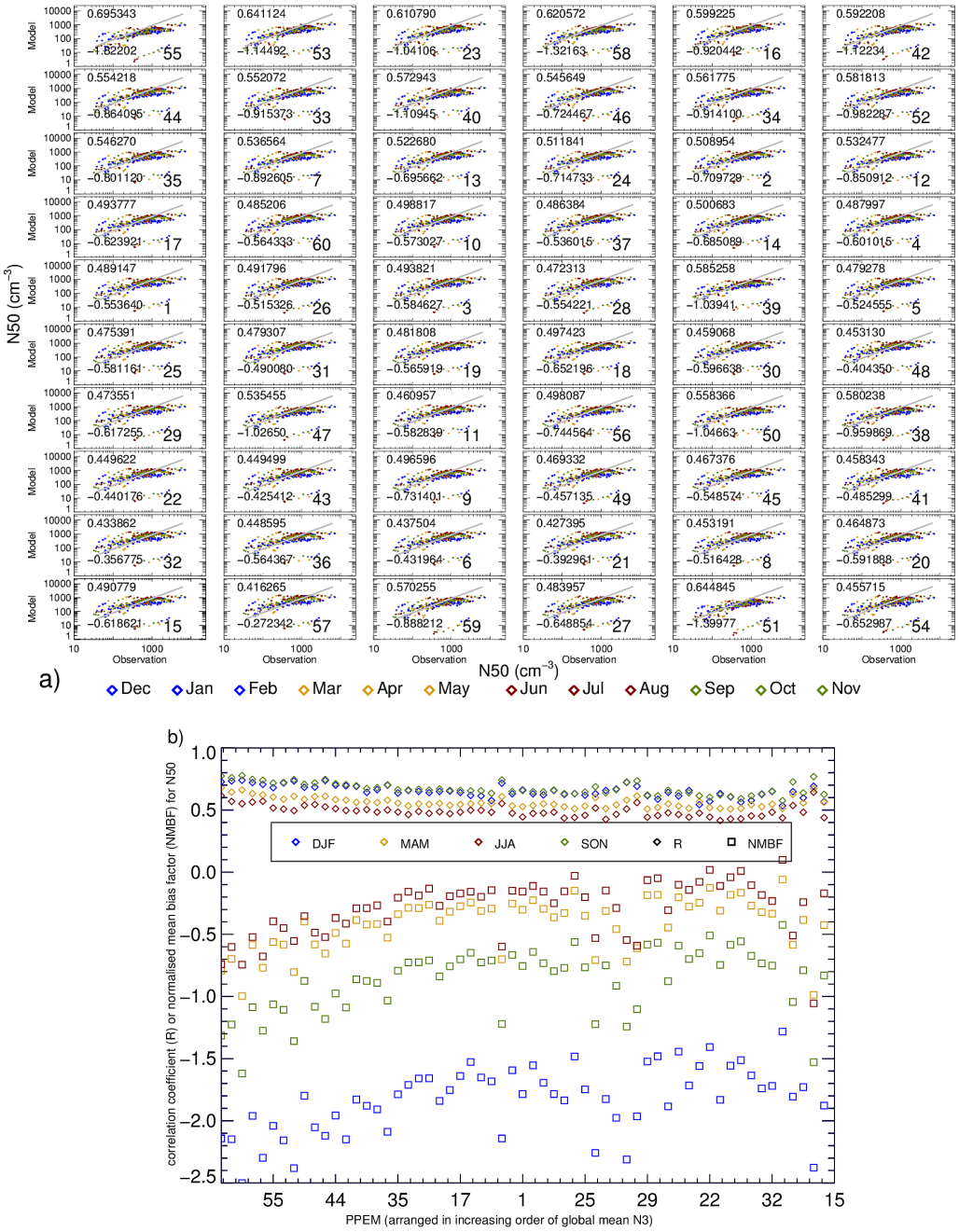

Figure 5.17: Comparison of simulated monthly mean and seasonal surface-level N50 against observations. a) Comparison of the monthly mean surface-level N50 simulated by each ensemble member (subplots numbered between 1 to 60) to observed N50 at 31 sites. The subplots are arranged in order of increasing global mean surface-level N3 (as in Figure 5.8). Each point within a subplot represents monthly mean surface-level N50 at one site. Months are color coded according to the season they represent - blue, yellow, red and green for winter, spring, summer and autumn respectively. The Pearson correlation coefficient (R) for each PPEM-observation match is shown on the top left and the normalised mean bias factor (NMBF) for each PPEM is shown on the bottom left of each subplot. b) Seasonal R (diamonds in blue for winter, yellow for spring, red for summer and green for autumn) and seasonal NMBF (squares in blue for winter, yellow for spring, red for summer and green for autumn) against each PPEM. The order of PPEM in the x-axis is the same as in a) with every sixth PPEM (last column of subplots in panel a) labelled.

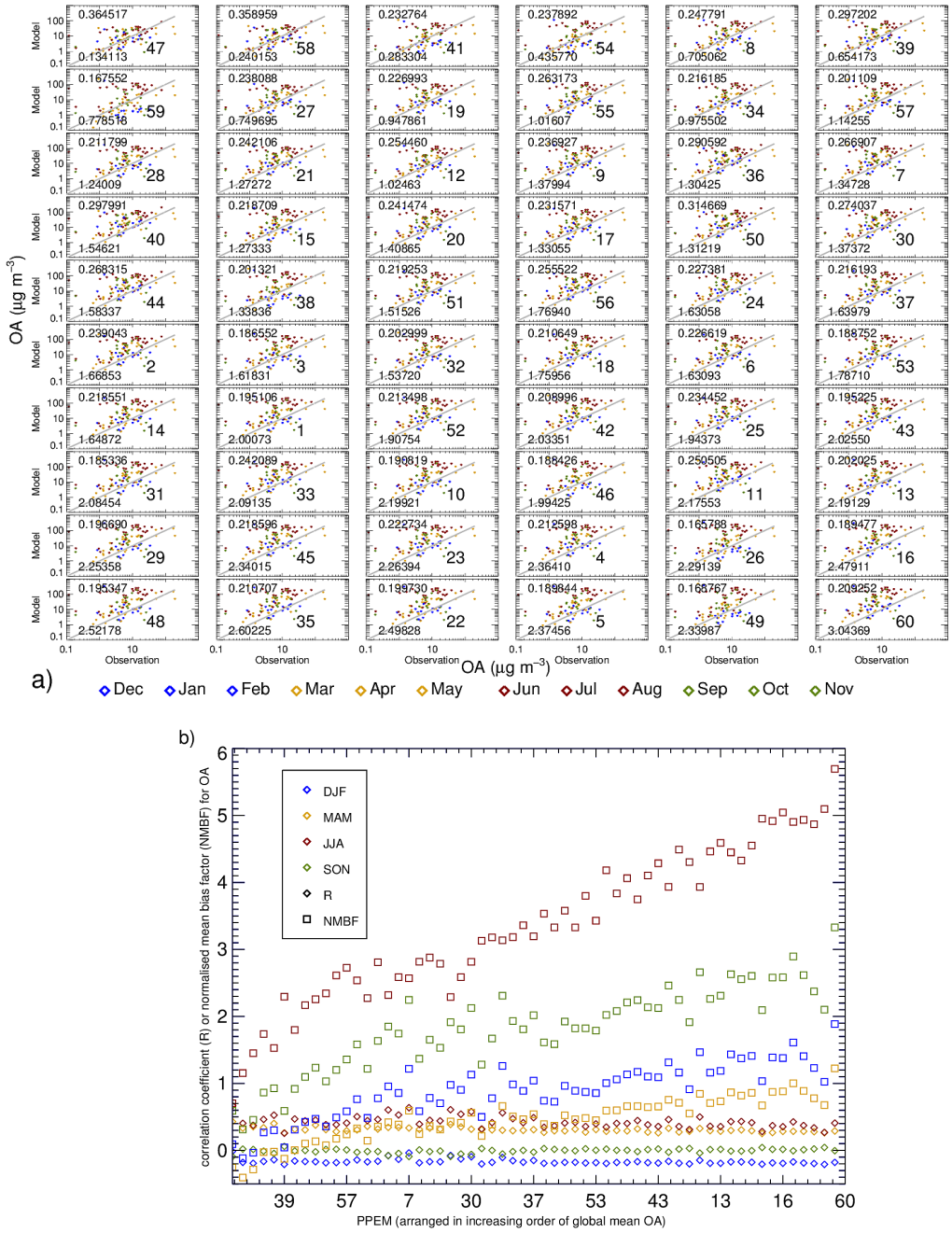

Figure 5.18: Comparison of simulated monthly mean and seasonal OA against observations. a) Comparison of the monthly mean N3 simulated by each ensemble member (subplots numbered between 1 to 60) to observed OA at 41 sites. The subplots are arranged in order of increasing global mean OA (as in Figure 5.5). Each point within a subplot represents monthly mean surface-level OA at one site. Months are color coded according to the season they represent - blue, yellow, red and green for winter, spring, summer and autumn respectively. The Pearson correlation coefficient (R) for each PPEM-observation match is shown on the top left and the normalised mean bias factor (NMBF) for each PPEM-observation match is shown on the bottom left of each subplot. b) Seasonal R (diamonds in blue for winter, yellow for spring, red for summer and green for autumn) and seasonal NMBF (squares in blue for winter, yellow for spring, red for summer and green for autumn) shown against each PPEM. The order of PPEM in x-axis is the same as in a) with every sixth PPEM (last column of subplots in panel a) labelled.

The statistics presented in Figure 5.18b should be viewed with caution as unlike N3 and N50 data which have the entire time series at each location, OA data is sparse in time and location. The overall statistics for each PPEM is based on 104 points out of which 17 observations are for winter months (blue), 33 for Spring (Yellow), 33 for summer (red) and 21 for autumn (green). Further none of the stations in the database has more than 4 months of data. Hence different locations contribute to the statistics in different seasons based on which month it has data for i.e. the 33 data points in spring and those in summer do not necessarily come from the same 33 locations. This is not a big limitation in this study as the OA data is not being used to infer upon location based model-observation agreement. Rather than assess how well the model agrees with the observation the aim is to assess where each of the PPEM stand in relation to each other with respect to the observed OA.

The important point to note from Figure 5.18 is that the model bias for OA concentrations at 41 sites worsens (model overestimation increases) as the global mean OA increases. All the PPEMs overestimate observed OA concentrations (positive NMBF) - the least overestimation (i.e. best model-observation agreement in OA concentrations) within the ensemble being a factor of 1.13 (PPEM 47 producing 220 Tg yr^{-1}) and the maximum overestimation within the ensemble being a factor of 4.04 (PPEM 60 producing 850 Tg yr^{-1}). SOA simulated by PPEM 47 and PPEM 60 encompass the full range of SOA simulated by the entire ensemble (section 5.2, Figure 5.4). The better match in modelled and observed OA concentrations for ensemble members which simulate SOA close to the lower end of ensemble SOA range (220 Tg yr^{-1}) agrees with Spracklen et al. (2011b) who found the best estimate of SOA to lie between $50-380$ Tg yr^{-1}. With anthropogenic sources of SOA restricted to 10 Tg yr^{-1} (to match with previous estimations of Henze et al., 2008; De Gouw and Jimenez, 2009) Spracklen et al. (2011b) estimated the best estimate of SOA to be 240 ± 140 Tg yr^{-1}. Without the restriction, the best SOA estimates was found

to be 140± 90 Tg yr^{-1} with 113 Tg yr^{-1} from ox-VOCs. In this study 9 PPEMs simulate SOA within the upper limit estimated by Spracklen et al. (2011b). In increasing order of simulated SOA they are PPEMs 47, 41, 58, 54, 27, 8, 59, 39 and 19. These 9 PPEMs and PPEM 34 simulating 397 Tg yr^{-1} also come up as the 10 best simulations with the minimum model bias (Table 5.3). When both model bias and correlation coefficient are considered (marked red in column TSS OA and NMBF OA in 5.3), the best models come out to be PPEM 8, 27, 39, 41, 47, 54, 58 simulating 337, 331, 335, 239, 220, 303, 251 Tg yr^{-1} respectively. Thus the best SOA estimate from this study is assessed to be between 220−337 Tg yr^{-1}.

However from Figure 5.4 it is clear that various combinations of biogenic and anthropogenic ox-VOCs can result in SOA production of this magnitude. In fact the PPEMs with maximum and minimum contribution from biogenic VOCs spanning a large range of biogenic to anthropogenic ratio (biogenic:anthropogenic from 1:2 in PPEM 47 to 32:1 in PPEM 59) both feature in the list of PPEMs that compare to OA observations with the least NMBF. This implies including either too little or too much SOA from anthropogenic VOCs yield very similar total SOA production, which might lead to an erroneous conclusion that anthropogenic VOCs do not make any significant contribution. In reality, the resultant SOA produced is very much a function of different ox-VOCs and their competing and compensating effects in the model with anthropogenic sources of VOCs having, as seen in previous sections, significant regional impact and potential to improve the simulated annual cycle of particle number concentration. In the next sections, we look into which of these parameter combinations yield the best results when modelled aerosol number concentrations are compared.

5.3.5 Statistical summary

	TSS				NMBF				CORR		
PPEM	N3	N50	OA		N3	N50	OA		N3	N50	OA
1	0.23	0.10	0.07		-0.49	-0.55	2.00		0.48	0.49	0.20
2	0.20	0.09	0.11		-0.72	-0.71	1.67		0.49	0.51	0.24
3	0.25	0.10	0.08		-0.48	-0.58	1.62		0.50	0.49	0.19
4	0.21	0.10	0.07		-0.56	-0.60	2.36		0.46	0.49	0.21
5	0.23	0.10	0.05		-0.43	-0.52	2.37		0.47	0.48	0.19
6	0.21	0.10	0.10		-0.20	-0.43	1.63		0.37	0.44	0.23
7	0.19	0.08	0.14		-0.89	-0.89	1.35		0.49	0.54	0.27
8	0.23	0.10	0.15		-0.19	-0.52	0.71		0.40	0.45	0.25
9	0.20	0.09	0.12		-0.40	-0.73	1.38		0.37	0.50	0.24
10	0.22	0.10	0.06		-0.57	-0.57	2.20		0.49	0.50	0.19
11	0.19	0.09	0.10		-0.40	-0.58	2.18		0.36	0.46	0.25
12	0.20	0.09	0.14		-0.70	-0.85	1.02		0.43	0.53	0.25
13	0.20	0.09	0.06		-0.73	-0.70	2.19		0.50	0.52	0.20
14	0.23	0.09	0.09		-0.55	-0.69	1.65		0.48	0.50	0.22
15	0.19	0.09	0.11		-0.27	-0.62	1.27		0.33	0.49	0.22
16	0.16	0.10	0.06		-1.28	-0.92	2.48		0.60	0.60	0.19
17	0.23	0.10	0.12		-0.59	-0.62	1.33		0.50	0.49	0.23
18	0.20	0.09	0.09		-0.47	-0.65	1.76		0.40	0.50	0.21
19	0.23	0.10	0.13		-0.45	-0.57	0.95		0.45	0.48	0.23
20	0.19	0.09	0.12		-0.22	-0.59	1.41		0.33	0.46	0.24
21	0.22	0.11	0.13		-0.23	-0.39	1.27		0.40	0.43	0.24
22	0.21	0.10	0.06		-0.28	-0.44	2.50		0.39	0.45	0.20
23	0.15	0.09	0.08		-1.44	-1.04	2.26		0.61	0.61	0.22
24	0.21	0.09	0.11		-0.73	-0.71	1.63		0.51	0.51	0.23
25	0.20	0.10	0.09		-0.49	-0.58	1.94		0.42	0.48	0.23
26	0.26	0.11	0.05		-0.44	-0.52	2.29		0.52	0.49	0.17
27	0.20	0.09	0.14		-0.20	-0.65	0.75		0.33	0.48	0.24
28	0.26	0.10	0.11		-0.44	-0.55	1.24		0.51	0.47	0.21
29	0.23	0.09	0.06		-0.33	-0.62	2.25		0.43	0.47	0.20
30	0.21	0.09	0.14		-0.40	-0.60	1.37		0.41	0.46	0.27
31	0.22	0.10	0.07		-0.43	-0.49	2.08		0.45	0.48	0.19
32	0.25	0.11	0.09		-0.19	-0.36	1.54		0.44	0.43	0.20
33	0.18	0.09	0.09		-1.02	-0.92	2.09		0.53	0.55	0.24
34	0.21	0.09	0.12		-0.92	-0.91	0.98		0.55	0.56	0.22
35	0.18	0.09	0.06		-0.96	-0.80	2.60		0.53	0.55	0.21
36	0.19	0.09	0.16		-0.33	-0.56	1.30		0.34	0.45	0.29
37	0.22	0.10	0.10		-0.56	-0.54	1.64		0.49	0.49	0.22
38	0.20	0.08	0.09		-0.55	-0.96	1.34		0.37	0.58	0.20
39	0.17	0.08	0.18		-0.80	-1.04	0.65		0.34	0.59	0.30
40	0.15	0.08	0.16		-1.18	-1.11	1.55		0.49	0.57	0.30
41	0.28	0.11	0.14		-0.21	-0.49	0.28		0.47	0.46	0.23
42	0.17	0.08	0.08		-1.23	-1.12	2.03		0.59	0.59	0.21
43	0.23	0.10	0.07		-0.27	-0.43	2.03		0.42	0.45	0.20
44	0.18	0.09	0.14		-1.10	-0.86	1.58		0.55	0.55	0.27
45	0.18	0.09	0.07		-0.35	-0.55	2.34		0.34	0.47	0.22
46	0.22	0.10	0.06		-0.86	-0.72	1.99		0.58	0.55	0.19
47	0.20	0.07	0.17		-0.50	-1.03	0.13		0.35	0.54	0.36
48	0.22	0.11	0.05		-0.33	-0.40	2.52		0.42	0.45	0.20
49	0.25	0.11	0.04		-0.22	-0.46	2.34		0.44	0.47	0.17
50	0.16	0.07	0.17		-0.72	-1.05	1.31		0.30	0.56	0.31
51	0.15	0.07	0.10		-0.35	-1.40	1.52		0.27	0.64	0.22
52	0.16	0.09	0.08		-1.10	-0.98	1.91		0.52	0.58	0.21
53	0.14	0.09	0.08		-1.62	-1.14	1.79		0.65	0.64	0.19
54	0.19	0.09	0.14		0.05	-0.65	0.44		0.35	0.46	0.24
55	0.12	0.07	0.14		-1.91	-1.82	1.02		0.63	0.70	0.26
56	0.17	0.09	0.12		-0.55	-0.74/	1.77		0.35	0.50	0.26
57	0.23	0.12	0.11		-0.09	-0.27	1.14		0.40	0.42	0.20
58	0.15	0.08	0.19		-1.38	-1.32	0.24		0.55	0.62	0.36
59	0.22	0.09	0.09		-0.25	-0.89	0.78		0.36	0.57	0.17
60	0.21	0.10	0.05		-0.58	-0.56	3.04		0.47	0.49	0.21
MIN	0.12	0.07	0.04	0.00	-1.91	-1.82	0.13	0.00	0.27	0.42	0.17
MAX	0.28	0.12	0.19	0.00	0.05	-0.27	3.04	0.00	0.65	0.70	0.36

Table 5.3: Summary statistics - Taylor Skill Score (TSS), Normalised Mean Bias Factor (NMBF) and Pearson correlation coefficient (R) - for each ensemble member, based on model comparison against observations of N3, N50 and OA. The 10 best and 10 worst simulations in each category are highlighted in red and blue respectively.

The good runs:

The 10 best PPEMs that give the smallest negative bias in N3 are, PPEM 6, 8, 20, 21, 27, 32, 49, 54 and 57 all of which have high concentrations of B_ELVOC. The 10 best PPEMs with the smallest negative bias for N50 are PPEM 6, 21, 22, 31, 32, 41, 43, 48, 49 and 57 (Table 5.3). The above simulations can be divided in three groups:

1. Small negative bias in N3, large negative bias in N50
   - PPEMs 8, 20, 27, 54

2. Large negative bias in N3, small negative bias in N50
   - PPEMs 31, 48, 22, 43, 41

3. Small negative bias in N3, small negative bias in N50
   - PPEMs 49, 32, 6, 21, 57

Categorising the parameter designs of PPEMs (Figure 5.9) in three groups makes it evident that the contribution from B_ELVOC is essential for the model to predict observed N3 well (small negative bias in Groups 1 and 3). If B_ELVOC or nucleation from organic compounds is under-represented in the model, the model predicted N3 has a large negative bias (Group 2). However without sufficient B_LVOC, PPEMs cannot match observed N50 and hence result in large negative bias in N50 despite having a small negative bias in N3 (Group 1). On the other hand, PPEMs with moderately high B_ELVOC can perform well in simulating N50 if B_LVOC is sufficiently high (Group 2). To predict both N3 and N50 with the smallest negative bias (Group 3), PPEMs have to include considerable amounts of B_ELVOC, B_LVOC and one of the SVOCs. Table 5.3 reconfirms the conclusions reached in previous sections as well as shows that the PPEMs that have closest agreement with observations are ones that have high yields of at least three different categories of ox-VOCs: B_ELVOC, B_LVOC and SVOCs.

As seen in Figures 5.15b and 5.17b, improvement in the negative model bias (NMBF closer to zero) for N3 or N50, is associated with poorer prediction of the seasonal variability (low R). Accordingly PPEMs that fall in the top 10 category according to NMBF score low according to R and vice versa (Table. 5.3). The calculation of TSS takes into consideration both the model error and its skill to capture the variability in the observation. The only PPEMs which come under the top 10 category in TSS *and* NMBF are PPEM 32, PPEM 41, PPEM 49 and PPEM 57.

The PPEMs in best agreement with observed OA (highest TSS and smallest positive NMBF) are PPEMs 8, 27, 39, 41, 47, 54 and 58, ranging from an overestimation of a factor of 1.13 (PPEM 47) to a factor of 1.78 (PPEM 59). Of these PPEMs 8, 27, 41 and 54 also feature in top 10 runs for best NMBF (smallest negative bias) in N3. The rest, on the other hand, feature in the bottom 10 runs for the worst NMBF (largest negative bias) in N3 (PPEM 58) or N50 (PPEMs 39, 47, 58). The only PPEM that features in the top 10 best models (highest TSS and smallest positive/negative NMBF) for all three of N3, N50 and OA is PPEM 41, characterised by relatively high A_LVOC, B_ELVOC and with maximum B_LVOC. Skill scores for all 7 PPEMs (PPEMs 8, 27, 39, 41, 47, 54, 58) with respect to the other PPEMs are shown in Figure 5.19.

The bad runs:

Table 5.3 highlights in blue the PPEMs that are least skilled in capturing observed N3, N50 and OA. The 10 worst PPEMs that give the largest negative bias in N3 are PPEMs 16, 23, 33, 40, 42, 44, 52, 53, 55 and 58, all of which have low concentrations of B_ELVOC. The 10 PPEMs with the largest negative bias for N50 are PPEMs 23, 39, 40, 42, 47, 50, 51, 53, 55 and 58 (Table 5.3). Unsurprisingly, all these PPEMs have extremely low concentrations of either B_ELVOC or B_LVOC.

Of the above, PPEMs 16, 23, 40, 50, 51, 52, 53, 55 and 58 also have the poorest TSS implying they predict the maximum error and poorest correlation with the observation. Table 5.4 lists the % yield of B_ELVOC and B_LVOC in these PPEMs and the contribution of B_LVOC to SOA. The PPEMs in Table 5.4 are listed in increasing order of global mean N3. This arrangement clearly highlights the pairing of a high B_ELVOC yield with a low B_LVOC yield (or vice versa) in these PPEMs which largely underestimate observed N50. To help the reader see the contrast in B_ELVOC and B_LVOC, columns tabulating their yields in Table 5.4 are shaded in green such that darker shades of green correspond to higher yields.

PPEM	Yield of B_ELVOC (%)	Yield of B_LVOC (%)	B_LVOC to total SOA (%)	Total SOA (Tg yr^{-1})
55	0.13	14.6	3.2	443.7
53	0.22	237.6	43.1	542.3
23	0.54	219.5	31.6	683.1
58	0.37	22.37	8.7	251.8
16	0.88	230.3	32.7	694
42	0.78	88.18	13.9	620.8
44	1.09	205.4	39.1	517.1
33	1.69	98	14.4	666.4
40	1.46	36.7	6.8	527.9
52	2.04	39.5	6.5	599.1
39	8.19	4.22	1.2	355.6
47	2.36	29.3	13.0	220.6
50	7.01	9.3	1.8	511.7
51	9.6	8.34	1.6	515.0

Table 5.4: List of PPEMs - which give the poorest agreement (maximum absolute NMBF) with observed N3 and N50 - with the respective yields of B_ELVOC and B_LVOC, the relative contribution of B_LVOC to the total simulated SOA and the total SOA produced from ox-VOCs in each PPEMs. The PPEMs are ordered in increasing order of simulated global mean surface-level N3. Of the simulations listed above, PPEMs 16, 23, 40, 50, 51, 52, 53, 55 and 58 also have the poorest TSS.

The 10 PPEMs that overestimate observed OA the most are PPEM 4, 5, 16, 22, 26, 35,45, 48, 49 and 60. 7 out of these 10 simulations - PPEMs 5, 16, 22, 26, 48, 49 and 60 - also give the poorest TSS. 4 out of these 7 simulations - PPEMs 5, 26, 48 and 49 - score well in matching observed number concentrations (TSS in N3 or TSS in

N50). Simulations such as these 4 are perfect examples that demonstrate occasions when modelled number concentrations match reasonably well with observations but for the wrong reasons. The yields of B_ELVOC, B_LVOC, the total SOA simulated and the contribution of B_LVOC to total SOA for these 4 PPEMs are tabulated in Table 5.5. PPEM 16, one of the poorest scorers in TSS for N3 as well as OA, is also shown in Table 5.5. Skill scores for these five PPEMs (PPEMs 5, 16, 26, 48, 49) with respect to the other PPEMs are shown in Figure 5.19.

PPEM	Yield of B_ELVOC (%)	Yield of B_LVOC (%)	B_LVOC to total SOA (%)	Total SOA (Tg yr^{-1})
5	5.7	197.4	27.5	706
26	4.7	246.3	36.4	665.4
48	8.35	247.8	33.0	739.6
49	8.63	184.4	25.9	699.6
16	0.88	230.4	32.7	693.9

Table 5.5: List of PPEMs - which give the poorest agreement (maximum absolute NMBF and lowest TSS) with observed OA but perform well (high TSS) when compared with observed N3 and N50 - with the respective yields of B_ELVOC and B_LVOC, the relative contribution of B_LVOC to the total simulated SOA and the total SOA produced from ox-VOCs in each PPEM. PPEM 16 is included in the list as a simulation that scores poor in TSS for both N3 and OA.

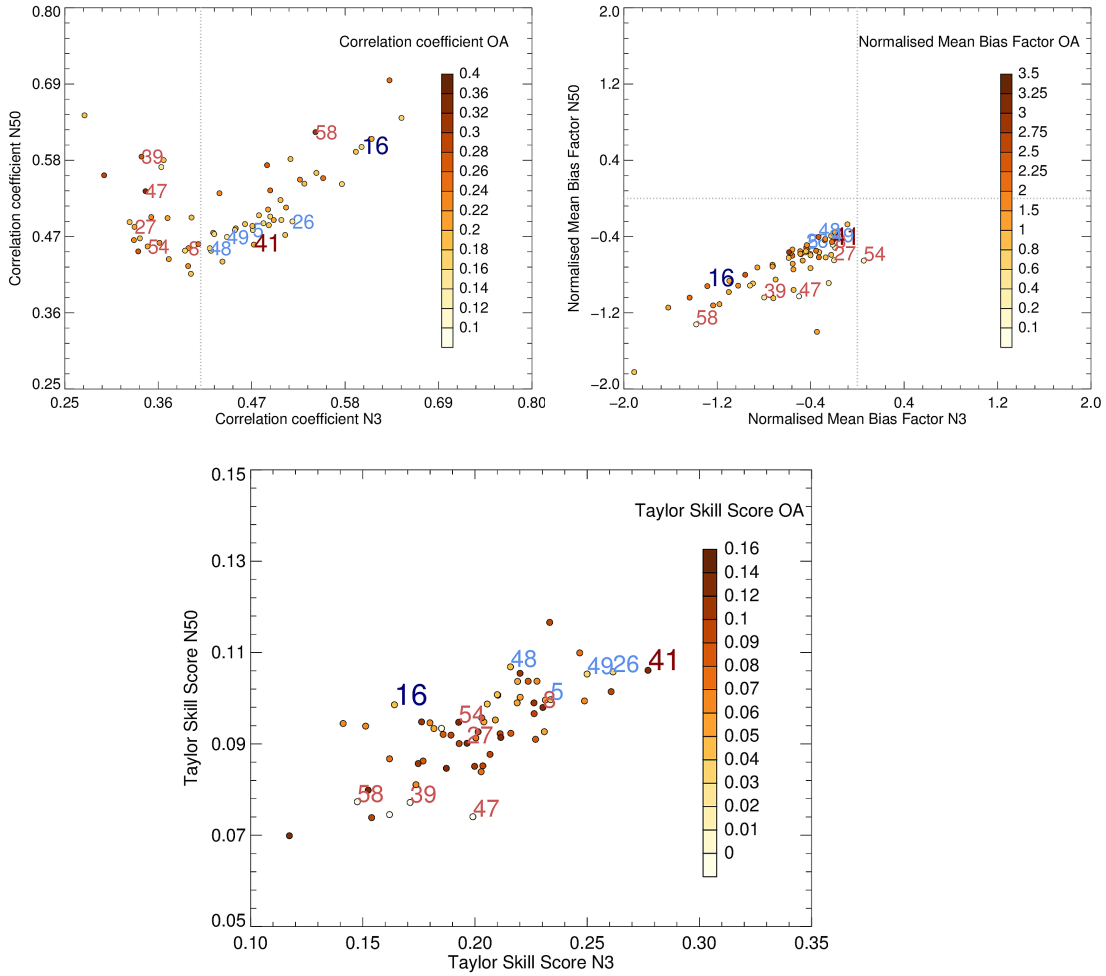

Figure 5.19: Relationship between the error metrics of model-observation comparison between the ensemble and observed N3, N50 and OA. The top left plot compares the Pearson correlation coefficient, the top right plot compares the Normalised Mean Bias Factor and the bottom plot compares the Taylor Skill Score for N3 (x-axis), N50 (y-axis) and OA (color scale). The best and the worst PPEM numbers are printed in dark red and dark blue respectively in each of the plots.

Figure 5.20 qualitatively portrays the performance of the entire ensemble (TSS) when compared to observed N3, N50 and OA at a glance. A bigger face corresponds to high (good) TSS_{N3}, a high vertical positioning of the mouth corresponds to high (good) TSS_{N3} and thinness of the jaw corresponds to a high (good) TSS_{OA}.

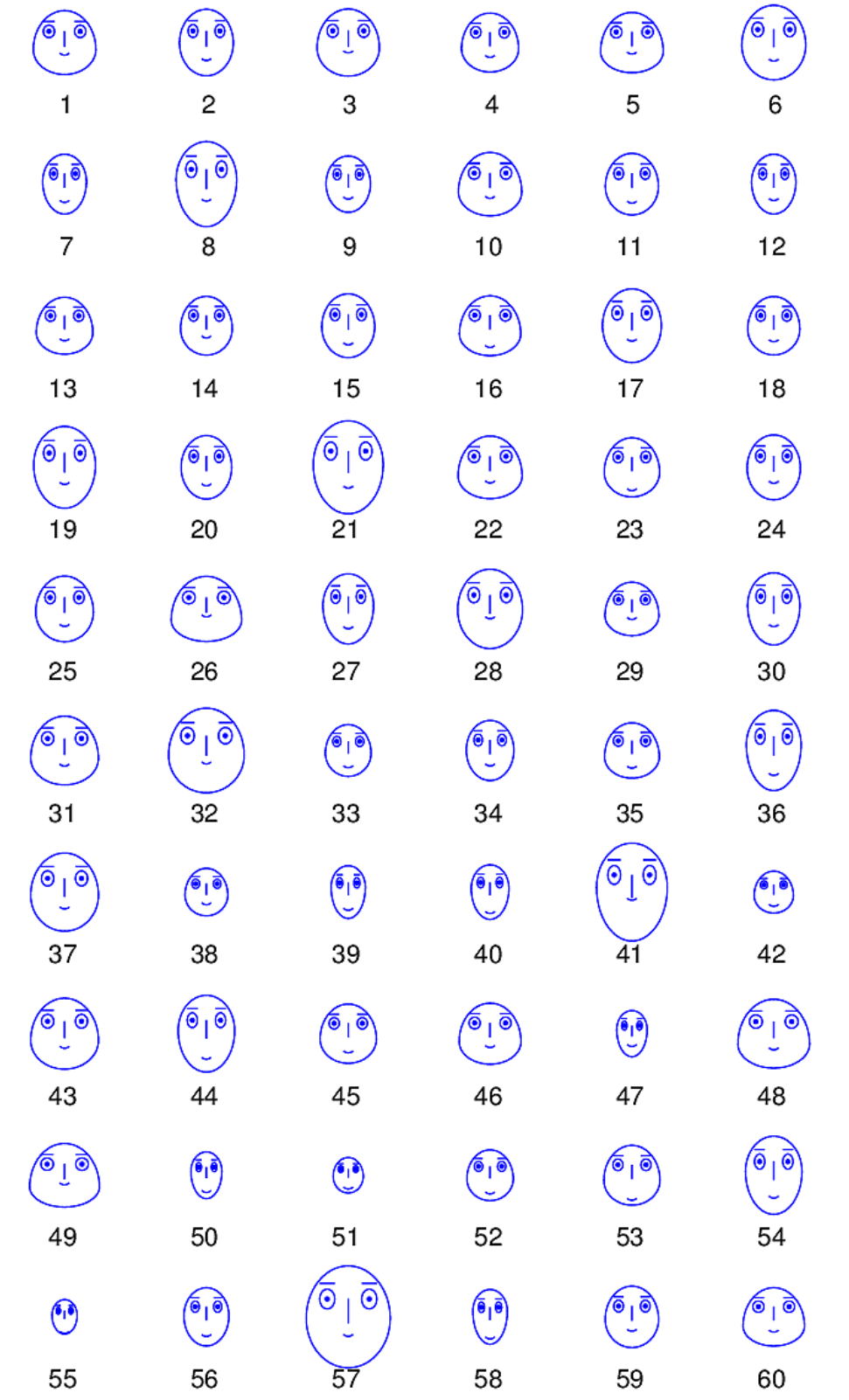

Figure 5.20: A qualitative representation of ensemble performance (Taylor Skill Score or TSS) against observations in N3, N50 and OA. Each face represents a PPEM wherein TSS_{N3} is indicated by the vertical position of the mouth, TSS_{N50} is indicated by the size of face and TSS_{OA} is indicated by the shape of jaw. The model with the best (highest) TSS_{N3}, TSS_{N50} and TSS_{OA} would be one with the biggest face, mouth positioned highest and the thinnest jaw.

5.3.6 The 6D perturbed parameter space

This section aims to reduce the uncertainty range for each of the ox-VOC parameters based on the ensemble performance against observations. Figures 5.21, 5.22 and 5.23 show the spacefilling design generated by the Latin hypercube sampling (Figure 5.2) where each PPEM is shaded according to its TSS for comparison against N3, N50 and OA. The plots identify parts of parameter space where it is plausible (or implausible) to get a good agreement between modelled and observed outputs of N3, N50 and OA. The PPEMs with increasingly good TSS score are represented by increasingly dark shades of red and the PPEMs with increasingly bad TSS score are represented by increasingly dark shades of blue.

A first-look at Figures 5.21, 5.22 and 5.23 show that the parts of the 6-D parameter space that produce good model-observation agreement for N3 or N50 tend to contradict with the parts of parameter space that produce a good model-observation agreement for OA. It is therefore common for models to predict observed number concentrations of particles reasonably well while greatly underestimating SOA production in the atmosphere. According to Figures 5.21, 5.22 and 5.23,

- TSS_{N3} has the strongest dependency on B_ELVOC, B_LVOC, A_LVOC.
- TSS_{N50} has the strongest dependency on B_LVOC, A_SVOC.
- TSS_{OA} has the strongest dependency on B_LVOC, B_SVOC_M.

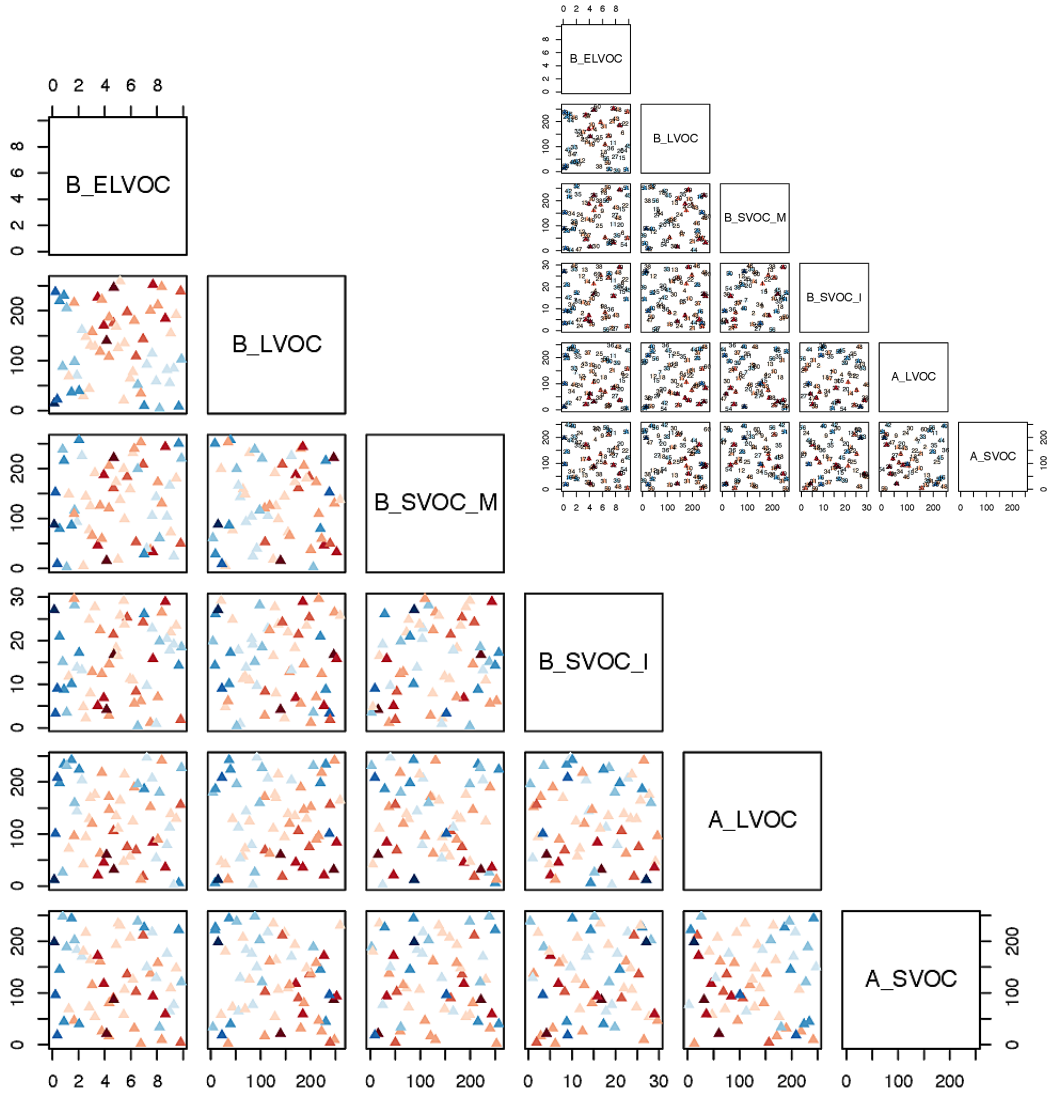

Figure 5.21: The 6-D space-filling design generated by the maximin Latin Hypercube Sampling (LHS) depicted in 2-D (as in Figure 5.2) and shaded according to the Taylor Skill Score of each experiment (as tabulated in Table 5.3). The x- and y-axes for a subplot show the total range of reaction yields (in %) over which each of the two parameters (as indicated by the plot labels at the top and right for each subplot respectively) is perturbed in the ensemble. Each point in a subplot represents a single simulation and the color of each point represents the TSS_{N3} of the simulation. Darker shades of blue indicate low/poor TSS and darker shades of red represent high/good TSS. The inset shows the same plot with ensemble members numbered.

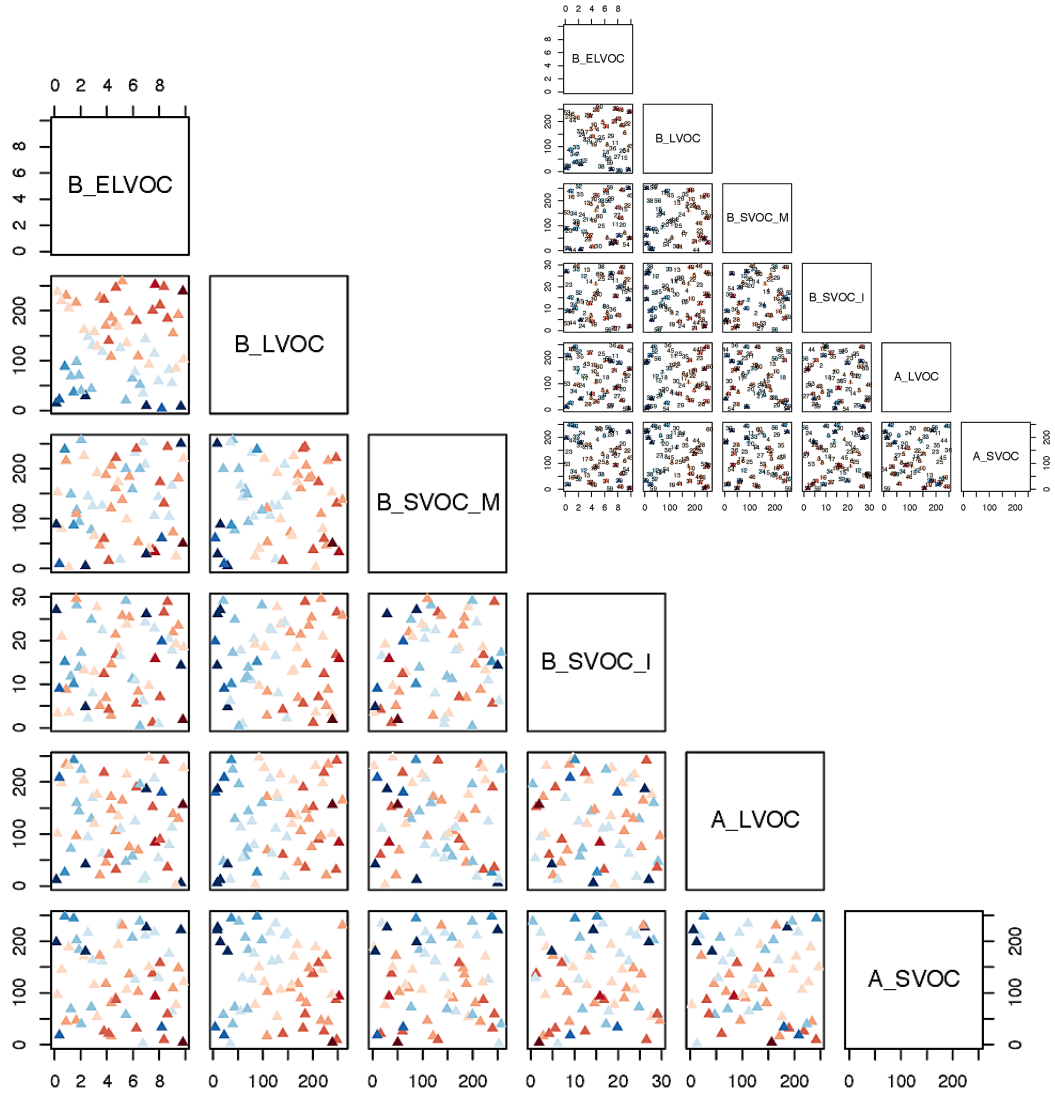

Figure 5.22: The 6-D space-filling design generated by the maximin Latin Hypercube Sampling (LHS) depicted in 2-D (as in Figure 5.2) and shaded according to the Taylor Skill Score of each experiment (as tabulated in Table 5.3). The x- and y-axes for a subplot show the total range of reaction yields (in %) over which each of the two parameters (as indicated by the plot labels at the top and right for each subplot respectively) is perturbed in the ensemble. Each point in a subplot represents a single simulation and the color of each point represents the TSS_{N50} of the simulation. Darker shades of blue indicate low/poor TSS and darker shades of red represent high/good TSS. The inset shows the same plot with ensemble members numbered.

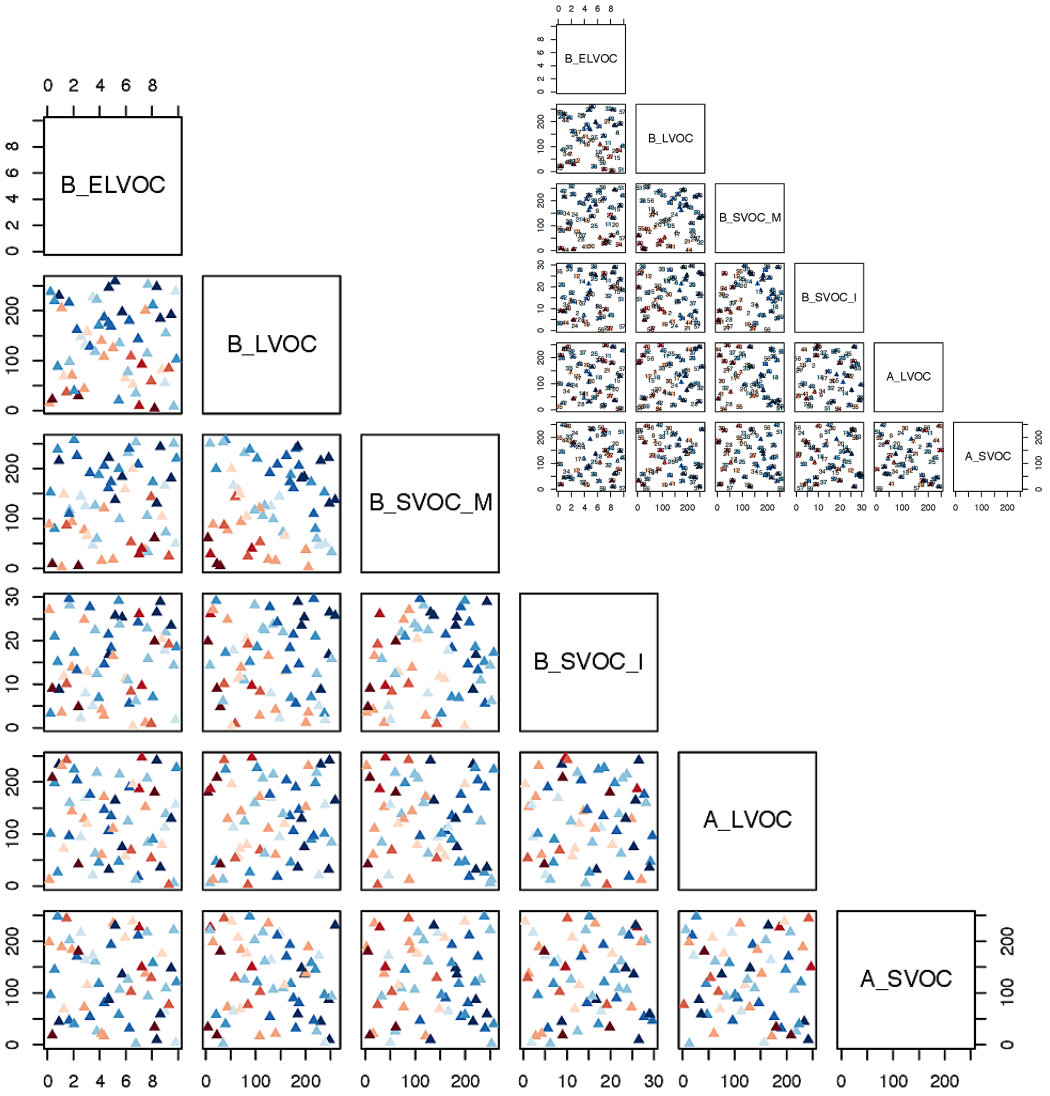

Figure 5.23: The 6-D space-filling design generated by the maximin Latin Hypercube Sampling (LHS) depicted in 2-D (as in Figure 5.2) and shaded according to the Taylor Skill Score of each experiment (as tabulated in Table 5.3). The x- and y-axes for a subplot show the total range of reaction yields (in %) over which each of the two parameters (as indicated by the plot labels at the top and right for each subplot respectively) is perturbed in the ensemble. Each point in a subplot represents a single simulation and the color of each point represents the TSS_{OA} of the simulation. Darker shades of blue indicate low/poor TSS and darker shades of red represent high/good TSS. The inset shows the same plot with ensemble members numbered.

A strong dependency of model performance (here, TSS) in a particular output (say for example N3) to a particular ox-VOC concentration (say for example B_ELVOC) in the model means :

- Of the 6 ox-VOCs, B_ELVOC is a dominant determinant of the model performance in N3.
- Improving B_ELVOC can largely (though never fully) improve a poor TSS_{N3}.
- Despite other ox-VOCs being represented realistically, if the representation of B_ELVOC is poor, the model performance in N3 is likely to be poor.
- The strong dependency of TSS_{N3} on B_ELVOC can be used to reduce the uncertainty in the parameter space of B_ELVOC. If more than one model output show strong dependency on one ox-VOC, its plausible (or implausible) parameter space can be narrowed down (or ruled out) with more confidence.

A weak dependency of model performance (here, TSS) in a particular output (say for example OA) to a particular ox-VOC concentration (say for example B_ELVOC) means :

- Of the 6 ox-VOCs, B_ELVOC is not a dominant determinant of the model performance in OA.
- Improving B_ELVOC can hardly (though may have an effect) improve a poor TSS_{OA}.
- With the other ox-VOCs are represented realistically, if the representation of B_ELVOC is poor, the model performance in OA is likely to be unaffected.
- The weak dependency of TSS_{OA} on B_ELVOC cannot be used to rule out parameter spaces of B_ELVOC completely. If all model outputs show weak dependency on one ox-VOC, its plausible (implausible) parameter space cannot be narrowed down (or ruled out) with confidence.

A weak dependency of model performance (for any output) on any ox-VOC does not necessarily mean the ox-VOC is unimportant to represent in the model. However it does mean its role in the model can be easily compensated for by another ox-VOC. It is difficult to infer upon the plausible parameter space for the yields of such ox-VOCs as irrespective of whether they have a high or low yield, the model performance (for that output) is largely determined by the values of the rest of the (stronger) ox-VOCs. Table 5.6 summarises which model outputs show a strong or medium or weak dependency on which ox-VOC based on Figures 5.21, 5.22 and 5.23.

ox-VOC	N3	N50	OA
B_ELVOC	**Strong**	Medium	Weak
B_LVOC	**Strong**	**Strong**	**Strong**
B_SVOC_M	Weak	Medium	**Strong**
B_SVOC_I	Weak	Weak	Weak
A_LVOC	**Strong**	Weak	Weak
A_SVOC	Weak	**Strong**	Weak

Table 5.6: Dependency of model performance (based on Taylor skill score) against observations in N3, N50 and OA (TSS_{N3}, TSS_{N50}, TSS_{OA}) to the ox-VOCs (B_ELVOC, B_LVOC, B_SVOC_M, B_SVOC_I, A_LVOC and A_SVOC) based on Figures 5.21, 5.22 and 5.23.

Figure 5.24 shows the 6-D parameter space in 1-D slices for each ox-VOC. The simulations covering the pre-defined ranges for each ox-VOC are shaded according to their performance in matching observed N3 (TSS_{N3}), N50 (TSS_{N50}) or OA (TSS_{OA}). The dependencies of model performance in different outputs are evident from Figure 5.24.

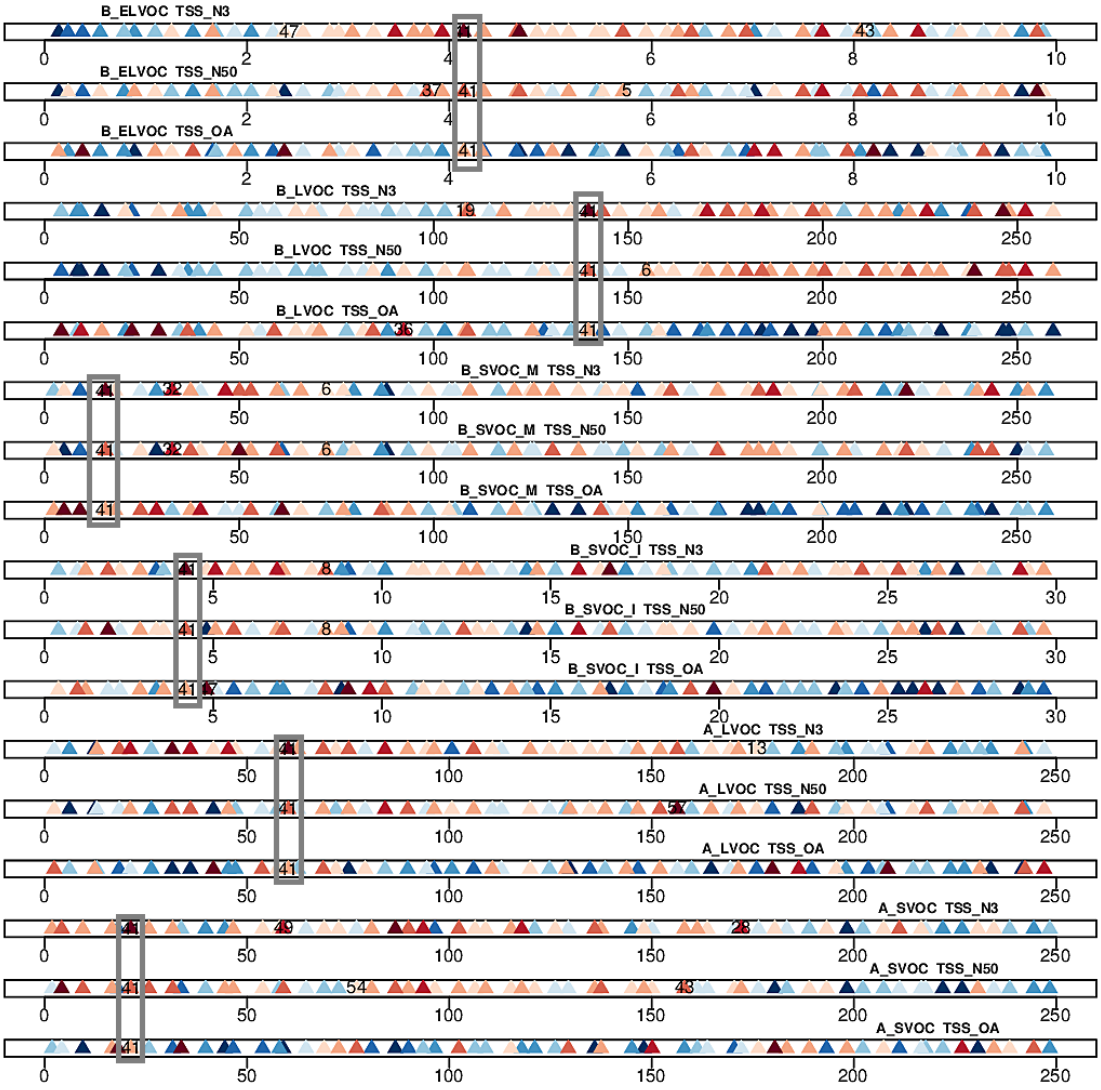

Figure 5.24: 1-D representation of the 6-D space filling design of experiments shaded by model performance. 18 subplots (labelled in plot) correspond to the design of experiments for six ox-VOCs, each shaded according to the Taylor skill score (TSS) in three model outputs (N3, N50, OA - in that order for each ox-VOC). Each subplot shows the entire pre-defined uncertainty range for the corresponding ox-VOC*. Each point on a subplot represents a single simulation and the color of the point indicates the performance of the simulation (TSS) against observed N3, N50 or OA. Darker shades of blue indicate low/poor TSS and darker shades of red represent high/good TSS. The plot identifies plausible and implausible parameter space for each ox-VOC. The PPEMs based on which the ranges are estimated in Table. 5.7 are labelled. The best simulation according to this study, PPEM 41, is also labelled and highlighted. PPEM 41 is representative of a region in the 6-D parameter space that reproduces the most realistic aerosol number *and* organic aerosol mass concentrations.

Note: Axis for B_ELVOC shows scaling factor for B_ELVOC yields. Axis for the rest show corresponding ox-VOC yields.

Based on Figure 5.24 the most plausible parameter space is identified for each parameter in Table. 5.7. The PPEMs based on which the ranges are determined are listed in the table and labelled in Figure 5.24.

Plausible parameter space for ox-VOC (%)	N3	N50	OA
B_ELVOC	2.36-8.06	3.78-5.71	-
based on PPEMs	47,43	37, 5	-
B_LVOC	>108	>154	<92.2
based on PPEMs	19	6	36
B_SVOC_M	32.7-72.4	32.7-72.4	<93.5
based on PPEMs	32, 6	32, 6	-
B_SVOC_I	<8.32	<8.32	<4.79
based on PPEMs	8	8	47
A_LVOC	<175.94	60.18-156.34	-
based on PPEMs	13	41, 57	-
A_SVOC	58.9-172.6	77-158.1	-
based on PPEMs	49,28	54,43	-

Table 5.7: Plausible parameter space for each ox-VOC based on the strength of relationship between ox-VOCs and model performance (Taylor Skill Score) in matching observed N3, N50 or OA as shown in Fig 5.24. The PPEMs based on which the ranges are determined, are labelled in Figure 5.24. *Note: Numbers for B_ELVOC correspond to scaling factor for B_ELVOC yields. Numbers for the rest of ox-VOCs correspond to absolute yields from bimolecular reactions.*

A model that scores high in matching both observed number (TSS_{N3}, TSS_{N50}) and mass concentrations (TSS_{OA}) requires the yield of ox-VOCs to lie within a thin belt of overlap in the 6-D space where the competing effects of ox-VOCs are minimised. The parameter settings for PPEM 41 is representative of that thin belt. The parameter combination in PPEM 41 is optimum for each ox-VOC leading to the best model-observation agreement in the 3 outputs considered in this study. The value of each ox-VOC with respect to the entire uncertainty range for each parameter in PPEM 41 can be seen from Figure 5.24. The prescribed parameter yields for GLOMAP-mode (as in Chapter 4), based on PPEM 41 is

- 4.14 times increase in current yield estimates of B_ELVOC i.e. about 13 % B_ELVOC from O_3 and 5 % from $OH^{\cdot}$,
- Yield of 139.75 % for B_LVOC (instead of 13 % in default model), producing 137.6 Tg yr^{-1} of SOA
- Yield of 15.59 % for B_SVOC_M (instead of 13 % in default model), producing 46.3 Tg yr^{-1} of SOA together with B_SVOC_I
- Yield of 4.17 % for B_SVOC_I (instead of 1.5 % in default model), producing 46.3 Tg yr^{-1} of SOA together with B_SVOC_M
- Yield of 60.18 % for A_LVOC (instead of 50 % in default model), producing 41 Tg yr^{-1} of SOA
- Yield of 21.25 % for A_SVOC (instead of 50 % in default model) producing 14.5 Tg yr^{-1} of SOA

In PPEM 41 the ratio of
$B\_ELVOC : B\_LVOC : B\_SVOC\_M : B\_SVOC\_I : A\_LVOC : A\_SVOC$
is $1 : 33.75 : 3.76 : 1 : 14.5 : 5.13$.
PPEM 41 produces 239 Tg yr^{-1} of SOA from ox-VOCs of which

76.7 % is from biogenic ox-VOCs (14 % from B_LVOC, 55.8 % from B_SVOC) and 23.2 % is from anthropogenic ox-VOCs (2.8 % from A_LVOC and 27.3 % from A_SVOC).

5.4 Conclusion

This study explores a wide range of parameter space for biogenic and anthropogenic ox-VOCs that produce atmospheric SOA using an ensemble of 60 model simulations. The range for each parameter is chosen on the basis of preliminary comparison to observations and the uncertainty range available in the literature, with the aim to encompass maximum uncertainty associated with each parameter. The model experiments are designed using the Latin Hypercube Sampling method to ensure optimum filling of the 6-D space. Simultaneous perturbation of the six parameters allow to assess the impact of combinations of parameters rather than individual parameters on model outputs. Three model outputs, N3, N50 and OA are compared against available observations and the model skill score is then used to reassess which parts of parameter space are most likely to result in the most realistic model. In conclusion, the questions posed at the start of this chapter are answered:

1. *Atmospheric organic molecules from single or multi-stage oxidation reactions of precursor VOCs (ox-VOCs) are known to span a large range of volatility. From a global modelling perspective, which ox-VOC interactions are necessary to simulate a realistic number concentration of particles along with the mass concentration of SOA? Which SOA production pathways (from ox-VOCs) are not crucial to account for?*

   To mimic the relationship between atmospheric ox-VOCs, global models need at least 3 categories of volatile organic compounds that have distinct roles to play in aerosol formation: ELVOC, LVOC and SVOC. B_ELVOC is neces-

sary for the formation of new particles from gaseous phase VOCs. Thereafter contributions from LVOCs and SVOCs contribute to the growth of these particles and allow the model to produce a realistic SOA mass. Without adequate B_ELVOC to *produce* particles via nucleation the model inevitably underestimates observed particle number concentrations irrespective of how much of other ox-VOCs are available for particle *growth*. The role of B_LVOC that grows the freshly nucleated particles is extremely crucial to ensure survival of nucleated clusters and for subsequent growth of the smaller particles in the model to CCN-relevant sizes. SVOCs (from monoterpene/isoprene/anthropogenic sources) are important to simulate realistic number concentrations of N50 and OA mass concentrations (Table. 5.6).

B_LVOC is by far the most important class of organic compound that strongly influences model-observation match in N3, N50 and OA. The difference in parameter setting between model simulations that produce high amount of OA despite particle number concentrations being low (PPEMs 16, 23, 35, 46) and those who do not (PPEMs 34, 55, 58) is the relative contribution of B_LVOC. Simulations in Group $L_{N3}M_{N50}$ in Table 5.2 show B_LVOC can, to an extent, compensate for low B_ELVOC. Relatively high concentrations of B_LVOC can ensure rapid growth of nucleated particles before they can be scavenged, thereby compensating to some extent for low B_ELVOC. This also means without representing B_LVOC adequately in models, introducing sophisticated nucleation mechanisms may greatly undermine the atmospheric impact of these mechanisms as the nucleated particles are lost before they can reach a climate-relevant size. Table 5.4 showing characteristics of PPEMs with poor TSS highlights the importance of an optimum coupling of B_ELVOC and B_LVOC to get good model-observation agreement. Thus it is important to identify and quantify atmospheric VOCs that can act as source of B_LVOCs.

Additionally it is important to explore the potential of anthropogenic sources of LVOC (A_LVOC) as such pathways could not only improve model-observation match but considerably impact model estimates of anthropogenic aerosol forcing by differentially affecting the present-day and pre-industrial atmospheres (Carslaw et al., 2013).

The importance of anthropogenic ox-VOCs is demonstrated by Figure 5.5 which highlights two model simulations producing similar total global SOA mass may differ substantially in regional simulations of OA mass concentrations. Model performance in simulating realistic N3 and N50 are highly dependent on A_LVOC and A_SVOC respectively (Figure 5.11, Figure 5.13, Table. 5.6). Given the strong dependency of TSS_{N3} on A_LVOC, future studies should aim to investigate the contribution of anthropogenic ox-VOCs to SOA, particularly their potential to nucleate and grow small clusters.

Based on the ensemble of 60 model simulations in this chapter it is concluded that global models should constrain the relationship between the ox-VOCs that result in realistic particle number **as well as** a realistic global distribution of organic aerosol mass rather than tune the model to get the best agreement in any one. A very good agreement in simulated and observed number concentration is very likely to be associated with a very poor agreement in mass concentrations and a compromise between the two must be made.

2. *How do additional complexities in chemical pathways of particle formation (which aim towards better model-observation agreement of particle number concentration), affect the model estimate of atmospheric SOA mass?*

The model underestimates observed particle number concentrations (Figures 5.15, 5.17) and overestimates OA concentrations (Figure 5.18). Figures 5.21, 5.22, 5.23 show model performance in all three outputs, N3, N50 and OA, are strongly dependent on B_LVOC concentrations. However while high values of B_LVOC are necessary to improve TSS_{N3} and TSS_{N50}, it worsens TSS_{OA}. The picture is further complicated by other ox-VOCs affecting the model performance in different outputs in different ways. Thus it is extremely challenging, though not impossible, to get **both** the modelled SOA and number concentrations right. This study identifies those parts of parameter space for each ox-VOC which are more plausible than others. It is not possible in a PPE study to isolate the effect of any one ox-VOC. However based on some strong dependencies shown by model outputs to particular ox-VOCs (Figure 5.24), an inference regarding the plausible parameter space is drawn and presented in Table. 5.7.

One of the ensemble members, PPEM 41, represents regions of the 6-D parameter space that leads to good model-observation match in N3, N50 and OA. The characteristics of PPEM 41 are described in section 5.3.6. The PPEM has high concentrations of both B_ELVOC and B_LVOC to produce and grow particle clusters. A relatively high B_LVOC and high A_LVOC sustain the growth of small particles in the nucleation mode, minimising their loss via coagulation with bigger particles. Increased nucleation and survival of small particles increase particles in the nucleation mode, improving TSS_{N3}. The moderate yields of SVOCs ensure growth of particles upto CCN relevant

sizes (improving TSS_{N50}) while ensuring not too many small particles are lost by coagulation with the bigger particles. Thus a balance is struck between producing particles, sustaining growth of small particles and growing bigger particles in PPEM 41 - all of which lead to a reasonable agreement between modelled and observed N3, N50 and OA. With TSS of 0.28, 0.11 and 0.14 for N3, N50 and OA, PPEM 41 has much scope for improvement. Nevertheless it exemplifies the characteristics required to improve SOA simulation in current models.

The other key findings of the study are listed below:

- A primary motivation behind this study is the significant uncertainty in estimation of the total SOA budget ranging from 12−1820 Tg yr^{-1} (Spracklen et al., 2011b). Models consistently fail to account for more than 70 Tg yr^{-1} of SOA (Kanakidou et al., 2005). In this study, within the parameter space explored, total global SOA ranges from 220−850 Tg yr^{-1}. PPEMs that simulate the highest SOA mass have comparable contributions from all the ox-VOCs. On the other hand overemphasizing the contribution of any one of the ox-VOCs while neglecting contributions from others leads to consistent underestimation of SOA. This is an important point to note as in most modelling studies (Mann et al., 2010; Riccobono et al., 2014; Gordon et al., 2016) - including Lee et al. (2013) which found modelled CCN is not very sensitive to biogenic ox-VOCs - models typically adopt an over-simplified approach (usually involving the traditional source of ox-VOC analogous to B_LVOC here) to simulate SOA (Shrivastava et al., 2016).

  The best estimate of SOA from this study, based on model-observation comparison of organic aerosol mass concentrations at 41 sites, is assessed to be between 220−337 Tg yr^{-1} which is within the range (50-380 Tg yr^{-1}) estimated

by Spracklen et al. (2011b). The PPEMs that simulate SOA within this range are PPEMs 8, 27, 39, 41, 47, 54, 58. Of these only PPEM 41 produces a good agreement with observed particle number as well (high TSS_{N3}, high TSS_{N50} and high TSS_{OA}) producing 239 Tg yr^{-1} SOA mass globally with an overall overestimation of a factor of 1.28 to observed OA mass concentrations.

- An important structural limitation of the model that has come forward in this study is the exaggeration of the annual cycle of particle number concentrations. An underestimation of particle number concentrations that is more pronounced in the winter months has been observed in previous studies such as Riccobono et al. (2014), Dunne et al. (2016), Gordon et al. (2016). This is evident from Figure 5.11 when the entire ensemble could not encompass the observed values. The inability to simulate the annual cycle is more pronounced in N3 than in N50 indicating it is related to a process that N3 is more sensitive to than N50. A worsening of R with the improvement of NMBF (Figure 5.11) implies potential future changes (increases) in the magnitude of B_ELVOC alone, by including more organic vapours from monoterpene to participate in particle formation, will not improve the simulated annual cycle of particle number concentrations. Fig 5.16 showing the monthly mean N3 simulated by the PPEMs with lowest and highest concentrations of N3 (global mean N3 531 and 1869 cm^{-3} respectively) against observed annual cycle of N3 at 34 locations, demonstrates the above.

The annual cycle simulated in the model (ground level) is highly influenced by the annual variations in monthly mean terpenes (also in Riccobono et al. (2014), Dunne et al. (2016), Gordon et al. (2016) and isoprene in this study) i.e. the seasonality in biogenic emissions is reflected in modelled N3 concentrations. In the atmosphere this would be highly dampened by influences from local or

transported anthropogenic emissions. The response of some anthropogenic sites in Figures 5.11 and 5.13 indicate a particle source that contributes most in the winter and least in summer - such as anthropogenic pollutants whose atmospheric concentrations are maximum in the winter due to low boundary layer height and increased local emissions from sources such as domestic heating - would balance the seasonal cycle in biogenic emissions and rectify the model bias significantly. It should also be noted that such changes are likely to have a greater climatic implication as anthropogenic sources of SOA would affect the pre-industrial and present-day atmosphere differently thereby increasing the relative difference and hence anthropogenic aerosol radiative forcing.

To summarise, it is important for global models to represent contributions of ELVOCs, LVOCs and SVOCs for realistic simulation of atmospheric SOA. Better agreement in modelled versus observed N3 can be achieved by reducing uncertainty in B_ELVOC, B_LVOC and A_LVOC. Better agreement in modelled versus observed N50 can be achieved by reducing uncertainty in B_LVOC and A_SVOC. Better agreement in modelled versus observed OA can be achieved by reducing uncertainty in B_LVOC and B_SVOC_M. Thus quantifying biogenic and anthropogenic sources of LVOCs is expected to lead to substantial improvement in all three outputs, N3, N50, OA. To improve the model-observation match for both simulated number concentrations (N3, N50) and simulated mass concentration (OA) is extremely challenging but not impossible. PPEM 41 exemplifies the parameter space and characteristics required for the above. Lastly, model-observation agreement in N3 and N50 are strongly dependent on the yields of ox-VOCs from anthropogenic sources making it vital to investigate the potential of anthropogenic VOCs to act as ELVOC, LVOC and SVOCs in the atmosphere.

Chapter 6

Discussions

6.1 Introduction

The CERN CLOUD chamber experiments conducted in 2013 laid the foundation of this thesis when it discovered that extremely low volatility oxidation products of biogenic volatile organic compounds (VOCs) alone can initiate particle formation in the atmosphere (Kirkby et al., 2016). This thesis set out to assess the climatic implication of pure biogenic nucleation and went on to introduce a new scheme of SOA formation from atmospheric VOCs in the model to reflect recent advances in the understanding of modelling secondary organic aerosol (SOA) chemistry (Spracklen et al., 2011b; Riipinen et al., 2012; Riccobono et al., 2014; Scott et al., 2015; Tröstl et al., 2016).

In Chapter 3 a parameterisation for pure biogenic nucleation was implemented in GLOMAP-mode to assess the climatic significance of extremely low volatility organic compounds (ELVOCs) that take part in nucleation. In Chapter 4 a new SOA formation scheme was implemented in GLOMAP-mode which additionally includes irreversible condensation of low volatility organic compounds (LVOCs) and mass-based partitioning of semi-volatile organic compounds (SVOCs) to aerosol particles.

In Chapter 5 an ensemble of 60 runs were analysed to evaluate the sensitivity of model performance in three outputs (number concentration of particles with dry diameter greater than 3 nm or N3, number concentration of particles with dry diameter greater than 50 nm or N50 and mass concentration of total organic aerosol or OA) to each of the VOC classes introduced in Chapter 4 and highlight plausible and implausible parameter space for each ox-VOC.

6.2 Summary of results

Chapter 3 set out to assess the climatic implications of pure biogenic nucleation of ELVOC. The main finding of this chapter is that including pure biogenic nucleation in a global aerosol model causes a reduction in the negative first indirect radiative forcing estimated due to anthropogenic aerosols. The global mean change in the first AIF is estimated to be +0.25 W m^{-2}, a 32.5 % reduction in the negative forcing from −0.8 W m^{-2} to −0.54 W m^{-2}.

The reduction in the (negative) radiative forcing due to anthropogenic aerosols is driven by a 19 % increase in the global mean CDNC concentrations in the pre-industrial atmosphere compared to a 6 % increase in the present-day. The results indicate that global models with heavily or entirely sulphuric acid-dependent nucleation mechanisms underestimate the cloud-aerosol interactions in the pre-industrial atmosphere when SO_2 concentrations were low. With pure biogenic nucleation to produce new particles in the model, the number concentration of CCN-sized N50 is found to increase by 47 % in the pre-industrial atmosphere compared to 14 % in the present-day.

Chapter 4 set out to assess the climatic implications of including a modified SOA formation scheme with biogenic and anthropogenic sources of LVOC and SVOCs,

along with the nucleating ELVOCs of Chapter 3, in a global aerosol model. The main finding of this chapter is that including SVOC and anthropogenic LVOC (in addition to biogenic LVOC and ELVOC) causes an increase in the negative radiative forcing estimated due to anthropogenic aerosols. The global mean change in the first AIF is estimated to be -0.29 W m^{-2}, a 49 % enhancement in the negative forcing from -0.59 W m^{-2} to -0.88 W m^{-2}. The enhancement in the (negative) radiative forcing due to anthropogenic aerosols is driven by a +15 % change in the present-day CDNC compared to +0.5 % change in the pre-industrial.

The increment of 49 % in the estimate of anthropogenic aerosol forcing occurs because anthropogenic LVOCs and biogenic and anthropogenic SVOCs in GLOMAP-mode suppress the effect of atmospheric nucleation and raise the number concentration of Aitken mode particles which grow up to CCN-relevant sizes. The preferential growth of larger particles by anthropogenic LVOCs and SVOCs in the model causes an increase of +16 % in the global annual mean Aitken mode dry diameter and +10 % in the global annual mean accumulation mode dry diameter. The preferential growth of larger particles in the model changes global annual mean nucleation mode particle number concentration (all particles below 10 nm) by -20 % and global annual mean Aitken mode particle number concentration (particles between 10-100 nm) by +11 %. This shows non-nucleating oxidation products of VOCs can be efficient modulators of the number concentration of CCN-sized aerosol particles in the atmopshere.

Further, additional condensable vapours in the gaseous phase leads more particles in the Aitken and accumulation modes to grow to CCN-relevant sizes. With the modified SOA scheme the model simulates 104 Tg y^{-1} of SOA (compared to 14 Tg y^{-1} SOA without the modified SOA scheme) which is close to the best estimate 140 Tg yr^{-1} given by Spracklen et al. (2011b) based on a study comparing modelled and

AMS measured organic aerosol.

Chapter 5 was motivated by two questions: (1) How much of the complexity in atmospheric SOA production chemistry (as introduced in Chapter 4) is necessary to represent in a global aerosol model? (2) With new nucleation mechanisms aimed to better estimate the aerosol number concentration and eventually CDNC and first AIF, are global models moving towards simulating the right amount of SOA? Results from this chapter establish the need to represent at least three categories of atmospheric organic compounds: those that take part in nucleation (ELVOC), those that grow nucleated clusters by irreversible condensation (LVOC) and those that partition on bigger particles (SVOC). Secondly the study identifies parts of parameter space where the parameter settings of ELVOC, LVOCs and SVOCs produce a reasonable model-observation agreement in particle number concentration *and* aerosol mass, and parts of parameter space where they do not.

Chapter 5 shows that due to the competing effects of ELVOC, LVOC and SVOCs in a global model it is relatively easy for models to realistically simulate either the number or the mass concentrations of aerosol particles and extremely challenging to get both right. Given the various different sources of uncertainty in a global model, attempts to improve model performance against observations for one output might lead to worsening model performance against observations in another. As an example, Chapter 5 identifies parameter settings that result in improved agreement of simulated and observed total particle number concentrations (an output commonly used by the modelling community to assess model performance) but simultaneously worsen the prediction of observed CCN-relevant particles or mass of organic aerosol. Chapter 5 identifies the narrow belt within the 6-D parameter space where the best compromise is reached. Chapter 5 also puts forward one ensemble member which exemplifies this parameter space and results in reasonable model-observation match

in all three outputs.

Overall this thesis demonstrates the necessity for global models to represent the contribution of atmospheric VOCs of varying volatilities on different parts of the aerosol size distribution in order to simulate realistic particle number and aerosol mass concentrations and estimate of the first AIF.

6.3 Broader implication

This thesis for the first time assesses the significance of a nucleation mechanism driven by biogenic ELVOCs alone (Gordon et al., 2016). The inclusion of this nucleation mechanisms in global models raises the baseline pre-industrial aerosol concentration and causes a reduction of 31 % in the first AIF (estimated to be 27 % in Gordon et al., 2016). Including pure biogenic nucleation in global models will shift the entire probability distribution of radiative forcings estimated by various models because this nucleation scheme adds more particles in the pre-industrial atmosphere. Pure biogenic nucleation is shown to be an important link that can improve the extrapolation of present-day atmospheric state to pre-industrial times in global models that estimate climate forcing. Chapter 3 re-emphasizes the importance of careful representation of the pre-industrial atmosphere in global models (Carslaw et al., 2013). It is suggested herein following Hamilton et al. (2014) that future observations in the more pristine Southern Hemisphere be made to better understand particle formation and growth in the pre-industrial atmosphere. Such understanding would significantly improve estimates of the climatic impacts of anthropogenic aerosols in the Northern Hemisphere.

This thesis for the first time assesses the significance of a SOA formation scheme in GLOMAP-mode that takes into account contributions from oxidation products

of biogenic and anthropogenic VOCs (ox-VOCs) through three distinct pathways: particle nucleation, particle growth via condensation and particle growth via mass-based partitioning. Chapter 4 builds on from the conclusions of Spracklen et al. (2011b) wherein the significance of anthropogenic VOCs in SOA formation was ascertained and those of Scott et al. (2015) which for the first time explored the effect of two different approaches of SOA formation in GLOMAP-mode. Chapter 4 quantifies the effect of more volatile organic compounds (particularly the semi-volatile) on the aerosol size distribution and highlights the significance of representing SVOCs in simulating realistic CCN-relevant particles alongside the nucleating (assumed non-volatile) VOCs in global models. Since SVOCs are abundant in the atmosphere, even a small fraction of SVOCs growing relatively large particles in the atmosphere makes this an efficient pathway of CCN-production.

This thesis for the first time highlights plausible and implausible regions in a 6-D parameter space of ox-VOCs, that contribute to SOA via different pathways, based on the sensitivity of model skill score in simulating N3, N50 and OA. The SOA formation scheme applied in Chapter 4, uses a first approximation of the amounts of each of the 6 ox-VOCs that contribute to SOA via three different pathways. In reality although nucleating ELVOCs are now identified in the atmosphere and their yields quantified, there is still considerable uncertainty regarding how representative these yields are of the atmosphere (Ehn et al., 2012, 2014; Kirkby et al., 2016; Gordon et al., 2016). To date, there has been no quantification of SOA production from LVOCs and SVOCs (Donahue et al., 2006; Tröstl et al., 2016).

Chapter 5 takes a top-down view of the uncertainty space associated with the 6 ox-VOCs and gives an estimate of each ox-VOC based on optimum model-observation agreement in all three outputs - N3, N50 and OA. In particular, Chapter 5 suggests biogenic ELVOC yields be a factor of 2 to 8 higher than that estimated by Kirkby

et al. (2016). This is in agreement with Ehn et al. (2012) who reported ELVOC production at 6−8 % molar yields with a ±50 % uncertainty. The ELVOC yield estimated from this study indicates more experimental studies need to be conducted to identify ELVOC sources other than α-pinene ozonolysis (Jokinen et al., 2015). Chapter 5 also demonstrates the critical importance of biogenic LVOCs that grow sub-3 nm clusters in a global aerosol model, often compensating for lower amounts of nucleating ELVOCs. Failure to represent realistic LVOC concentrations in global models leads to unrealistic loss of nucleated clusters (which though produced, fail to grow up to consequential sizes) thereby undermining the significance of a nucleation mechanism. It is therefore important that future experimental studies identify atmospheric molecules that may act as LVOC (Kulmala et al., 2014; Tröstl et al., 2016). Chapter 5 shows the model skill in simulating N3 is more sensitive to A_LVOC that kinetically condenses while the skill in simulating N50 is more sensitive to A_SVOC that undergoes mass-based partitioning - demonstrating that it is important to represent both processes in global models (Riipinen et al., 2011; Scott et al., 2015).

6.4 Recommendations for future research

1. *Improvement in the parameterisation of ELVOC nucleation*

   The nucleation mechanism currently used in this thesis linearly adds the nucleation rates calculated from ternary nucleation of sulphuric acid and organic molecules derived from oxidation by $OH^{\cdot}$ and the nucleation rates calculated from binary nucleation mechanism involving monoterpene ozonolysis products only, due to inadequate experimental data to allow a ternary sulphuric acid-organic parameterisation.

   Riccobono et al. (2014) showed that considerable uncertainty in model outputs and forcing estimates may be caused by the varying dependence of a

nucleation mechanism on the same vapours. Further, in the atmosphere the yields of ELVOCs and their nucleating potential are bound to be affected by the presence of other vapours which may compete for the same gaseous phase oxidants or aerosol particle surface. It is therefore important that both the sulphuric acid-dependent and sulphuric acid-independent parameterisations take into account the behaviour of the same organic molecules and realistically reflect the dependence of ELVOC nucleation on sulphuric acid concentrations.

Further, understanding the dependence between nucleating ELVOCs and sulphuric acid in the laboratory could potentially highlight the conditions required to observe pure biogenic nucleation in the present-day atmosphere (when sulphuric acid concentrations are abundant) and obtain more realistic baseline aerosol concentrations for the modelling community (Carslaw et al., 2013; Spracklen and Rap, 2013; Hamilton et al., 2014).

2. *Implementation of a single nucleation parameterisation reflecting the interaction of amines and ammonia along with sulphuric acid and organic compounds*
The nucleation mechanism currently used in this thesis does not include contributions from ammonia or amines. Atmospheric nucleation rates differ significantly in different environments (Kulmala et al., 2004; Holmes, 2007). Future laboratory experiments are needed to calculate realistic nucleation rates under varying atmospheric conditions of temperature and relative humidity in the presence of sulphuric acid, ammonia, amines, organic compounds and ions. Such a parameterisation would realistically reflect the regional variation in the availability of precursor gases for nucleation and particle growth rather than assume a single particle formation mechanism globally. Dunne et al. (2016), based on the results of the CERN CLOUD experiment, studied the effect of ternary nucleation of ammonia-sulphuric acid and that of organic compounds-

sulphuric acid on modelled aerosol number. However Dunne et al. (2016), like this thesis, 'added' nucleation rates from different parameterisations. The cloud-albedo forcing estimated in this thesis, Dunne et al. (2016); Gordon et al. (2016) can be more realistically estimated if the nucleation parameterisation reflected the complex interaction between all participating vapours and atmospheric conditions.

3. *Investigation of the role of anthropogenic VOCs in SOA formation*

   An important structural limitation in the model identified in Chapter 5 is the exaggerated seasonal cycle of N50 and particularly N3, simulated in several locations worldwide. An indication of this limitation had been seen in previous studies (Riccobono et al., 2014; Dunne et al., 2016; Gordon et al., 2016) and in previous chapters (Chapters 3 and 4) of this thesis when the model consistently underestimated N3 in the winter. After exploring a wide range of ox-VOC concentrations in Chapter 5 it is found that the issue is not just the underestimation of N3 in winter but also the over-estimation of N3 in the summer. Simulations that improve the low model bias in particle number worsen the correlation coefficient because higher ox-VOCs result in high number of particles in the summer only. The exaggeration of seasonal cycle may be linked to uncertainty in primary carbonaceous emissions in the model which in earlier studies have been found to be a major contributor to uncertainty in modelled CCN (Lee et al., 2013).

   Chapter 5 shows that the correlation coefficient between model and observation worsens with improvement in the model bias - the worsening being more in modelled N3 than in modelled N50. This indicates the issue is likely to be associated with the simulation of number concentrations of smaller particles in the model. Currently the seasonal cycle of particles is highly influenced by the

seasonal variation in emissions of biogenic VOCs which peak in the summer. In a study including nucleation from organic compounds, ammonia and sulphuric acid, Dunne et al. (2016) suggests ternary organic nucleation is a major source of particles in the summer whereas in winter ternary ammonia nucleation (not included in this thesis) is the major source. In contrast to biogenic VOCs, anthropogenic VOC emissions and concentrations peak in the winter months favoured by low mixing heights, low winds and clear sky conditions (Strader et al., 1999; Na et al., 2005). Lee et al. (2013) found anthropogenically controlled SOA had a greater effect on CCN uncertainty than biogenic SOA, and the widespread hemispheric effect was particularly enhanced in winter. Recent studies (Ehn et al., 2017; Wang et al., 2017) suggest new HOM formation pathways from autoxidation of anthropogenic aromatic compounds, to date missing from models simulating atmospheric SOA. It is suggested herein that including boundary layer nucleation or cluster growth from anthropogenic VOCs or other trace gases such as ammonia in GLOMAP-mode may rectify the issue of simulating an exaggerated seasonal cycle of particles. More research on the atmospheric chemistry of anthropogenic VOCs, including pathways of HOM formation (Ehn et al., 2017), are necessary before this suggestion can be validated. However it is worth noting that if discovered to be a significant source of ELVOC or LVOC, anthropogenic ox-VOCs will have a considerable impact on model estimates of aerosol radiative forcing by differentially affecting the pre-industrial and present-day atmospheres.

4. *Improvement in the model's dry deposition scheme*

   The model is found to overestimate the total organic aerosol concentrations throughout the ensemble in Chapter 5. The work done in this thesis relates only to the secondary fraction of total aerosols derived from ox-VOCs and hence does not allow to be conclusive as to the cause of overestimation in

modelled OA (which icludes primary + secondary OA) concentrations. However it is plausible that an overestimation of OA concentrations is linked to an underestimation in the removal rate of accumulation mode particles via dry deposition. Dry deposition was identified as the most important contributor to modelled CCN uncertainty in Lee et al. (2013); Carslaw et al. (2013). Hodzic et al. (2013) found dry deposition of gaseous phase organic compounds to compete with the uptake of these gases by the aerosol phase. Hodzic et al. (2014) shows removal of SOA and gaseous phase condensable from the atmosphere is dominated by the dry deposition of semi-volatile organic compounds and model results of surface OA are consistent with ambient observations when removal of SVOCs are considered. Dry deposition affects modelled aerosol concentrations all over the globe (Lee et al., 2013). Developments in the removal schemes of condensable ox-VOCs or aerosol particles in the model, may therefore lead to a better match between measured and modelled OA.

5. *Build emulators to obtain full probability density function of model outputs*
Chapter 5 uses Latin Hypercube Sampling to create a space-filling design for 60 simulations. The 60 simulations represent 60 combinations of ox-VOC parameter settings within the 6-D space and provide information about the effect of those 60 combinations on model performance in simulating N3, N50 and OA. Using the same 60 simulations emulators can be built (Lee et al., 2011; Johnson et al., 2015). The advantage of building emulators to do variance-based sensitivity analysis is that emulators can be used to assess every possible combination in the parameter space (whereas the results of Chapter 5 are based on 60 distinct simulations that represent a diverse combination of parameters). Emulators can provide an entire probability density function of N3, N50, OA for every model grid box for each month. This may then be used to rank the ox-VOCs according to their contribution to uncertainty in each grid box to

investigate regional differences closely. Further, the study can be extended to quantify the entire probability distribution function of estimated cloud-albedo forcing pertaining to the 6-D parameter space of oxygenated VOCs.

Bibliography

Abdul-Razzak, H. and Ghan, S. J. (2000). A parameterization of aerosol activation: 2. multiple aerosol types. *Journal of Geophysical Research: Atmospheres*, 105(D5):6837–6844.

Aiken, A. C., Decarlo, P. F., Kroll, J. H., Worsnop, D. R., Huffman, J. A., Docherty, K. S., Ulbrich, I. M., Mohr, C., Kimmel, J. R., Sueper, D., et al. (2008). O/c and om/oc ratios of primary, secondary, and ambient organic aerosols with high-resolution time-of-flight aerosol mass spectrometry. *Environmental Science & Technology*, 42(12):4478–4485.

Ainsworth, E. A., Yendrek, C. R., Sitch, S., Collins, W. J., and Emberson, L. D. (2012). The effects of tropospheric ozone on net primary productivity and implications for climate change. *Annual review of plant biology*, 63:637–661.

Almeida, J., Downard, A. J., Flagan, R. C., and Seinfeld, J. H. (2013). Molecular understanding of sulphuric acid–amine particle nucleation in the atmosphere. *Nature*, 502(7471):359–363.

Anderson, T. L., Charlson, R. J., Schwartz, S. E., Knutti, R., Boucher, O., Rodhe, H., and Heintzenberg, J. (2003). Climate forcing by aerosols–a hazy picture. *Science*, 300(5622):1103–1104.

Andreae, M. O. and Crutzen, P. J. (1997). Atmospheric aerosols: Biogeochemical sources and role in atmospheric chemistry. *Science*, 276(5315):1052–1058.

Andres, R. and Kasgnoc, A. (1998). A time-averaged inventory of subaerial volcanic sulfur emissions. *Journal of Geophysical Research: Atmospheres*, 103(D19):25251–25261.

Appel, K. W., Bhave, P. V., Gilliland, A. B., Sarwar, G., and Roselle, S. J. (2008). Evaluation of the community multiscale air quality (cmaq) model version 4.5: sensitivities impacting model performance; part iiâĂŤparticulate matter. *Atmospheric Environment*, 42(24):6057–6066.

Arnold, S., Chipperfield, M., and Blitz, M. (2005). A three-dimensional model study of the effect of new temperature-dependent quantum yields for acetone photolysis. *Journal of Geophysical Research: Atmospheres*, 110(D22).

Asmi, E., Kivekäs, N., Kerminen, V.-M., Komppula, M., Hyvärinen, A.-P., Hatakka, J., Viisanen, Y., and Lihavainen, H. (2011). Secondary new particle formation in northern finland pallas site between the years 2000 and 2010. *Atmospheric Chemistry and Physics*, 11(24):12959–12972.

Atkinson, R. (2000). Atmospheric chemistry of VOCs and NOx. *Atmospheric environment*, 34(12):2063–2101.

Atkinson, R. and Arey, J. (2003). Gas-phase tropospheric chemistry of biogenic volatile organic compounds: a review. *Atmospheric Environment*, 37:197–219.

Atkinson, R., Baulch, D., Cox, R., Crowley, J., Hampson, R., Hynes, R., Jenkin, M., Rossi, M., Troe, J., and Subcommittee, I. (2006). Evaluated kinetic and photochemical data for atmospheric chemistry: Volume ii–gas phase reactions of organic species. *Atmospheric Chemistry and Physics*, 6(11):3625–4055.

Baek, S.-O. and Jenkins, R. A. (2004). Characterization of trace organic compounds associated with aged and diluted sidestream tobacco smoke in a controlled

atmosphere-volatile organic compounds and polycyclic aromatic hydrocarbons. *Atmospheric Environment*, 38(38):6583–6599.

Bakshi, S., He, Z. L., and Harris, W. G. (2015). Natural nanoparticles: implications for environment and human health. *Critical Reviews in Environmental Science and Technology*, 45(8):861–904.

Ball, S., Hanson, D., Eisele, F., and McMurry, P. (1999). Laboratory studies of particle nucleation: Initial results for H2SO4, H2O, and NH3 vapors. *Journal of Geophysical Research: Atmospheres*, 104(D19):23709–23718.

Barsanti, K. C., Kroll, J. H., and Thornton, J. A. (2017). Formation of low-volatility organic compounds in the atmosphere: Recent advancements and insights. *The Journal of Physical Chemistry Letters*, 8(7):1503–1511.

Benson, D. R., Erupe, M. E., and Lee, S.-H. (2009). Laboratory-measured H2SO4-H2O-NH3 ternary homogeneous nucleation rates: Initial observations. *Geophysical Research Letters*, 36(15).

Benson, D. R., Young, L.-H., Kameel, F. R., and Lee, S.-H. (2008). Laboratory-measured nucleation rates of sulfuric acid and water binary homogeneous nucleation from the SO2+OH reaction. *Geophysical Research Letters*, 35(11).

Berndt, T., Böge, O., Stratmann, F., Heintzenberg, J., and Kulmala, M. (2005). Rapid formation of sulfuric acid particles at near-atmospheric conditions. *Science*, 307(5710):698–700.

Berndt, T., Stratmann, F., Sipilä, M., Vanhanen, J., Petäjä, T., Mikkilä, J., Grüner, A., Spindler, G., Mauldin III, L., Curtius, J., et al. (2010). Laboratory study on new particle formation from the reaction OH+SO2: influence of experimental conditions, H2O vapour, NH3 and the amine tert-butylamine on the overall process. *Atmospheric Chemistry and Physics*, 10(15):7101–7116.

Bigi, A. and Ghermandi, G. (2011). Particle number size distribution and weight concentration of background urban aerosol in a po valley site. *Water, Air, & Soil Pollution*, 220(1-4):265–278.

Birmili, W., Berresheim, H., Plass-Dülmer, C., Elste, T., Gilge, S., Wiedensohler, A., and Uhrner, U. (2003). The hohenpeissenberg aerosol formation experiment (HAFEX): a long-term study including size-resolved aerosol, H2SO4, OH, and monoterpenes measurements. *Atmospheric Chemistry and Physics*, 3(2):361–376.

Birmili, W. and Wiedensohler, A. (2000). New particle formation in the continental boundary layer: Meteorological and gas phase parameter influence. *Geophysical Research Letters*, 27(20):3325–3328.

Bond, T. C., Streets, D. G., Yarber, K. F., Nelson, S. M., Woo, J.-H., and Klimont, Z. (2004). A technology-based global inventory of black and organic carbon emissions from combustion. *Journal of Geophysical Research: Atmospheres*, 109(D14).

Boucher, O., Randall, D., Artaxo, P., Bretherton, C., Feingold, G., Forster, P., Kerminen, V.-M., Kondo, Y., Liao, H., Lohmann, U., et al. (2013). Clouds and aerosols. In *Climate change 2013: the physical science basis. Contribution of Working Group I to the Fifth Assessment Report of the Intergovernmental Panel on Climate Change*, pages 571–657. Cambridge University Press.

Boy, M. and Kulmala, M. (2002). Nucleation events in the continental boundary layer: Influence of physical and meteorological parameters. *Atmospheric Chemistry and Physics*, 2(1):1–16.

Boy, M., Kulmala, M., Ruuskanen, T. M., Pihlatie, M., Reissell, A., Aalto, P. P., Keronen, P., Maso, M. D., Hellen, H., Hakola, H., et al. (2005). Sulphuric acid closure and contribution to nucleation mode particle growth. *Atmospheric Chemistry and Physics*, 5(4):863–878.

Browse, J., Carslaw, K., Schmidt, A., and Corbett, J. (2013). Impact of future arctic shipping on high-latitude black carbon deposition. *Geophysical Research Letters*, 40(16):4459–4463.

Canagaratna, M., Jayne, J., Jimenez, J., Allan, J., Alfarra, M., Zhang, Q., Onasch, T., Drewnick, F., Coe, H., Middlebrook, A., et al. (2007). Chemical and microphysical characterization of ambient aerosols with the aerodyne aerosol mass spectrometer. *Mass Spectrometry Reviews*, 26(2):185–222.

Carlton, A., Wiedinmyer, C., and Kroll, J. (2009). A review of secondary organic aerosol (SOA) formation from isoprene. *Atmospheric Chemistry and Physics*, 9(14):4987–5005.

Carslaw, K., Lee, L., Reddington, C., Pringle, K., Rap, A., Forster, P., Mann, G., Spracklen, D., Woodhouse, M., Regayre, L., et al. (2013). Large contribution of natural aerosols to uncertainty in indirect forcing. *Nature*, 503(7474):67–71.

Carver, G. D., Brown, P. D., and Wild, O. (1997). The asad atmospheric chemistry integration package and chemical reaction database. *Computer Physics Communications*, 105(2-3):197–215.

Chang, R.-W., Slowik, J., Shantz, N., Vlasenko, A., Liggio, J., Sjostedt, S., Leaitch, W., and Abbatt, J. (2010). The hygroscopicity parameter (κ) of ambient organic aerosol at a field site subject to biogenic and anthropogenic influences: relationship to degree of aerosol oxidation. *Atmospheric Chemistry and Physics*, 10(11):5047–5064.

Charlson, R. J., Seinfeld, J. H., Nenes, A., Kulmala, M., Laaksonen, A., and Facchini, M. C. (2001). Reshaping the theory of cloud formation. *Science*, 292(5524):2025–2026.

Charney, J. G., Arakawa, A., Baker, D. J., Bolin, B., Dickinson, R. E., Goody, R. M., Leith, C. E., Stommel, H. M., and Wunsch, C. I. (1979). *Carbon dioxide and climate: a scientific assessment.* National Academy of Sciences, Washington, DC.

Chipperfield, M. (2006). New version of the tomcat/slimcat off-line chemical transport model: Intercomparison of stratospheric tracer experiments. *Quarterly Journal of the Royal Meteorological Society*, 132(617):1179–1203.

Chow, J. C., Watson, J. G., Doraiswamy, P., Chen, L.-W. A., Sodeman, D. A., Lowenthal, D. H., Park, K., Arnott, W. P., and Motallebi, N. (2009). Aerosol light absorption, black carbon, and elemental carbon at the fresno supersite, california. *Atmospheric Research*, 93(4):874–887.

Claeys, M., Graham, B., Vas, G., Wang, W., Vermeylen, R., Pashynska, V., Cafmeyer, J., Guyon, P., Andreae, M. O., Artaxo, P., et al. (2004). Formation of secondary organic aerosols through photooxidation of isoprene. *Science*, 303(5661):1173–1176.

Clarke, A., Davis, D., Kapustin, V., Eisele, F., Chen, G., Paluch, I., Lenschow, D., Bandy, A., Thornton, D., Moore, K., et al. (1998). Particle nucleation in the tropical boundary layer and its coupling to marine sulfur sources. *Science*, 282(5386):89–92.

Coakley, J., Hansen, J., and Hofmann, D. (1992). Climate forcing by anthropogenic aerosols. *Science*, 255(5043):423–430.

Cofala, J., Amann, M., Klimont, Z., and Schopp, W. (2005). Scenarios of world anthropogenic emissions of SO2, NOx, and CO up to 2030. *International Institute for Applied Systems Analysis, Laxenburg.*

Coffman, D. J., Hegg, D., et al. (1995). A preliminary study of the effect of ammonia on particle nucleation in the marine boundary layer. *Journal of Geophysical Research: Atmospheres*, 100(D4):7147–7160.

Corrigan, C. and Novakov, T. (1999). Cloud condensation nucleus activity of organic compounds: a laboratory study. *Atmospheric Environment*, 33(17):2661–2668.

D'Andrea, S., Häkkinen, S., Westervelt, D., Kuang, C., Levin, E., Kanawade, V., Leaitch, W., Spracklen, D., Riipinen, I., and Pierce, J. (2013). Understanding global secondary organic aerosol amount and size-resolved condensational behavior. *Atmospheric Chemistry and Physics*, 13(22):11519–11534.

De Gouw, J. and Jimenez, J. L. (2009). Organic aerosols in the earthâĂŹs atmosphere.

De Gouw, J., Middlebrook, A., Warneke, C., Goldan, P., Kuster, W., Roberts, J., Fehsenfeld, F., Worsnop, D., Canagaratna, M., Pszenny, A., et al. (2005). Budget of organic carbon in a polluted atmosphere: Results from the new england air quality study in 2002. *Journal of Geophysical Research: Atmospheres*, 110(D16).

Dentener, F., Kinne, S., Bond, T., Boucher, O., Cofala, J., Generoso, S., Ginoux, P., Gong, S., Hoelzemann, J., Ito, A., et al. (2006). Emissions of primary aerosol and precursor gases in the years 2000 and 1750 prescribed data-sets for aerocom. *Atmospheric Chemistry and Physics*, 6(12):4321–4344.

Ding, X., Wang, X.-M., Gao, B., Fu, X.-X., He, Q.-F., Zhao, X.-Y., Yu, J.-Z., and Zheng, M. (2012). Tracer-based estimation of secondary organic carbon in the pearl river delta, south china. *Journal of Geophysical Research: Atmospheres*, 117(D5).

Donahue, N., Robinson, A., Stanier, C., and Pandis, S. (2006). Coupled partitioning,

dilution, and chemical aging of semivolatile organics. *Environmental Science & Technology*, 40(8):2635–2643.

Donahue, N. M., Epstein, S., Pandis, S. N., and Robinson, A. L. (2011). A two-dimensional volatility basis set: 1. organic-aerosol mixing thermodynamics. *Atmospheric Chemistry and Physics*, 11(7):3303–3318.

Donahue, N. M., Hartz, K. E. H., Chuong, B., Presto, A. A., Stanier, C. O., Rosenhørn, T., Robinson, A. L., and Pandis, S. N. (2005). Critical factors determining the variation in SOA yields from terpene ozonolysis: A combined experimental and computational study. *Faraday Discussions*, 130:295–309.

Donahue, N. M., Kroll, J., Pandis, S. N., and Robinson, A. L. (2012). A two-dimensional volatility basis set–part 2: Diagnostics of organic-aerosol evolution. *Atmospheric Chemistry and Physics*, 12(2):615–634.

Donahue, N. M., Robinson, A. L., and Pandis, S. N. (2009). Atmospheric organic particulate matter: From smoke to secondary organic aerosol. *Atmospheric Environment*, 43(1):94–106.

Dunne, E. M., Gordon, H., Kürten, A., Almeida, J., Duplissy, J., Williamson, C., Ortega, I. K., Pringle, K. J., Adamov, A., Baltensperger, U., et al. (2016). Global atmospheric particle formation from cern cloud measurements. *Science*, 354(6316):1119–1124.

Echalar, F., Artaxo, P., Martins, J. V., Yamasoe, M., Gerab, F., Maenhaut, W., and Holben, B. (1998). Long-term monitoring of atmospheric aerosols in the amazon basin: Source identification and apportionment. *Journal of Geophysical Research: Atmospheres*, 103(D24):31849–31864.

Edwards, J. and Slingo, A. (1996). Studies with a flexible new radiation code. i:

Choosing a configuration for a large-scale model. *Quarterly Journal of the Royal Meteorological Society*, 122(531):689–719.

Ehn, M., Berndt, T., Wildt, J., and Mentel, T. (2017). Highly oxygenated molecules from atmospheric autoxidation of hydrocarbons: A prominent challenge for chemical kinetics studies. *International Journal of Chemical Kinetics*, 49(11):821–831.

Ehn, M., Kleist, E., Junninen, H., Petäjä, T., Lönn, G., Schobesberger, S., Maso, M. D., Trimborn, A., Kulmala, M., Worsnop, D., et al. (2012). Gas phase formation of extremely oxidized pinene reaction products in chamber and ambient air. *Atmospheric Chemistry and Physics*, 12(11):5113–5127.

Ehn, M., Thornton, J. A., Kleist, E., Sipilä, M., Junninen, H., Pullinen, I., Springer, M., Rubach, F., Tillmann, R., Lee, B., et al. (2014). A large source of low-volatility secondary organic aerosol. *Nature*, 506(7489):476–479.

Engelhart, G., Asa-Awuku, A., Nenes, A., and Pandis, S. (2008). CCN activity and droplet growth kinetics of fresh and aged monoterpene secondary organic aerosol. *Atmospheric Chemistry and Physics*, 8(14):3937–3949.

Farina, S. C., Adams, P. J., and Pandis, S. N. (2010). Modeling global secondary organic aerosol formation and processing with the volatility basis set: Implications for anthropogenic secondary organic aerosol. *Journal of Geophysical Research: Atmospheres*, 115(D9).

Fischer, E., Ziemba, L., Talbot, R., Dibb, J. E., Griffin, R. J., Husain, L., and Grant, A. (2007). Aerosol major ion record at mount washington. *Journal of Geophysical Research: Atmospheres*, 112(D2).

Forster, P., Ramaswamy, V., Artaxo, P., Berntsen, T., Betts, R., Fahey, D. W., Haywood, J., Lean, J., Lowe, D. C., Myhre, G., et al. (2007). Changes in atmo-

spheric constituents and in radiative forcing. chapter 2. In *Climate Change 2007. The Physical Science Basis*.

Fountoukis, C. and Nenes, A. (2005). Continued development of a cloud droplet formation parameterization for global climate models. *Journal of Geophysical Research: Atmospheres*, 110(D11).

Gentner, D. R., Isaacman, G., Worton, D. R., Chan, A. W., Dallmann, T. R., Davis, L., Liu, S., Day, D. A., Russell, L. M., Wilson, K. R., et al. (2012). Elucidating secondary organic aerosol from diesel and gasoline vehicles through detailed characterization of organic carbon emissions. *Proceedings of the National Academy of Sciences*, 109(45):18318–18323.

Goldstein, A. H. and Galbally, I. E. (2007). Known and unexplored organic constituents in the earth's atmosphere.

Gong, S. (2003). A parameterization of sea-salt aerosol source function for sub-and super-micron particles. *Global biogeochemical cycles*, 17(4).

Gordon, H., Kirkby, J., Baltensperger, U., Bianchi, F., Breitenlechner, M., Curtius, J., Dias, A., Dommen, J., Donahue, N. M., Dunne, E. M., et al. (2017). Causes and importance of new particle formation in the present-day and pre-industrial atmospheres. *Journal of Geophysical Research: Atmospheres*.

Gordon, H., Sengupta, K., Rap, A., Duplissy, J., Frege, C., Williamson, C., Heinritzi, M., Simon, M., Yan, C., Almeida, J., et al. (2016). Reduced anthropogenic aerosol radiative forcing caused by biogenic new particle formation. *Proceedings of the National Academy of Sciences*, 113(43):12053–12058.

Graedel, T. (1979). Terpenoids in the atmosphere. *Reviews of Geophysics*, 17(5):937–947.

Granier, C., Bessagnet, B., Bond, T., DâĂŹAngiola, A., van Der Gon, H. D., Frost, G. J., Heil, A., Kaiser, J. W., Kinne, S., Klimont, Z., et al. (2011). Evolution of anthropogenic and biomass burning emissions of air pollutants at global and regional scales during the 1980–2010 period. *Climatic Change*, 109(1-2):163.

Grieshop, A. P., Miracolo, M. A., Donahue, N. M., and Robinson, A. L. (2009). Constraining the volatility distribution and gas-particle partitioning of combustion aerosols using isothermal dilution and thermodenuder measurements. *Environmental science & technology*, 43(13):4750–4756.

Grosjean, D. and Friedlander, S. K. (1975). Gas-particle distribution factors for organic and other pollutants in the los angeles atmosphere. *Journal of the Air Pollution Control Association*, 25(10):1038–1044.

Guenther, A., Hewitt, C. N., Erickson, D., Fall, R., Geron, C., Graedel, T., Harley, P., Klinger, L., Lerdau, M., McKay, W., et al. (1995). A global model of natural volatile organic compound emissions. *Journal of Geophysical Research: Atmospheres*, 100(D5):8873–8892.

Guenther, A., Jiang, X., Heald, C., Sakulyanontvittaya, T., Duhl, T., Emmons, L., and Wang, X. (2012). The model of emissions of gases and aerosols from nature version 2.1 (megan2. 1): an extended and updated framework for modeling biogenic emissions.

Guenther, C. (2006). Estimates of global terrestrial isoprene emissions using megan (model of emissions of gases and aerosols from nature). *Atmospheric Chemistry and Physics*, 6.

Gunthe, S., King, S., Rose, D., Chen, Q., Roldin, P., Farmer, D., Jimenez, J., Artaxo, P., Andreae, M., Martin, S., et al. (2009). Cloud condensation nuclei in pristine tropical rainforest air of amazonia: size-resolved measurements and

modeling of atmospheric aerosol composition and CCN activity. *Atmospheric Chemistry and Physics*, 9(19):7551–7575.

Hallquist, M., Wenger, J., Baltensperger, U., Rudich, Y., Simpson, D., Claeys, M., Dommen, J., Donahue, N., George, C., Goldstein, A., et al. (2009). The formation, properties and impact of secondary organic aerosol: current and emerging issues. *Atmospheric Chemistry and Physics*, 9(14):5155–5236.

Halmer, M. M., Schmincke, H.-U., and Graf, H.-F. (2002). The annual volcanic gas input into the atmosphere, in particular into the stratosphere: a global data set for the past 100 years. *Journal of Volcanology and Geothermal Research*, 115(3-4):511–528.

Hamilton, D. S., Lee, L. A., Pringle, K. J., Reddington, C. L., Spracklen, D. V., and Carslaw, K. S. (2014). Occurrence of pristine aerosol environments on a polluted planet. *Proceedings of the National Academy of Sciences*, 111(52):18466–18471.

Hansen, J., Sato, M., Lacis, A., and Ruedy, R. (1997). The missing climate forcing. *Philosophical Transactions of the Royal Society of London B: Biological Sciences*, 352(1350):231–240.

Heald, C. L., Jacob, D. J., Park, R. J., Russell, L. M., Huebert, B. J., Seinfeld, J. H., Liao, H., and Weber, R. J. (2005). A large organic aerosol source in the free troposphere missing from current models. *Geophysical Research Letters*, 32(18).

Henze, D., Seinfeld, J., Ng, N., Kroll, J., Fu, T.-M., Jacob, D. J., and Heald, C. (2008). Global modeling of secondary organic aerosol formation from aromatic hydrocarbons: high-vs. low-yield pathways. *Atmospheric Chemistry and Physics*, 8(9):2405–2420.

Henze, D. K. and Seinfeld, J. H. (2006). Global secondary organic aerosol from isoprene oxidation. *Geophysical Research Letters*, 33(9).

Hodzic, A., Aumont, B., Knote, C., Lee-Taylor, J., Madronich, S., and Tyndall, G. (2014). Volatility dependence of henry's law constants of condensable organics: Application to estimate depositional loss of secondary organic aerosols. *Geophysical Research Letters*, 41(13):4795–4804.

Hodzic, A., Madronich, S., Aumont, B., Lee-Taylor, J., Karl, T., Camredon, M., and Mouchel-Vallon, C. (2013). Limited influence of dry deposition of semivolatile organic vapors on secondary organic aerosol formation in the urban plume. *Geophysical Research Letters*, 40(12):3302–3307.

Holmes, N. S. (2007). A review of particle formation events and growth in the atmosphere in the various environments and discussion of mechanistic implications. *Atmospheric Environment*, 41(10):2183–2201.

Hoppel, W., Frick, G., Fitzgerald, J., and Larson, R. (1994). Marine boundary layer measurements of new particle formation and the effects nonprecipitating clouds have on aerosol size distribution. *Journal of Geophysical Research: Atmospheres*, 99(D7):14443–14459.

Hoyle, C., Boy, M., Donahue, N., Fry, J., Glasius, M., Guenther, A., Hallar, A., Huff Hartz, K., Petters, M., Petäjä, T., et al. (2011). A review of the anthropogenic influence on biogenic secondary organic aerosol. *Atmospheric Chemistry and Physics*, 11(1):321–343.

Hyvärinen, A.-P., Lihavainen, H., Komppula, M., Panwar, T., Sharma, V., Hooda, R., and Viisanen, Y. (2010). Aerosol measurements at the gual pahari EUCAARI station: preliminary results from in-situ measurements. *Atmospheric Chemistry and Physics*, 10(15):7241–7252.

Jacobson, M., Hansson, H.-C., Noone, K., and Charlson, R. (2000). Organic atmospheric aerosols: Review and state of the science. *Reviews of Geophysics*, 38(2):267–294.

Jacobson, M. Z., Tabazadeh, A., and Turco, R. P. (1996). Simulating equilibrium within aerosols and nonequilibrium between gases and aerosols. *Journal of Geophysical Research: Atmospheres*, 101(D4):9079–9091.

Jathar, S., Farina, S., Robinson, A., and Adams, P. (2011). The influence of semi-volatile and reactive primary emissions on the abundance and properties of global organic aerosol. *Atmospheric Chemistry and Physics*, 11(15):7727–7746.

Jimenez, J., Canagaratna, M., Donahue, N., Prevot, A., Zhang, Q., Kroll, J. H., DeCarlo, P. F., Allan, J. D., Coe, H., Ng, N., et al. (2009). Evolution of organic aerosols in the atmosphere. *Science*, 326(5959):1525–1529.

Johnson, D., Utembe, S., Jenkin, M., Derwent, R., Hayman, G., Alfarra, M., Coe, H., and McFiggans, G. (2006). Simulating regional scale secondary organic aerosol formation during the torch 2003 campaign in the southern UK. *Atmospheric Chemistry and Physics*, 6(2):403–418.

Johnson, J., Cui, Z., Lee, L., Gosling, J., Blyth, A., and Carslaw, K. (2015). Evaluating uncertainty in convective cloud microphysics using statistical emulation. *Journal of Advances in Modeling Earth Systems*, 7(1):162–187.

Jokinen, T., Berndt, T., Makkonen, R., Kerminen, V.-M., Junninen, H., Paasonen, P., Stratmann, F., Herrmann, H., Guenther, A. B., Worsnop, D. R., et al. (2015). Production of extremely low volatile organic compounds from biogenic emissions: Measured yields and atmospheric implications. *Proceedings of the National Academy of Sciences*, 112(23):7123–7128.

Jonsson, Å. M., Hallquist, M., and Ljungström, E. (2006). Impact of humidity on the ozone initiated oxidation of limonene, δ3-carene, and α-pinene. *Environmental science & technology*, 40(1):188–194.

Kanakidou, M., Seinfeld, J., Pandis, S., Barnes, I., Dentener, F., Facchini, M., Dingenen, R. V., Ervens, B., Nenes, A., Nielsen, C., et al. (2005). Organic aerosol and global climate modelling: a review. *Atmospheric Chemistry and Physics*, 5(4):1053–1123.

Kerminen, V.-M. and Kulmala, M. (2002). Analytical formulae connecting the âĂIJrealâĂİ and the âĂIJapparentâĂİ nucleation rate and the nuclei number concentration for atmospheric nucleation events. *Journal of Aerosol Science*, 33(4):609–622.

Kesselmeier, J. and Staudt, M. (1999). Biogenic volatile organic compounds (VOC): an overview on emission, physiology and ecology. *Journal of atmospheric chemistry*, 33(1):23–88.

Kettle, A. and Andreae, M. (2000). Flux of dimethylsulfide from the oceans: A comparison of updated data sets and flux models. *Journal of Geophysical Research: Atmospheres*, 105(D22):26793–26808.

Kiehl, J. and Briegleb, B. (1993). The relative roles of sulfate aerosols and greenhouse gases in climate forcing. *Science*, 260(5106):311–314.

Kiendler-Scharr, A., Wildt, J., Dal Maso, M., Hohaus, T., Kleist, E., Mentel, T. F., Tillmann, R., Uerlings, R., Schurr, U., and Wahner, A. (2009). New particle formation in forests inhibited by isoprene emissions. *Nature*, 461(7262):381.

Kirkby, J., Curtius, J., Almeida, J., Dunne, E., Duplissy, J., Ehrhart, S., Franchin, A., Gagné, S., Ickes, L., Kürten, A., et al. (2011). Role of sulphuric acid, ammonia and galactic cosmic rays in atmospheric aerosol nucleation. *Nature*, 476(7361):429–433.

Kirkby, J., Duplissy, J., Sengupta, K., Frege, C., Gordon, H., Williamson, C., Hein-

ritzi, M., Simon, M., Yan, C., Almeida, J., et al. (2016). Ion-induced nucleation of pure biogenic particles. *Nature*, 533(7604):521–526.

Kleffmann, J., Gavriloaiei, T., Hofzumahaus, A., Holland, F., Koppmann, R., Rupp, L., Schlosser, E., Siese, M., and Wahner, A. (2005). Daytime formation of nitrous acid: A major source of oh radicals in a forest. *Geophysical Research Letters*, 32(5).

Koch, D. and Del Genio, A. (2010). Black carbon semi-direct effects on cloud cover: review and synthesis. *Atmospheric Chemistry and Physics*, 10(16):7685–7696.

Kroll, J. H., Ng, N. L., Murphy, S. M., Flagan, R. C., and Seinfeld, J. H. (2005). Secondary organic aerosol formation from isoprene photooxidation under high-nox conditions. *Geophysical Research Letters*, 32(18).

Kroll, J. H., Ng, N. L., Murphy, S. M., Flagan, R. C., and Seinfeld, J. H. (2006). Secondary organic aerosol formation from isoprene photooxidation. *Environmental science & technology*, 40(6):1869–1877.

Kuang, C., McMurry, P., McCormick, A., and Eisele, F. (2008). Dependence of nucleation rates on sulfuric acid vapor concentration in diverse atmospheric locations. *Journal of Geophysical Research: Atmospheres*, 113(D10).

Kulmala, M. (2003). How particles nucleate and grow. *Science*, 302(5647):1000–1001.

Kulmala, M., Kerminen, V.-M., Anttila, T., Laaksonen, A., and O'Dowd, C. D. (2004). Organic aerosol formation via sulphate cluster activation. *Journal of Geophysical Research: Atmospheres*, 109(D4).

Kulmala, M., Kontkanen, J., Junninen, H., Lehtipalo, K., Manninen, H. E., Nieminen, T., Petäjä, T., Sipilä, M., Schobesberger, S., Rantala, P., et al. (2013). Direct observations of atmospheric aerosol nucleation. *Science*, 339(6122):943–946.

Kulmala, M., Laaksonen, A., and Pirjola, L. (1998). Parameterizations for sulfuric acid/water nucleation rates. *Journal of Geophysical Research: Atmospheres*, 103(D7):8301–8307.

Kulmala, M., Lehtinen, K., and Laaksonen, A. (2006). Cluster activation theory as an explanation of the linear dependence between formation rate of 3nm particles and sulphuric acid concentration. *Atmospheric Chemistry and Physics*, 6(3):787–793.

Kulmala, M., Maso, M. D., Mäkelä, J., Pirjola, L., Väkevä, M., Aalto, P., Miikkulainen, P., Hämeri, K., and O'Dowd, C. (2001). On the formation, growth and composition of nucleation mode particles. *Tellus B: Chemical and Physical Meteorology*, 53(4):479–490.

Kulmala, M., Petäjä, T., Ehn, M., Thornton, J., Sipilä, M., Worsnop, D., and Kerminen, V.-M. (2014). Chemistry of atmospheric nucleation: on the recent advances on precursor characterization and atmospheric cluster composition in connection with atmospheric new particle formation. *Annual review of physical chemistry*, 65:21–37.

Kulmala, M., Pirjola, L., and Mäkelä, J. M. (2000). Stable sulphate clusters as a source of new atmospheric particles. *Nature*, 404(6773):66–69.

Kurtén, T., Loukonen, V., Vehkamäki, H., and Kulmala, M. (2008). Amines are likely to enhance neutral and ion-induced sulfuric acid-water nucleation in the atmosphere more effectively than ammonia. *Atmospheric Chemistry and Physics*, 8(14):4095–4103.

La, Y., Camredon, M., Ziemann, P., Valorso, R., Matsunaga, A., Lannuque, V., Lee-Taylor, J., Hodzic, A., Madronich, S., and Aumont, B. (2016). Impact of chamber wall loss of gaseous organic compounds on secondary organic aerosol

formation: explicit modeling of SOA formation from alkane and alkene oxidation. *Atmospheric Chemistry and Physics*, 16(3):1417–1431.

Laakso, L., Mäkelä, J. M., Pirjola, L., and Kulmala, M. (2002). Model studies on ion-induced nucleation in the atmosphere. *Journal of Geophysical Research: Atmospheres*, 107(D20).

Laakso, L., Merikanto, J., Vakkari, V., Laakso, H., Kulmala, M., Molefe, M., Kgabi, N., Mabaso, D., Carslaw, K., Spracklen, D., et al. (2013). Boundary layer nucleation as a source of new CCN in savannah environment. *Atmospheric Chemistry and Physics*, 13(4):1957–1972.

Lamarque, J.-F., Bond, T. C., Eyring, V., Granier, C., Heil, A., Klimont, Z., Lee, D., Liousse, C., Mieville, A., Owen, B., et al. (2010). Historical (1850–2000) gridded anthropogenic and biomass burning emissions of reactive gases and aerosols: methodology and application. *Atmospheric Chemistry and Physics*, 10(15):7017–7039.

Lavanchy, V., Gäggeler, H., Nyeki, S., and Baltensperger, U. (1999). Elemental carbon (EC) and black carbon (BC) measurements with a thermal method and an aethalometer at the high-alpine research station jungfraujoch. *Atmospheric Environment*, 33(17):2759–2769.

Leck, C. and Bigg, E. K. (2010). New particle formation of marine biological origin. *Aerosol Science and Technology*, 44(7):570–577.

Lee, L., Carslaw, K., Pringle, K., and Mann, G. (2012). Mapping the uncertainty in global CCN using emulation. *Atmospheric Chemistry and Physics*, 12(20):9739–9751.

Lee, L., Carslaw, K., Pringle, K., Mann, G., and Spracklen, D. (2011). Emulation

of a complex global aerosol model to quantify sensitivity to uncertain parameters. *Atmospheric Chemistry and Physics*, 11(23):12253–12273.

Lee, L., Pringle, K., Reddington, C., Mann, G., Stier, P., Spracklen, D., Pierce, J., and Carslaw, K. (2013). The magnitude and causes of uncertainty in global model simulations of cloud condensation nuclei. *Atmospheric Chemistry and Physics*, 13(17):8879.

Lee, L. A., Reddington, C. L., and Carslaw, K. S. (2016). On the relationship between aerosol model uncertainty and radiative forcing uncertainty. *Proceedings of the National Academy of Sciences*, 113(21):5820–5827.

Lee, S.-H., Reeves, J., Wilson, J., Hunton, D., Viggiano, A., Miller, T., Ballenthin, J., and Lait, L. (2003). Particle formation by ion nucleation in the upper troposphere and lower stratosphere. *Science*, 301(5641):1886–1889.

Levy, H., Horowitz, L. W., Schwarzkopf, M. D., Ming, Y., Golaz, J.-C., Naik, V., and Ramaswamy, V. (2013). The roles of aerosol direct and indirect effects in past and future climate change. *Journal of Geophysical Research: Atmospheres*, 118(10):4521–4532.

Liu, X. and Wang, J. (2010). How important is organic aerosol hygroscopicity to aerosol indirect forcing? *Environmental Research Letters*, 5(4):044010.

Lovejoy, E., Curtius, J., and Froyd, K. (2004). Atmospheric ion-induced nucleation of sulfuric acid and water. *Journal of Geophysical Research: Atmospheres*, 109(D8).

Lyubovtseva, Y. S., Zagaynov, V., Khodzher, T., Kulmala, M., Boy, M., Dal Maso, M., Junninen, H., Obolkin, V., Potyomkin, V., Biryukov, Y. G., et al. (2010). Comparison of formation conditions of secondary aerosol particles in boreal forests of southern finland and siberia. *Russian Journal of Earth Sciences*, 11(4):1–11.

Mäkelä, J., Aalto, P., Jokinen, V., Pohja, T., Nissinen, A., Palmroth, S., Markkanen, T., Seitsonen, K., Lihavainen, H., and Kulmala, M. (1997). Observations of ultrafine aerosol particle formation and growth in boreal forest. *Geophysical Research Letters*, 24(10):1219–1222.

Makkonen, R., Asmi, A., Korhonen, H., Kokkola, H., Järvenoja, S., Räisänen, P., Lehtinen, K., Laaksonen, A., Kerminen, V.-M., Järvinen, H., et al. (2008). Sensitivity of aerosol concentrations and cloud properties to nucleation and secondary organic distribution in ECHAM5-HAM global circulation model. *Atmospheric Chemistry and Physics Discussions*, 8(3):10955–10998.

Mann, G., Carslaw, K., Spracklen, D., Ridley, D., Manktelow, P., Chipperfield, M., Pickering, S., and Johnson, C. (2010). Description and evaluation of GLOMAP-mode: A modal global aerosol microphysics model for the UKCA composition-climate model. *Geoscientific Model Development*, 3(2):519–551.

Marais, E. A., Jacob, D. J., Jimenez, J. L., Campuzano-Jost, P., Day, D. A., Hu, W., Krechmer, J., Zhu, L., Kim, P. S., Miller, C. C., et al. (2016). Aqueous-phase mechanism for secondary organic aerosol formation from isoprene: Application to the southeast united states and co-benefit of so 2 emission controls. *Atmospheric Chemistry and Physics*, 16(3):1603–1618.

Marais, E. A., Jacob, D. J., Turner, J. R., and Mickley, L. J. (2017). Evidence of 1991–2013 decrease of biogenic secondary organic aerosol in response to so2 emission controls. *Environmental Research Letters*, 12(5):054018.

Martin, S. T., Andreae, M. O., Artaxo, P., Baumgardner, D., Chen, Q., Goldstein, A. H., Guenther, A., Heald, C. L., Mayol-Bracero, O. L., McMurry, P. H., et al. (2010). Sources and properties of amazonian aerosol particles. *Reviews of Geophysics*, 48(2).

Matsunaga, S., Mochida, M., and Kawamura, K. (2003). Growth of organic aerosols by biogenic semi-volatile carbonyls in the forestal atmosphere. *Atmospheric Environment*, 37(15):2045–2050.

Matsunaga, S., Wiedinmyer, C., Guenther, A., Orlando, J., Karl, T., Toohey, D., Greenberg, J., and Kajii, Y. (2005). Isoprene oxidation products are a significant atmospheric aerosol component. *Atmospheric Chemistry and Physics Discussions*, 5(6):11143–11156.

McMurry, P. and Friedlander, S. (1979). New particle formation in the presence of an aerosol. *Atmospheric Environment (1967)*, 13(12):1635–1651.

McMurry, P. H., Fink, M., Sakurai, H., Stolzenburg, M., Mauldin, R., Smith, J., Eisele, F., Moore, K., Sjostedt, S., Tanner, D., et al. (2005). A criterion for new particle formation in the sulfur-rich atlanta atmosphere. *Journal of Geophysical Research: Atmospheres*, 110(D22).

Menon, S., Hansen, J., Nazarenko, L., and Luo, Y. (2002). Climate effects of black carbon aerosols in china and india. *Science*, 297(5590):2250–2253.

Merikanto, J., Spracklen, D., Mann, G., Pickering, S., and Carslaw, K. (2009). Impact of nucleation on global CCN. *Atmospheric Chemistry and Physics*, 9(21):8601–8616.

Merikanto, J., Spracklen, D., Pringle, K., and Carslaw, K. (2010). Effects of boundary layer particle formation on cloud droplet number and changes in cloud albedo from 1850 to 2000. *Atmospheric Chemistry and Physics*, 10(2):695–705.

Meskhidze, N., Nenes, A., Conant, W. C., and Seinfeld, J. H. (2005). Evaluation of a new cloud droplet activation parameterization with in situ data from crystal-face and cstripe. *Journal of Geophysical Research: Atmospheres*, 110(D16).

Metzger, A., Verheggen, B., Dommen, J., Duplissy, J., Prevot, A. S., Weingartner, E., Riipinen, I., Kulmala, M., Spracklen, D. V., Carslaw, K. S., et al. (2010). Evidence for the role of organics in aerosol particle formation under atmospheric conditions. *Proceedings of the National Academy of Sciences*, 107(15):6646–6651.

Mikkonen, S., Korhonen, H., Romakkaniemi, S., Smith, J., Joutsensaari, J., Lehtinen, K., Hamed, A., Breider, T., Birmili, W., Spindler, G., et al. (2011). Meteorological and trace gas factors affecting the number concentration of atmospheric aitken (Dp= 50 nm) particles in the continental boundary layer: parameterization using a multivariate mixed effects model. *Geoscientific Model Development*, 4(1):1–13.

Mönkkönen, P., Koponen, I., Lehtinen, K., Hämeri, K., Uma, R., and Kulmala, M. (2005). Measurements in a highly polluted asian mega city: observations of aerosol number size distribution, modal parameters and nucleation events. *Atmospheric Chemistry and Physics*, 5(1):57–66.

Monks, S. A., Arnold, S. R., Hollaway, M. J., Pope, R. J., Wilson, C., Feng, W., Emmerson, K. M., Kerridge, B. J., Latter, B. L., Miles, G. M., et al. (2017). The tomcat global chemical transport model v1. 6: description of chemical mechanism and model evaluation. *Geoscientific Model Development*, 10(8):3025.

Murphy, S., Sorooshian, A., Kroll, J., Ng, N., Chhabra, P., Tong, C., Surratt, J., Knipping, E., Flagan, R., and Seinfeld, J. (2007). Secondary aerosol formation from atmospheric reactions of aliphatic amines. *Atmospheric Chemistry and Physics*, 7(9):2313–2337.

Na, K., Moon, K.-C., and Kim, Y. P. (2005). Source contribution to aromatic VOC concentration and ozone formation potential in the atmosphere of seoul. *Atmospheric environment*, 39(30):5517–5524.

Napari, I., Noppel, M., Vehkamäki, H., and Kulmala, M. (2002). Parametrization of ternary nucleation rates for H2SO4-NH3-H2O vapors. *Journal of Geophysical Research: Atmospheres*, 107(D19).

Nenes, A., Ghan, S., Abdul-Razzak, H., Chuang, P. Y., and Seinfeld, J. H. (2001). Kinetic limitations on cloud droplet formation and impact on cloud albedo. *Tellus B: Chemical and Physical Meteorology*, 53(2):133–149.

Nenes, A. and Seinfeld, J. H. (2003). Parameterization of cloud droplet formation in global climate models. *Journal of Geophysical Research: Atmospheres*, 108(D14).

Ng, N. L., Brown, S. S., Archibald, A. T., Atlas, E., Cohen, R. C., Crowley, J. N., Day, D. A., Donahue, N. M., Fry, J. L., Fuchs, H., et al. (2017). Nitrate radicals and biogenic volatile organic compounds: oxidation, mechanisms, and organic aerosol. *Atmospheric Chemistry and Physics*, 17(3):2103–2162.

Ng, N. L., Herndon, S. C., Trimborn, A., Canagaratna, M. R., Croteau, P., Onasch, T. B., Sueper, D., Worsnop, D. R., Zhang, Q., Sun, Y., et al. (2011). An aerosol chemical speciation monitor (acsm) for routine monitoring of the composition and mass concentrations of ambient aerosol. *Aerosol Science and Technology*, 45(7):780–794.

Nightingale, P. D., Malin, G., Law, C. S., Watson, A. J., Liss, P. S., Liddicoat, M. I., Boutin, J., and Upstill-Goddard, R. C. (2000). In situ evaluation of air-sea gas exchange parameterizations using novel conservative and volatile tracers. *Global Biogeochemical Cycles*, 14(1):373–387.

O'Dowd, C., McFiggans, G., Creasey, D. J., Pirjola, L., Hoell, C., Smith, M. H., Allan, B. J., Plane, J., Heard, D. E., Lee, J. D., et al. (1999). On the photochemical production of new particles in the coastal boundary layer. *Geophysical Research Letters*, 26(12):1707–1710.

O'Dowd, C. D., Aalto, P., Hmeri, K., Kulmala, M., and Hoffmann, T. (2002). Aerosol formation: Atmospheric particles from organic vapours. *Nature*, 416(6880):497–498.

O'Dowd, C. D., Facchini, M. C., Cavalli, F., Ceburnis, D., Mircea, M., Decesari, S., Fuzzi, S., Yoon, Y. J., and Putaud, J.-P. (2004). Biogenically driven organic contribution to marine aerosol. *Nature*, 431(7009):676.

Odum, J. R., Hoffmann, T., Bowman, F., Collins, D., Flagan, R. C., and Seinfeld, J. H. (1996). Gas/particle partitioning and secondary organic aerosol yields. *Environmental Science & Technology*, 30(8):2580–2585.

Odum, J. R., Jungkamp, T., Griffin, R., Flagan, R. C., and Seinfeld, J. H. (1997). The atmospheric aerosol-forming potential of whole gasoline vapor. *Science*, 276(5309):96–99.

Paasonen, P., Nieminen, T., Asmi, E., Manninen, H., Petäjä, T., Plass-Dülmer, C., Flentje, H., Birmili, W., Wiedensohler, A., Hõrrak, U., et al. (2010). On the roles of sulphuric acid and low-volatility organic vapours in the initial steps of atmospheric new particle formation. *Atmospheric Chemistry and Physics*, 10(22):11223–11242.

Pandis, S. N., Harley, R. A., Cass, G. R., and Seinfeld, J. H. (1992). Secondary organic aerosol formation and transport. *Atmospheric Environment. Part A. General Topics*, 26(13):2269–2282.

Pandis, S. N., Paulson, S. E., Seinfeld, J. H., and Flagan, R. C. (1991). Aerosol formation in the photooxidation of isoprene and β-pinene. *Atmospheric Environment. Part A. General Topics*, 25(5-6):997–1008.

Pankow, J. F. (1994). An absorption model of the gas/aerosol partitioning in-

volved in the formation of secondary organic aerosol. *Atmospheric Environment*, 28(2):189–193.

Paulot, F., Crounse, J. D., Kjaergaard, H. G., Kürten, A., Clair, J. M. S., Seinfeld, J. H., and Wennberg, P. O. (2009). Unexpected epoxide formation in the gas-phase photooxidation of isoprene. *Science*, 325(5941):730–733.

Paulson, S. E. and Orlando, J. J. (1996). The reactions of ozone with alkenes: An important source of HOx in the boundary layer. *Geophysical Research Letters*, 23(25):3727–3730.

Perraud, V., Bruns, E. A., Ezell, M. J., Johnson, S. N., Yu, Y., Alexander, M. L., Zelenyuk, A., Imre, D., Chang, W. L., Dabdub, D., et al. (2012). Nonequilibrium atmospheric secondary organic aerosol formation and growth. *Proceedings of the National Academy of Sciences*, 109(8):2836–2841.

Petters, M. and Kreidenweis, S. (2007). A single parameter representation of hygroscopic growth and cloud condensation nucleus activity. *Atmospheric Chemistry and Physics*, 7(8):1961–1971.

Philip, S., Martin, R., Pierce, J., Jimenez, J.-L., Zhang, Q., Canagaratna, M., Spracklen, D., Nowlan, C., Lamsal, L., Cooper, M., et al. (2014). Spatially and seasonally resolved estimate of the ratio of organic mass to organic carbon. *Atmospheric environment*, 87:34–40.

Pierce, J. and Adams, P. (2009). Uncertainty in global CCN concentrations from uncertain aerosol nucleation and primary emission rates. *Atmospheric Chemistry and Physics*, 9(4):1339–1356.

Pierce, J., Leaitch, W., Liggio, J., Westervelt, D., Wainwright, C., Abbatt, J., Ahlm, L., Al-Basheer, W., Cziczo, D., Hayden, K., et al. (2012). Nucleation and condensational growth to CCN sizes during a sustained pristine biogenic

SOA event in a forested mountain valley. *Atmospheric Chemistry and Physics*, 12(7):3147–3163.

Pierce, J., Riipinen, I., Kulmala, M., Ehn, M., Petäjä, T., Junninen, H., Worsnop, D., and Donahue, N. (2011). Quantification of the volatility of secondary organic compounds in ultrafine particles during nucleation events. *Atmospheric Chemistry and Physics*, 11(17):9019–9036.

Pöschl, U. (2003). Aerosol particle analysis: challenges and progress. *Analytical and Bioanalytical chemistry*, 375(1):30–32.

Pöschl, U. (2005). Atmospheric aerosols: composition, transformation, climate and health effects. *Angewandte Chemie International Edition*, 44(46):7520–7540.

Pöschl, U., Martin, S., Sinha, B., Chen, Q., Gunthe, S., Huffman, J., Borrmann, S., Farmer, D., Garland, R., Helas, G., et al. (2010). Rainforest aerosols as biogenic nuclei of clouds and precipitation in the Amazon. *science*, 329(5998):1513–1516.

Prather, M. J. (1986). Numerical advection by conservation of second-order moments. *Journal of Geophysical Research: Atmospheres*, 91(D6):6671–6681.

Pringle, K., Carslaw, K., Spracklen, D., Mann, G., and Chipperfield, M. (2009). The relationship between aerosol and cloud drop number concentrations in a global aerosol microphysics model. *Atmospheric Chemistry & Physics Discussions*, 9(1).

Pye, H. O. and Seinfeld, J. H. (2010). A global perspective on aerosol from low-volatility organic compounds. *Atmospheric Chemistry and Physics*, 10(9):4377–4401.

Raes, F., Janssens, A., and Van Dingenen, R. (1986). The role of ion-induced aerosol formation in the lower atmosphere. *Journal of Aerosol Science*, 17(3):466–470.

Raes, F., Van Dingenen, R., Vignati, E., Wilson, J., Putaud, J.-P., Seinfeld, J. H., and Adams, P. (2000). Formation and cycling of aerosols in the global troposphere. *Atmospheric environment*, 34(25):4215–4240.

Ramanathan, V., Crutzen, P., Kiehl, J., and Rosenfeld, D. (2001). Aerosols, climate, and the hydrological cycle. *science*, 294(5549):2119–2124.

Rap, A., Scott, C. E., Spracklen, D. V., Bellouin, N., Forster, P. M., Carslaw, K. S., Schmidt, A., and Mann, G. (2013). Natural aerosol direct and indirect radiative effects. *Geophysical Research Letters*, 40(12):3297–3301.

Reddington, C., Carslaw, K., Stier, P., Schutgens, N., Coe, H., Liu, D., Allan, J., Pringle, K., Lee, L., Yoshioka, M., et al. (2017). The global aerosol synthesis and science project (gassp): measurements and modelling to reduce uncertainty.

Reddington, C. L., Spracklen, D. V., Artaxo, P., Ridley, D. A., Rizzo, L. V., and Arana, A. (2016). Analysis of particulate emissions from tropical biomass burning using a global aerosol model and long-term surface observations. *Atmospheric Chemistry and Physics*, 16(17):11083–11106.

Regayre, L., Pringle, K., Booth, B., Lee, L., Mann, G., Browse, J., Woodhouse, M., Rap, A., Reddington, C., and Carslaw, K. (2014). Uncertainty in the magnitude of aerosol-cloud radiative forcing over recent decades. *Geophysical Research Letters*, 41(24):9040–9049.

Regayre, L. A., Pringle, K. J., Lee, L. A., Rap, A., Browse, J., Mann, G. W., Reddington, C. L., Carslaw, K. S., Booth, B. B., and Woodhouse, M. T. (2015). The climatic importance of uncertainties in regional aerosol–cloud radiative forcings over recent decades. *Journal of Climate*, 28(17):6589–6607.

Riccobono, F., Schobesberger, S., Scott, C. E., Dommen, J., Ortega, I. K., Rondo, L., Almeida, J., Amorim, A., Bianchi, F., Breitenlechner, M., et al. (2014). Ox-

idation products of biogenic emissions contribute to nucleation of atmospheric particles. *Science*, 344(6185):717–721.

Richters, S., Herrmann, H., and Berndt, T. (2016). Highly oxidized ro2 radicals and consecutive products from the ozonolysis of three sesquiterpenes. *Environmental science & technology*, 50(5):2354–2362.

Riipinen, I., Pierce, J., Yli-Juuti, T., Nieminen, T., Hakkinen, S., Ehn, M., Junninen, H., Lehtipalo, K., Petaja, T., Slowik, J., et al. (2011). Organic condensation: a vital link connecting aerosol formation to cloud condensation nuclei (CCN) concentrations. *Atmospheric Chemistry and Physics*, 11:3865.

Riipinen, I., Yli-Juuti, T., Pierce, J. R., Petäjä, T., Worsnop, D. R., Kulmala, M., and Donahue, N. M. (2012). The contribution of organics to atmospheric nanoparticle growth. *Nature Geoscience*, 5(7):453–458.

Rinne, J., Bäck, J., and Hakola, H. (2009). Biogenic volatile organic compound emissions from the eurasian taiga: current knowledge and future directions. *Boreal Environment Research*, 14(4).

Rissler, J., Vestin, A., Swietlicki, E., Fisch, G., Zhou, J., Artaxo, P., and Andreae, M. (2006). Size distribution and hygroscopic properties of aerosol particles from dry-season biomass burning in amazonia. *Atmospheric Chemistry and Physics*, 6(2):471–491.

Rizzo, L., Artaxo, P., Guenther, A., Karl, T., and Greenberg, J. (2006). Measurement of aerosol and VOC turbulent fluxes over a pristine forest in amazonia. In *AGU Fall Meeting Abstracts*.

Rizzo, L. V., Artaxo, P., Karl, T., Guenther, A., and Greenberg, J. (2010). Aerosol properties, in-canopy gradients, turbulent fluxes and VOC concentrations at a pristine forest site in amazonia. *Atmospheric Environment*, 44(4):503–511.

Robinson, A. L., Donahue, N. M., Shrivastava, M. K., Weitkamp, E. A., Sage, A. M., Grieshop, A. P., Lane, T. E., Pierce, J. R., and Pandis, S. N. (2007). Rethinking organic aerosols: Semivolatile emissions and photochemical aging. *Science*, 315(5816):1259–1262.

Robinson, N., Hamilton, J., Allan, J., Langford, B., Oram, D., Chen, Q., Docherty, K., Farmer, D., Jimenez, J., Ward, M., et al. (2011). Evidence for a significant proportion of secondary organic aerosol from isoprene above a maritime tropical forest. *Atmospheric Chemistry and Physics*, 11(3):1039–1050.

Rossow, W. B. and Schiffer, R. A. (1999). Advances in understanding clouds from isccp. *Bulletin of the American Meteorological Society*, 80(11):2261–2287.

Rotstayn, L. D. and Liu, Y. (2005). A smaller global estimate of the second indirect aerosol effect. *Geophysical research letters*, 32(5).

Sack, T. M., Steele, D. H., Hammerstrom, K., and Remmers, J. (1992). A survey of household products for volatile organic compounds. *Atmospheric Environment. Part A. General Topics*, 26(6):1063–1070.

Schmidt, A., Carslaw, K., Mann, G., Rap, A., Pringle, K., Spracklen, D., Wilson, M., and Forster, P. (2012). Importance of tropospheric volcanic aerosol for indirect radiative forcing of climate. *Atmospheric Chemistry and Physics*, 12(16):7321–7339.

Schröder, F., Kärcher, B., Fiebig, M., and Petzold, A. (2002). Aerosol states in the free troposphere at northern midlatitudes. *Journal of Geophysical Research: Atmospheres*, 107(D21).

Scott, C., Rap, A., Spracklen, D., Forster, P., Carslaw, K., Mann, G., Pringle, K., Kivekäs, N., Kulmala, M., Lihavainen, H., et al. (2014). The direct and indirect

radiative effects of biogenic secondary organic aerosol. *Atmospheric Chemistry and Physics*, 14(1):447–470.

Scott, C., Spracklen, D., Pierce, J., Riipinen, I., D'Andrea, S., Rap, A., Carslaw, K., Forster, P., Artaxo, P., Kulmala, M., et al. (2015). Impact of gas-to-particle partitioning approaches on the simulated radiative effects of biogenic secondary organic aerosol. *Atmospheric Chemistry and Physics*, 15(22):12989–13001.

Shrivastava, M., Cappa, C. D., Fan, J., Goldstein, A. H., Guenther, A. B., Jimenez, J. L., Kuang, C., Laskin, A., Martin, S. T., Ng, N. L., et al. (2016). Recent advances in understanding secondary organic aerosol: implications for global climate forcing. *Reviews of Geophysics*.

Shulman, M. L., Jacobson, M. C., Carlson, R. J., Synovec, R. E., and Young, T. E. (1996). Dissolution behavior and surface tension effects of organic compounds in nucleating cloud droplets. *Geophysical Research Letters*, 23(3):277–280.

Simon, H., Bhave, P., Swall, J., Frank, N., and Malm, W. (2011). Determining the spatial and seasonal variability in om/oc ratios across the us using multiple regression. *Atmospheric Chemistry and Physics*, 11(6):2933–2949.

Sipilä, M., Berndt, T., Petäjä, T., Brus, D., Vanhanen, J., Stratmann, F., Patokoski, J., Mauldin, R. L., Hyvärinen, A.-P., Lihavainen, H., et al. (2010). The role of sulfuric acid in atmospheric nucleation. *Science*, 327(5970):1243–1246.

Sorjamaa, R., Svenningsson, B., Raatikainen, T., Henning, S., Bilde, M., and Laaksonen, A. (2004). The role of surfactants in köhler theory reconsidered. *Atmospheric Chemistry and Physics*, 4(8):2107–2117.

Sorokin, A. and Arnold, F. (2007). Laboratory study of cluster ions formation in H2SO4-H2O system: implications for threshold concentration of gaseous H2SO4 and ion-induced nucleation kinetics. *Atmospheric environment*, 41(18):3740–3747.

Spracklen, D., Carslaw, K., Kulmala, M., Kerminen, V.-M., Mann, G., and Sihto, S.-L. (2006). The contribution of boundary layer nucleation events to total particle concentrations on regional and global scales. *Atmospheric Chemistry and Physics*, 6(12):5631–5648.

Spracklen, D., Carslaw, K., Pöschl, U., Rap, A., and Forster, P. (2011a). Global cloud condensation nuclei influenced by carbonaceous combustion aerosol. *Atmospheric Chemistry and Physics*, 11(17):9067–9087.

Spracklen, D., Jimenez, J., Carslaw, K., Worsnop, D., Evans, M., Mann, G., Zhang, Q., Canagaratna, M., Allan, J., Coe, H., et al. (2011b). Aerosol mass spectrometer constraint on the global secondary organic aerosol budget. *Atmospheric Chemistry and Physics*, 11(23):12109–12136.

Spracklen, D., Pringle, K., Carslaw, K., Chipperfield, M., and Mann, G. (2005a). A global off-line model of size-resolved aerosol microphysics: I. model development and prediction of aerosol properties. *Atmospheric Chemistry and Physics*, 5(8):2227–2252.

Spracklen, D., Pringle, K., Carslaw, K., Chipperfield, M., and Mann, G. (2005b). A global off-line model of size-resolved aerosol microphysics: Ii. identification of key uncertainties. *Atmospheric Chemistry and Physics*, 5(12):3233–3250.

Spracklen, D. and Rap, A. (2013). Natural aerosol–climate feedbacks suppressed by anthropogenic aerosol. *Geophysical Research Letters*, 40(19):5316–5319.

Spracklen, D. V., Carslaw, K. S., Kulmala, M., Kerminen, V.-M., Sihto, S.-L., Riipinen, I., Merikanto, J., Mann, G. W., Chipperfield, M. P., Wiedensohler, A., et al. (2008). Contribution of particle formation to global cloud condensation nuclei concentrations. *Geophysical Research Letters*, 35(6).

Spracklen, D. V., Carslaw, K. S., Merikanto, J., Mann, G. W., Reddington, C. L., Pickering, S., Ogren, J. A., Andrews, E., Baltensperger, U., Weingartner, E., et al. (2010). Explaining global surface aerosol number concentrations in terms of primary emissions and particle formation. *Atmospheric Chemistry and Physics*, 10(10):4775–4793.

Staudt, M., Bertin, N., Frenzel, B., and Seufert, G. (2000). Seasonal variation in amount and composition of monoterpenes emitted by young pinus pinea trees–implications for emission modeling. *Journal of Atmospheric Chemistry*, 35(1):77–99.

Stier, P., Feichter, J., Kinne, S., Kloster, S., Vignati, E., Wilson, J., Ganzeveld, L., Tegen, I., Werner, M., Balkanski, Y., et al. (2005). The aerosol-climate model ECHAM5-HAM. *Atmospheric Chemistry and Physics*, 5(4):1125–1156.

Stier, P., Feichter, J., Kloster, S., Vignati, E., and Wilson, J. (2006). Emission-induced nonlinearities in the global aerosol system: Results from the ECHAM5-HAM aerosol-climate model. *Journal of climate*, 19(16):3845–3862.

Stocker, T. F., Qin, D., Plattner, G.-K., Tignor, M., Allen, S. K., Boschung, J., Nauels, A., Xia, Y., Bex, B., and Midgley, B. (2013). Ipcc, 2013: climate change 2013: the physical science basis. contribution of working group i to the fifth assessment report of the intergovernmental panel on climate change.

Stokes, R. and Robinson, R. (1966). Interactions in aqueous nonelectrolyte solutions. i. solute-solvent equilibria. *The Journal of Physical Chemistry*, 70(7):2126–2131.

Strader, R., Lurmann, F., and Pandis, S. N. (1999). Evaluation of secondary organic aerosol formation in winter. *Atmospheric Environment*, 33(29):4849–4863.

Sun, J. and Ariya, P. A. (2006). Atmospheric organic and bio-aerosols as cloud condensation nuclei (CCN): A review. *Atmospheric Environment*, 40(5):795–820.

Surratt, J. D., Chan, A. W., Eddingsaas, N. C., Chan, M., Loza, C. L., Kwan, A. J., Hersey, S. P., Flagan, R. C., Wennberg, P. O., and Seinfeld, J. H. (2010). Reactive intermediates revealed in secondary organic aerosol formation from isoprene. *Proceedings of the National Academy of Sciences*, 107(15):6640–6645.

Taylor, K. E. (2001). Summarizing multiple aspects of model performance in a single diagram. *Journal of Geophysical Research: Atmospheres*, 106(D7):7183–7192.

Tiedtke, M. (1989). A comprehensive mass flux scheme for cumulus parameterization in large-scale models. *Monthly Weather Review*, 117(8):1779–1800.

Tröstl, J., Chuang, W. K., Gordon, H., Heinritzi, M., Yan, C., Molteni, U., Ahlm, L., Frege, C., Bianchi, F., Wagner, R., et al. (2016). The role of low-volatility organic compounds in initial particle growth in the atmosphere. *Nature*, 533(7604):527–531.

Tsigaridis, K., Daskalakis, N., Kanakidou, M., Adams, P., Artaxo, P., Bahadur, R., Balkanski, Y., Bauer, S., Bellouin, N., Benedetti, A., et al. (2014). The aerocom evaluation and intercomparison of organic aerosol in global models. *Atmospheric Chemistry and Physics*, 14(19):10845–10895.

Tsigaridis, K. and Kanakidou, M. (2003). Global modelling of secondary organic aerosol in the troposphere: a sensitivity analysis. *Atmospheric Chemistry and Physics*, 3(5):1849–1869.

Tunved, P., Hansson, H.-C., Kerminen, V.-M., Ström, J., Dal Maso, M., Lihavainen, H., Viisanen, Y., Aalto, P., Komppula, M., and Kulmala, M. (2006). High natural aerosol loading over boreal forests. *Science*, 312(5771):261–263.

Vakkari, V., Beukes, J., Laakso, H., Mabaso, D., Pienaar, J., Kulmala, M., and Laakso, L. (2013). Long-term observations of aerosol size distributions in semi-

clean and polluted savannah in south africa. *Atmospheric Chemistry and Physics*, 13(4):1751–1770.

Van Der Werf, G. R., Randerson, J. T., Collatz, G. J., and Giglio, L. (2003). Carbon emissions from fires in tropical and subtropical ecosystems. *Global Change Biology*, 9(4):547–562.

Vehkamäki, H., Maso, M. D., Hussein, T., Flanagan, R., Hyvärinen, A., Lauros, J., Merikanto, P., Mönkkönen, M., Pihlatie, K., Salminen, K., et al. (2004). Atmospheric particle formation events at värriö measurement station in finnish lapland 1998-2002. *Atmospheric Chemistry and Physics*, 4(7):2015–2023.

Vehkamäki, H. and Riipinen, I. (2012). Thermodynamics and kinetics of atmospheric aerosol particle formation and growth. *Chemical Society Reviews*, 41(15):5160–5173.

Vignati, E., Karl, M., Krol, M., Wilson, J., Stier, P., and Cavalli, F. (2010). Sources of uncertainties in modelling black carbon at the global scale. *Atmospheric chemistry and physics*, 10(6):2595–2611.

Vignati, E., Wilson, J., and Stier, P. (2004). M7: An efficient size-resolved aerosol microphysics module for large-scale aerosol transport models. *Journal of Geophysical Research: Atmospheres*, 109(D22).

Volkamer, R., Jimenez, J. L., San Martini, F., Dzepina, K., Zhang, Q., Salcedo, D., Molina, L. T., Worsnop, D. R., and Molina, M. J. (2006). Secondary organic aerosol formation from anthropogenic air pollution: Rapid and higher than expected. *Geophysical Research Letters*, 33(17).

Wang, J., Lee, Y.-N., Daum, P. H., Jayne, J., and Alexander, M. (2008). Effects of aerosol organics on cloud condensation nucleus (CCN) concentration and first indirect aerosol effect. *Atmospheric Chemistry and Physics*, 8(21):6325–6339.

Wang, M. and Penner, J. (2009). Aerosol indirect forcing in a global model with particle nucleation. *Atmospheric Chemistry & Physics*, 9(1).

Wang, S., Wu, R., Berndt, T., Ehn, M., and Wang, L. (2017). Formation of highly oxidized radicals and multifunctional products from the atmospheric oxidation of alkylbenzenes. *Environmental Science & Technology*, 51(15):8442–8449.

Weber, R., Marti, J., McMurry, P., Eisele, F., Tanner, D., and Jefferson, A. (1996). Measured atmospheric new particle formation rates: Implications for nucleation mechanisms. *Chemical Engineering Communications*, 151(1):53–64.

Weber, R., Marti, J., McMurry, P., Eisele, F., Tanner, D., and Jefferson, A. (1997). Measurements of new particle formation and ultrafine particle growth rates at a clean continental site. *Journal of Geophysical Research: Atmospheres*, 102(D4):4375–4385.

Weber, R. J., Sullivan, A. P., Peltier, R. E., Russell, A., Yan, B., Zheng, M., De Gouw, J., Warneke, C., Brock, C., Holloway, J. S., et al. (2007). A study of secondary organic aerosol formation in the anthropogenic-influenced southeastern united states. *Journal of Geophysical Research: Atmospheres*, 112(D13).

Wehner, B., Petäjä, T., Boy, M., Engler, C., Birmili, W., Tuch, T., Wiedensohler, A., and Kulmala, M. (2005). The contribution of sulfuric acid and non-volatile compounds on the growth of freshly formed atmospheric aerosols. *Geophysical research letters*, 32(17).

White, W. and Roberts, P. (1977). On the nature and origins of visibility-reducing aerosols in the los angeles air basin. *Atmospheric Environment (1967)*, 11(9):803–812.

Woo, K., Chen, D., Pui, D., and McMurry, P. (2001). Measurement of atlanta

aerosol size distributions: observations of ultrafine particle events. *Aerosol Science & Technology*, 34(1):75–87.

Young, L.-H., Benson, D. R., Kameel, F. R., Pierce, J. R., Junninen, H., Kulmala, M., and Lee, S.-H. (2008). Laboratory studies of H2SO4/H2O binary homogeneous nucleation from the SO2+OH reaction: evaluation of the experimental setup and preliminary results. *Atmospheric Chemistry and Physics*, 8(16):4997–5016.

Yu, F. and Luo, G. (2009). Simulation of particle size distribution with a global aerosol model: contribution of nucleation to aerosol and CCN number concentrations. *Atmospheric Chemistry and Physics*, 9(20):7691–7710.

Yu, S. (2000). Role of organic acids (formic, acetic, pyruvic and oxalic) in the formation of cloud condensation nuclei (CCN): a review. *Atmospheric Research*, 53(4):185–217.

Yu, S., Eder, B., Dennis, R., Chu, S.-H., and Schwartz, S. E. (2006). New unbiased symmetric metrics for evaluation of air quality models. *Atmospheric Science Letters*, 7(1):26–34.

Zdanovskii, A. (1948). New methods for calculating solubilities of electrolytes in multicomponent systems. *Zh. Fiz. Khim*, 22(1475):1475–85.

Zhang, Q., Jimenez, J., Canagaratna, M., Allan, J., Coe, H., Ulbrich, I., Alfarra, M., Takami, A., Middlebrook, A., Sun, Y., et al. (2007). Ubiquity and dominance of oxygenated species in organic aerosols in anthropogenically-influenced northern hemisphere midlatitudes. *Geophysical Research Letters*, 34(13).

Zhang, R., Suh, I., Zhao, J., Zhang, D., Fortner, E. C., Tie, X., Molina, L. T., and Molina, M. J. (2004). Atmospheric new particle formation enhanced by organic acids. *Science*, 304(5676):1487–1490.

Zhang, X., Cappa, C. D., Jathar, S. H., McVay, R. C., Ensberg, J. J., Kleeman, M. J., and Seinfeld, J. H. (2014). Influence of vapor wall loss in laboratory chambers on yields of secondary organic aerosol. *Proceedings of the National Academy of Sciences*, 111(16):5802–5807.

Zhang, Y., Wang, X., Barletta, B., Simpson, I. J., Blake, D. R., Fu, X., Zhang, Z., He, Q., Liu, T., Zhao, X., et al. (2013). Source attributions of hazardous aromatic hydrocarbons in urban, suburban and rural areas in the pearl river delta (prd) region. *Journal of hazardous materials*, 250:403–411.

Zhao, J., Ortega, J., Chen, M., McMurry, P., and Smith, J. (2013). Dependence of particle nucleation and growth on high-molecular-weight gas-phase products during ozonolysis of α-pinene. *Atmos. Chem. Phys*, 13(15):7631–7644.

Zhou, J., Swietlicki, E., Hansson, H. C., and Artaxo, P. (2002). Submicrometer aerosol particle size distribution and hygroscopic growth measured in the amazon rain forest during the wet season. *Journal of Geophysical Research: Atmospheres*, 107(D20).